MATERIALS AND TECHNIQUES FOR THERMOLUMINESCENCE DATING

by

Riaz Ahmad Akber
M. Sc. (Physics)
M. Sc. (Nuclear Technology)

A Thesis
presented for the degree of
DOCTOR OF PHILOSOPHY
at the
UNIVERSITY OF ADELAIDE
(Department of Physics)

October, 1986.

STATEMENT

To the best of my knowledge and belief, the work presented in this thesis has not previously been published or written by another person, except where duly cited. It contains no material submitted for the award of any other degree or diploma from any educational institution.

Riaz Ahmad Akber

Adelaide

October, 1986.

CONTENTS

CHAPTER THREE: REVISED DESIGN OF THE EQUIPMENT

CHAPTER FOUR: COMPUTATION OF SPECTRA

CHAPTER FIVE: THE FELDSPARS

SUMMARY

Research work in the present thesis is related to the physics of methods, particularly thermoluminescence (TL) which can be applied to the solution of problems associated with the provision of dates and time scales in geological and archaeological context.

For most thermoluminescence work in dating and elsewhere, a two dimensional glowcurve (i.e. an intensity vs. temperature plot) suffices. But for a better understanding of the physics involved, and for reinforcement of the technique, it is important to have information about the emission spectrum as well. The significance of thermoluminescence emission spectroscopy has been discussed in detail in the introductory Chapter One.

The natural minerals used for thermoluminescence dating have a TL sensitivity such that their emission spectra cannot be efficiently seen by the conventional devices, unless subjected to very high radiation doses. High radiation doses may, on the other hand, change the spectral character through additional radiation damage to the crystal structure and the entire information may thus become non-representative. Chapters Two to Four describe the design details and working principles of a Fourier transform spectrometer capable of registering TL spectra induced by natural, or comparable number of Grays of laboratory radiation dose given to most natural minerals used for thermoluminescence dating.

The following four chapters deal with some applications of this equipment particularly to the study of thermoluminescence in feldspars. The name 'feldspar' covers a wide range of structural and compositional variety of alumino-silicate minerals and the present study is based on

the natural and beta radiation induced emission spectra of twenty eight different samples covering this wide range. Chapter Five provides a basic introduction to feldspars along with some details about the present samples.

Chapters Six and Seven deal with the thermoluminescence in K-Na and Na-Ca feldspars respectively. High sodic plagioclases and K-feldspars show an emission band in the 380-400 nm region. High sodic plagioclases exhibit another band near 540 nm. Both the intermediate composition K-Na feldspars and high calcic plagioclases show a broad band emission spectrum with its peak around 430-450 nm. Other small emission bands are also seen in different samples. Anomalies with mixed thermoluminescence behaviour also exist and are discussed in separate sections. The TL intensity appears to vary systematically by several orders of magnitude, particularly on the Na-Ca axis. This explains potential difficulties in dating high calcic feldspars.

Other interesting applications to the problems like dating the Pacific Island pottery and pre-dose effect in 110°C peak in quartz have been described in Chapter Eight.

The present limited study can by no means be regarded as complete or comprehensive on the subject of TL in feldspars. However, it adequately demonstrates the potential of the equipment and suggests several areas for research and further investigation, some of which have been pointed out in the last chapter of the thesis.

A part of the research work on estimating the low-level alpha activity in soils has been included in the Appendix to the main text.

ACKNOWLEDGEMENTS

'A person who is not thankful to people is not thankful to God.'

Muhammad.

I would like to acknowledge the continuing help and enthusiasm received from my supervisor Professor John Prescott. Sincere thanks are also due to the other members of the group: John Hutton, Gillian Robertson, Nigel Spooner and Phil Fox. John Hutton carried out the XRF analysis of most of the feldspars and also fused the lithium borate glass for alpha counting. Dr. Gillian Robertson provided the Pacific Island and Thai pottery samples used in the present studies. Hans Jensen was nearing completion of his Ph.D. studies at the beginning of my research project. His contribution to the first design of the equipment is gratefully acknowledged.

The revised design was made possible through the invaluable technical assistance and support of the Mechanical Workshop and the Electronic Services groups of the department. Bill Old constructed the mechanical components, Brian Fuller modified the electronics, designed the machine-computer interface and wrote programmes to run it. Much help came from several other members of the department and I extend my sincere thanks to all of them.

Dr. John Jones from the Department of Geology supplied most of the feldspar samples and useful information about their structure. His

support through several discussions is also worth acknowledging. Dr. Jones is recovering from a stroke at the time of writing these lines and I extend my sincere wishes to him to get well soon. Thanks are also due to the Geology Museum curator, Mrs. Stojanovic.

Many families helped us settling in the Australian social setup and thanks are due to all of them. Particularly I extend my sincere thanks to Elaine Gregory for the efficient typing of the thesis, but above all, being such a nice family friend. Steve Marks helped creating some of the diagrams used in this thesis.

I was in receipt of a scholarship from the University of Adelaide Research Grant.

I would also like to thank Sadia for her support and encouragement, for typing the first draft of some chapters and being such a good mother to Rizwana, Fatima and Hajra. I am deeply grateful to my mother for her contribution through continuous prayers and encouraging letters.

CHAPTER ONE

INTRODUCTION

"I tried the experiment myself also. And at the same time observed that as it grew hot in the fire its green colour was changed into a sky-blue; which it likewise retained so long as it continued to shine. But after that, recovered its native green again."

Nathanial Grew (1681)
while classifying the gem collection
belonging to Gresham College, London.

1.1 INTRODUCTION

This small introductory chapter only provides some basic thermoluminescence information related to the work presented in this thesis. The phenomenon of thermoluminescence (or strictly speaking, radiation induced thermally stimulated emission) refers to the virtue of a material of emitting light as it is heated after its exposure to ionizing radiation. Several natural minerals, dielectric solids, glasses and even some organic materials exhibit this property to a varying degree of sensitivity.

Applications of thermoluminescence (commonly abbreviated as TL) have increased during the past few decades and extend to various branches of science and technology. According to a recent review by Singhvi and Wagner (1985), there is a research publication almost every day covering one or other of the aspects of thermoluminescence. Historically, the phenomenon was certainly reported by Sir Robert Boyle in 1664. Becker (1973) writes that medieval alchemists were aware that certain minerals glow faintly when heated in the dark.

1.2 THERMOLUMINESCENCE: BASIC

The basic process of thermoluminescence comprises the following main steps:

(i) Interaction of ionizing radiation produces a series of free electrons and holes in the medium. Most of these charges promptly recombine and the energy is dissipated as either heat or prompt luminescence. A fraction of the free charges may, however, diffuse through the lattice and be 'trapped' at locations of lattice defects due to the presence of impurities, interstitions and ion vacancies.

(ii) The residence time of a charge carrier in a certain trap location is determined by the trap depth and the storage temperature, the probability 'p' being given by

$$p = s \exp(-E/kT) \qquad (1.1)$$

Where the activation energy 'E' corresponds to the trap depth, 'T' is the temperature in °K and 'k' the Boltzman constant. The factor 's' is a lattice dependant frequency or pre-exponential factor. Typically, mean lifetimes (1/p) at ambient temperature may vary from about 1 second to 10^{15} seconds for very shallow to very deep traps.

(iii) Equation (1.1) suggests that the average residence or mean lifetime decreases by orders of magnitude as the sample is heated to a few hundred Celsius above the room temperature. External thermal stimulation, therefore, results in emptying the trapping sites and promoting the charge carriers to their respective

bands. Some of these recombine with an opposite charge carrier located at another appropriate centre, and the emitted light is seen in the UV-visible region of the electromagnetic spectrum - hence the name 'thermoluminescence'.

Details of relationships between the detrapping rates, temperature and TL intensity have been developed and discussed by various authors (see e.g. Randall and Wilkins, 1945 a,b; Garlick and Gibson, 1948 and Halperin and Braner, 1960, for pioneering work and latest books like Chen and Kirsh, 1981; Horowitz, 1984 and McKeever, 1985 for comprehensive discussions).

The above scheme is illustrated in Figure 1.1. In practice, the thermoluminescence phenomenon is more complicated than this. More than one trapping and luminescence centre exists in most natural minerals. The charge liberation and recombination may also take place in more than one way.

1.3 THERMOLUMINESCENCE DATING

Major applications of thermoluminescence include radiation dosimetry in health and environmental physics (Horowitz, 1984), age determination of samples of archaeological and geological interest (Fleming, 1979; Aitken, 1985), mineral identification and other specific applications in geology and mineralogy (McDougall, 1968; Sankaran et al. 1982, 1983).

Thermoluminescence dating is of more concern for the purpose of the present thesis and it is appropriate to include a brief section for further reference. Details of various dating methods cited in this section and at other places in this thesis can be seen in various books like Fleming (1979), Aitken (1985), McKeever (1985) and proceedings of

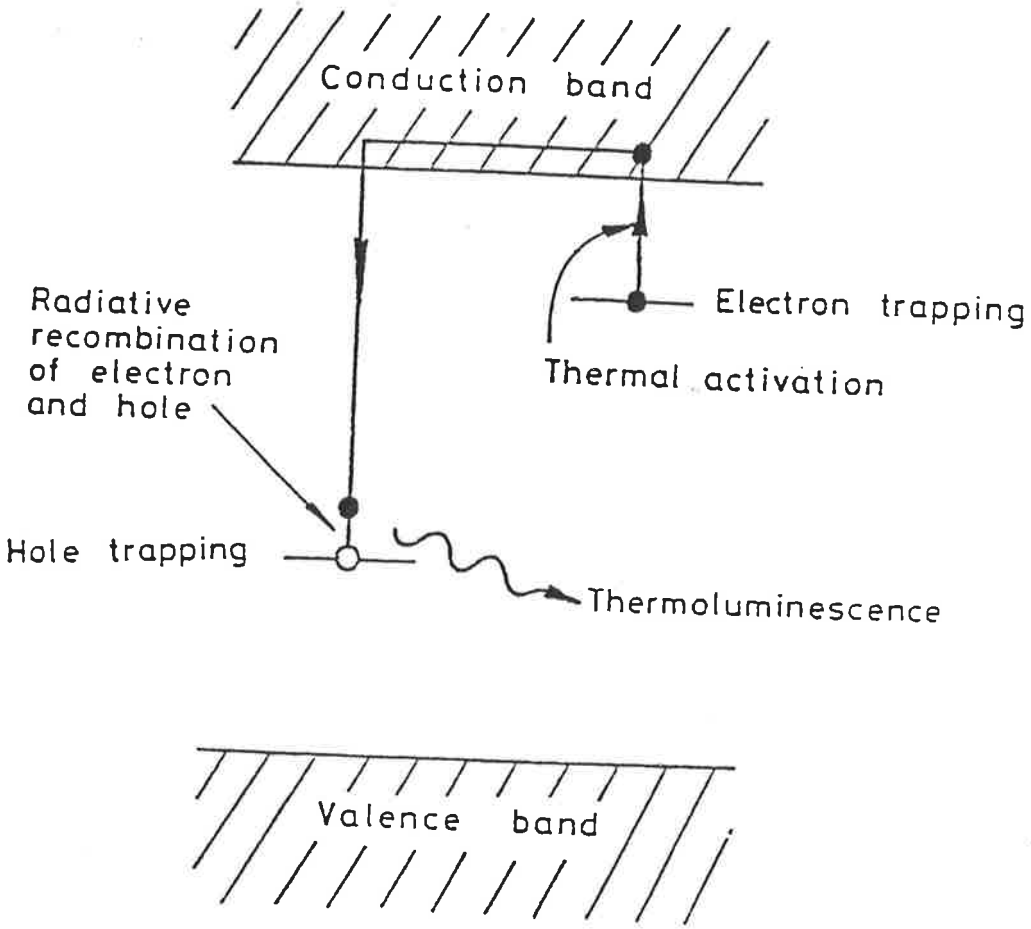

FIGURE 1.1: Thermoluminescene as commonly explained using the band theory. The (electron) trapping and (hole) emission centres are due to lattice defects. Thermal excitation detraps the electron first which is at lesser depth relative to the respective free charge band. It recombines with the hole at the emission centre and a light photon is emitted. Earlier the ionizing radiation produces an avalanche of the charge carriers, a fraction of which gets trapped at the centres like those shown in the figure.

various conferences on this subject (like PACT Journal, Volumes 2, 6 and 9 and Nuclear Tracks Vol 10, Nos. 4-6).

The basic principle of thermoluminescence dating is described through an age equation, which states that the time 'τ' elapsed since the last heating and/or exposure to light of a sample is given by the thermoluminescence signal from a suitable fraction of the sample, provided it is measured in the units of the thermoluminescence induction rate, i.e.

$$\text{Age, } \tau \text{ (yrs)} = \text{TL}/(\text{TL/yr}) \qquad (1.2)$$

The thermoluminescence induction rate (TL/yr) can be found by estimating the annual radiation dose at the site of the sample and the TL sensitivity of the mineral fraction used for dating. The latter is determined by measuring the TL against known radiation dose supplied by calibrated sources while the former is found by employing one or more of different low level in-situ and in-lab radiation monitoring facilities.

Selection of suitable methods for annual dose estimates is also determined by the techniques used for dating. In the feldspar inclusion method, for example, the dominating portion of the radiaiton dose is internally supplied by K-40 when high K-feldspar grains of 0.1-0.3 mm size are extracted from the sample for the purpose of dating (Mejdahl and Winther-Nielsen, 1982; Mejdahl, 1985). Zircon grains, too, tend to contain significantly high uranium compared with the general clay matrix around them and the internal dose is consequently much higher than that supplied by the environments of the grain (Zimmerman, 1979). External radiation dose will dominate if the quartz inclusion technique is

employed for dating using (typically) 0.1 mm quartz grain fraction (Fleming 1970). Both for feldspar and quartz inclusion methods, the (external) alpha dose will be attenuated within a few micrometres of the outer layer, which is eliminated by skinning the grain through acid etching.

The 'inclusion techniques' as described above cannot be used for fine sedimentary deposits and for rock fragments which can be considered homogeneous only on fine grain level. The 'fine grain method' as developed by Zimmerman (1971a) may then be best used. Typically, 1-8 μm grain size fraction is taken and the multi-mineral nature of the sample is ignored. Such a grain size fraction receives a significant alpha dose from its environment.

The 'pre-dose technique' differs from the above mentioned dating methods in the sense that the archaeological age is determined not by finding the natural thermoluminescence but by the sensitivity of the 110°C glow peak of quartz which depends on the amount of radiation dose previously received (Fleming, 1973).

Thermoluminescence dating based on phototransfer technique has also been proposed (Bailiff et al. 1977b, Huntley et al. 1985). The phototransfer involves the transfer of charge from deeper to relatively shallower traps by optical excitation.

1.4 THERMOLUMINESCENCE EMISSION SPECTROSCOPY

1.4.1 Colours in Thermoluminescence

Variety of colours in thermoluminescence attracted TL workers from the time of the early discoveries. Grew (1681) observed the blue thermoluminescence of a green coloured stone. Wedgwood (1792) observed a

blue fluor emitting 'bright green light, resembling that of the the glow-worm' which 'quickly changed into a beautiful lilac, which gradually faded away'. Earlier in 1664, Boyle also observed a warm diamond to give out light almost equal to that of a 'glow-worm'.

According to McKeever (1985), the first thorough thermoluminescence emission spectral studies were, however, caried out by Morse in 1905. The mineral fluorspar was the subject of Morse's observation. McKeever also points out that most of the modern-day theory on trapping, recombination and luminescence has remained unchanged since the pioneering work of Shockley, Rose and Williams from the late 1940's to early 1960s. Harvey (1957) provides an excellent historical perspective up till 1900. More recent work on spectra and some contemporary emission spectrometers are discussed in Chapter 5 of this thesis.

1.4.2 Significance of TL Spectroscopy

Although techniques for spectral measurements are available, most of the routine thermoluminescence applicications in fields like dosimetry and dating appear to make use of the conventional two dimensional (2-D) glowcurves in which the TL intensity is displayed as a function of temperature only and the differences in the light wavelength are disregarded. Nevertheless, a sound understanding of the basic phenomenon almost invariably requires the initial information of 3-D glow curves in which the intensity is displayed as a function of both temperature and wavelength. The temperature and wavelength peaks carry information about the trapping and luminescence centres, respectively. The significance of TL emission spectroscopy or 3-D TL glow curves is illustrated through the following examples.

1.4.2.1 Applications in TL Kinetics

The nature and stability of a thermoluminescence glow-curve is determined through its kinetic parameters like E and s as described in Equation (1.1). Most glow curve kinetics has, however, been developed for applications where the spectral response of the light sensing device is assumed to be constant. In reality, the optical sensitivity of most instruments changes somewhat with the input wavelength. The information extracted from the 2-D glow curves is, therefore, only suitable for kinetic analysis if all the glow peaks arise from a single emission centre. In general more than one emission centre may participate in thermoluminescence from a given mineral and 2-D TL intensities as measured by overlooking the spectral changes may lead to results far from reality.

Only 3-D TL glow curves, corrected for the instrument spectral response, hence provide sufficient information for the glow peak intensities suitable for any kinetic analysis. This argument can be supported by several examples from Chapters Six and Seven of this thesis, where, for a number of samples, the relative intensities of various emission bands will be seen to vary both with the temperature and the radiation dose.

1.4.2.2 Nature of the Emission Centres

Sound information about the nature of the emission centres is often required for establishing specific applications on a stronger fundamental base. An interesting example is that of exploring the nature of thermoluminescence mechanism responsible for the sensitization of the 110°C peak in quartz. As described in the previous section, the sensitivity of

this peak depends upon the radiation dose previously absorbed in the sample. McKeever et al. (1985) suggested that two different emission centres namely $Al^{3}-h^{+}$ and $U-h^{+}$ (U refers to an unknown ion) may be operative at 110°C, leading to 470 nm and 380 nm emission respectively, one of them being related to the pre-dose effect. They predicted that the pre-dose activated quartz should show a greater ratio of 380/470 nm emission. Investigations of this point on archaeological ceramics are included in Chapter Eight.

1.4.2.3 Mineral Identification

In several applications, it is desirable to know the nature of minerals responsible for thermoluminescence signal. Under suitable circumstances the emission spectrum can provide adequate information for mineral identification. An interesting example from fine grain dating of Pacific Islands pottery is discussed in Chapter Eight.

1.4.3 The Spectrometer Design Challenge

During the last two decades or so, several types of equipment have been developed for thermoluminescence emission spectroscopy. Horowitz (1984) and McKeever (1985) provide a comprehensive review. Basic working principles of such equipment is discussed in Chapter Five of this thesis. Whereas most contemporary equipment is capable of providing adequate spectral information, their scope is seriously limited by the fact that, for most natural minerals, radiation dose of several kGy is required to obtain a meaningful spectrum above the background. Such instruments are, therefore, not of much use in context with applications in thermoluminescence dating, where the samples are irradiated to doses

only of the order of natural radiation dose (typically up to a few hundred Gy). The TL sensitivity of the present equipment is discussed in Chapter Five.

1.5 THIS THESIS

This thesis can be divided into two parts. Part one, comprising the first three chapters following this introduction, deals with the design and working principles of a Fourier transform spectrometer for TL emission spectroscopy. The next four chapters, which make the second part, are related to the application of this instrument, particularly for the three dimensional view of the thermoluminescence in feldspars. Emission spectra of some archaeological samples are discussed in Chapter Eight.

Chapter Nine summarises some of the main findings and future research directions.

CHAPTER TWO

FOURIER TRANSFORM SPECTROSCOPY: SOME RELEVANT THEORETICAL DETAILS

" A simple and general law capable of explaining a number of the phenomena of coloured light, which, without this law, would remain insulated and unintelligible. The law is that 'wherever two portions of the same light arrive at the eye by different routes, either exactly or very nearly in the same direction, the light becomes most intense when the difference of the routes is any multiple of a certain length, and least intense in the intermediate state of the interfering portions; and this length is different for light of different colours.' "

Thomas Young in
'An account of some cases of the production of colours not hitherto described'
the Philosophical Transactions (1802)

2.1 INTRODUCTION

Fourier transform spectroscopy is a widely useful and versatile tool in optical techniques today. Its basic principles and uses in a variety of light wave analysis problems have been well established and reported (see for example Bell 1972; Chamberlain, 1979; Park, 1983; Birch, 1984 and many others). Theoretical consideration of Fourier transform spectroscopy (FTS) with particular reference to the present equipment have been given by Jensen and Prescott (1982) and in greater detail by Jensen (1982). The purpose of this chapter is, therefore, neither to describe the theoretical aspects leading to the selection of a Michelson interferometer as a TL emission spectrometer, nor to discuss the general basis of FTS in any great detail. It has been introduced to help in later explaining the working principles and the scope and limitations of the experimental tool. Only topics of some relevance to the present

application have been included and they are not elaborated upon in any great detail. All the illustrative examples have been selected from spectral analyses carried out on our own equipment. The chapter, therefore, provides useful information about the working of the present equipment as well.

2.2 BASIC

Gebbie (1984) rightly points out that "it cannot be said too often, or too loudly, that the real inventor of Fourier transform spectroscopy was A.A. Michelson" - yet most two beam equipment used for FTS today resembles closely the one used and described by Michelson (1891, 1892). The incident light in such equipment is split into two beams normal to each other and of (ideally) equal intensity. It is done with the aid of a partially coated beam-splitter. Two mirrors placed normal to the optical axis in planes perpendicular to each other, reflect the beams back to recombine and generate an interference pattern. The interference pattern will depend upon the difference in the paths traversed by the two beams, which can be changed by to and fro movements of one of the two mirrors (Figure 2.1).

For a monochromatic light input, the intensity of the interference pattern vs. the optical path difference (interferogram) is a cosinusoidal wave. Constructive interference is seen when the optical path difference (OPD) is an integral multiple of the wavelength of the incident light - the input intensity being maximum at this stage. Minima are seen for path differences each given by $n\lambda/2$, n being an odd integer (Figure 2.2a).

For a broad-band light spectrum, the interference pattern is just a

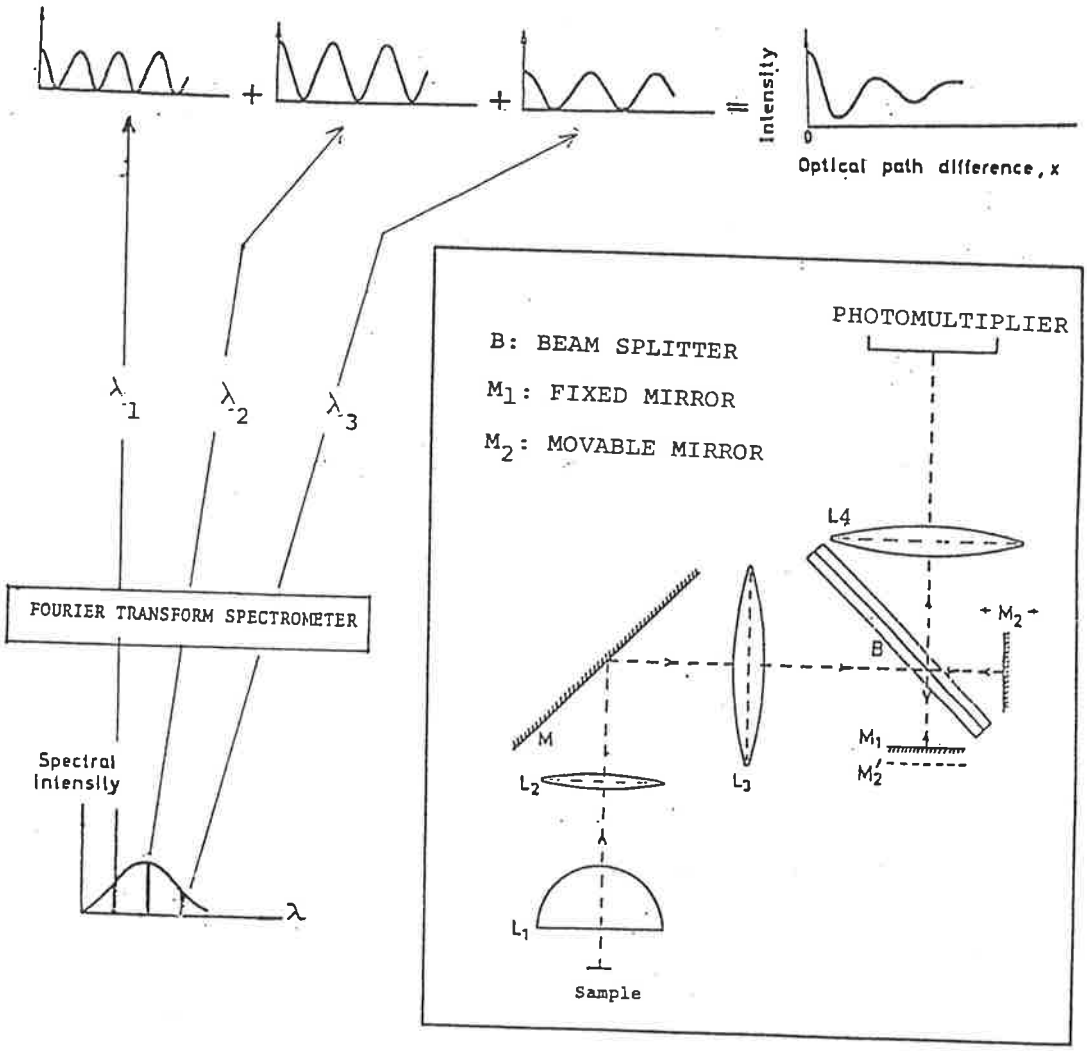

FIGURE 2.1: The essential components of a Michelson type interferometer. The optical path difference between the two beams of (ideally) equal intensities is changed through translating one of the mirrors, which then gives rise to a changing interference pattern. A light input and collecting set up has also been shown.

summation of several closely-spaced "monochromatic" bands of incident light. The output intensity in this case passes through a maximum at zero-path-difference (ZPD) between the two beams. Here all the incident wavelengths of light interfere constructively. As the optical path difference changes on both sides of the ZPD, the light of different wavelengths will gradually become incoherent and the troughs and crests due to different monochromatic bands will fall at different locations. The overall effect is that the difference in the intensities of alternate maxima and minima will gradually decrease, till after a certain OPD it will become indistinguishable above the noise fluctuations (Figure 2.2b). What we see in the output are the 'coloured fringes' of decreasing visibility. The central bright fringe at the ZPD should have the same colour as the input light, followed by others depending upon what wavelengths dominate in constructive interference at that particular path difference. The coloured fringe visibility will gradually fade into a uniform input light colour of approximately half its intensity. The light at this stage becomes completely incoherent.

Mathematically,

$$I(x) = C \int_{-\infty}^{\infty} B(k) e^{ikx} dk + 1/2\, I(0) \qquad (2.1)$$

I(x) is the intensity at a path difference 'x' between the two interfering beams, $k = 2\pi/\lambda$ is the wave-number and B(k) is the input power spectrum. I(0) is the intensity at ZPD and is given by

$$I(0) = I(x)\,\Big|_{x=0} = 2C \int_{-\infty}^{\infty} B(k)dk \qquad (2.2)$$

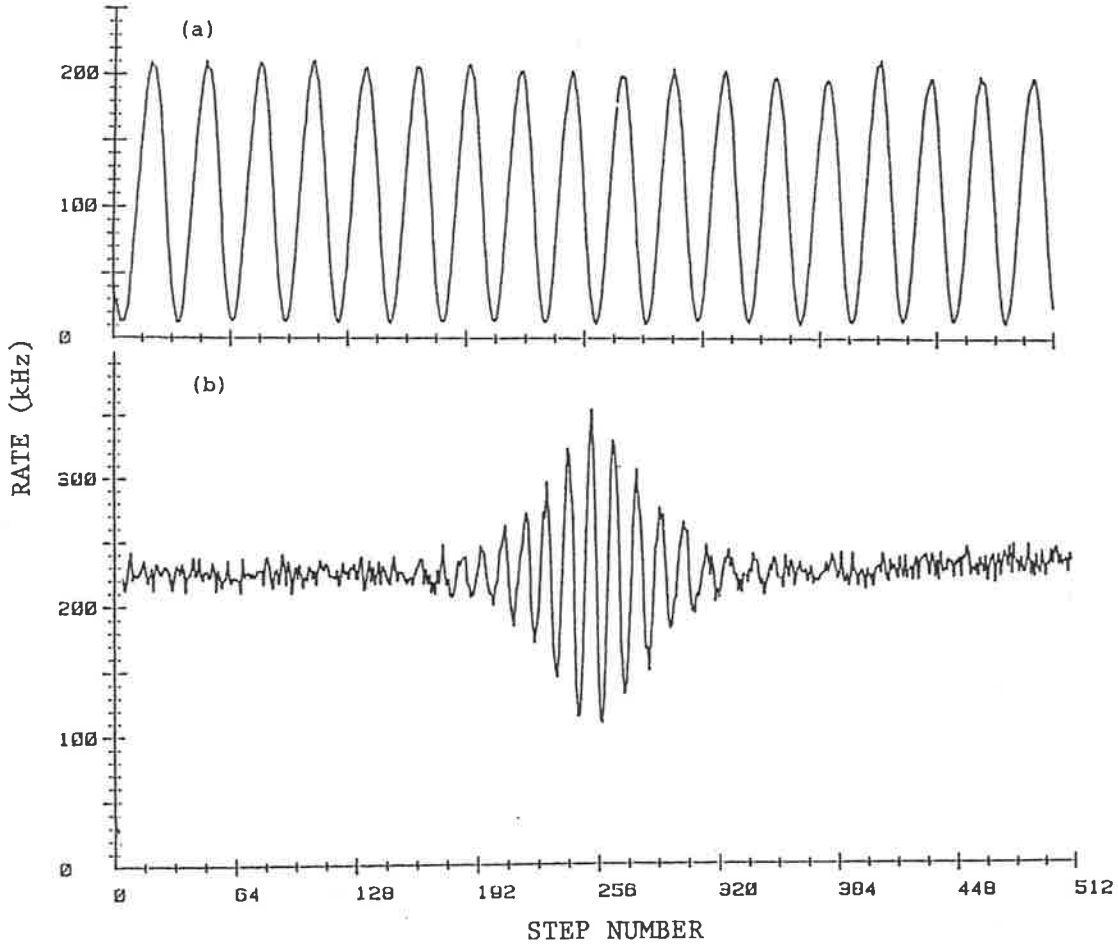

FIGURE 2.2: The interferograms for (a) a monochromatic and (b) a broad band light source input as registered on the existing equipment.

The constant of proportionality C depends upon factors like reflection and transmission coefficients of the optical components and the refractive index of the medium. As has been pointed out above, all wavelengths of light at ZPD are assumed to be exactly in phase; $x = 0$ is therefore the point of maximum intensity, i.e.

$$I(0) \geq I(x)\Big|_{x \neq 0} \tag{2.3}$$

where the equality may hold for monochromatic sources only at points $x = n\lambda$, n being an integer. It can be shown that

$$I(x)\Big|_{x \to \infty} = \tfrac{1}{2} I(0) \tag{2.4}$$

Practically, the infinite limits refer to a state of large arm displacement where the light becomes too incoherent to generate a distinguishable interference pattern.

Fourier inverse transformation is used to compute the spectral intensities from the recorded interferogams. According to the Fourier inversion theorem B(k) will be given by

$$B(k) = C' \int_{-\infty}^{\infty} [I(x) - I(\infty)]\, e^{-ikx} dx \tag{2.5}$$

where C' is another constant of proportionality. For practical applications where either the instrument can be calibrated using sources of standard luminosity or relative spectral intensity is the ultimate desire, this constant can be either determined experimentally or assumed to be unity.

Ideally, an interferogram should be symmetrical about the ZPD i.e. I(x) should be an even function of x. Only a cosine Fourier transformation for the positive values of x alone is therefore needed. The spectrum can then be computed using an integration like

$$B(k) = \int_0^\infty [I(x) - I(\infty)]\cos kx \, dx. \qquad (2.6)$$

The constant of proportionality has been dropped here without any loss of generality. The practical requirements for the Fourier transform spectral analysis are therefore (a) to locate the point of zero-path-difference (ZPD) and (b) to measure I(x) as a function of x on one side of ZPD. Equation 2.6 or one or other of its special forms can later be used to compute B(k). It will, however, be shown in a later chapter that, in order to obtain meaningful spectral information, the TL emission interferograms will require some additional corrections as well.

For derivations of the Equations 2.1 to 2.6 and for further explanation of the subject see the references like Bell (1972), Chamberlain (1979).

Connes (1984) points out that expressions similar to 2.1 were used by Michelson (1891, 1892) and by Rayleigh (1892) who actually introduced the Fourier theorem in interference spectroscopy. Yet these workers never developed it for the general case of broad-band spectral analysis. Rubens and Hollnagel (1910) were the first to record true interferograms in the infra-red region using a micro-radiometer as the detector. They did not actually Fourier transform these interferograms to obain the spectral information.

2.3 THE INSTRUMENT LINE SHAPE

An interesting feature of Equations 2.5 and 2.6 is the limits of integration ($x = \pm\infty$) as imposed by the Fourier inverse transformation theorem. Practically, no interferograms are traced to infinite limits. What we, therefore, record and calculate is a somewhat modified spectrum given by

$$B_m(k) = \int_{-L}^{L} [I(x) - I(\infty)]e^{-ikx}\, dx \qquad (2.7)$$

where $\pm L$ are the finite limits of integration. A relation between the instrumental spectrum $B_m(k)$ and the input spectrum $B(k)$ can be found by introducing a box-car function like rect(x) where

$$\text{rect}(x) = 1 \text{ when } L \geq x \geq -L$$

$$= 0 \text{ elsewhere.}$$

Equation 2.7 can therefore be rewritten as

$$B_m(k) = \int_{-\infty}^{\infty} [I(x) - I(\infty)]\ \text{rect}(x)\ e^{-ikx}\, dx \qquad (2.8)$$

Applying the convolution theorem of Fourier transformation to Equation 2.8 we get

$$B_m(k) = B(k) * F[\text{rect}(x)]. \qquad (2.9)$$

The instrumental spectrum $B_m(k)$ is, therefore, related to the input spectrum $B(k)$ through a convolution function $F[\text{rect}(x)]$, which is the Fourier transform of a box-car function. This convolution function is a characteristic of the instrument and it is often referred to as the

instrument line shape (ILS). The effect of the instrument line shape is well exhibited for a monochromatic light source. The idealized output spectrum corresponding to such input should be a delta function with a finite value at the input wavelength and zero elsewhere where the symmetric delta function in negative reciprocal space is ignored. The finite truncation limits at L result in a broader output spectrum with sidelobes ranging up to several percent in intensity of the main peak. The output spectrum is mathematicaly given by

$$B_m(k) = 2L \left[\frac{\sin\{(k_o + k)L\}}{(k_o + k)L} + \frac{\sin\{(k_o - k)L\}}{(k_o - k)L}\right] \qquad (2.10)$$

Figure 2.3 shows the instrumental spectrum for a He-Ne laser recorded on this equipment. The laser emits a red line at λ = 632.8 nm. The computed spectrum, as indicated through the dots at 5 nm intervals, shows a peak between λ = 630 and 635 nm with a full width at half maximum (FWHM) value of about 17 nm. The limits of integration in this case were twenty two laser wavelengths (L = 22λ) from ZPD. The continuous line is the expected spectrum calculated using Equation 2.10. Both the instrumental and the expected spectrum agree very well with each other. Significant sidelobes of decreasing intensity extend up to a few hundred nanometres on both sides of the main peak.

The effect of finite truncation cannot be easily recognized for a broad-band spectrum, where the output intensity is scanned for path differences long enough to reach the incoherent steady-state signal limits. This is because beyond these limits the bracketed term in the integral part of the Equation 2.8 approaches zero before the box-car function, suggesting that the instrumental spectrum will approach the

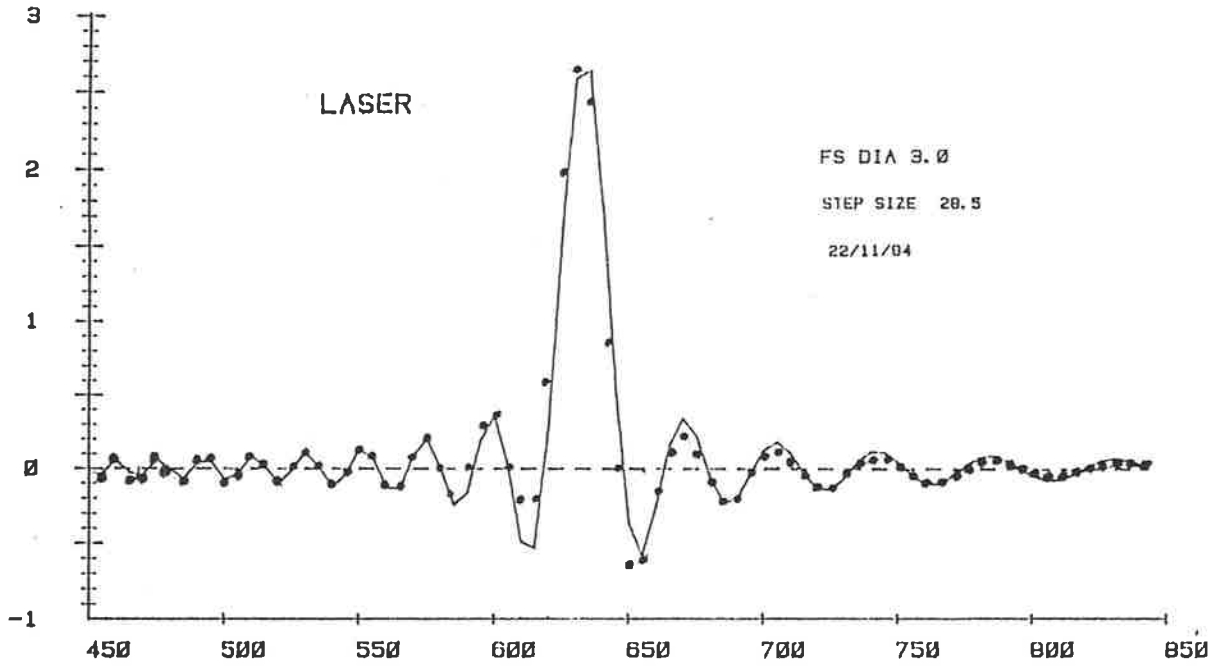

FIGURE 2.3: The computed spectrum for a He-Ne laser monochromatic input (dots). The side lobes and the broadening of the main peak are the effects of finite truncation limit. The continuous line is the theoretically expected curve as given by the Equation 2.10 of the main text.

infinite spectrum i.e. for a broad-band source

$$B_m(k) \cong B(k). \tag{2.11}$$

2.4 INTENSITY ERRORS

In addition to the effect of interferogram truncation at the finite limits, there are some other sources of errors in Fourier transform spectrometers leading to complex instrument line shapes and modified calculated spectra. These sources of errors are generally bracketed into "intensity" and "phase" errors (Park, 1983). Those errors, which result in the distortion of individual spectral lines symmetrically and sometimes create strong sidelobes, are generally referred to as intensity errors. Intensity errors are introduced due to factors like the limited scanning, apodization, extended sources, and drifts in environmental factors affecting the light transmission, mirror maladjustment or optical surface non-uniformities. Of these, the effect of scanning limits has already been discussed in the previous section. The other three of greatest relevance are briefly discussed next.

2.4.1 Apodization

As has been shown in the last section, because of the finite limits of integration, the instrumental spectrum may have lobes on each side which may interfere with the other spectral lines nearby. To overcome this error, the interferogram is sometimes intentionally distorted, usually multiplying it by a triangular function with its vertex at ZPD (Bell, 1972; Norton and Beer, 1976; Park, 1982). This is known as apodization, the effect of which is to reduce the sidelobes at the

expense of resolution. Park (1982) has shown that the area under the peak will remain conserved as long as the apodization function is normalized to unity at ZPD.

2.4.2 Extended Source Intensity Error

Extended source intensity errors are perhaps of more concern particularly in the higher wave number or visible light region. Fourier spectroscopy using extended sources has been discussed by Steel (1964) and Bell (1972). Steel's article gives a historical perspective of the subject as well.

With an extended source, we need to consider the effect of both the normally incident (parallel to the optical axis) and the oblique incident (making an angle say 'θ' with the optical axis) rays. It is easy to visualize that, for normal incident rays, the optical path difference (OPD) between the two beams will be twice the difference of the distance between either of the mirrors and the beam splitter. For the oblique incidence (Figure 2.4 a,b) it can be shown that the OPD will reduce by the cosine of the incident angle i.e.

$$OPD(\theta) = 2d \cos\theta \qquad (2.12)$$

For a given relative mirror displacement 'd' the overall output intensity can be obtained by integrating the radiant flux over all angles from zero to a maximum, say θ_{max}. The average path difference over the entire field of view will be less than 2d, and the expansion in the interferogram will produce a measured spectrum broader and shifted to lower wave numbers. Moreover, these changes in the spectrum will depend both

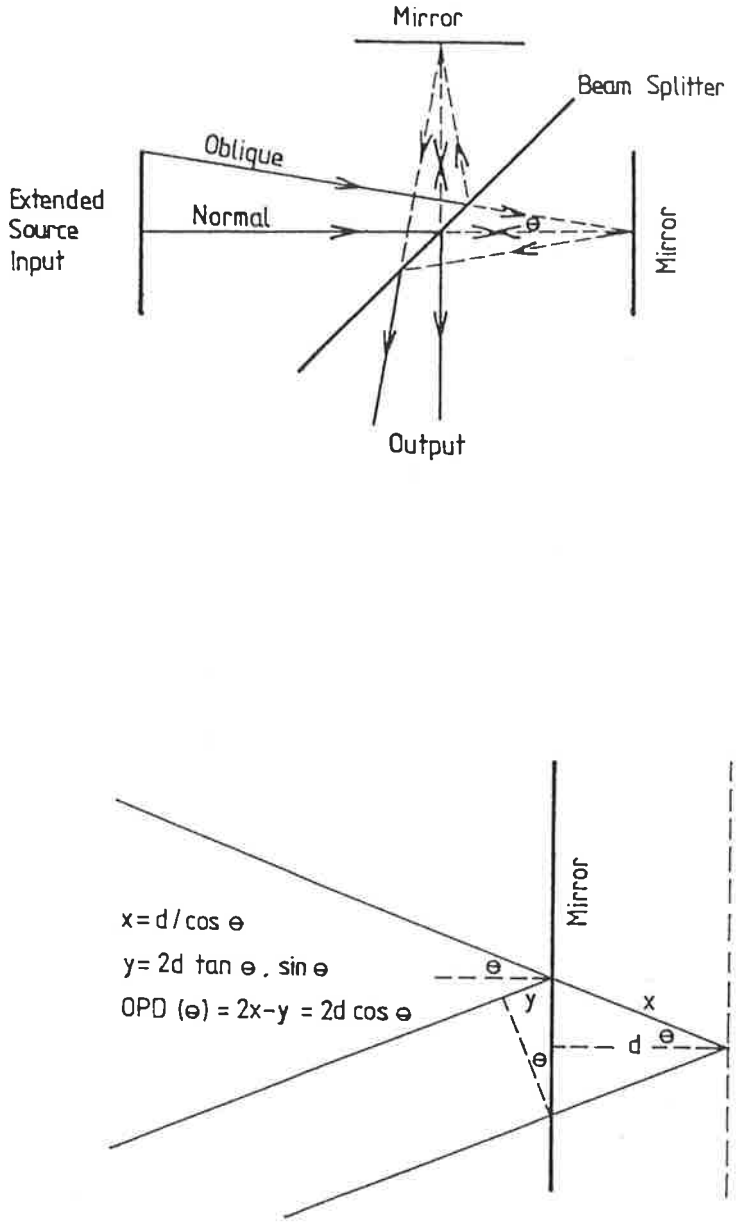

FIGURE 2.4: Figures to illustrate the effect of extended source input on the optical path difference (OPD) between the light beams travelling in the two arms of the interferometer. (a) The actual set up, the rays have been traced for zero OPD. (b) The equivalent optical set up, the beam splitter has been omitted and the image of the movable mirror has been shown behind the other mirror. The rays have been traced for non-zero OPD.

on the wave number and the solid angle subtended by the source. Bell (1972) has shown that for a monochromatic light input of wave number k_o from an extended source subtending a solid angle Ω, the computed spectrum will show a mean wave number $\bar{k}$ as

$$\bar{k} = k_o(1 - \Omega/4\pi) \tag{2.13}$$

The spectrum will spread between the limits k_o and $k_o(1-\Omega/2\pi)$ as

$$\Delta k = k_o\Omega/2\pi \tag{2.14}$$

Here

$$\Omega = 2\pi\ (1 - \cos\theta_{max}) \tag{2.15}$$

For those Fourier transform spectrometers where the optical path difference between the beams is measured through the actual displacement of the movable mirror, the knowledge about the absolute shift of various lines and bands in the computed spectrum is important. For others which are calibrated using a set of standard input lines, only the relative displacement of the experimental spectrum with respect to the observed locations of the standard lines need to be known. It is important to use the same field of view both for the experimental spectrum and the standard lines. Otherwise changed input solid angle will lead to a modified placement of the lines.

For the existing equipment the field of view subtends a solid angle of about 0.24 steradians ($\theta_{max} = 16^0$) with the centre of the mirror. A He-Ne laser (λ = 632.8 nm) is used to calibrate the spectral range (350 to 750 nm) within the error limits of a few nanometres. We expect a

backward shift of the spectra up to six nanometres around λ = 350 nm. Figure 2.5 shows the instrumental spectra recorded for narrow band incident light beams from a xenon lamp and diffraction grating monochromator arrangement. We notice that the instrument is well calibrated within a few nanometres. A shift at lower wavelengths is evident. As expected, the instrumental spectrum broadens with increasing wavelength. The peak broadening can partly be explained using the equation 2.14 (where $k_o = 2\pi/\lambda_o$ and $\Delta k = -\Delta\lambda/\lambda_o^2$). Further broadening is due to finite limits of the scan. The effect of finite limits of the scan on spectral resolution will be discussed in a later section.

2.4.3 Errors due to Reflecting Surface Defects and Mirror Misalignments

Perhaps the most serious intensity errors in Fourier Transform spectroscopy for visible light range will occur due to the strict tolerance limits of the reflecting surface defects and maladjustments of the mirrors. The reflecting mirrors in an ideal Fourier transform spectrometer are assumed to be perfectly flat and adjusted in such a way that the output images due to the two beams fall exactly parallel to each other. Practically these requirements can be met only within certain limits and both constant and variable maladjustments and surface non-uniformity do exist to a smaller or greater extent. Griffiths (1975) and Chamberlain (1979) have discussed the case of misaligned mirrors in a Fourier spectrometer.

The effect of constant maladjustment will be independent of the movable mirror scan over the interferogram. If we suppose that the circular mirrors of radius 'r' are misaligned by a small angle ϕ then the modified spectrum $B_m(k)$ due to this effect will be related to the

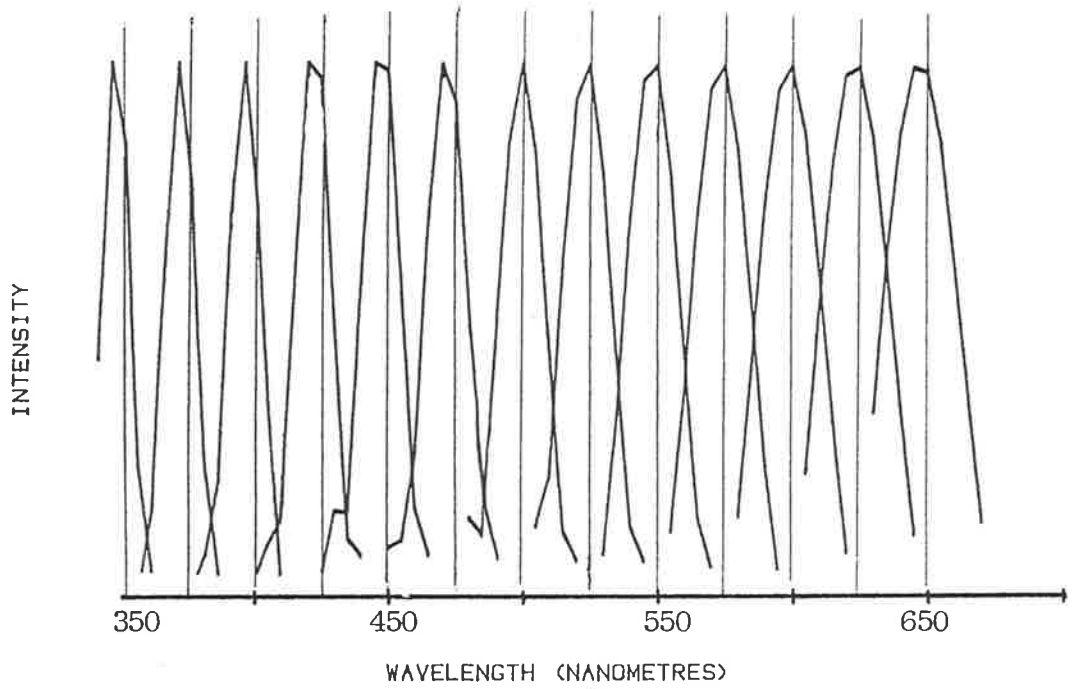

FIGURE 2.5: Computed spectra for narrow-band input light beams of known wavelengths indicated by the thin lines. The maximum intensities have been normallised to the same value. A slight spectral shift and change in FWHM is explained in the text.

unmodified instrumental spectrum B(k) through a Bessel's function of the first order as,

$$B_m(k) = 2\left[\frac{J_1(2kr\phi)}{(2kr\phi)}\right] B(k) \qquad (2.16)$$

The spectral distortion factor $2\left[\frac{J_1(2kr\phi)}{(2kr\phi)}\right]$ falls to zero when $2kr\phi = 3.83$. It means that for mirror misalignment angles approaching $1.92/kr$, the output radiant flux integrated over the entire beam area will stay constant and maxima and minima caused due to the interference will not be distinguishable. Chamberlain (1979) mentions that the spectral attenuation will be less than 1.7% if the maximum wave number $\sigma_m (= k_m/2\pi)$ involved in the spectral analysis is such that

$$\sigma_m \leq \frac{0.041}{r\phi} \qquad (2.17)$$

For our equipment, the effective mirror radius is about 15 mm. For the shortest spectral wavelength of 350 nm, ϕ comes out to be 1.52×10^{-7} radians. It would mean that for 1.7% attenuation limit the maximum tolerable tangential tilt in the mirror plane could be 5 nm. For tilts beyond 34 nm or so, the equipment will cease to resolve spectral lines below 350 nm.

The effect of surface non-uniformity is equivalent to the constant maladjustment as discussed above. There is a variation of the path difference over the aperture of the mirrors and to take account of this variation each element of the beam should be considered separately. Surface strains near the holding points can produce substantial distortions and should be kept to their minimum. The major error will,

however, come through the limit to which the uniformity of the substratum glass surface under the mirror coating has been achieved. Most surfaces used for interferometry are claimed to be flat up to $\lambda/10$ or at the most $\lambda/20$, where λ is typically 500 nm or so. This can offer serious limitations on the efficiency of the spectrometer in the violet or ultraviolet region. The surface non-uniformities can be seen by looking at the beam image in the interferometer output near ZPD for white light. The variable path difference due to surface non-uniformities gives rise to an incoherent light component with an increasing proportion at lower wavelengths. We have actually observed this effect on our equipment. Figure 2.6 shows the interferograms recorded for narrow band input lights of 600, 500, 400 and 350 nm. The optical alignment was kept the same. Lower wavelengths show a higher incoherent light component indicated by the height to width comparisons of the interferograms.

The application of Fourier transform spectroscopy in the ultraviolet region is yet to be seen. Tittel et al (1984) maintain the view that the optical and mechanical concepts of their visible light Fourier transform spectrometer should apply at lower wavelengths as well, if the optical elements in question were made from quartz.

A variable tilt with the mirror translation will lead to a variable maladjustment. It may be random and oscillatory or periodic and definite with translation. Chamberlain (1979) shows that the defect function in this case may not strictly be a Fourier transform and a general spectrum distortion function may, therefore, be hard to arrive at in theory. Guelachvili (1981) suggests that oscillations of a mirror may cause a sinusoidally modulated intensity error in the spectra.

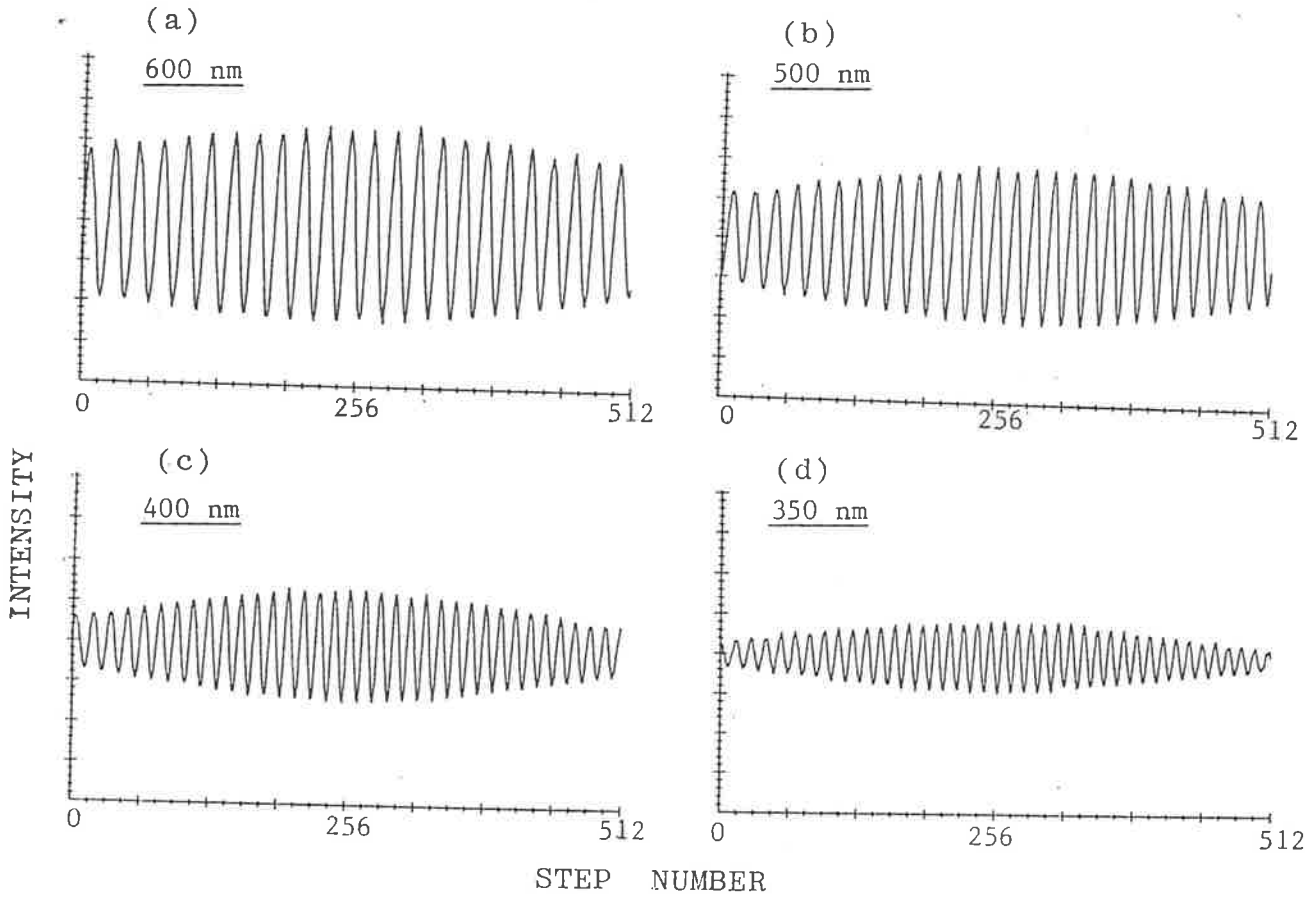

FIGURE 2.6: Interferograms corresponding to the narrow-band light inputs at (a) 600nm (b) 500nm, (c) 400nm and (d) 350nm wavelengths. The mirror alignment was unchanged. The increasing heights of the interferograms is most probably due to an increasing incoherent light component at lower wavelengths.

2.5 THE PHASE ERRORS

The wave-number dependent phase errors commonly encountered in the Fourier transform spectrometers are mostly due to factors like difficulties in correctly locating the ZPD (particularly in discrete sampling) or due to wavelength dependent phase shifts produced by the presence of extra surfaces or layers (like anti-reflection coatings etc.) in either of the beam paths.

Suppose that the analogue interferogram is truly symmetrical but the interferogram has actually been sampled at discrete points to facilitate the data storage and later computer-based analysis. Now suppose the sampling comb misses the true ZPD by a small displacement, say δ. The recorded one-sided interferogram will therefore start with an initial displacement and the instrumental spectrum as given by Equation 2.5 now becomes

$$B_m(k) = \int_{-\infty}^{\infty} [I(x-\delta) - I(\infty)]e^{-ikx}\, dx \qquad (2.18)$$

This gives

$$B_m(k) = B(k)e^{-ik\delta} \qquad (2.19)$$

The instrumental spectrum is therefore modified by a phase dependent factor $e^{-ik\delta}$. This distortion depends upon both the wave number as well as the displacement size. Average step size for most of our spectral recording was about 30 nm. If we assume the maximum ZPD displacement error by one such step then the corresponding spectral distortion in the spectral range from 350 to 750 nm will vary from about 14 to 3%. These figures on the maximum distortion refer to a single-sided interferogram

starting from the experimentally located ZPD. Slight differences in the instrumental and expected spectrum for a He-Ne laser as shown in Figure 2.3 can be attributed to such phase errors.

Various methods have been proposed to correct the results of Fourier spectrometers against some of the intensity and phase errors (see for example Forman et al, 1966; Bell, 1972; Chamberlain, 1979; Park 1983). Each method has its own merit and scope of application depending upon the desirable purity of the spectrum, nature of the data, wavenumber range of interest and availability of the computer time.

For several reasons to be discussed in a coming chapter, we found it most appropriate to use the method based upon the two sided interferogram analysis for the computation of the spectra. The spectral response curve of the instrument is found using a standard light source and the alignment is frequently rechecked during the course of operation.

2.6 JACQUINOT AND FELLGETT ADVANTAGES

Contributions of Jacquinot (1954) and Fellgett (1951) are of fundamental significance in the revival and present day status of the Fourier transform spectroscopy. The extended source throughput and multiplex advantages as pointed out by these two scientists have been explained both in historical perspective and technical details by various authors (Steel, 1964; Bell, 1972; Connes, 1984 and many others). Jensen (1982) discussed Jacquinot and Fellgett advantages in detail with reference to the optical design of the present apparatus. On the basis of these studies, he correctly arrived at the conclusion that an apparatus based on Fourier transform spectroscopy will make a sensitive thermoluminescence emission spectrometer (also see Jensen and Prescott

1982). As the basic optical components have not been replaced since then, only a very brief mention of these advantages is included in this chapter. Readers interested in further details are referred to Chapters 8, 9 and 10 of Jensen (1982).

If the resolving power 'R' of the instrument is measured as $k/\Delta k$ then Equation 2.14 can be re-written as

$$\Omega = 2\pi/R. \qquad (2.20)$$

The extended source throughput advantage can only, therefore, be achieved at the expense of resolution. Jacquinot (1954) basically showed that the resolution trade-off for a Michelson interferometer will be much less than that in case of a dispersive type spectrometer. This means that, for a preset limit of the spectrum resolving power, much broader solid angles and beam fluxes can be tolerated through a Michelson type interferometer as compared to a diffraction grating. Bell (1972) points out that even for the best diffraction grating systems, the solid angle tolerance limits will be less by at least two orders of magnitude.

Results of an experiment to demonstrate the resolving power of the existing equipment are shown in Figure 2.7. Here, two narrow band light beams from a He-Ne laser (632.8 nm) and a xenon lamp and grating monochromator set up at 608 nm were thrown simultaneously through the same pupil of the equipment. The input light was intercepted through field stops of varying aperture. The equipment, with a field stop of 10mm diameter, was calibrated with laser light prior to the resolution experiment. Decreasing resolving power with increasing aperture diameters is evident from both increasing peak widths and decreasing peak

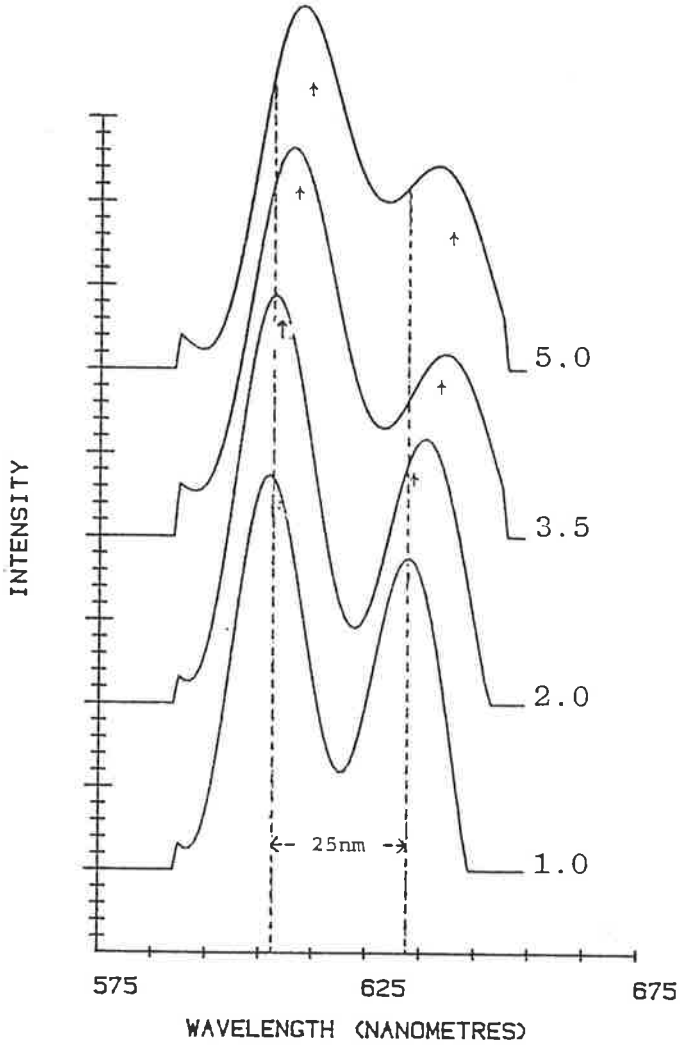

FIGURE 2.7: Results of an experiment to illustrate the effect of input solid angle on the spectral resolution. The numbers with each curve indicate the field stop diameter in cms. Two narrow band inputs are shown through the dotted lines. Note the peak broadening and the spectral shift with increasing field stop diameter. The arrowheads indicate the expected shift in the average wavelength (see text).

to valley ratios in the instrumental spectra. Another interesting feature is the spectral shift as expected from Equation 2.13, indicated by the arrowheads in the Figure. Within an error of ±2nm, the computed instrumental spectrum agrees well with the expected values. The spectral shift also indicates the importance of calibration of the equipment using the same input angle as is used for recording the actual spectrum; a wavenumber-dependent spectral shift correction factor will otherwise be required. Under its normal operating conditions with no field stops, our instrument will resolve better than 20nm throughout its present spectral range.

The Fellgett advantage associated with the spectroscopy is based upon the time available to scan each segment of the wavelength. The thermoluminescence signal is temperature dependent and, depending upon the heating rate, continuously changes with the time. A rapid spectral scanning is, therefore, desirable. In previous TL spectrometers this is achieved by rotating either a set of interference filters (Bailiff et al, 1977a) or a dispersive optical device like a grating or a prism (Mattern et al, 1971). Each wavelength segment is, therefore, scanned only for a smaller time interval as compared to a Fourier transform spectrometer where information about all the wavelengths is recorded simultaneously. It should be noted, however, that since the recording system is based on single-photon counting the Felgett advantage is only partly realised. This aspect has been discussed in detail in Bell (1972).

2.7 THE OPTIMUM STEP SIZE AND SCAN LIMITS

For ease in computation of the spectra with digital computers it is preferable to record Fourier transforms at discrete steps of known

optical path size. The Fourier integral thus becomes a summation of the form

$$B(k) = \sum_{j=-N}^{N} [I(j\Delta x) - I(\infty)] e^{-kj\Delta x} \qquad (2.21)$$

where N is the total number of steps on each side of the point of maximum intensity (i.e. observed ZPD) and Δx is the step size, assumed to be constant throughout the scan. Experimentally it is achieved by translating the movable mirror in equal steps. The translation time has to be kept negligible compared to the stationary time which, at each stage, has to be precisely constant. The effect of missing the analogue ZPD in discrete stepping has already been discussed in a previous section on phase errors. In this section the selection of optimum step size and scan limits will briefly be discussed.

Selection of the total number and size of the steps strongly depends upon the nature and range of the input spectrum and the desired purity and resolution of the results. As can be seen from Equation 2.21, the computation of the spectrum from discrete interferogram data basically involves a summation over all steps of a product of the recorded interferogram as $[I(j\Delta x) - I(\infty)]$ with a function $e^{-ikj\Delta x}$ of unit amplitude. It can be shown that if we are interested in a unique solution for each wavenumber in the spectral range, an upper limit on the step size has to be imposed. If the interferogram is sampled at intervals longer than that upper limit, then a set of more than one wave function will fall at identical points leading to the repetition of the same spectrum (Figure 2.8). This phenomenon is known as aliasing. It can be shown that the condition for no aliasing is that

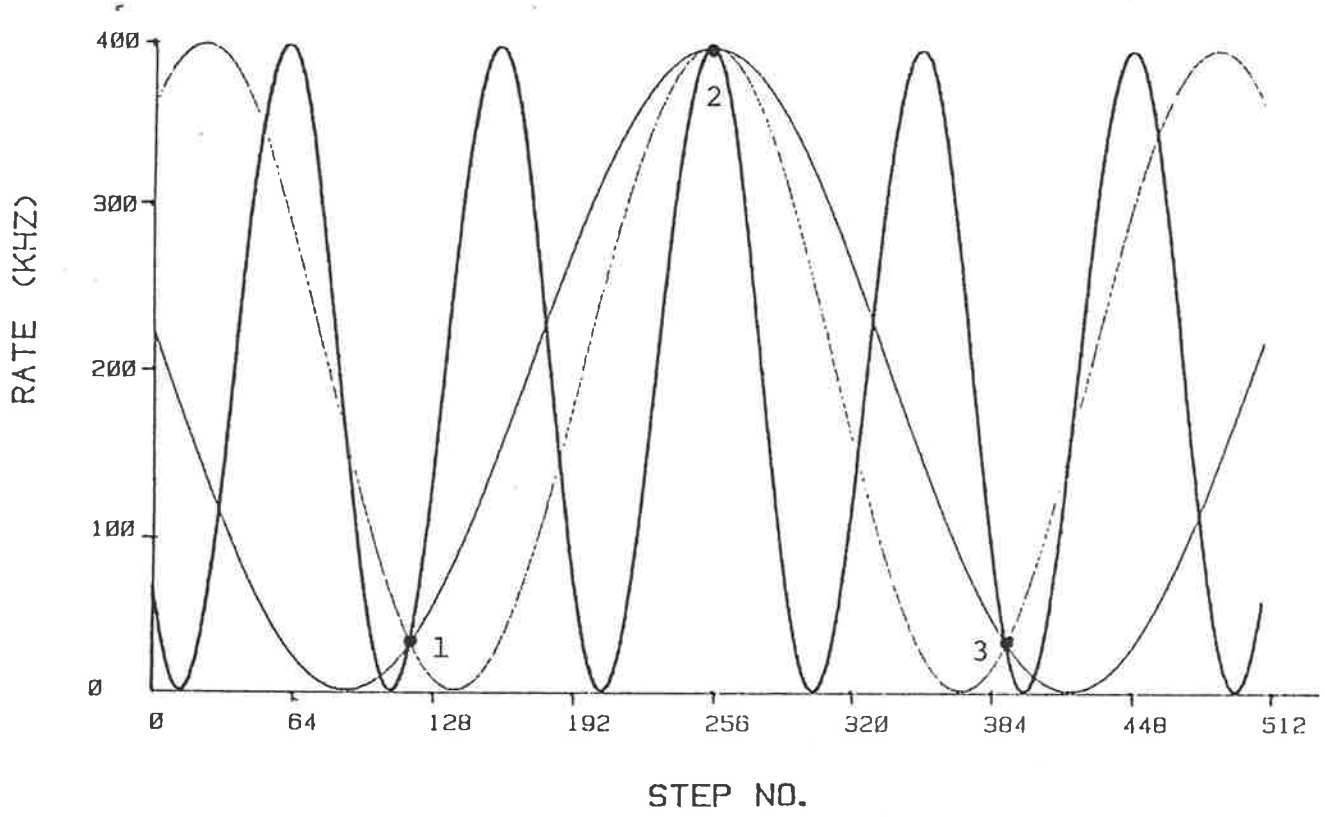

FIGURE 2.8: A figure to illustrate the phenomena of aliasing. All the three wave functions will give identical spectral values if the interferogram is sampled at discrete points like 1,2,3 ... .

$$\Delta x < \pi/k_{max} \tag{2.22}$$

Aliasing, therefore, sets the upper limit of the sampling step size as half the minimum wavelength of the spectrum. The lower limt of our spectral range is 350 nm, which sets the maximum allowable step size as 175 nm. It is worth noting that the step here refers to the optical path difference step between the two beams, twice the actual movable mirror translation. The effect of aliasing on one of the computed spectra is shown in Figure 2.12

A relationship between the scan limits 'L' on either side of the ZPD and the resolution of a Fourier transform spectrometer has been discussed by Jensen in Section 8.4 of his Ph.D thesis (Jensen, 1982). Referring to the work of Bell (1972), Chantry and Fleming (1976), Chamberlain (1979) and Chantry (1979), he states the well-known conclusion that the resolution should improve with increasing L. He also points out the upper limit L_{max} of the scan length, beyond which no further improvement in the spectrum can be seen, as

$$L_{max} = 2\pi R/k \tag{2.23}$$

where R is the resolving power of the equipment obtained from Equation 2.20. L_{max} here refers to a scan limit beyond which the oscillations in the interferogram due to a monochromatic light input of wavenumber k damp down to a diminishing value due to an extended source input. For our equipment with no field stops

$$L_{max} = 162/k \tag{2.24}$$

Figure 2.9(a) and (b) show the results of an experiment on the resolution of a laser spectrum recorded on our instrument. The results are essentially for the same interferogram but the truncation limit 'L' has been varied up to 22λ. The interferogram has been recorded using a fieldstop to extend the L_{max} up to about a hundred laser wavelengths. The effect of spectral broadening due to extended source input is therefore negligible. The results show that the resolution (= 100 x FWHM/λ) varies linearly with λ/L. For a monochromatic input, therefore, the resolving power is related to the scanning limit as

$$L \sim 1/\Delta k. \tag{2.25}$$

The absolute limit is, however, imposed through the relation (2.23) but it is due to the extended source intensity error. In general, the peak broadening in the computed spectrum would be the composite of the effects due to the finite truncation limits and the extended source input.

L_{max} corresponding to the lowest wave number in the spectrum, therfore, sets the limit for the scan on either side of the ZPD in an interferogram. If N is a preset number in the computer memory for the data points on one side of the interferogram, then the limiting step size will be given as

$$\Delta x_{limit} = L_{max}(k_{min})/N. \tag{2.26}$$

For our instrument Δx_{limit} comes out to be about 75 nm for 256 steps on each side of ZPD. L_{max} for λ = 750 nm is 19.4 μm.

The above relationship has, however, been derived by keeping in mind

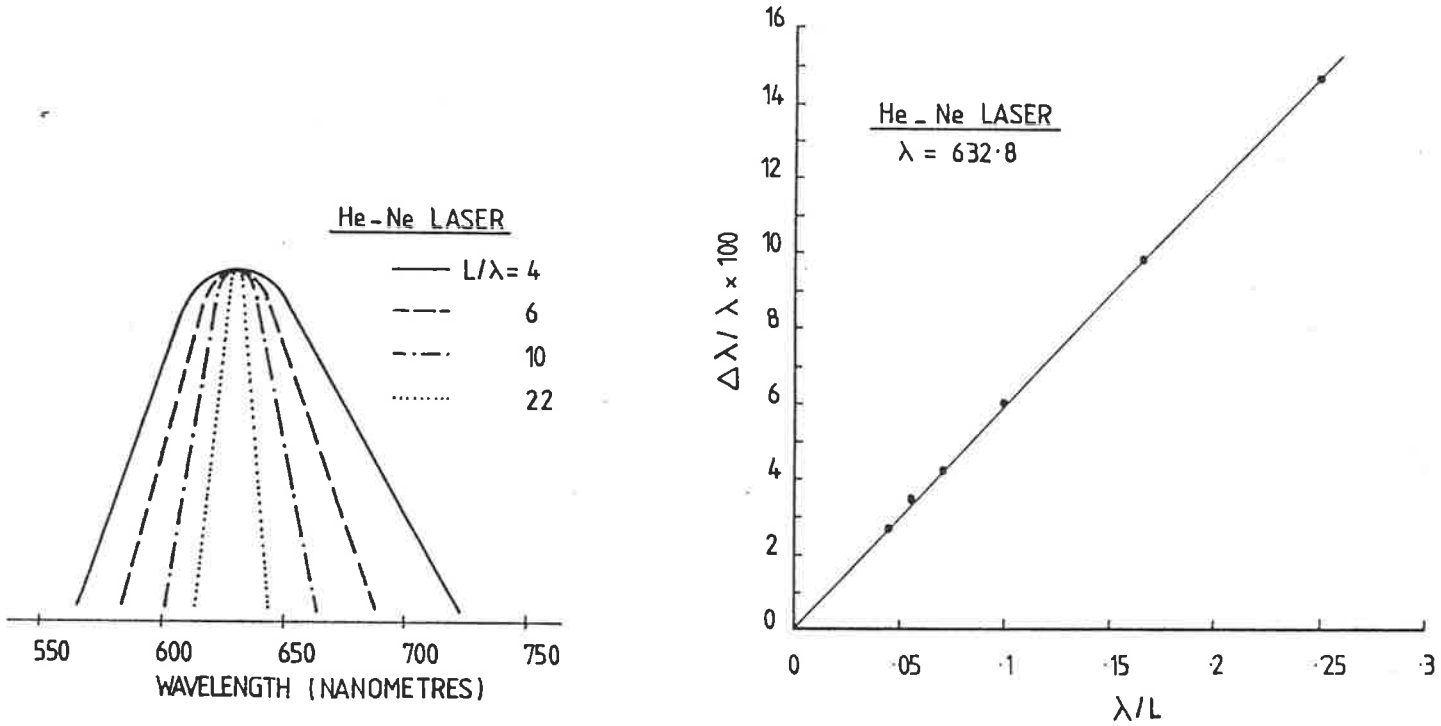

FIGURE 2.9: Results of an experiment on the effect of the scanning limit 'L' on the instumental spectrum due to a monochromatic light source (an He-Ne laser). L has been varied in multiples of the wavelength λ. (a) shows the main peak broadening with lower scan limits and (b) shows a linear improvement of the resolution ($\lambda^2/\Delta\lambda$) with L.

the application of the Fourier transform spectroscopy to monochromatic or discrete sharp line spectra. Most thermoluminescence emission spectra to be analysed on the existing equipment are broad-band. The spectral information is, therefore, mostly contained in the first few oscillations on each side of the ZPD, which then quickly tend to decrease to a steady state value. Whereas longer scanning in the steady state region can help to improve the signal to noise ratio to a small or large extent, depending upon the signal level, it cannot be carried out at the expense of many data points in the oscillatory part of the interferogram. The optimum step size for a broad band spectrum can, therefore, be much less than the one suggested by Equation (2.26) providing more data points within the oscillatory part of the interferogram. Figure 2.10 shows a one-sided interferogram for alpha radiation induced scintillations in a silver activated zinc sulphide phosphor screen. The interferogram has been recorded for 256 steps, each of about 30 nm. The computed spectra for different truncation limits are shown in Figure 2.11 (a-d). We notice that practically the same spectral information is obtained with no loss of resolution till the truncation limits are reduced down well into the oscillatory part of the interferogram. The spectrum appears to be rather smoothed by omitting the data points in the steady state region. Figure 2.12 (b-d) shows the spectra computed using every third, fifth and eighth data step starting from the ZPD. Practically this would be equivalent to raising the step size to 90, 150 and 240 nm respectively. We observe that, although still within the aliasing limits, the spectral information from 90 and 150 nm step sizes starts getting distorted compared to the one from 30 nm step size. This can be attributed to the poor statistics due to lesser and lesser number of data points in the

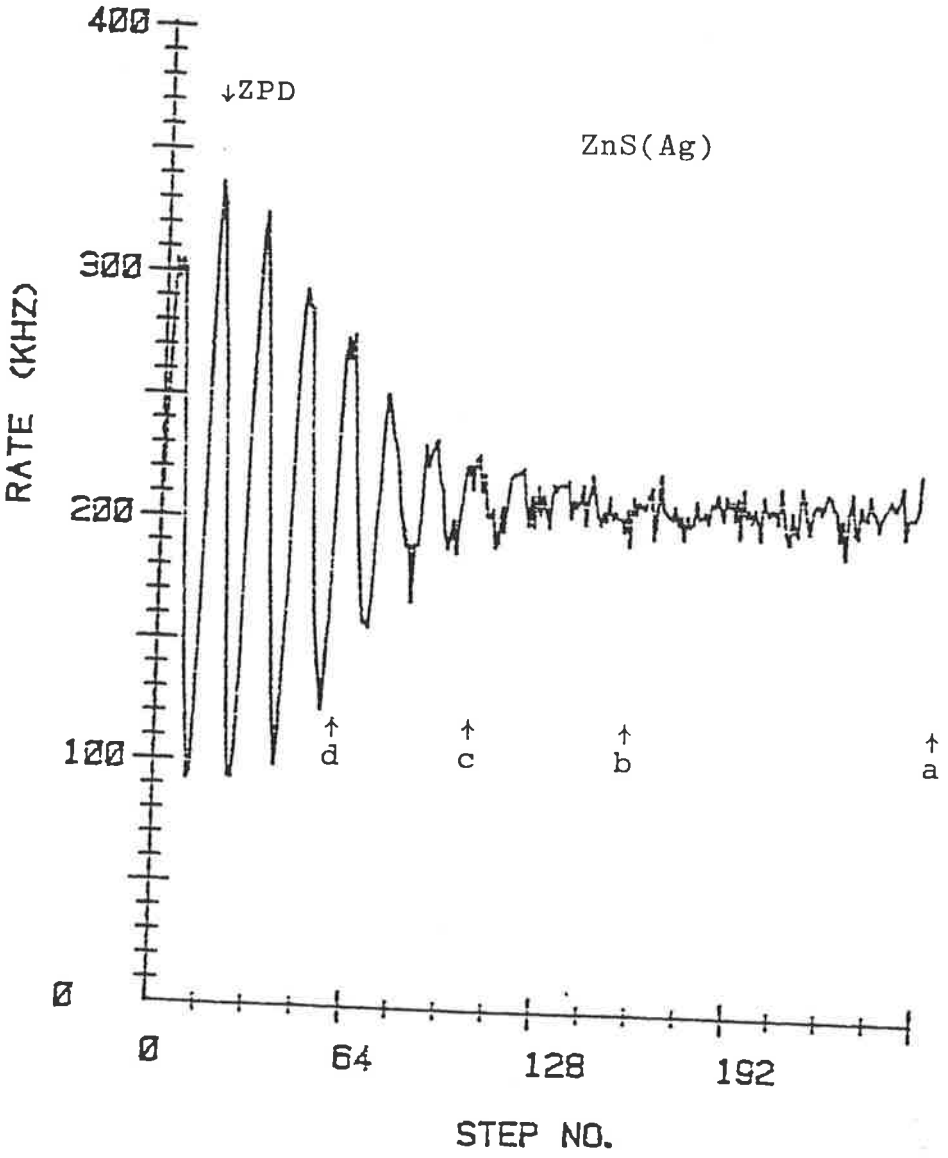

FIGURE 2.10: A one-sided interferogram for alpha radiation induced scintillations in a ZnS(Ag) phosphor screen. The interferogram has been recorded for 256 steps each at about 30nm apart. The marks a,b,c,and d indicate the limits to which the spectra were computed as displayed in Figure 2.11 .

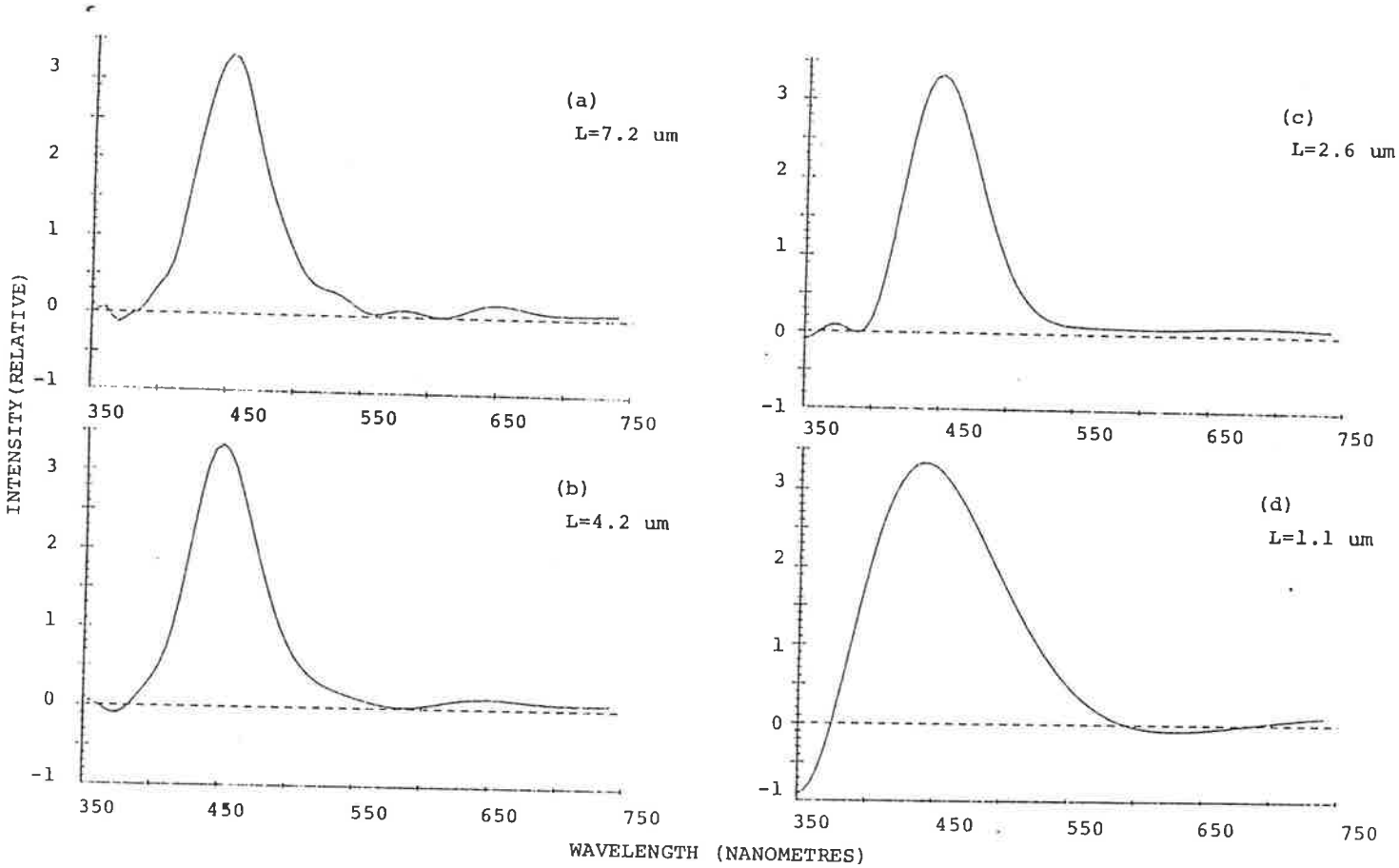

FIGURE 2.11 : The computed spectra for different truncation limits of the interferogram due to a broad band light input (Figure 2.10). The truncation limits were (a) 7.2 (b) 4.2 (c) 2.6 and (d) 1.1 μm . Despite these limits were much less than L_{max} at 450nm, no loss of resolution was seen except in (d) which truncates before the oscillatory part of the interferogram.

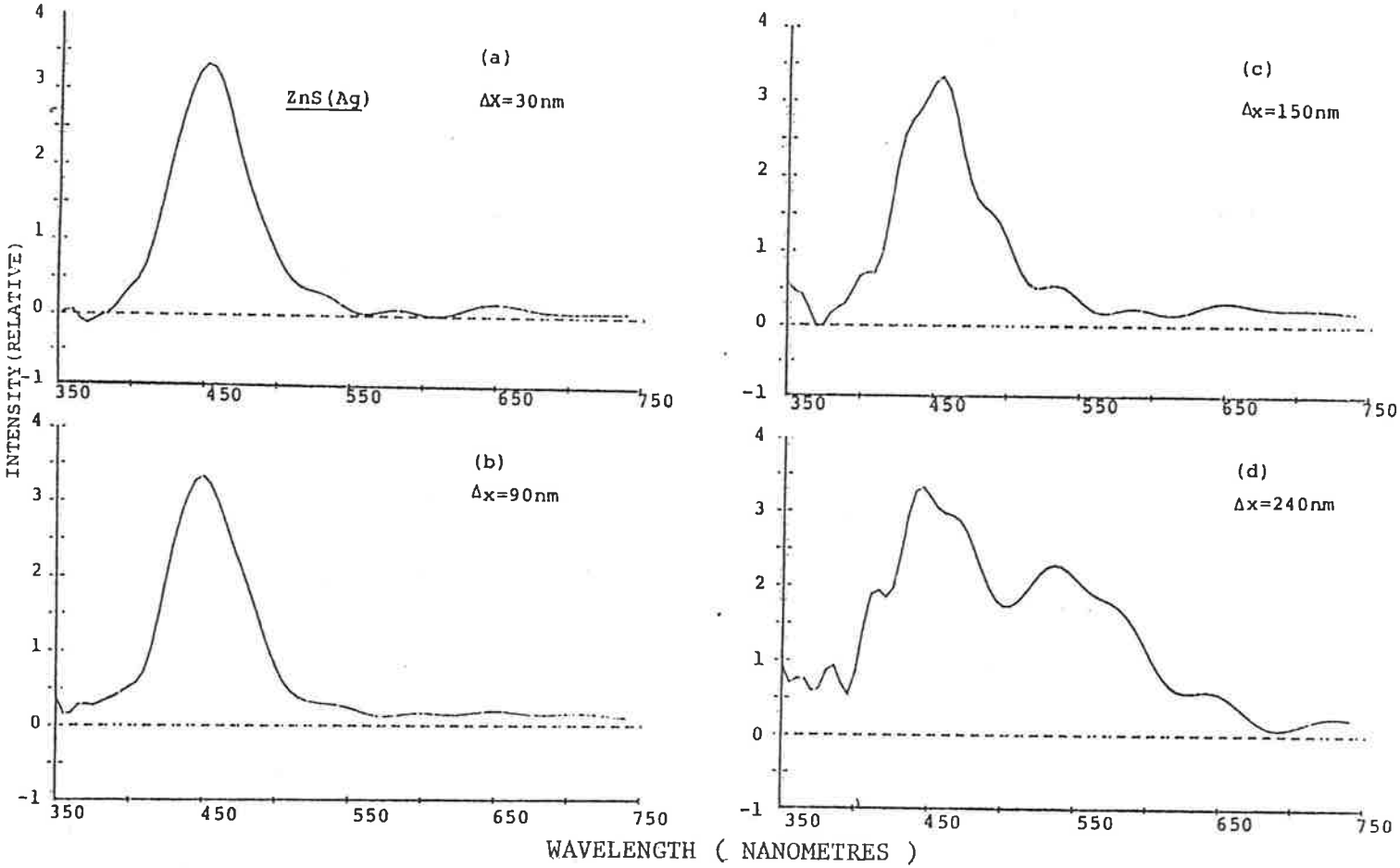

FIGURE 2.12:-Spectra computed from the interferogram as shown in the Figure 2.10 for every one, third, fifth and eighth step number starting from the ZPD. This is equivalent to the instrumental spectra for step sizes of about (a) 30nm, (b) 90nm, (c)150nm and (d) 240nm respectively. Comparing (b) and (c) with (a) suggests that although within the aliasing limits, larger step sizes lead to distorted spectra due to lesser points in the oscillatory part of the interferogram. (d) shows both the statistical and aliasing distortions. Figure (a) is essentially the same as Figure 2.11(a). It has been redrawn for the sake of comparison.

oscillatory region of the interferogram. The 240 nm step size lies beyond the no aliasing condition limit. The effects of poor statistics as well as aliasing are apparent from the computed spectrum for this step size. The aliasing here gives rise to the additional broad band near 550 nm. We therefore conclude that the selection of the step size and scan limits is mostly controlled by the nature of the spectra. Although equations like 2.23 and 2.26 provide limiting values of the scan and step size, these can only be regarded as an upper limit guide for the broad band Fourier spectroscopy, where the ultimate quality of the spectrum appears to be related more to the number of data points in the oscillatory part of the interferogram.

CHAPTER THREE

REVISED DESIGN OF THE EQUIPMENT

"This experiment required an almost unbelievable delicacy of observation. ....It was not surprising that the first instrument built should have been found not to possess sufficient rigidity of structure ...."

H.B. Lemmon on 'Albert Abraham Michelson, 1852-1931'
The American Physics Teacher, Vol. 4 No. 1 (1936)

3.1 INTRODUCTION

This chapter is a description of the equipment. Mechanical, optical and electronics aspects have been illustrated. As indicated in the previous chapter, the work done by Jensen and Prescott (1982, Jensen 1982) showed that the design was feasible and brought it to the first working status. However, revision of the previous design was essential to ensure reliable regular operation of the TL spectrometer. It was carried out by keeping in mind the utility of the design and of the components already available. Detailed specifications of several optical and electronics components reused in the existing design can therefore be seen in the references cited above. This chapter may be regarded as a supplement of what has already been said by Jensen and Prescott, and repetition has been avoided as far as the continuity of the text allowed.

Another aspect of this chapter is some discussion on the performance of salient components, which is either included with the description of the design or mentioned in separate sub-sections. The over-all performance of the equipment and its status as a TL spectrometer is the subject of the following chapter.

3.2 THE DESIGN REQUIREMENTS

The equipment has been designed considering the research needs of a thermoluminescence dating laboratory. Its primary operation is to provide the thermoluminescence curves for types of samples and glowing conditions commonly employed for dating work, but with additional information about the emission spectra. Characteristics and operational details of most two-dimensional thermoluminescence equipment in use in various archaeometry laboratories can be seen in books and reviews on thermoluminescence dating (see e.g. Aitken, 1974, 1985; Fleming, 1979; Singhvi and Wagner, 1985).

For thermoluminescence dating work, the sample is either in the form of grains taken in a planchette or spread over a metal disc, typically 10mm in diameter. A sample chip of comparable dimensions, a fraction of a millimetre thick, is also used for hard samples like flint or pre-dose dating of porcelain and stoneware (Göksu and Fremlin, 1972; Stoneham, 1983; Robertson and Prescott, 1986). The sample is heated in a moisture and oxygen free atmosphere of argon or nitrogen. Constant heating rates up to several degrees Kelvin (typical from 5 to 20) per second are maintained for sample heating from room temperature to a maximum of several hundred Celsius. An electrically heated plate is used for this purpose. Some proposals for direct heating of the samples with pulsed infrared lasers have yet to see development (Gasiot et al, 1982).

The light output is generally low, typically $\sim 10^5$ photons per second per steradian (Fleming 1979). Efficient photomultipliers, preferably with photon counting electronics are used for luminescence detection. The TL-inducing radiation levels are also not very high. Natural radiation dose is typically 2 to 7 mGy per year (Fleming 1979).

Artificial radiation dose to a maximum of a few hundred Gy is provided by laboratory radiation sources.

The thermoluminescence is usually observed through filters biased towards the violet-blue end of the spectrum. Fleming (1979) suggests that this spectral range will cover the TL emission spectra of the most likely crystalline minerals in pottery (i.e. quartz and feldspar) while offering quite effective reduction of the red incandescence background. He maintains that it will also help to subdue any non-radiation induced spurious TL as its emission lies around 550 nm in the yellow-red region of the spectrum. The commonly used combination of Chance Pilkington HA3 heat reduction and Corning 7-59 (or 5-58) blue filters has also been discussed by Fleming and other references cited above. Replacement of Corning 5-58 by a Schott UGA-11 filter from Normandy and Komarów Górny has also been proposed (see e.g. Singhvi and Wagner, 1985). Aitken (1985) suggests that the thermal signal, with a significant green component by the time the temperature reaches 500C, means that only samples with thermoluminescence emission reaching to blue and shorter wavelengths can be dated.

The spectral response curves of the filters mentioned here and the commonly used EMI 9635 QA photomultiplier tube are shown in Figure 3.1 which is after Singhvi and Wagner (1985). In general, the natural minerals are known to have TL emission bands outside these spectral limits as well (see e.g. Medlin, 1968; Sankaran et al 1982, 1983 and McKeever, 1985). The emission spectrum in most cases is expected to be broad-band, at least up to a few tens of nanometres.

The existing 3D TL equipment can provide excellent spectral information under the above mentioned conditions of TL sensitivity,

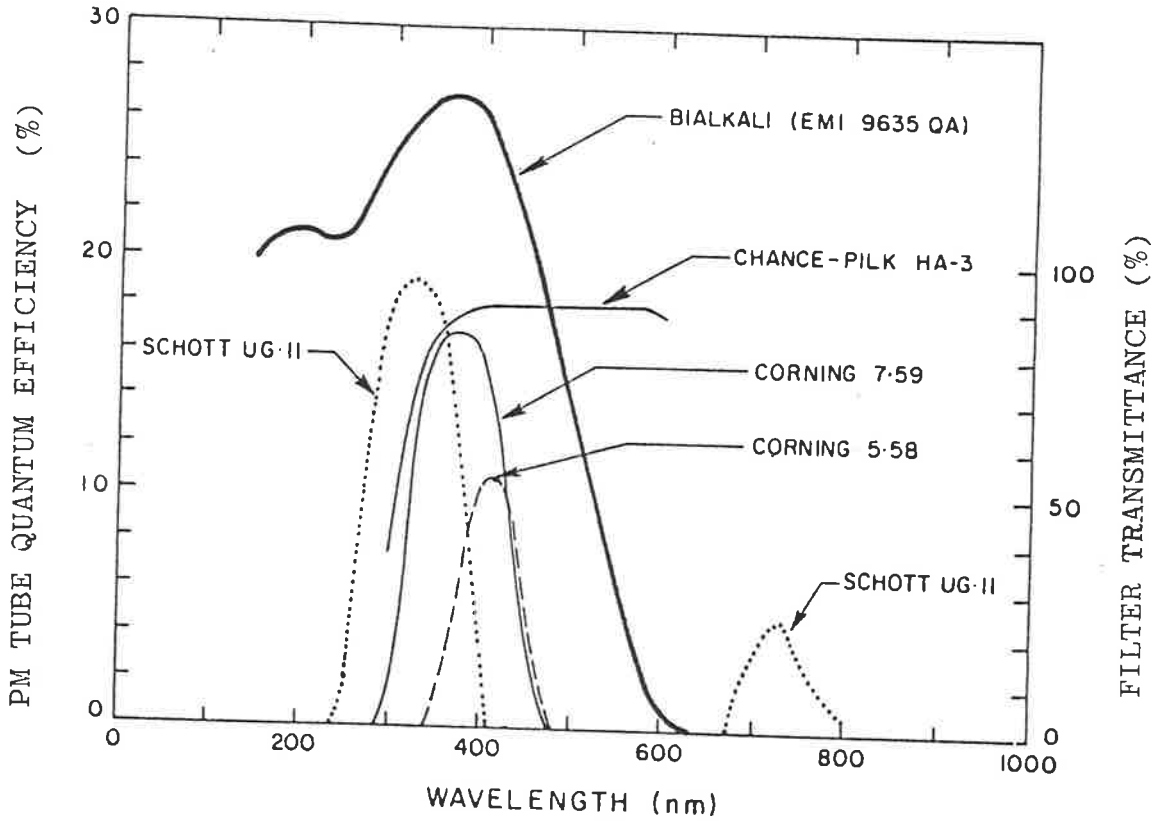

FIGURE 3.1: Spectral response of filters and a photomultiplier tube commonly used in thermoluminescence dating labs. The figure is after Singhvi and Wagner (1985) and indicates that the most TL is observed in the violet-blue region.

radiation dose limit and glowing conditions of the sample. Its only major limitation is a spectral cut-off at 350 nm, which is due to the crown-glass and acrylic optical components. The upper limit around 620nm is due to the diminishing photomultiplier spectral response. Strong red-glow signals can, however, be observed up to 700 nm or even above.

As it will be shown later in this and the next chapter, the equipment is quite versatile in its operation. It can easily be used with constant intensity light sources or isothermal operations at room temperature or above. It is therefore equally useful for scintillation and phosphorescence research. Both the oven and the Fourier transform spectrometer can be driven independently of each other. The oven can thus be coupled directly to a photomultiplier assembly for conventional 2D glow curve operation. The spectrometer can be used for general demonstration, study and applications of Fourier transform spectroscopy in the visible region. Some experiments on the spectrometer have been used to explain relevant principles of the Fourier transform spectroscopy in the previous chapter.

3.3 THE PREVIOUS DESIGN

It is perhaps most appropriate briefly to discuss the main features of the previous design in a separate section at this stage. That design has been explained in detail by Jensen (1982 Ch. 9, 10).

The oven chamber was similar in design to those supplied by the Littlemore Scientific Engineering Company, Oxford (see their catalogue on Thermoluminescence Apparatus, Type 711).

The optical components were mounted on a 20 mm thick steel base plate and consisted of three major parts, the input light gathering

assembly, the interferometer with its movable mirror stepped by a piezo-electric transducer, and the output light detection assembly. These components provided by Cole Precision Optics, Adelaide (now a division of Quentron Optics, Adelaide) and the oven chamber have been retained with a few improvements in the present design. The equipment was interfaced to a PET Commodore minicomputer (Basic 2, 24 k RAM) which also had the soft-ware for computation of the spectra through Cooley Tuckey algorithm. The associated electronics included the oven and movable mirror drive stepping ramps, the EHT for the photomultiplier tube, a discriminator amplifier, a rate-meter and a control panel.

The optical base plate was originally held by metallic stems screwed upon a heavy wooden table. The oven chamber was mounted on rails running on the table top and, after placing the sample on the heating plate, it could be driven under and lifted up with a spring loaded cam arrangement to couple it with the input light gathering assembly fixed to the optical bench. Here, it was evacuated, flushed with an inert gas and then glowed for TL signal as interferograms. A cover on the optical base plate ensured the light tight operation. This cover had to be removed and photomultiplier housing to be replaced for fine adjustment of the alignment.

The accessories included a 'calibration/test light source' assembly which could be used for constant intensity light sources, and a photo-multiplier assembly for the 2D glow-curve mode.

Jensen (1982, Ch.10) obtained interferograms and corresponding spectra for some constant intensity light sources (laser and LED's) and one selected fine grain pottery sample for its fairly constant intensity response in the region of interest. The early design clearly, therefore,

demonstrated the feasibility of Fourier transform spectroscopy applied to thermoluminescence studies but Jensen also pointed out that 'several design modifications were desirable before the interferometer could be used for fully routine measurements of TL emission spectra'. He identified the problem areas and suggested possible improvements. These problems and their proposed solutions (Jensen 1982, Ch. 10 Section 5) were critically evaluated and formed the starting point for consideration of design modifications.

Perhaps the most necessary (and, interestingly, overlooked by Jensen) were the changes pertaining to the mechanical rigidity of the optical system under actual experimental conditons. It was soon realized that the stresses experienced by the steel base plate during its evacuation and later supply of the inert gas, were enough to cause drastic distortions in any previously achieved optical alignment.

Stability and isolation of the optical table was, therefore, given primary attention in the revised design. Several other essential changes and additions were made in the optical and electronics design. These changes also include the introduction of a 'remote' fine alignment setup, improvements in the mirror and oven drive ramps and revision of the data accumulation and processing methods (hard and software). The revised design has been described in the following sections.

Bill Old from the Departmental workshop was mostly responsible for the mechanical fabrication, Brian Fuller from Electronics Services improved the electronics and wrote the machine language programmes for operation and analysis.

3.4 THE MECHANICAL CONSTRUCTION

Primary thought behind the mechanical reconstruction of the equipment was the added stability of the Michelson interferometer.

3.4.1. The Oven Chamber

The purpose of the oven chamber is to provide a sample heating facility up to several hundred degrees celsius at a constant rate in oxygen- and moisture-free environments. Its central feature is an electrically heated nichrome plate about 30 x 60 mm in dimensions. About 10 mm length on each end of the strip is firmly clamped in high current electrode junctions connected to the secondary winding of a transformer. The current through the primary windings of this transformer is controlled for the heating rate and temperature. Feed back signal from a thermocouple spot welded under the oven plate is used for this purpose (see the electronics design for more details).

Other important features are a coolant line through the electrode junctions, a vacuum line and a high purity gas line. Components in these lines have been described through block diagrams in Figure 3.2 (a-c). Although most components have been remounted to suit the new requirements, the over all chamber design is the same as the previous one. The improvements include the introduction of a water filter on the coolant line, a remote controlled electromagnetic isolation valve in the vacuum line and a ball head control valve in the gas line. The former was necessary to guard against long-term scaling and rust settling in the coolant line, while the latter two provided a handy control from the front panel. The high purity nitrogen in the gas line has been replaced by relatively low cost special grade argon, with no expected loss in the

a: THE VACUUM LINE

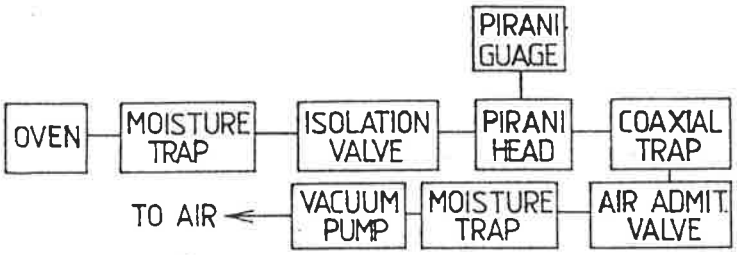

COMPONENT DETAILS

MOISTURE TRAPS	P_2O_5 POWDER	
ISOLATION VALVE	DYNAVAC, MELBOURNE	VS-050-B
PIRANI HEAD	EDWARDS, SUSSEX	PR-10-S
PIRANI GUAGE	EDWARDS, SUSSEX	PR-10
COAXIAL TRAP	VEECO, PLAINVIEW	VS-120
AIR ADMIT VALVE	EDWARDS, SUSSEX	D11102000
VACUUM PUMP	RUD BROWNE, BURWOOD	DYNAVAC

FIGURE 3.2a: Arrangement and some specifications of the components in the vacuum line of the oven chamber.

b: THE GAS LINE

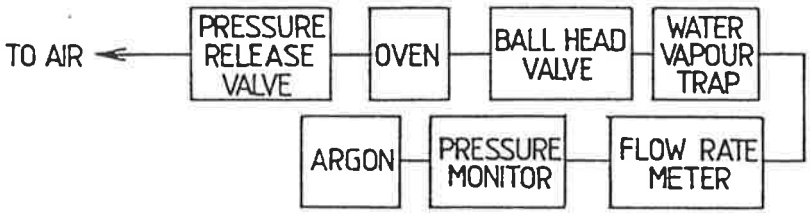

COMPONENT DETAILS

MOISTURE/HYDROCARBON TRAP	VEECO, PLAINVIEW	TR-101
FLOW RATE METER	CIG	0-14ℓ/min
PRESSURE MONITOR	CIG	MONITOR 2
ARGON	CIG	SPECIAL GRADE 062 SIZE G

c: THE COOLANT LINE

COMPONENT DETAILS

FILTER	CLACK, WINDSOR	HYDROCURE WATER FILTER
LINE DIAMETER	3mm	
FLOW RATE	~2ℓ/min	

FIGURE 3.2b,c: The oven chamber gas and coolant line components; arrangement and some specifications.

quality of signal (Smith, 1983a). The maximum heating temperature limit has also been extended from 500 to 1000°C and the heating step ramp has been smoothed for heating rates below $5Ks^{-1}$.

3.4.2 The Oven Table

For a two dimensional glow-curve operation, a housing containing an EMI 9635QA photomultiplier and a set of HA3 and 59-7 filters can be placed on the top of the oven chamber. This housing has been described by Jensen (1982, Ch.9). For a three dimensional TL glow-curve, the oven has to be translated under a fixed and rigid optical bench. It has therefore been mounted on a laboratory jack which can be raised and lowered through a shaft and wheel arrangement. Three rod in tube guides between the upper (movable) and the lower (fixed) plates of the jack ensure smooth lift. The jack rests on rails so that the chamber can be driven to the right position under the optical table before it is lifted up for coupling. This position is fixed with a buffer on the rails. For 3D operation the chamber is covered with a 'light guide'. It can then be evacuated, isolated from the rest of the vacuum line, and flushed with the argon gas. The light guide includes an aspheric lens which, in the previous design, was fixed in the optical base plate. It also has provisions for field stops and filters. The light guide has been sketched in Figure 3.5 and operation of the aspheric lens will be described further in connection with the optical design. Figure 3.3 is an overall view of the main part of the equipment.

Also fixed on the rails is the fine alignment set up for the interferometer. It has been installed just behind the oven chamber and comes in line with the input light assembly of the interferometer when

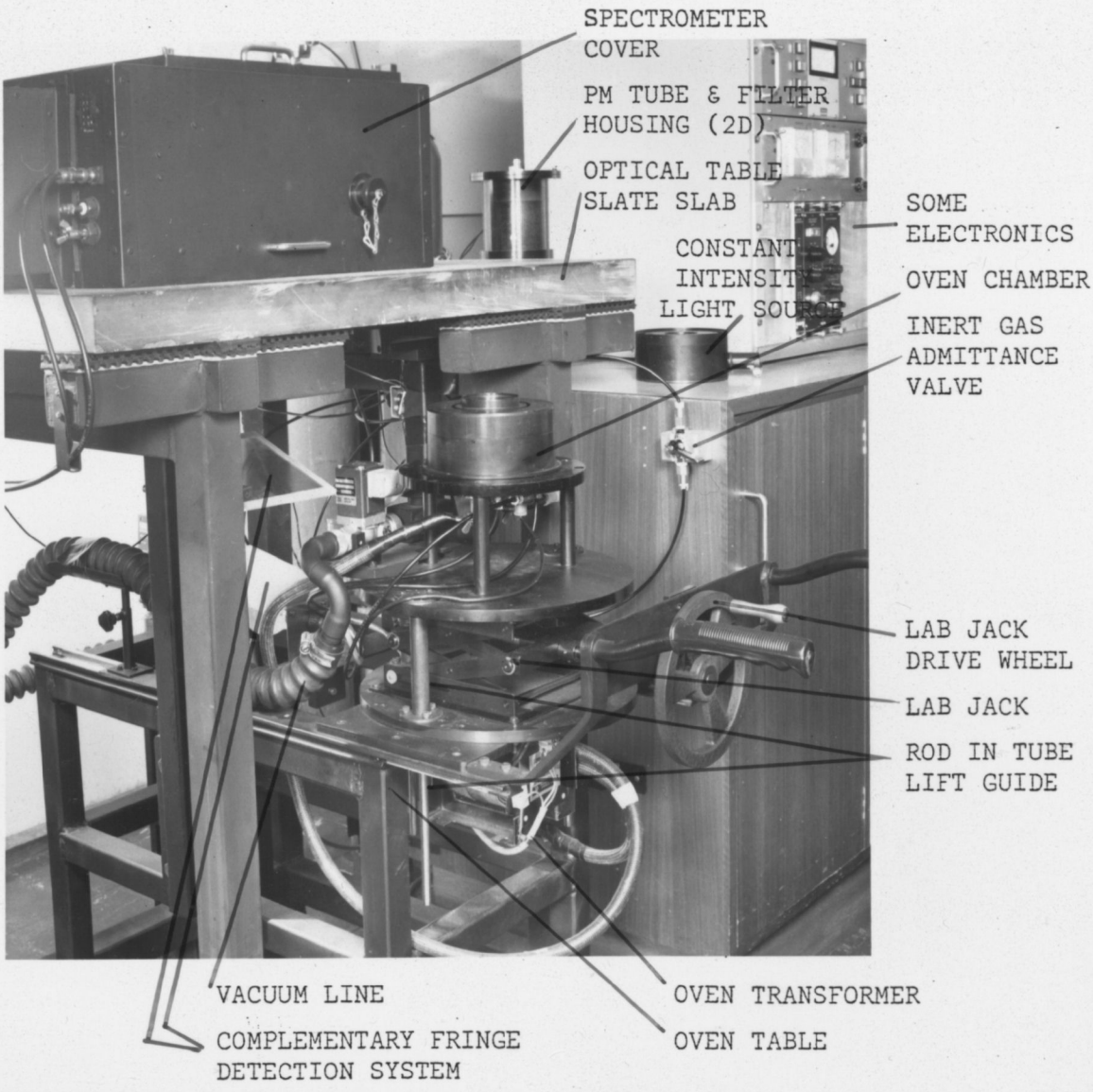

FIGURE 3.3: An over all view of the equipment.

the chamber is drawn forward (Figure 3.3). It consists of a broad-band light source (an ordinary tungsten bulb), a translucent glass light diffuser and a partially silvered glass plate. The operation of the fine alignment set up will also be described with the optical design of the equipment.

An essential feature of the design is that the oven chamber and light guide assembly does not couple directly with the optical table. It is, instead, guided into a canopy fixed to the top of the oven table itself (Figure 3.4). The periphery of this canopy is joined to the optical table through a light tight unstretched black rubber sheet (Figure 3.5). Movements and vibrations of the oven table are consequently not transmitted directly to the optical table. Holes through the canopy and slate of the optical table allow light transmission from the oven chamber light guide to the input light assembly of the spectrometer. An EHT interlocking microswitch inside the canopy senses the light guide in its "up" position. Threaded feet and locking nuts help adjust the oven table level relative to the optical table.

3.4.3 The Optical Table

As can be seen in Figure 3.3, the optical table is basically a slate slab held separate from, but on the top of the oven table. The 890 x 610 x 50 mm^3 slab weighs about 75.5 kg (density about 2.8 g/cm^3). It rests on a frame of hollow 50 x 50 mm square tubing and a 30 mm thick rubber padding is provided under the feet of the structure. Two layers of a special vibration absorbing neoprene mounting pad (M164, Mackay Silentruba, Kent Town, Adelaide) have been introduced underneath the slate. A 155 mm diameter hole through the slate accommodates the oven

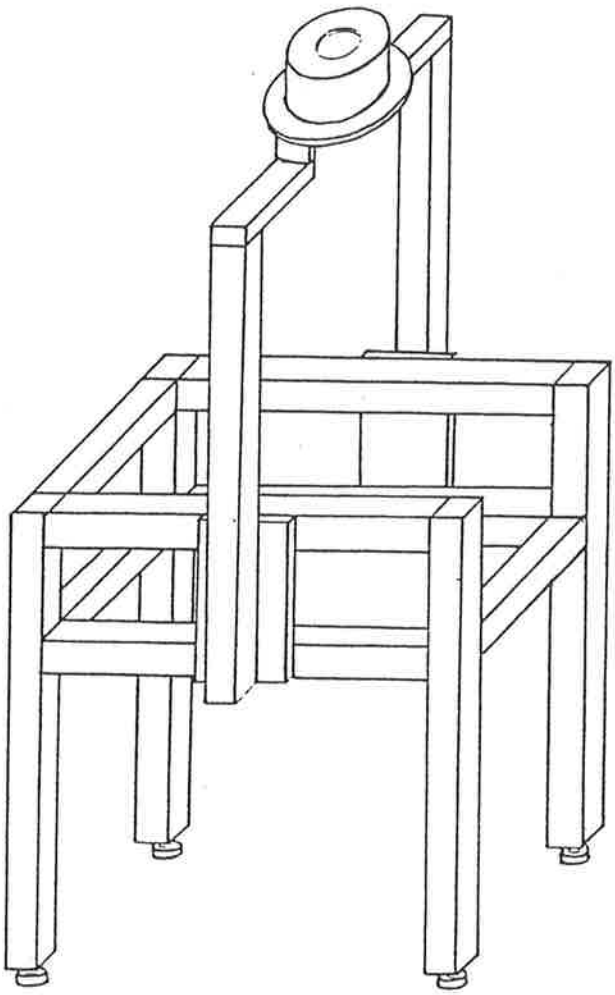

FIGURE 3.4: The oven table with its canopy. The oven chamber fixed on jack and rails on the table top (see previous figure) is directed into this canopy for 3D TL operation.

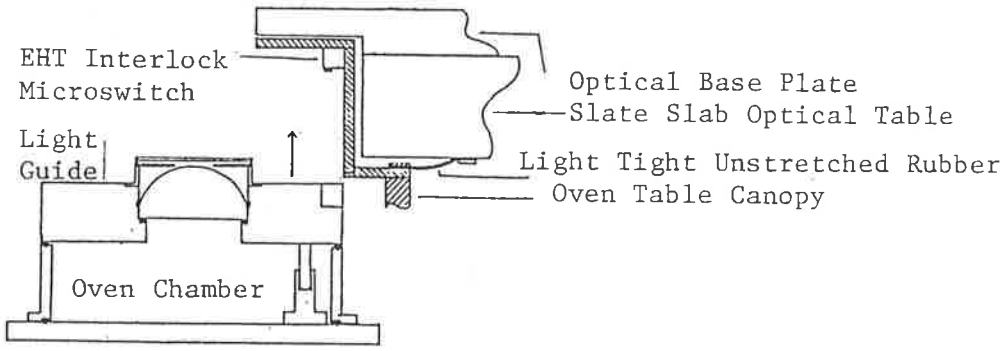

FIGURE 3.5: The oven table canopy and the optical table join through an unstretched light tight rubber sheet for vibration isolation. The figure also shows the light guide on the oven chamber.

table canopy (Figure 3.5).

The 470 x 470 x 20 mm^3 (32.5 kg) mild steel optical base plate is the same as used in the previous design. In the present design, however, the slate slab and the steel plate have been bolted at twenty three points in a nearly equally spaced pattern (Figure 3.6). The surfaces were initially flattened to better than 0.05 mm and a 25 μm thick teflon sheet was spread in between. The adjoining surfaces of the bolts were also machined for a uniform contact and an equal torque of about 50 Nm was applied on each bolt. These measures were thought to be necessary for a fairly uniform degree of stiffness throughout the optical base. The gun-blue blackening of the base plate provides a non-reflecting and rust protected surface for the optical components.

It is worth mentioning at this stage that the measures taken to modify the optical table design for added stiffness and stability may not be the best methods available from the point of view of contemporary technology. They are, however, much cheaper!

The two options considered for stiffness were to fabricate an open cell ribbed structure with metallic tubing and then weld the existing plate on it or, otherwise, to bolt it on a rigid slate slab. The latter was preferred for the ribbed structures are known for persistent, low resonant frequencies of high amplitude which are hard to isolate ('Table system alternatives at a glance', Newport Research Corporation Catalogue 1980, p.3).

The sources of disturbing vibrations in the laboratory considered were the motor of the vacuum pump, the air conditioner, the oven chamber translation, and operator's movements in the laboratory. Two isolation systems were considered: the rubber composite pads usable for damping

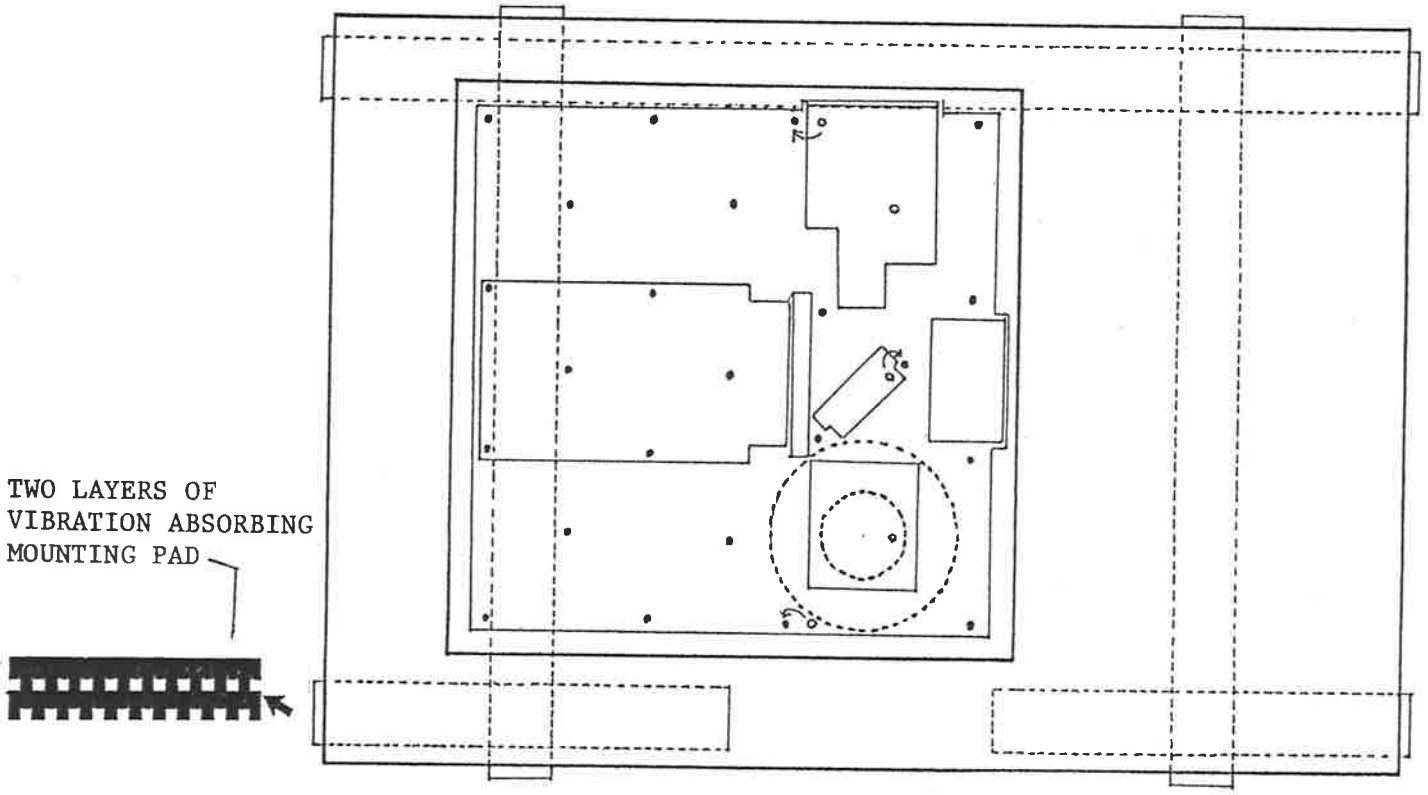

FIGURE 3.6: Steel optical base plate and slate slab stiffening bolts pattern. Each bolt was tightened to the same torque of 50Nm. The vibration isolation rubber sheet under the slab is also shown.

frequencies from above 15 Hz (see Silentruba Catalogue No. 58 1983 pp 1-2), and the pneumatic pressurised tubes usable for frequencies above 1-2 Hz (see e.g. an article on 'Vibration Isolation' in NRC Catalogue 1980 pp 12-19). The former was tried first for its relative rigidity and less constant care problems.

The low frequency noise between two to fifteen Hz is attributed to the floor motion (see reference above). Once completed, the optical system was tested for any adverse effects due to normal laboratory operation. Results of one such experiment are shown in Figure 3.7. The instrument was aligned for a bright light fringe output for the He-Ne laser light (no field stop) and common laboratory operations and some credible accidents were performed to observe any fringe deflection. No adverse effects were seen for common lab opeations and movements.

For credible accidents like dropping a tool on the optical table or abnormal floor vibrations, a strongly damped vibration of about 1 Hz and 1/3 rd of a fringe took place. The system was therefore approved and no instability due to common lab operations have been experienced over the past few years.

3.4.4. The Optical Components

Most optical components reused from the previous design have been remounted on the steel base plate in the same manner as before. The reflecting surfaces have been repolished and recoated. The major addition in the interferometer is an (SG 101) star gimbal mount for the fixed mirror. It has been supplied by Burleigh Instruments Inc. (New York) but its base and mirror frame have been modified to match the rest of the optical setup with the optical axis at about 66 mm above the base

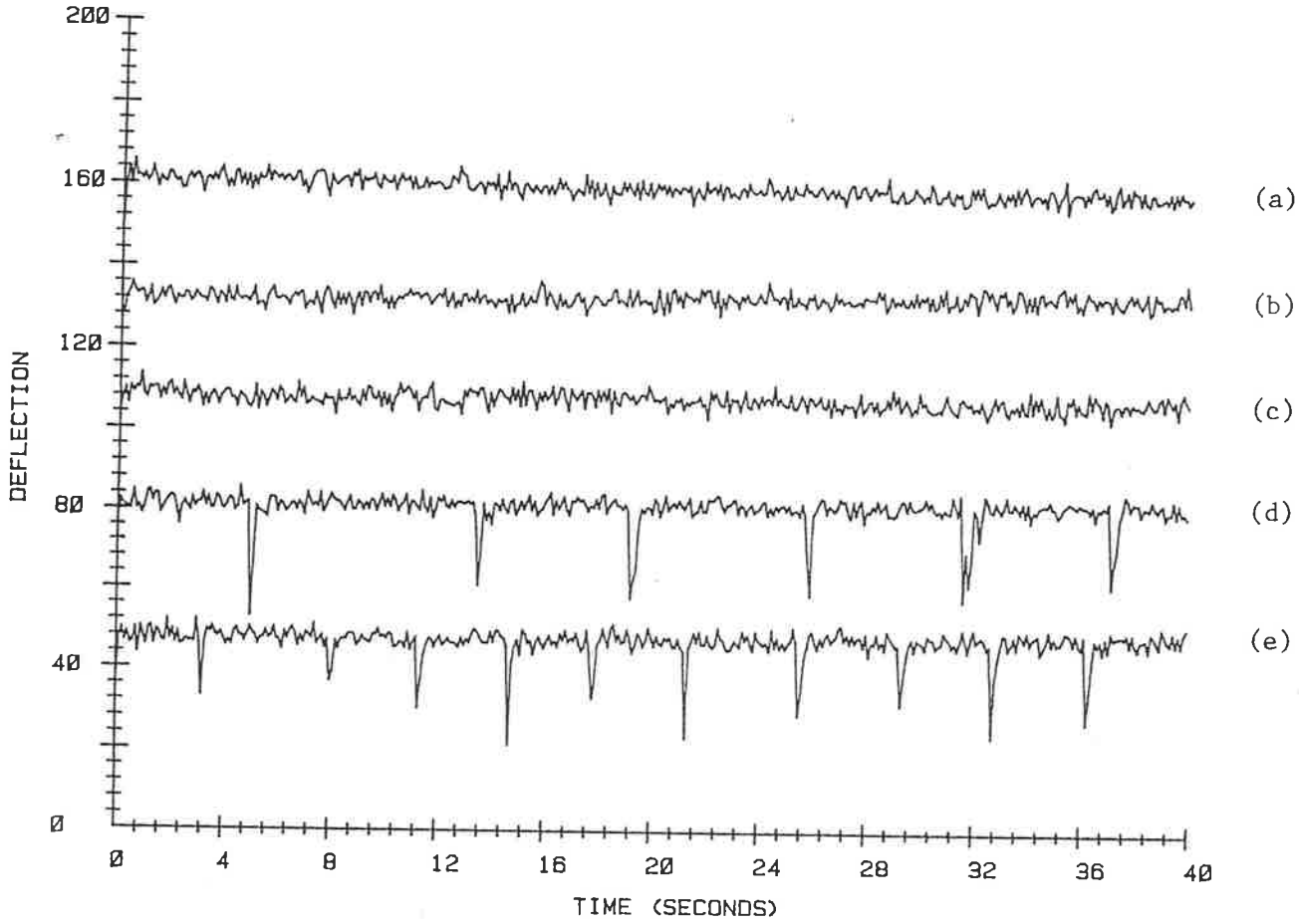

FIGURE 3.7: Results of an experiment to test the alignment stability of the optical system under various operating and credible accident conditions. (a) Still (b) lab operational i.e. vacuum pump, air conditioner on and operator working (c) a tool weighing 250g dropped several times from a height of about 30cm on the oven plate (d) the same tool dropped on the optical table and (e) author (79kg) jumping in the lab. The figures have been plotted with an off-set and deflection refers to about 1/3rd fringe.

plate. The gimbal mount enables fine alignment control through the bias voltages on two (PZ 40) piezoelectric transducers. A sliding door, fitted with an EHT interlock microswitch in the light tight cover, provides access to the micrometers, both on the gimbal mount and the movable mirror, for any adjustments that may be required. The light tight chamber can also be opened from the top for better access to most components on the base plate. Figure 3.8 is a view of the optical components as taken from the top. This figure has been labelled with an overlay explaining various components.

The input light assembly comprises a field lens, a front surface mirror and a Fresnel lens. The 50 mm diameter and about 200 mm focal length field lens, with its focal plane parallel to the base plate is coaxial with the aspheric lens of the light guide on the top of the oven chamber. The 115 x 80 mm front surface aluminium coated mirror inclined at an angle of 45° reflects the light input normal to its previous course and along the optical axis of the interferometer (Figure 3.9a). The 81 mm diameter and about 102 mm focal length Fresnel lens guides it on to the interferometer. Further details on the interdistances and operation of this input light assembly are given in the optical design of the equipment.

The optical components of the interferometer require additional mounting care for firm but unstrained holdings. Distorted or strained surfaces clearly show, particularly through the colour contrast and distortions in the white light fringe patterns near the compression. Loose mounts lead to an unstable pattern and can often be detected by gentle tapping or by a finger stress and release on the suspected component.

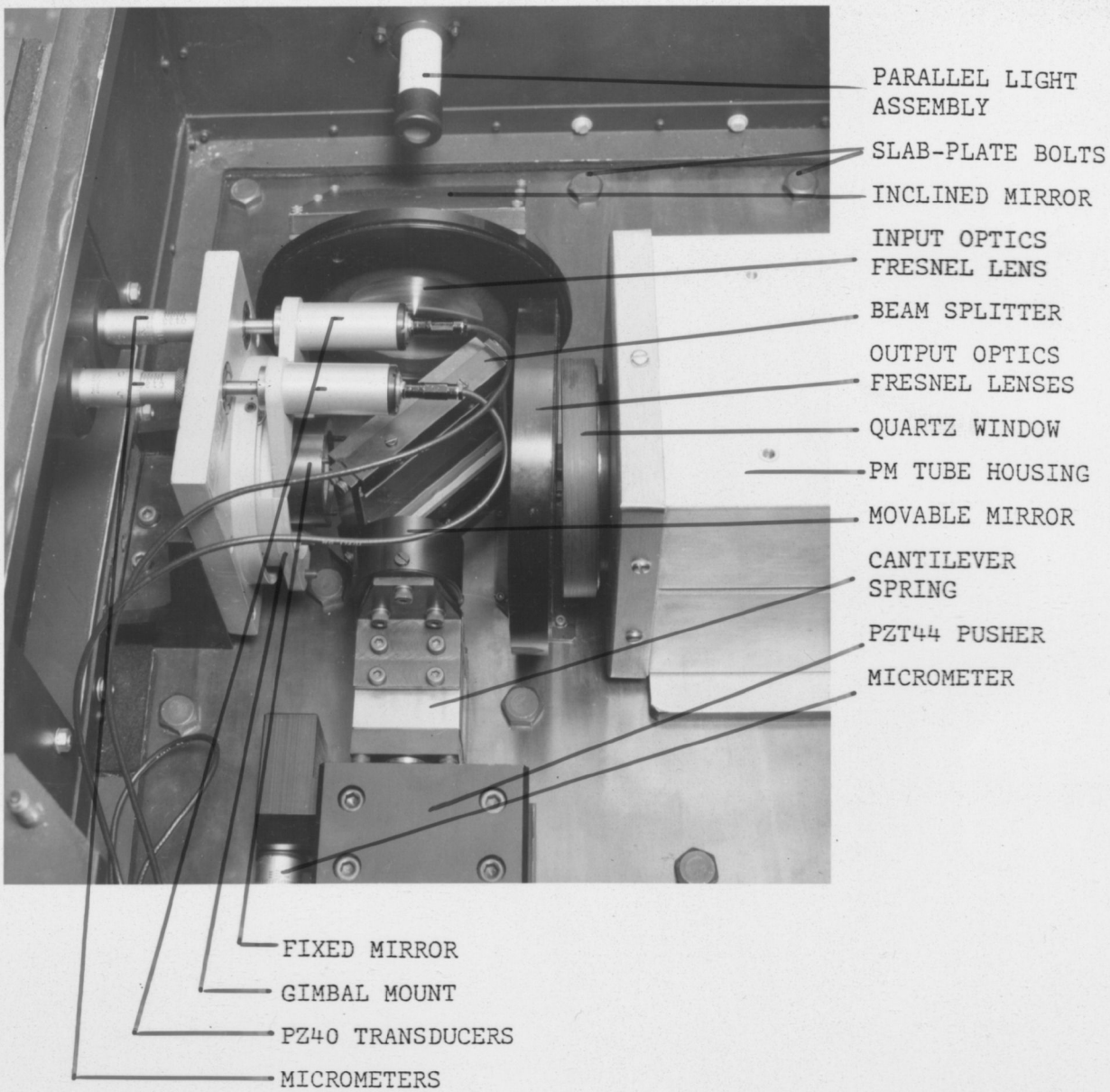

FIGURE 3.8: A view of the optical components of the spectrometer.

The aluminium coated 10 mm thick 33 mm in diameter glass substrate mirrors of the present interferometer rest on three point contact phosphor bronze discs. They are held in frames with three grub screws pressing against a paper ring, padded at the front surface. The fixed mirror frame can be adjusted in the threaded holder of the gimbal mount (Figure 3.9b). The movable mirror frame is mounted on a parallel leaf cantilever spring arrangement as shown in Figure 3.9 (c). The mirror can be pushed forwards and backwards in steps between two selected limits just by selecting appropriate initial bias and step size for a PZT 44 (Burleigh, New York) piezoelectric transducer pusher. Coarser adjustments can be made through a fractional micrometer which pushes an optical grade stage with the PZT pusher fixed on it. Jensen (1982, Ch. 9) gives a detailed discussion on the merits and construction of the movable mirror stepping mechanism. Some relevant aspects of the scanning cycle of this mechanism are cited in Section 3.7 of this chapter.

Figure 3.9(d) is a side view of the beam splitter/compensator holder. The two plates spaced by thin paper strips are held with phosphor bronze curled leaf springs. Each plate measures 76 x 54 x 6.5 mm^3 and the sandwiched surface on the beam splitter is partially coated with aluminium for nearly equal output transmission efficiency over the entire region of spectral interest.

The output light gathering assembly has been shown in Figure 3.9(e). A combination of two thin Fresnel lenses (81 mm diameter, 37 mm combined focal length) is held in front of the EMI 9635QA photomultiplier tube in its cooling unit. The Products of Research (Massachusetts) thermoelectric-liquid heat exchange unit TE104, with a double non-fogging quartz window, has been raised on an 8 mm high plate to match the optical

S: Sample disc, ϕ = 10mm

L_1: Aspheric lens, BK7 crown glass, ϕ=50mm, fl=37.5mm

F: Filters, ND1-4, broad-band (optional)

FS: Field stops (optional)

L_2: Field lens, BK7 crown glass, ϕ=50mm, fl=200mm

M: Front surface mirror, Al

L_3: Fresnel lens, acrylic =81mm, fl=102mm

M_1: Fixed mirror, Al, ϕ=38mm

M_2: Movable mirror, Al, ϕ=38mm

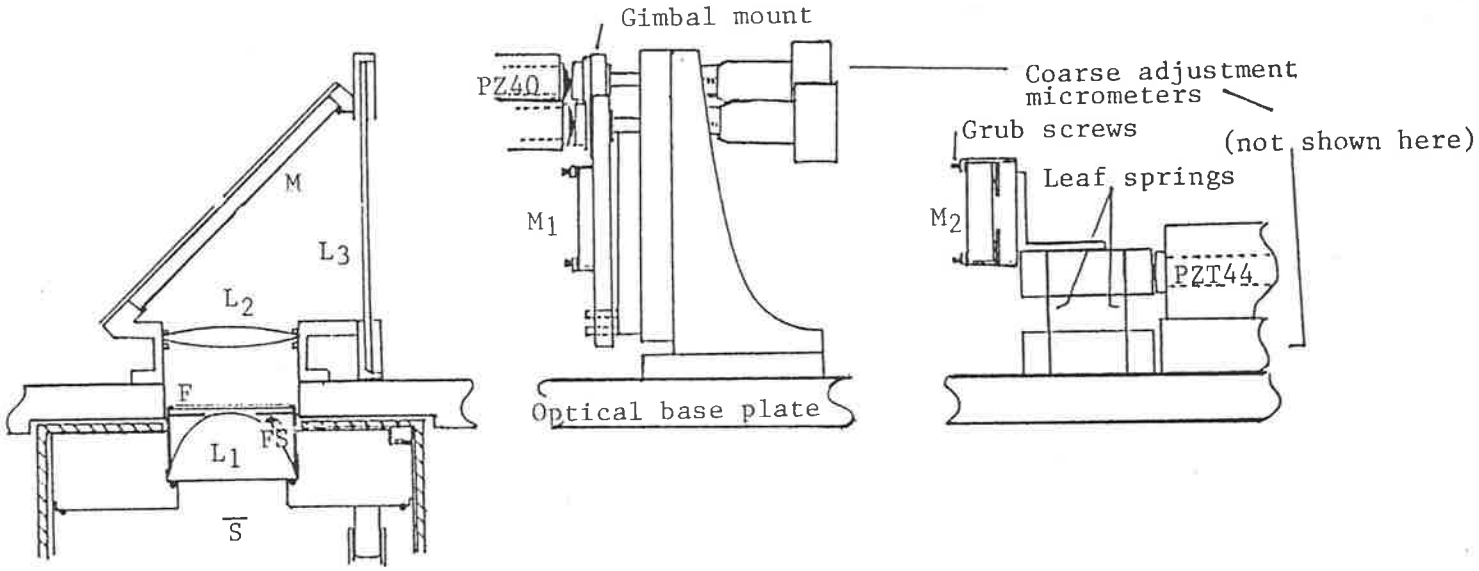

a: INPUT LIGHT ASSEMBLY

b: FIXED MIRROR

c: MOVABLE MIRROR

FIGURE 3.9: Sketches of variuos optical components (a) input light assembly, (b) fixed mirror and (c) movable mirror ... (contd.)

B: Beam splitter, BK7 crown glass, Al

C: Compensator

L_4: Two thin Fresnel lenses, acrylic, ϕ =81mm
f1(combined)=39mm

PM Tube: EMI9635QA

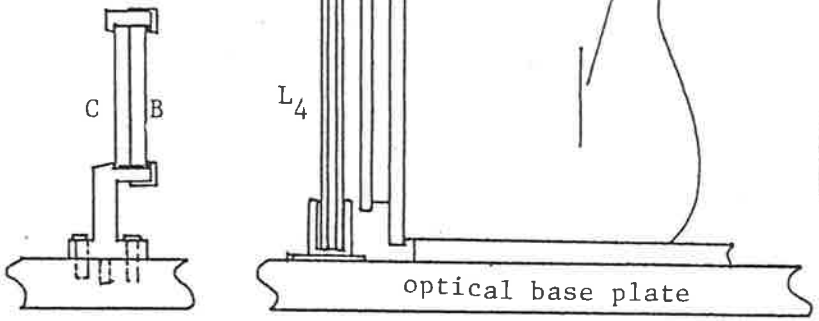

d: BEAM SPLITTER

e: OUTPUT LIGHT ASSEMBLY

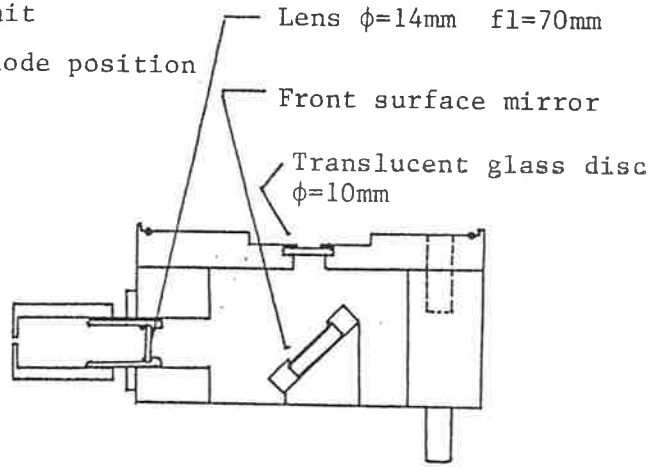

f: CONSTANT INTENSITY LIGHT SOURCE

(contd.)... FIGURE 3.9: Sketches of various optical components (d) beam splitter and compensator (e) output light assembly and (f) constant intensity light source.

axis. Holes at the appropriate places on this plate allow for the bolts on the optical base plate as shown in Figure 3.6.

A parallel light input assembly with an aperture and lens arrangement can be seen in Figure 3.8. A 3 mm diameter gap in the aluminium coating of the front surface mirror (Figure 3.9a) allows the light through the optical axis of the interferometer. The assembly can be illuminated externally by opening a window provided in the light tight chamber.

A similar parallel light arrangement illuminates a 10 mm diameter diffused glass 'simulated' TL disc of the constant intensity light source (Figure 3.9f). This assembly fits on the oven chamber and, with the light guide on its top, can be interfaced with the interferometer for experiments through the same optical set-up. The name 'constant intensity light source' only refers to the fact that, unlike the thermoluminescence signal, the light throughput does not change as a function of temperature (or time) during the course of operation. Several illustrative experiments reported in the previous chapter were performed using this assembly.

3.5 THE OPTICAL DESIGN

Mounting of most optical components used in the present design has been illustrated in a previous sub-section. The present section is confined to the optical operation of these components as a part of a Fourier transform spectrometer. General principles of performance and the theory of a Michelson interferometer are well illustrated in several books on interferometry and spectroscopy (see e.g. Michelson, 1927; Bell, 1972; Tolansky, 1973; Chamberlain, 1979; Steel, 1983). Except

for a very brief introduction and some relevant citation, these principles will not be described in any detail.

3.5.1 The Beam Splitter

As has been mentioned earlier in introducing basic principles of Fourier transform spectroscopy (Chapter 2), the essential features of a Michelson interferometer are a half silvered surface and two mirrors arranged to reflect back the light beams split at the surface. An identical plate placed in front of the beam splitting layer compensates for additional path and phase changes introduced by the substrate.

Design specifications of these plates are given in Figure 3.9(d). The surfaces are specified to be flat to $\lambda/20$ ($\lambda \sim 500$ nm) on both sides, with parallelism better than 5 arc seconds. The 50:50 splitting aluminium layer in fact refers to a 44% reflectivity measurement monitored for a 570 nm wavelength of light beam incident at 45° during evaporative aluminium coating.

The optical properties of aluminium films vary significantly with light wavelength and coating thickness in this region. Reflection and transmission lines in Figure 3.10(a) have been drawn using the data from Table 6g-4 (p6-159) of the American Institute of Physics Handbook (3rd edition). The dotted lines for 570 nm have been interpolated. The bold line which joins the points of equal splitting ratios for various wavelengths indicates that it is achieved at different coating thicknesses and at different reflection (R) or transmission (T) coefficients. The line passes through 42% reflectivity at 570 nm which is close to the one quoted by the supplier for this specific beam-splitter.

Bell (1972, Ch.9) discusses the spectral response and efficiency of

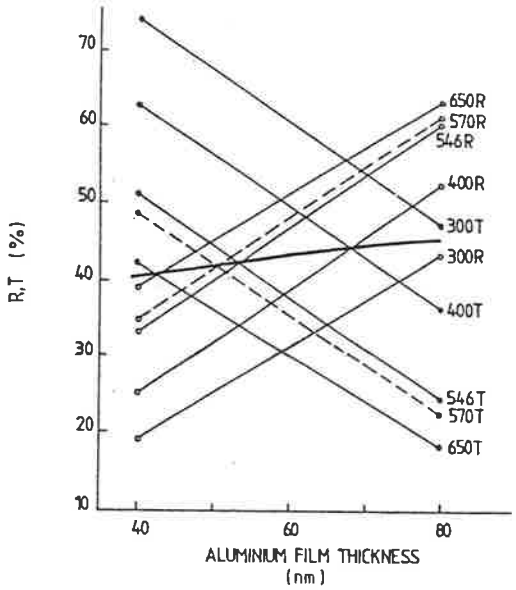

(a)

λ (nm)	300	400	546	570	650	Al (nm)
2RT	·34	·36	·35	·35	·33	50
	·35	·37	·35	·34	·33	54

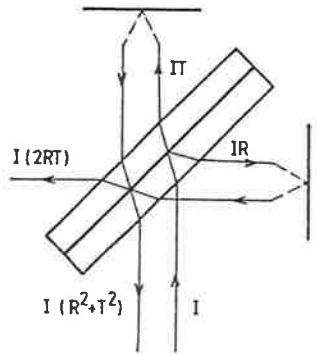

(b)

FIGURE 3.10: (a) Reflection and transmission coefficients for different light wavelengths through freshly evaporated aluminium coating between 40 and 80 nanometre thickness.
(b) The power loss through the beam-splitter of a Michelson interferometer. Insert shows the estimated absolute efficiency 2RT for the present beam-splitter. A slight shift (about 4mm) in the optical axis due to light refraction is also evident.

different types of beam splitter coatings (mostly applicable to infra-red spectroscopy). It is easy to visualise that the pair of beams interfering in the output arm are reflected and transmitted once through the beam splitter (Figure 3.10,b). Neglecting any other light losses, the efficiency of a Michelson interferometer is given by

$$\text{Efficiency } (\lambda) = 2R(\lambda) \times T(\lambda) \qquad (3.1)$$

For an ideal beam splitter both R and T equal 0.5 and a maximum 50% of the input light power will, therefore, be transmitted through the output. Absolute efficiency value estimates for different wavelengths are shown as an insert in Figure 3.10(b). These values correspond to coating thicness for 42% (estimated) and 44% (specified) reflectivity at 570 nm. The results indicate the absolute efficiency of about 0.35 with a maximum of about 10% variation over the spectral range. These figures, obtained through interpolation between two data points may, however, be regarded as a fair but nominal estimate and a further decrease by a few percent due to an oxide layer formation may also be possible (see e.g. Holland, 1966). The oxide formation is somewhat logarithmic in nature with time (e.g. Eley and Wilkinson, 1959) and the effect slows down after a few months of deposition. Holland (1966) shows 4% and 8% decrease in reflectivity around 530 nm light after exposure in air for fifty days and four years respectively. The corresponding numbers for 600 nm light input are 2% and 5%.

3.5.2 The Mirrors

The effective diameter of the front surface aluminium coated mirrors

in the present design is about 30 mm, while about 4 mm width on the peripheries is held under the frame (Figure 3.9, b. and c). According to the suppliers, the mirror surface is flat to $\lambda/20$. For $\lambda \sim$ 500 nm, a surface ripple of 25 nm is therefore possible. The effect of mirror surface non-uniformities and maladjustments has been discussed in the previous chapter with reference to the performance of the existing equipment (Section 2.4.3). It has been shown for example that the interferograms can be recorded for light input over the entire range of interest (350-750 nm) but for a given input light intensity the incoherent component increases with decreasing wavelength (Figure 2.6). A corresponding decrease in the computed spectral intensity will therefore be seen. Figure 3.11 shows the interferograms for a ~ 550 nm light input from a light emitting diode. These have been recorded for restricted fields of view using field stops of varying diameters. The purpose of this experiment was to resolve the contribution of the (field of view dependent) mirror alignment limits and the (random) surface non-uniformities. The incoherent component varies only slightly which is, therefore, mostly attributed to the surface non-uniformities in the range of $\lambda/20$. This experiment also shows the effectiveness of the mirror alignment procedure which will be illustrated in a following sub-section.

3.5.3 The Input Optics

The input optics of the equipment comprise a light guide that fits on the oven chamber (Figure 3.5) and input light assembly fixed on the steel base plate (Figure 3.9a). Various components of the input optics

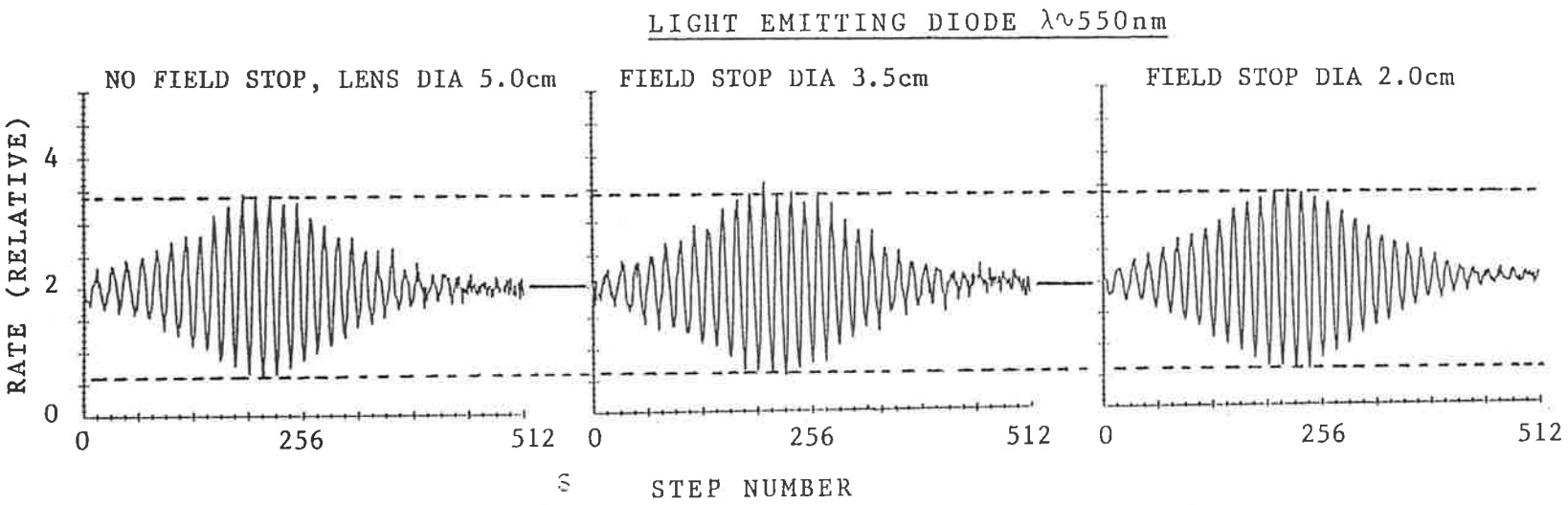

FIGURE 3.11: Interferograms for an LED light input through stops of varying diameter. The figures have been normalized to the same average value. The nearly equal incoherent light component is indicated by nearly the same width of the interferograms.

can be seen in Figure 2.1 of the previous chapter, where these were drawn as a part of an overall sketch of a Fourier transform spectrometer. Some specifications of these components have also been given in a previous section in connection with the mechanical design of the equipment.

As can be seen from the rays traced in Figure 3.12, the input optical components form a real and about three times magnified image of the sample disc (on the oven plate) in the mirror planes of the spectrometer. The front surface inclined mirror and the beam splitter have been omitted in the equivalent design for ray tracing. Refraction through the beam splitter, however, introduces about 4mm displacement of the optical axis which has been accounted for in the actual design (Figure 3.10b).

The angle of incidence 'Θ' of the rays upon the interferometer mirrors as determined by the input optics controls the resolving power of the instrument (Section 2.4.2, Chapter 2). With no field stop, Θ_{max} for this instrument is about 16° or solid angle about 0.24 steradians. The resolving power ($\lambda^2/\Delta\lambda$) as obtained using the Equation 2.20 of the previous chapter is therefore about 26. The étendue of the equipment (defined as the product of the beam area and the solid angle) is about 182 πmm^2.

3.5.4 The Output Optics

The output optics consist of a pair of thin Fresnel lenses and a photomultiplier tube in its cooling unit (Figure 3.9e). The set of Fresnel lenses forms the image of interferometer mirrors in the plane of the photocathode of the photomultiplier tube (Figure 3.13).

Temperature dependent dark current of the tube can be reduced

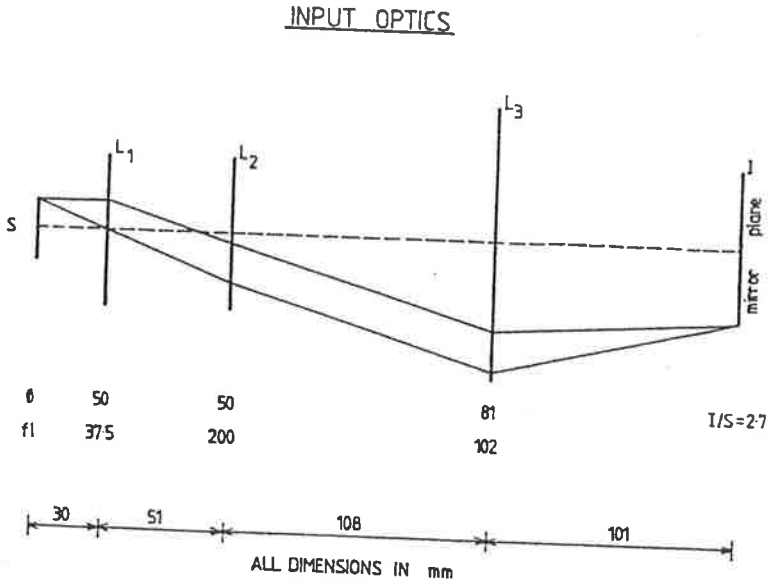

FIGURE 3.12: A ray diagram to illustrate the working of the input optics. For convenience in drawing, the source has been doubled in size over the commonly used (10mm diameter) disc. The front surface mirror and the beam-splitter have also been omitted in the equivalent design.

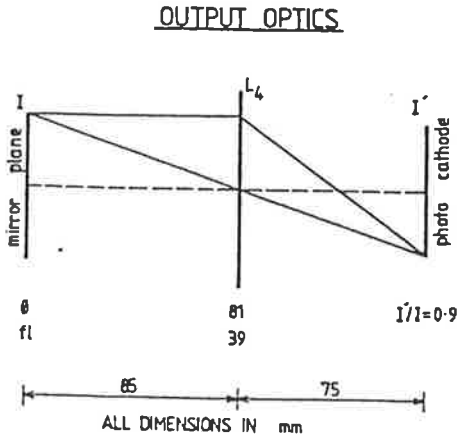

FIGURE 3.13; The output optics ray diagram. Once again the beam-splitter is omitted.

through the thermoelectric liquid cooling unit. This cooling unit was not operated for the work presented in this thesis because of already low background counts typically less than 100 Hz (or 5 counts per channel) for the existing photomultiplier.

3.5.5 Fine Alignment

Methods of Michelson interferometer alignment and various types of fringes are well discussed in books on interferometry (e.g. Michelson 1927, Tolansky 1973, Steel 1983, and Bell 1972). Jensen (1982, Ch.9) describes in detail a method applicable to the existing interferometer.

The coarsest alignment involves locating the mirrors and beam splitter holders in appropriate positions so that the later alignment is well within the adjustment range on the mounts.

No matter what technique is used for the intermediate alignment step, the aim is to observe what is commonly referred to as the 'white light fringes'. These multicoloured fringes, formed by the broad-band (white) light sources, are seen near ZPD and, as expected from the broad band interference patterns (Chapter 2), fade sharply in intensity on the two sides. The first few coloured fringes can easily be seen separated by dark destructive interference lines. The symmetry of the colour pattern on both sides of a central fringe provides (although coarse) first hand information about the absence of any phase error. The intermediate alignment may require adjustments on the micrometers and grub screws of the mirror holders. These provisions are easily accessible in the present design by opening the side and top lids of the interferometer cover.

The final step is the fine alignment of the mirrors. The central

bright fringe is brought in the middle so that it intersects with the optical axis and the mirrors are aligned parallel to ensure that it covers the entire field of view. Several coloured fringes covering the whole field of view can then be observed through stepping the mirror on either side of ZPD. Unless by choice, the white light fringes, once obtained in the intermediate setting, were never lost over the operation of the last few years; which says much for the stability of the equipment. The fine alignment is, however, a day to day requirement before operation and the set up is now described.

In a Michelson interferometer a second complementary set of fringes is produced by the pair of reflected beams which travel towards the source (Figure 3.10b). These complementary fringes can be seen by intercepting the beam using another beam splitter in the input arm (see e.g. Steel, 1983). This property has been used for fine alignment. As has been described in a previous section on the mechanical design, diffused white light is shown to the interferometer through the field lens in the input assembly. The complementary interference pattern is viewed using a partly coated glass plate. The interferometer mirrors can now be aligned by adjusting the bias voltages both for the gimbal mount and the movable mirror pusher, viewing simultaneously the entire circular image through the partially coated glass plate. This set up is partly visible in Figure 3.3.

3.5.6 The Movable Mirror Drive

It can be derived from Equation (2.24) in Chapter 2 that the maximum useful optical path difference scan limits in an interferogram turn out to be 19.4 μm on each side of the ZPD. Even for a monochromatic light

input in the present spectral range of interest, no further improvement in the resolution is expected in scanning beyond this limit. The total of 38.8 μm (or 19.4 μm on each side of ZPD) is an optical path difference (OPD) well within the range of the movable mirror drive, which is up to 80 μm optical path difference or 40 μm physical displacement of the mirror and corresponds to the transducer bias change from 0 to 1000V.

As has been discussed in Section 2.7 of the previous Chapter, the optimum OPD step size for the present work is about 30 nm. Both the initial bias and step size can be selected through potentiometer knobs on the front panel of the transducer control unit, while the total number of steps and stepping rate are options in the control computer programme. The data presented in this thesis have mostly been collected for 512 steps, each of about 30 nm optical path difference and at a stepping rate of 100 Hz. The equipment design, however, offers a variety of combinations of movable mirror stepping parameters and this aspect will be further illustrated in the next section on the electronics design of the equipment.

The effect of step non-linearity of the piezo electirc pushers on the performance of the existing equipment will be discussed in Section 3.7.

3.6 THE ELECTRONICS

In principle, the electronic design of the equipment is simple. Appropriately pre-scaled pulses from the same voltage controlled oscillator (VCO XR2206) are used to provide step ramps for the current through the oven transformer, for cycling the movable mirror of the interferometer and for advancing the data output channels. The heating

rate from 0.2 to 100 Ks^{-1} is determined by the frequency of these pulses, which can be dialled on a calibrated ten turn potentiometer provided on the front panel of the control unit (Figure 3.14).

The oven control voltage ramp ranges from zero to 10.24 volts covered in 256 steps. A total of 10240 pulses from the VCO are pre-scaled by 40 for this purpose. A chromel alumel thermo-couple welded under the middle of the heating plate provides the oven-temperature signal with reference to an autocold junction (ACJ2). The signal output is swtitchable to gains such that 10.24 volts correspond either to 512° or to 1024°C. The latter enables heating up to about 1000°C but the system was not actually used above 800°C or so. The difference between the ramp and the thermocouple output is read as the servo-error, which in fact determines the current increment through the primary coils of the oven transformer. Each of the 256 ramp steps, therefore, corresponds to heating up to 2 or 4K depending upon the mode of operation.

As the oven is driven by the servo-error, the physical (or thermo-couple) signal always lags the ramp signal which is actually used as a temperature index for the purpose of recording. Figure 3.15 indicates that, due to increasing heat loss, the lag increases with temperature, the maximum being about 25K at 800C. A linear correction by about -3% of temperature above 300°C to all presentations in this thesis will therefore lead to more realistic estimates.

Discrete stepping of the oven temperature is not noticed at higher heating rates ($10Ks^{-1}$ or above). At comparatively lower heating rates (up to about 5 Ks^{-1}), the discrete heating produces a small undesirable ripple in the TL signal, depending upon the heating rate (Figure 3.16a). A switchable capacitor has therefore been provided in the

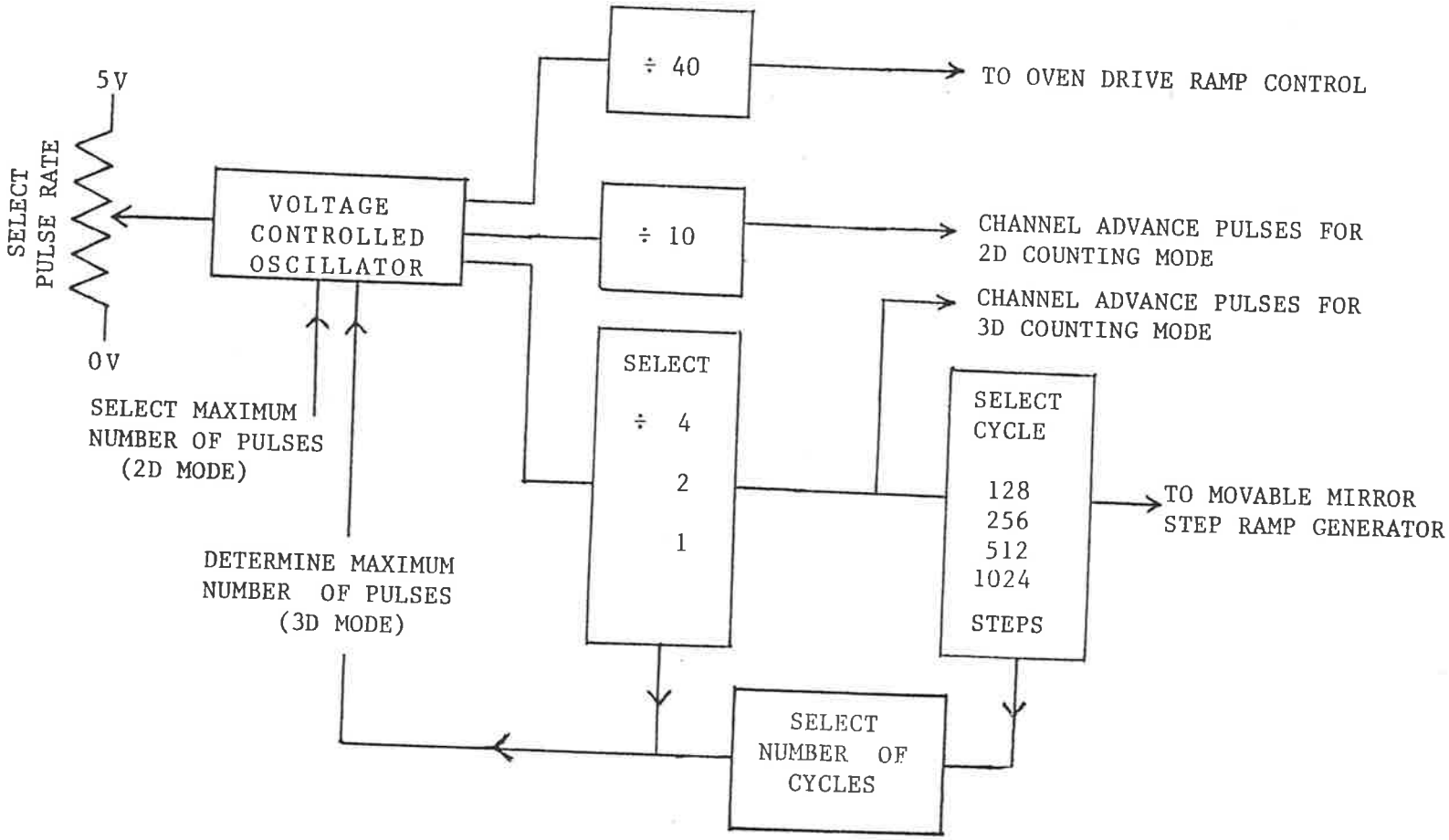

FIGURE 3.14: A block diagram to illustrate the VCO control for synchronised TL operation.

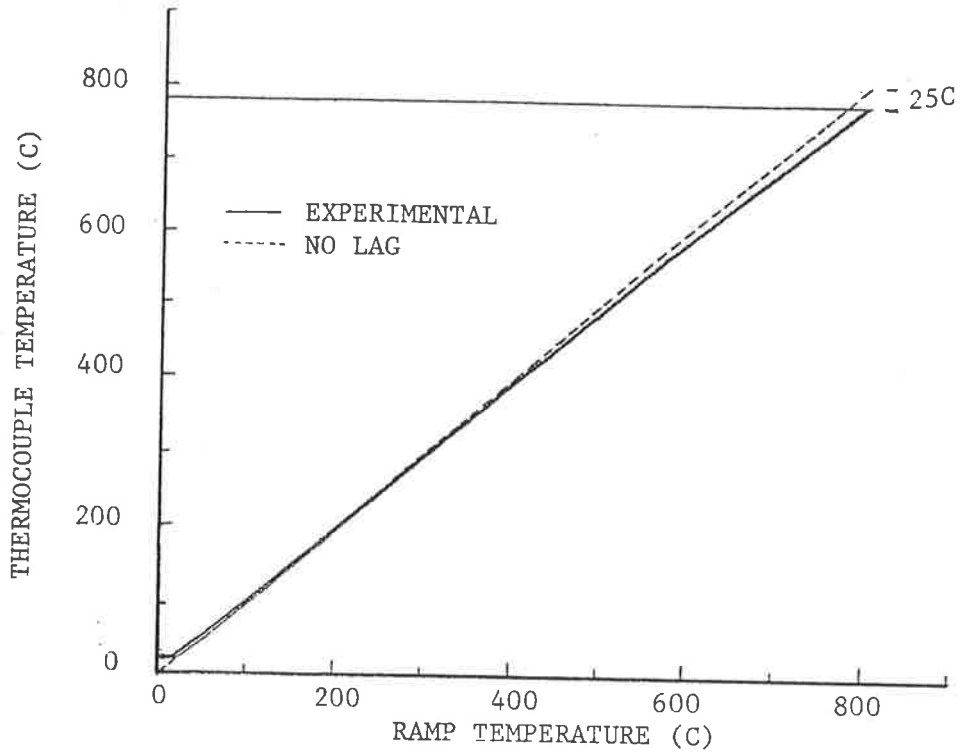

FIGURE 3.15: The ramp (recorded) vs. thermocouple (physical) temperature signal up to 800C. A small physical temperature lag is necessary for the servo-drive. It increases with temperature due to increasing heat losses.

present design which smoothes the amplified thermocouple output and hence the servo-error (Figure 3.16b). Its use is recommended at low heating rates between 1 to 5 Ks^{-1}.

As can be seen through Figure 3.14, the data accumulation channels can be advanced for 20, 10, 5 or 2 signals per degree rise in temperature, the last option being exclusive to the 2D mode of operation. Two sixteen bit buffer counters share TTL pulse counting from alternate channels while the other is read by the Commodore 2001 PET computer. A maximum of 65025 counts can be stored per channel. Once saturated the channel recycles itself so that the useful information is not lost.

Both photomultiplier tubes (EMI 9635QA) for the 3D and 2D glow curve outputs are used in photon counting mode. The NIM output pulses from the discriminator-amplifier (ORTEC 9302) go to a rate-meter (ORTEC 9349) and a NIM to TTL pulse stretcher. A switchable pre-scalar (1,2,4,8,16) is also incorporated on the front panel to accommodate high intensity signals without channel saturation. The optimum EHT voltages for 2D and 3D photomultipliers are +1400V and -1650V respectively (the opposite signs are correct).

The movable mirror drive ramp can be cycled in 64, 128, 256 or 512 steps each side, so that several interferograms can be recorded while the sample is heated. The temperature interval limits per interferogram in the present design vary from 3.2 to 204.8 K. For TL spectra reported in this thesis, twenty interferograms each covering a temperature range of 25.6 K are recorded while the sample is heated to 512 C at a rate of $5Ks^{-1}$. It has been mentioned earlier that the step size and initial position of the mirror can be adjusted through knobs on an RC44 (Burleigh) ramp generator, which has been modified to supply independent

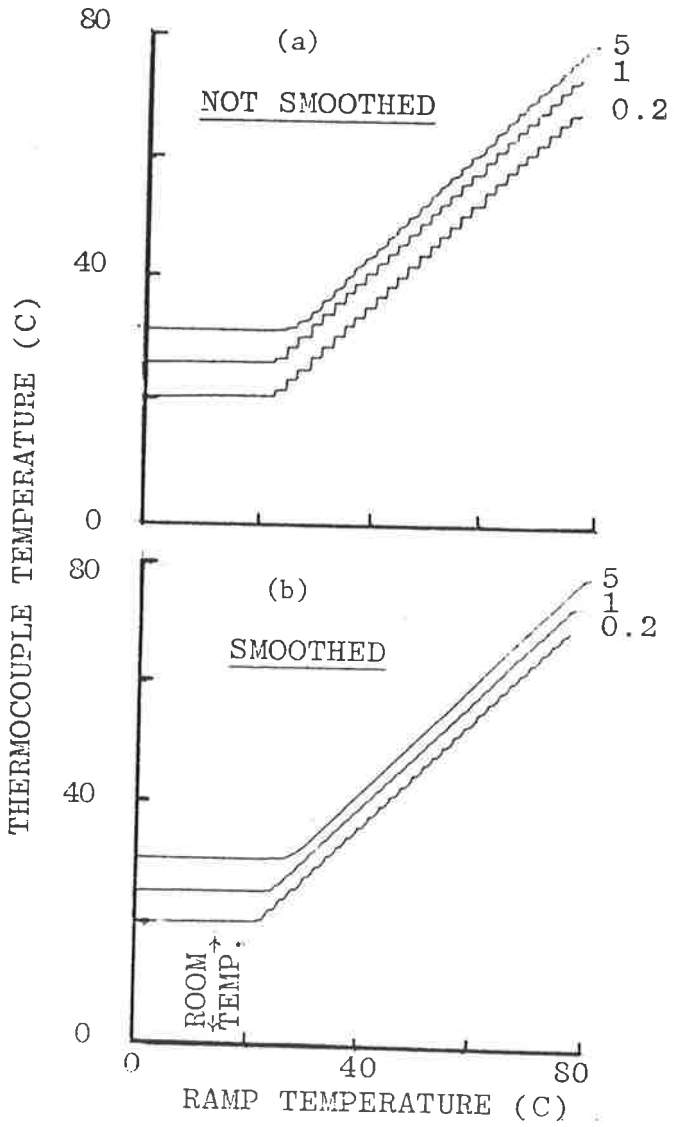

FICURE 3.16: (a) Discreteness in the oven heating at low rates results in significant uneven heating. (b) The oven heating ramp is smoothed by introducing a switchable capacitor in the thermocouple amplified output. Heating rates have been indicated by the numbers along the curves which have been plotted here with a certain zero offset.

bias voltages for two PZ40 transducers of the fixed mirror star gimbal mount as well.

Figure 3.17 is a block diagram of various electronic components in data accumulation and anlysis. The raw data are transferred over a serial RS 232 link to an MS-DOS personal computer (Olivetti M24) for analysis with a superior processing power. Presently up to twenty data files can be transferred, analysed and retrieved overnight through this method. The PET Commodore interfaced to the system is not used for this purpose and the data stored on the floppy discs is instead analysed on an independent set up. A possibility to analyse the data on the University main computer VAX F exists but it is not preferred, mainly for a long queue due to heavy day and night work load. Spectrum printing and plotting routines do exist for MS-DOS, but part of the the data presented in this thesis has been plotted using the facilities around the Commodore in the 3D TL Laboratory (i.e. a Hewlett Packard 7225A X-Y plotter, Commodore Tractor Printer 4022P printer and Commodore CBM Model 8050 dual disc drive).

3.7 HYSTERESIS IN PIEZO ELECTRIC PUSHERS

Non linearity of the step size due to hysteresis in the piezo electric transducer cycles has been noticed by various users of (Fabry-Perot) spectrometers (see e.g. Hernandez, 1978; Basedow and Cocks, 1979). According to the suppliers, the Burleigh PZT pushers 'exhibit typical characteristics of high motion PZT materials i.e. substantial non-linearity, creep and hysteresis'. The suppliers pointed out that for applications requiring large, precise and rapid linear steps the PZT

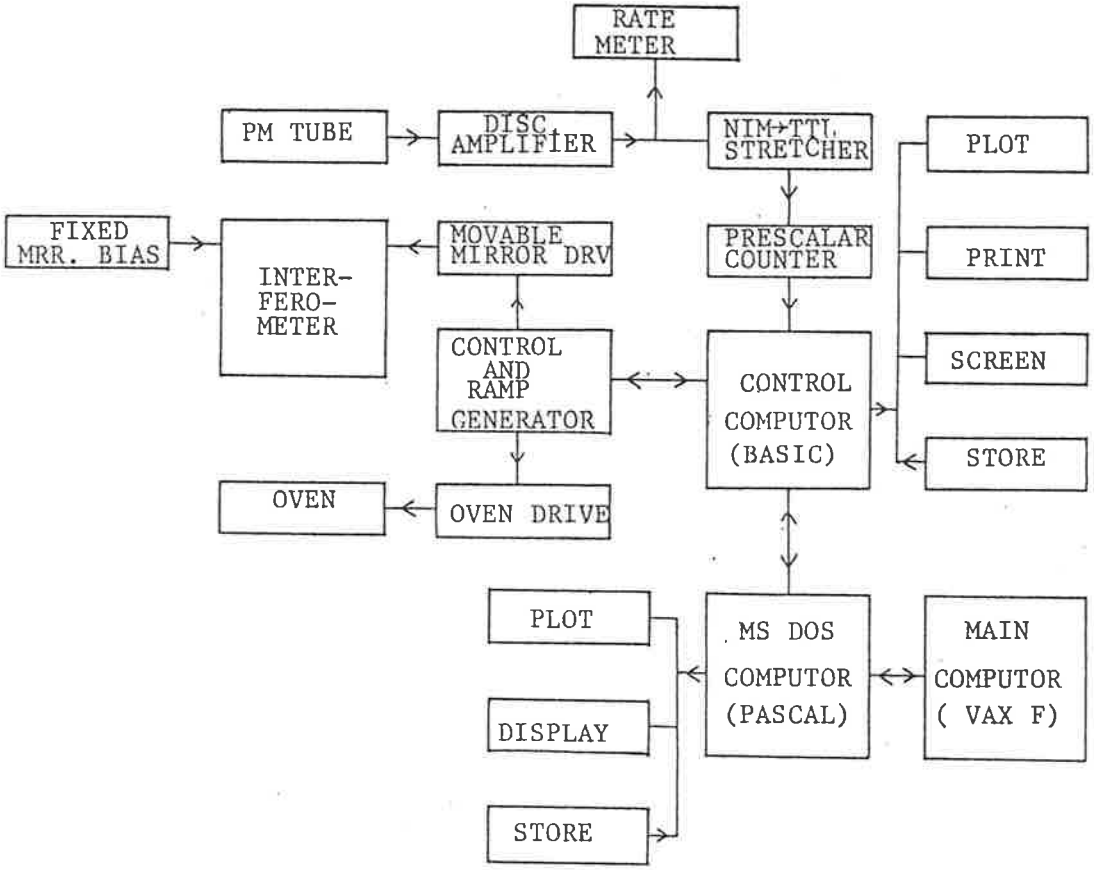

FIGURE 3.17: A block diagram to illustrate the electronics set up. Some components drawn as separate actually share a common housing. MS-DOS system is interfaced to a separate PET Commodore similar to the control computor.

pushers will probably present some problems (Instruction Manual for PZT Pushers, Burleigh Instrument Inc. New York).

Operation of the movable mirror drive with a PZT44 pusher was, therefore, examined. Results shown in Figure 3.18 (a-d) indicate that considerable non linearity exists in the stepping mechanism over the frequency range of operation of normal interest. It is also evident that after the first half cycle (plotted as a dotted line), the mirror drive tends to stay in the same hysteresis loop for the rest (up to twenty) half cycles. Each half cycle here corresponds to the stepping for an interferogram. Curves for the second half cycle have been replotted in Figure 3.18e for convenience of comparison. These curves show a slight increase in the 'mechanical resistance' at higher stepping rates. This observation is in line with what has been expected from the PZT pushers.

If the shape of the hysteresis curve is known, then some improvement in the scan linearity can be made by applying a non-linear scan voltage. This facility actually exists on the RC44 ramp generator, and the value of a quadratic correction factor can be adjusted with a programmable ramp adjust potentiometer (Tech Memo/Instruction Manual for RC-43/44 Ramp Generators, Burleigh Instruments Inc., New York). With the existing set up, this facility is useful for a fairly linear scan in one direction at the expense of added non-linearity on the reverse half cycle. Changing the stepping rate will require readjustments (see Figure 3.18e).

An alternate solution would be to independently monitor the step size by incorporating an additional small referencing interferometer sharing the same mirror drive, or by mounting a capacitance displacement transducer and using the output in a servo system to control the ramp.

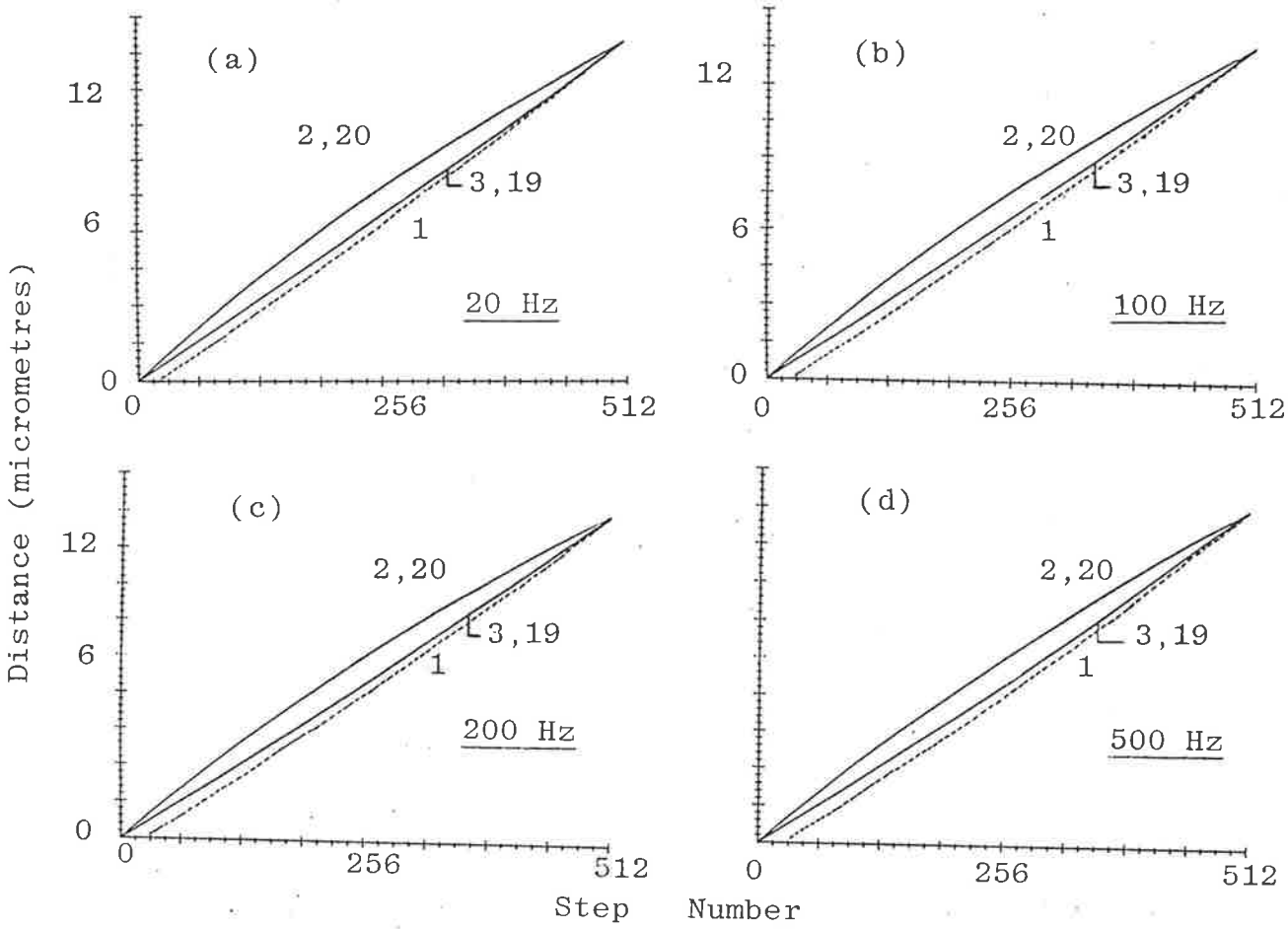

FIGURE 3.18(a-d): Non linearity and hysteresis in the movable mirror stepping mechanism as seen at different stepping rates. The numbers indicate the half cycle corresponding to the curve.

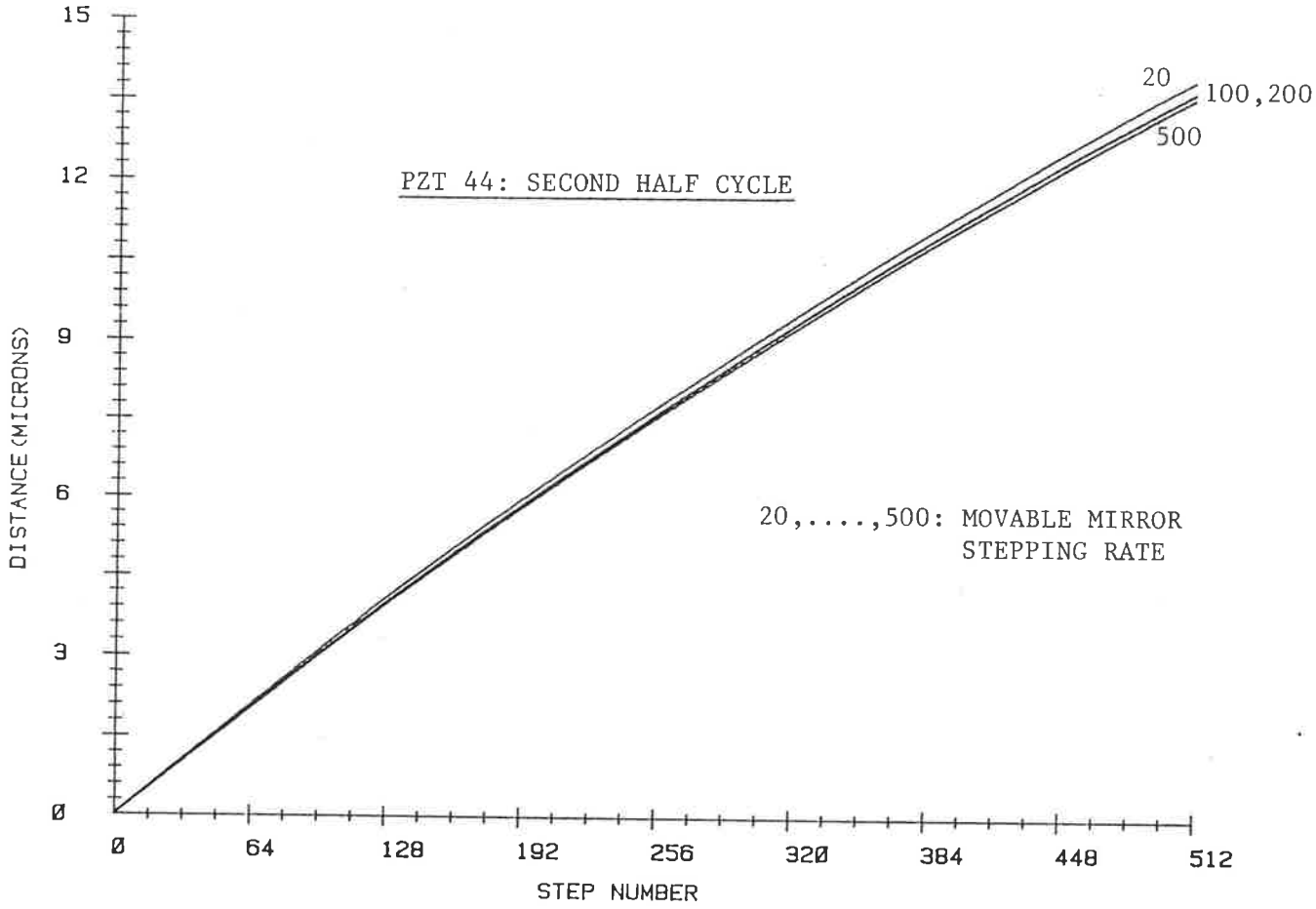

FIGURE 3.18(e): The second half cycle of the PZT44 pusher hysteresis loop. These curves have been replotted using the data from the figures a-d to indicate that the load resistance increases slightly with the increasing stepping rate . The increase in load resistance is shown by the decrease in the distance covered for a given number of steps (or the bias voltage).

This has not been necessary in the present case.

Results presented in Figures 3.18(a-e) are in fact the plots of second order polynomial fits upon the points corresponding to the maxima and minima of a monochromatic (laser) light interferogram which, in the absence of any non-linearity, are expected to fall at equally spaced step numbers. Figures 3.19(a-c) show that all odd (with the exception of the first) and all even half cycle scans produce sets of nearly identical interferograms, leading practically to the same loop.

Use of such polynomials has been found to provide satisfactory correction for the mirror step size at the analysis stage of each run comprising several samples. A laser light calibration run of four or six interferograms is, therefore, performed using the constant intensity light source assembly and for the same knob settings as in the actual sample run. Third and fourth interferograms are usually used for computing the odd and even polynomial coefficients.

The step non-linearity correction is important and its significance increases with narrowing input light band width. Figure 3.20(a) shows the corrected spectrum for a laser and a broad-band light input which will look different from the expected shape if no correction is applied for the non-linear step size.

3.8 THE TEMPERATURE EFFECT

Performance of most electronic and optical components is affected to a smaller or greater extent by changing laboratory temperature. Some results of experiments to observe the effect of temperature on the performance of this equipment are summarised in this section.

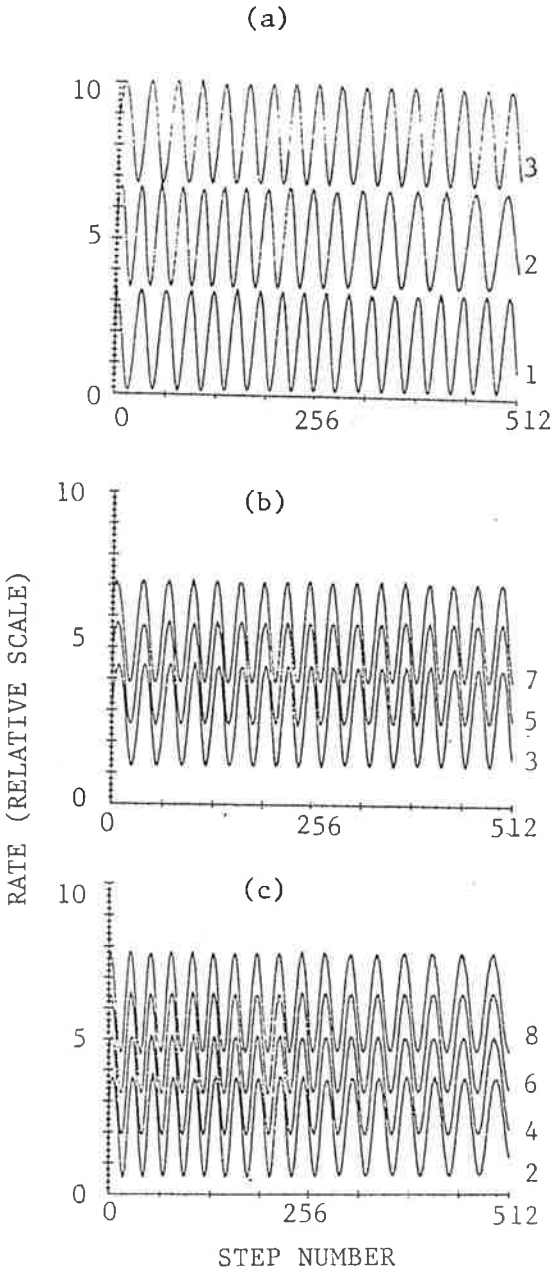

FIGURE 3.19: He-Ne laser interferograms as recorded for the first three half cycles of the movable mirror indicate deviations in positions of the maxima and minima (see a). These deviations are attributed to the nature of hysteresis. All odd with the exception of the first and all even number interferograms make two sets (see b and c). Polynomials fit to these interferograms are used to correct for the step size in the analysis stage.

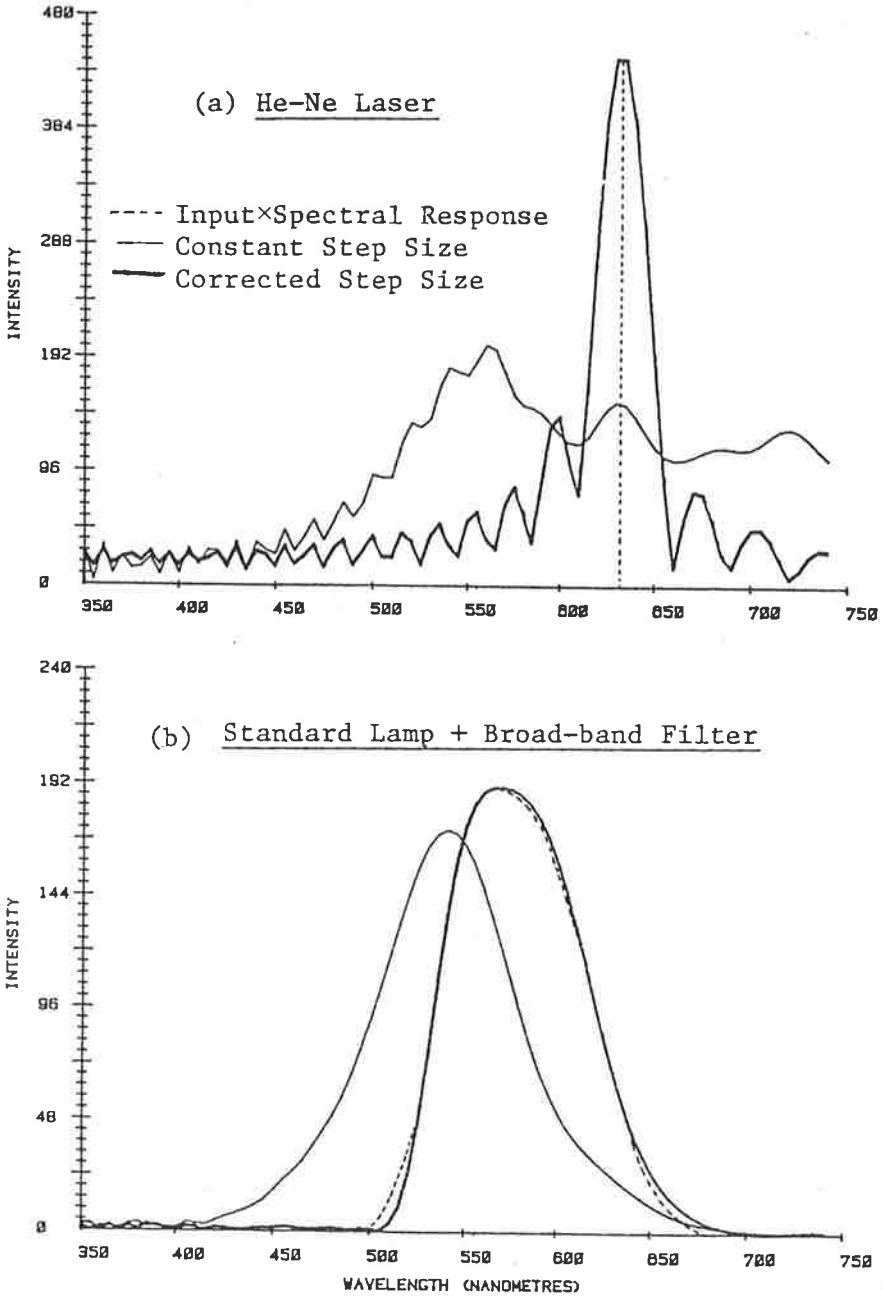

FIGURE 3.20: (a) A He-Ne laser and (b) a broad-band light spectra computed with (bold line) and without (thin line) correcting for the non-linearity of the movable mirror stepping mechanism. The broken line is the expected value obtained by multiplying the input spectrum with the spectral response of the equipment (Figure 4.7b). Peak broadening and sidelobes for a monochromatic light input have been discussed in Chapter2.

Figure 3.21(a-c) shows the effect of laboratory temperature change on the counting electronics (2D mode). It leads to a correction factor of about -1% per degree rise in temperature. The change was brought about artificially by readjusting the room air-conditioning which is normally kept at 22±1°C. No temperature corrections (within 2% or so) have, therefore, been applied to the count rates presented in this thesis.

With the linear thermal expansion coefficient of 1.2×10^{-5}, the steel optical base plate will expand by about nine wavelengths of He-Ne light per degree change in temperature. This expansion is only about one laser wavelength longer than that of the underneath slate optical table which has an expansion coefficient of 1.04×10^{-5} (for these coefficients see Newnes Engineer's Reference Book p.1627, 10th ed. George Newnes Ltd., London 1965). The overall expansion along the thickness of the slate slab and steel plate will be about 760 nm. Such small tangential and vertical expansions can easily be accommodated in the fittings of the bolts and against the teflon layer between the coupling surfaces. Little temperature change is expected during a run of several hours and minor effects can be corrected using the fine alignment set up described in the optical design of the equipment (Section 3.5.5). Day to day fine setting requirements can partly be attributed to slight temperature changes.

A possibility of serious effect of any relatively local temperature rise due to heating the oven strip to several hundred degrees in the vicinity of the optical base plate was also examined. Figure 3.22 shows the results of an experiment based on observing any temperature dependant fringe shift. White light was shone through the parallel light assembly (Section 3.4.4, Figure 3.8) while the oven was heated up to 500C at a rate of $5Ks^{-1}$. No adverse effects of oven tempeature changes are evident.

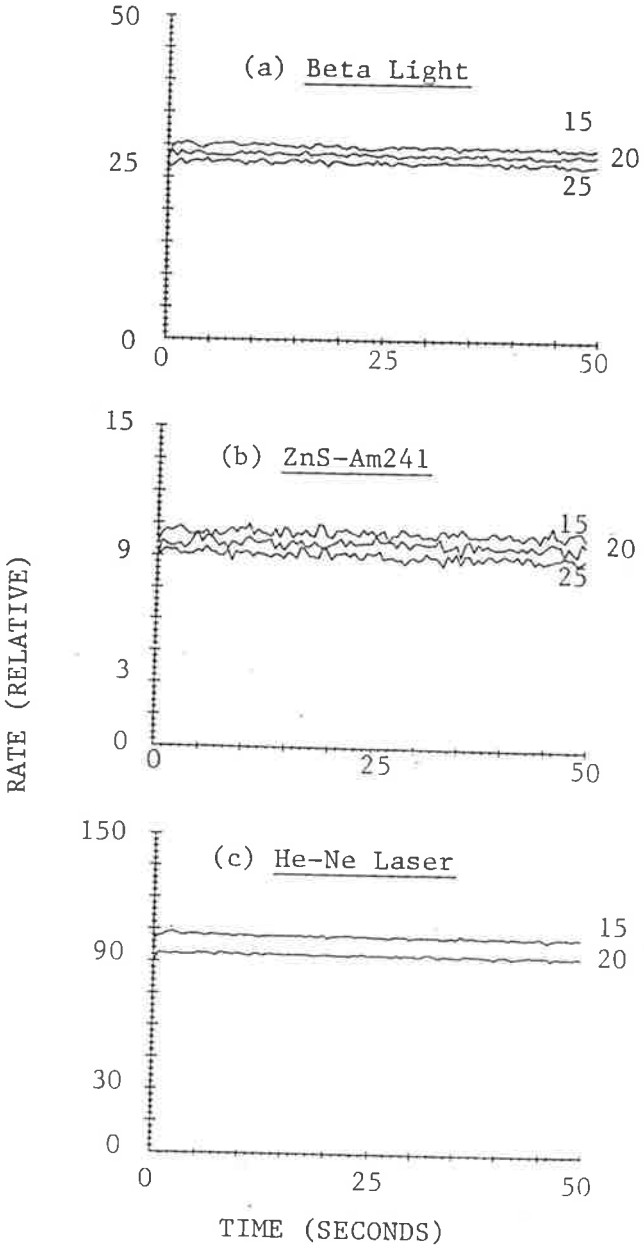

FIGURE 3.21: Temperature dependence of the TL counting system as seen for (a) NE 120 beta light source, (b) ZnS-Am241 scintillator and (c) He-Ne laser light inputs. The signal decreases at an average rate of 1% per degree temperature rise. The numbers with the figures show the corresponding laboratory temperature in Celsius.

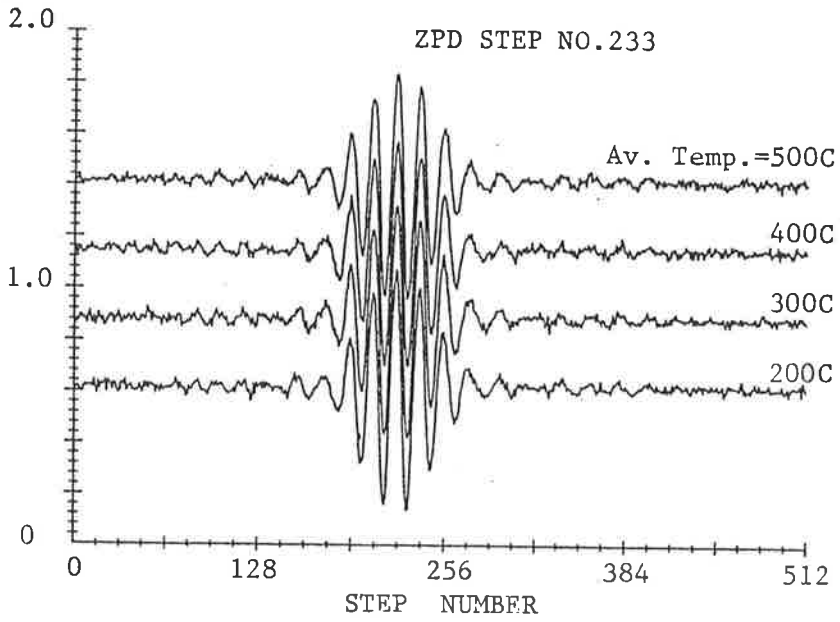

FIGURE 3.22: The results of an experiment to check the stability of the optical system during oven heating. The light was shone through the parallel light pupil in the light tight box while the chamber was heated as for normal TL operation. No fringe distortion was apparant.

rate of $5Ks^{-1}$. No adverse effects of oven temperature changes are evident.

CHAPTER FOUR

COMPUTATION OF SPECTRA

"While it may be admitted that the analysis of spectral lines by the method of visibility curves is somewhat indirect and not entirely certain, it has nevertheless proved of considerable value, especially in cases where the effects to be observed are beyond the power of spectroscope..."

(A.A. Michelson, 1927)

4.1 INTRODUCTION

This chapter is about the overall performance of the equipment as a 3D-TL spectrometer. The method adopted to compute the spectra from the raw interferogram data has been described and results compared with the spectra of known constant intensity sources and thermoluminescence phosphors. A section is devoted to describing the status of the equipment among other existing thermoluminescence spectrometers. Thermoluminescence (2D) glow-curve recording is also mentioned.

4.2 RUNNING THE EQUIPMENT

The 2D TL glow curve system is not much different from most other TL equipments (McKeever, 1985; Aitken, 1985; Singhvi and Wagner, 1985). The oven chamber and the photomultiplier system have been described in the previous chapter on the equipment design. The chamber is evacuated below 4×10^{-3} torr, isolated from the vacuum line, supplied with high purity argon at 2ℓ/min and heated to a chosen temperature (maximum 800°C) at a suitable heating rate (rated between 0.2-100 Ks^{-1}, not tried above 20 Ks^{-1}). The TL signal output is simultaneously registered for half a degree heating intervals (Figure 4.1). The main operation is controlled

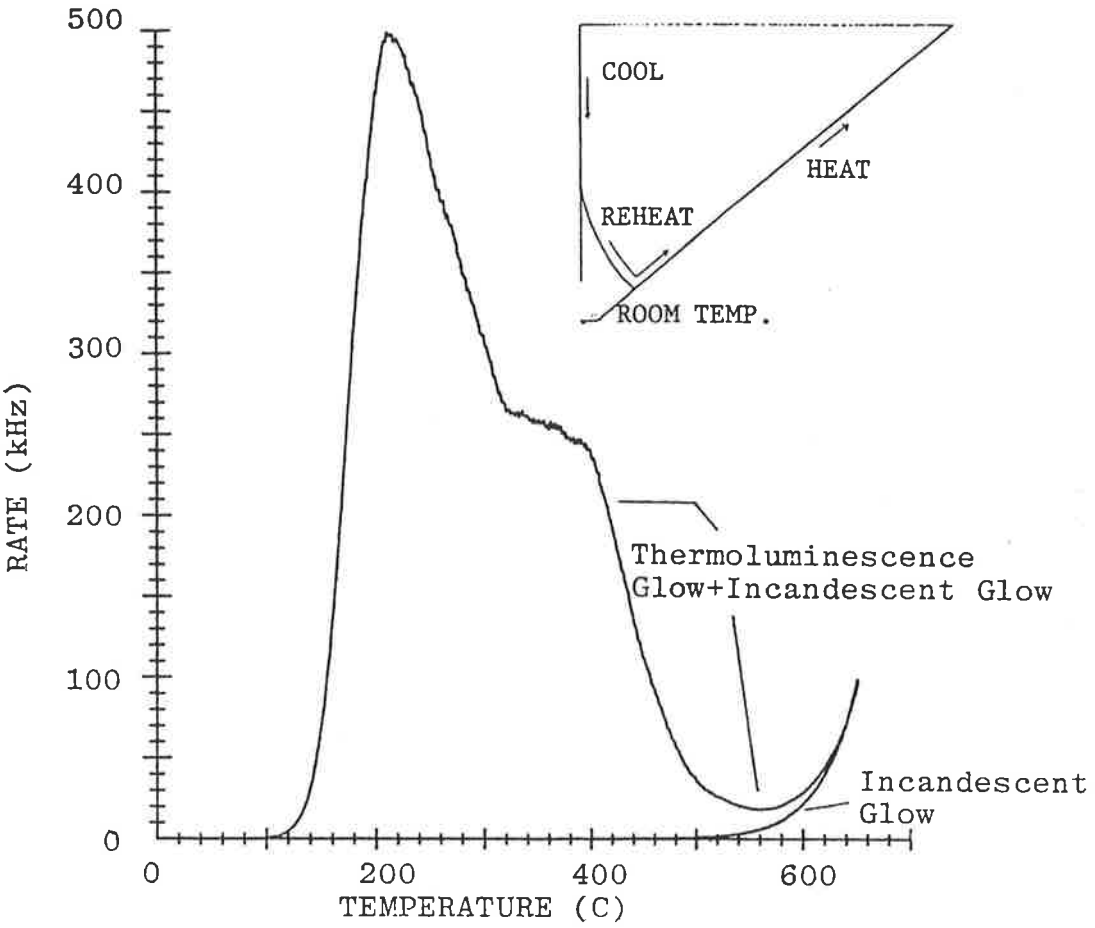

FIGURE 4.1: A two dimensional glow curve as recorded on this equipment. The black body during reheat is also shown. Insert shows the corresponding thermocouple temperature cycle.

through a computer programme, and the data can be stored, retrieved, printed and plotted with various options, like black body subtraction, regions of interest, normalization and scaling.

The major use of the equipment is, however, as a 3D TL spectrometer. As can be seen from Figure 4.2, its operation is, in principle, similar to the 2D TL glow-curve system; the only addition being an interferometer between the oven and the photo-multiplier. The data are registered more frequently (i.e. from 5 to 20 signals per degree rise in temperature) while the movable mirror of the interferometer is scanning a given optical path difference in a preset number of steps. Each of the one way scan outputs represents what is called a (raw) interferogram. The data are stored if later spectral information is desired. Individual interferogram display, print and plot routines are available in the main control programme.

Four to six interferograms for a He-Ne laser light input are recorded for the same settings as for the TL operation. This information is used for calibrating the movable mirror stepping mechanism, as explained in Section 3.7 of Chapter 3.

The piezo-electric pusher PZT 44 is subject to some creep and the fringe position tends to shift by one or two steps from one to another interferogram. This effect is apparent in Figure 3.19 of Chapter 3, where alternate odd and even numbered interferograms are plotted for the sake of comparison. This small change does not affect the movable mirror step size polynomial fit (Figure 3.18, Chapter 3) and, in most cases, cycling the mirror for a few minutes prior to the actual operation overcomes the creep and corresponding fringe shifts (Figure 3.22, Chapter 3).

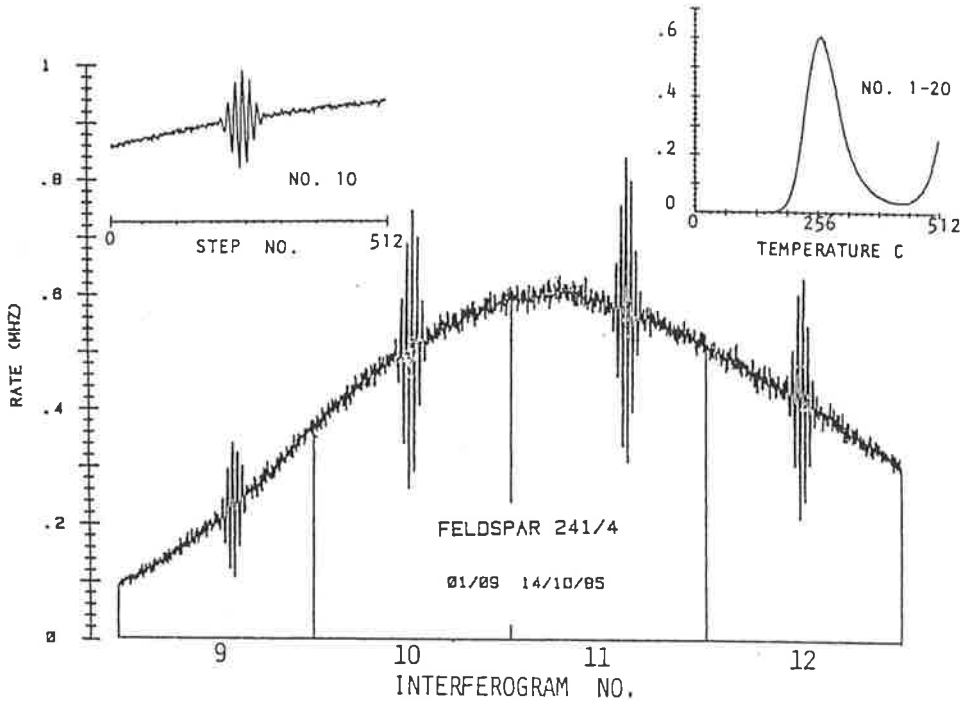

FIGURE 4.2: Raw data during 3D TL glow curve registration. The broad band thermoluminescence signal gives an interference pattern only when the optical path difference is close to ZPD during movable mirror scan. Each oneway scan makes an interferogram (of 512 steps in this case) and raw data can be summed together to produce a 2D like glow curve (see inserts).

Generally, an equipment warming-up time of some 30 minutes is required, particularly for the RC-44 PZT bias supply and initial de-gassing of the vacuum line.

As has been mentioned in the previous chapter, ten-turn potentiometers provided on the front panel can be dialed for suitable heating rate, and movable mirror average step size. The computer control programme then offers a variety of options to select the total number of interferograms, number of steps per interferogram and stepping rate (as the number of steps per degree rise in temperature). These selections are flexible to suit various possible situations of input spectra.

4.3 COMPUTATION OF THE SPECTRA FROM THE INTERFEROGRAMS

Mathematical treatment of Fourier transform spectroscopy has been discussed in Chapter 2. Greater detail can be found in references like Bell (1972) and Chamberlain (1979). The computation of the spectra from interferograms involves solutions of one or other form of Equation 2.5 or 2.21 of Chapter 2. The zero-path-difference (ZPD) is generally easily located as the step of maximum intensity. The incoherent light intensity $I(\infty)$ ideally equals half the intensity at ZPD, but for a broad-band input, is more precisely determined by the average intensity over the interferogram (Bell, 1972). The optical path difference 'x' as measured from the ZPD equals twice the movable mirror displacement, which, for the present set up, does not change linearly with the step number. The exact value of x at each step can, however, be determined using the procedure laid down in Section 3.7 of the previous chapter.

It may be recalled from Chapter 2 that the output intensity $I(x)$ stored as the raw interferogram data is related to the input spectrum

B(k) as

$$I(x) = C\int_o^\infty B(k)e^{-ikx}dk + \tfrac{1}{2} I(o) \qquad (4.1)$$

where 'C' is a constant and I(o), the intensity at ZPD, is given by:

$$I(o) = 2C\int_o^\infty B(k)\, dk \qquad (4.2)$$

The input light spectrum from the mineral samples depends upon the thermoluminescence properties plus incandescent glow. It therefore varies continuously over the sampling time. The output intensity I(x) as given by Equation 4.1 has, therefore, to be replaced by its time dependant counterpart as

$$I_n(x,t) = C\int_o^\infty B_n(k,t)e^{-ikx}dk + \tfrac{1}{2} I_n(o,t) \qquad (4.3)$$

$I_n(o,t)$ here denotes the intensity as it would be seen at the output of the interferometer while recording the nth interferogram if, at time 't', the optical path difference 'x' between the two beams is set to zero. The time dependent intensity variation of the interferograms can be well appreciated through Figure 4.2.

The derivation of Equation 4.3 offers no problems due to its time-dependence. The inverse Fourier transform to obtain $B_n(k,t)$ is, however, not possible in principle. Such intensity variations are not related to the movable mirror position as an interference pattern and produce errors quite independent of the input spectrum. The optical path difference 'x' changes in physical time 't' which makes the input spectrum a function of

'x' as well. i.e.

$$B_n(k,t) \equiv B_n(k,x) \tag{4.4}$$

Now the Fourier theorem is strictly valid for constant spectral emission in the x domain; and as is shown in Figure 4.3 (a,b), attempts to transform Equation 4.3 generate misleading information changing with the shape of the intensity curves (or raw interferograms). Single sided interferograms offer an added difficulty of exactly locating the ZPD.

This problem is overcome through defining a time function and correcting the interferograms for intensity variations. In most practical cases of TL spectroscopy, the recording time interval for each interferogram can be selected such that the spectral intensity $B_n(k,t)$ for the nth interferogram appears only as a slowly varying function of time. A pure time function $F_n(t)$ can then be selected such that

$$B_n(k,t) = F_n(t)\ \overline{B_n(k)} \tag{4.5}$$

and

$$[\int_{t_{n-1}}^{t_n} F(t)dt]/[t_n - t_{n-1}] = 1 \tag{4.6}$$

Here $[t_n - t_{n-1}] = \Delta t$ is the time interval and $\overline{B_n(k)}$ is the average (time independent) spectral intensity over the registration of the nth interferogram.

Substituting $B_n(k,t)$ from the Equation 4.5 in 4.3 we obtain

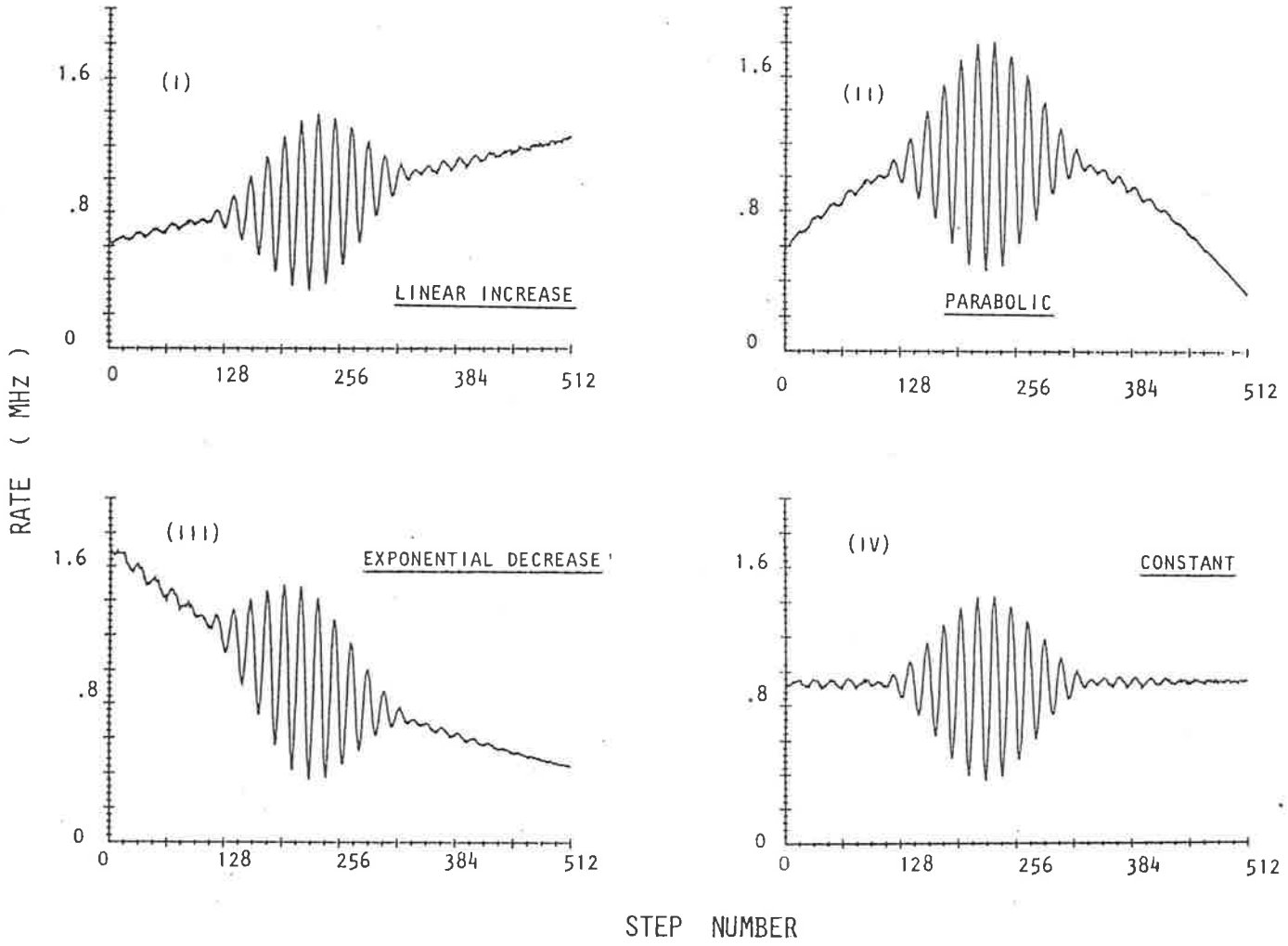

FIGURE 4.3(a): A set of interferograms corresponding to an identical broad band source but with spectral intensity (i) linearly increasing (ii) parabolic (iii) exponentially decreasing and (iv) constant during registration. All interferograms are normalized to the same average intensity. Intensity changes over the registration time are common for thermoluminescence signals (Figure 4.2).

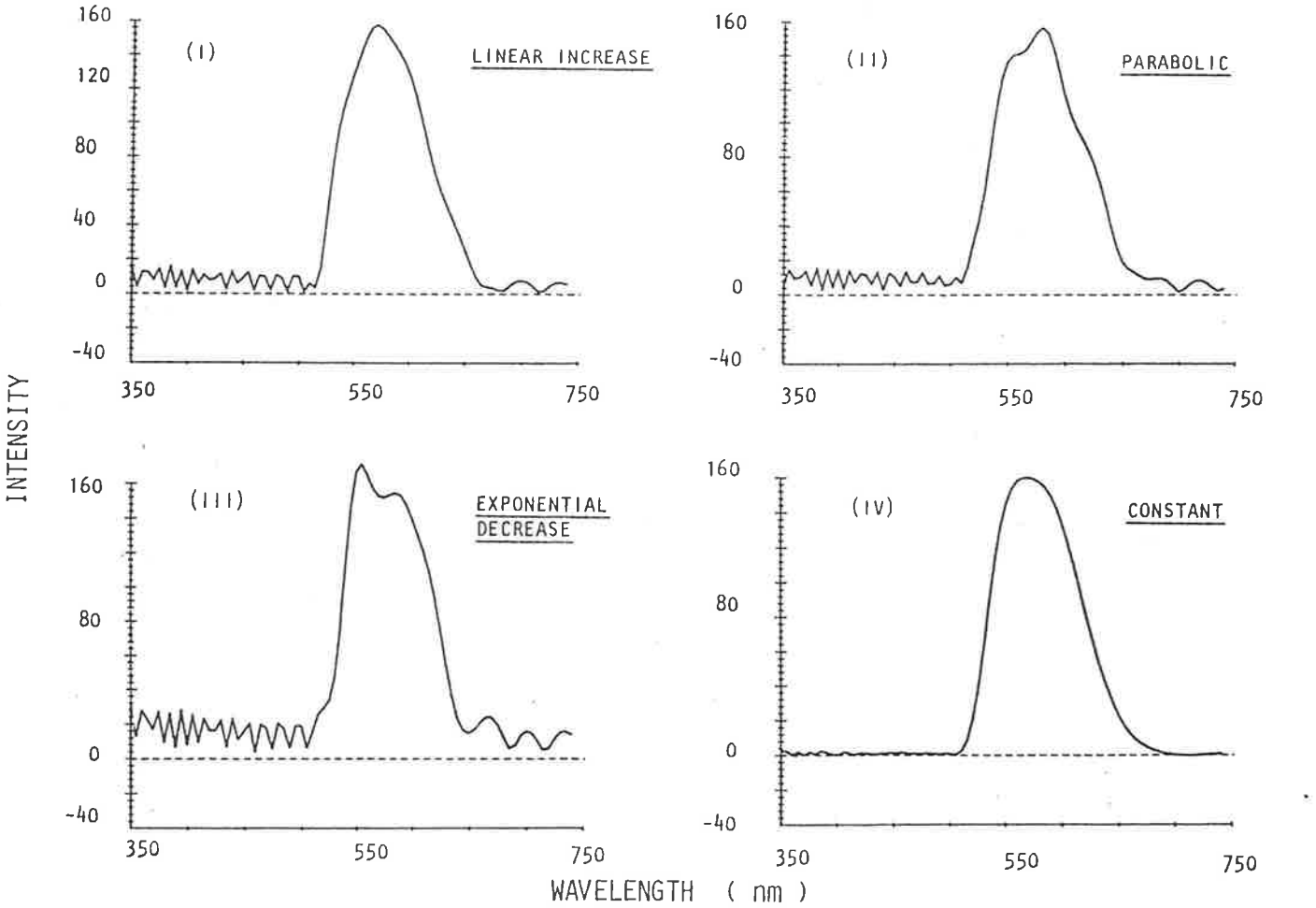

FIGURE 4.3(b) Two sided spectra corresponding to the interferograms shown in Figure 4.3(a). Intensity variations introduce misleading spectral information, changing with the shape of the raw interferogram.

$$\left[\frac{I_n(x,t)}{F_n(t)} - \tfrac{1}{2}\frac{I_n(o,t)}{F_n(t)}\right] = C\int_o^\infty \overline{B_n(k)}\, e^{-ikx} dk \qquad (4.7)$$

Comparing Equation 4.7 with Equation 4.1, we realize that the L.H.S. of Equation 4.7 gives the interferogram corresponding to the time independent spectral intensity $\overline{B_n(k)}$. This interferogram is then transformed to compute $\overline{B_n(k)}$, representing the nth interval. For x = o, Equation 4.7 gives

$$\frac{I_n(o,t)}{F_n(t)} = 2C\int_o^\infty \overline{B_n(k)}\, dk \qquad (4.8)$$

Comparing it with Equation 4.2, we obtain $\overline{I_n(o)}$, i.e. the intensity at ZPD corresponding to $\overline{B_n(k)}$, as

$$\overline{I_n(o)} = \frac{I_n(o,t)}{F_n(t)} \qquad (4.9)$$

Eliminating $F_n(t)$ between Equations 4.7 and 4.9, we obtain

$$\overline{I_n(o)}\left[\frac{I(x,t)}{I(o,t)} - \tfrac{1}{2}\right] = C\int_o^\infty \overline{B_n(k)}\, e^{-ikx} dk \qquad (4.10)$$

As has been mentioned earlier, I(o,t) is the output intensity at t if the optical path difference between the interferometer mirrors is unchanged from ZPD. Analogous to its time independent counterpart, this intensity will be twice the value if the mirrors are set at large path difference for incoherent light output, i.e.

$$I_n(o,t) = 2\, I_n(\infty,t) \qquad (4.11)$$

Equation 4.10 thus becomes

$$\overline{I_n(\infty)}\left[\frac{I_n(x,t)}{I_n(\infty,t)} - 1\right] = C\int_o^\infty \overline{B_n(k)}\, e^{-ikx} dk \qquad (4.12)$$

$\overline{I_n(\infty)}$ $(= \frac{1}{2}\overline{I_n(o)})$ here determines the average incoherent intensity corresponding to $\overline{B_n(k)}$.

Equation 4.12 is just another form of Equation 4.7 and gives an interferogram for transformation. All terms on the L.H.S. can be determined from the raw interferogram data $I_n(x,t)$. $I_n(\infty,t)$ is the "intensity trend" over the time of recording the nth interferogram. As has been shown in Figure 4.4, this trend can be fairly determined by a second-order polynomial fit on the raw interferogram data. The average intensity $\overline{I_n(\infty)}$ is also determined as a part of the polynomial fitting procedure.

Consistent spectral information can be retrieved using this correction technique (Figure 4.5, where it has been applied to the data of Figure 4.3a).

Two sided interferograms are used to compute the spectra using the relation

$$B = \left[\left\{\sum_{j=1}^{N}[I(x_j) - I(\infty)]\cos(kx_j)\right\}^2 + \left\{\sum_{j=1}^{N}[I(x_j) - I(\infty)]\sin(kx_j)\right\}^2\right]^{1/2} \qquad (4.13)$$

Here x_j is the optical path difference (measured from ZPD) and $I(x_j)$ is the jth step output data corrected for the intensity changes, N is the total number of steps in the interferogram.

Two sided interferograms are computed to avoid possible spectral

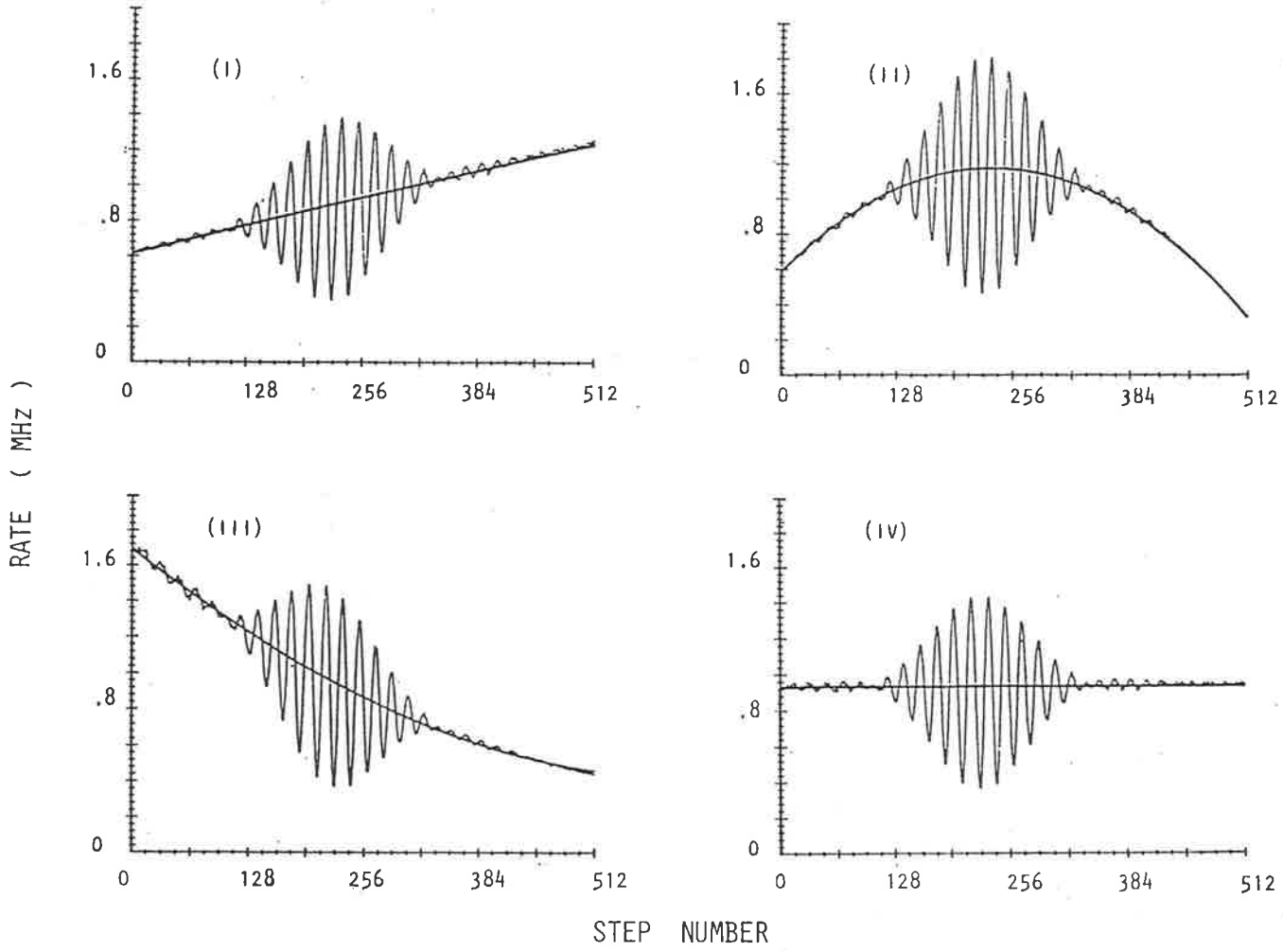

FIGURE 4.4: A figure to demonstrate the effectiveness of a second order polynomial fit over the raw interferogram data of different shapes. The interferograms are the same as shown in Figure 4.3(a).

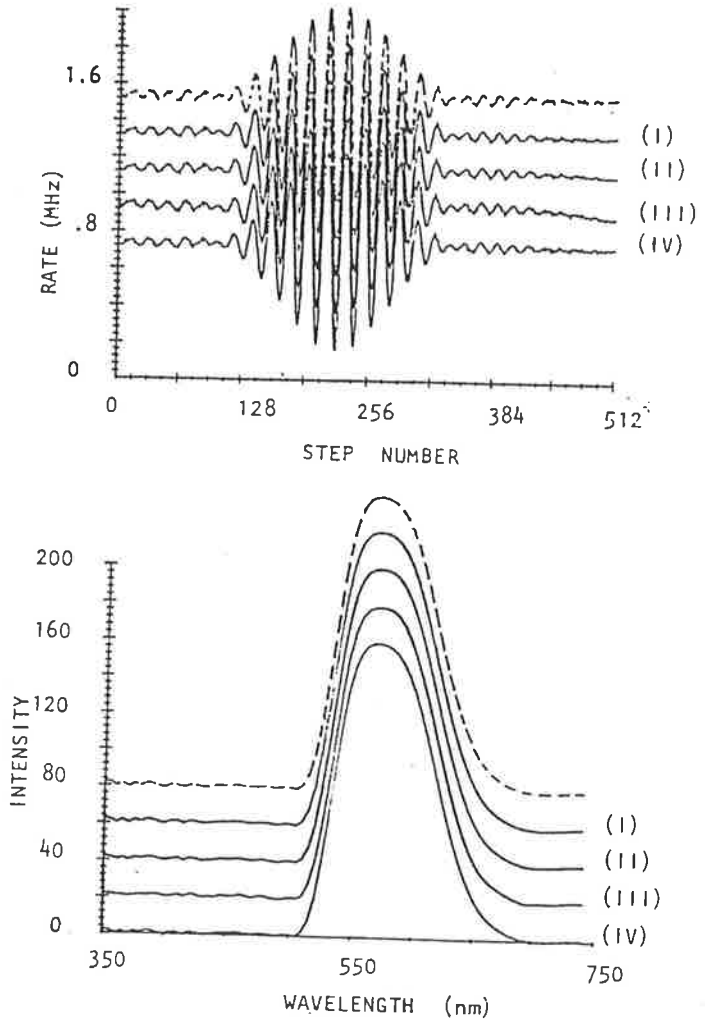

FIGURE 4.5: (a) The interferograms of Figure 4.4(a) after time depenent correction using the second order polynomials and (b) spectra computed for the corrected interferograms. The broken lines show the (parent) interferogram and spectrum for constant light input and have been redrawn from Figure 4.3 (iv).

distortions caused by any phase error (Chapter 2). The results are computed for wavelength ($\lambda = 2\pi/k$) range of 350-750 nm at 5 or 10 nm interval. Fast Fourier transformation using the Cooley-Tuckey algorithm (Bell, 1972) is not suitable for this specific application because of the non-linear interferogram step size and limited spectral range of interest.

4.4 CALIBRATION

The light throughput efficiency of the optical system was experimentally measured using a Xe-lamp, grating monochromator and pin diode. Theoretical estimates were made using information on refractive indices, ray optics, mirror and beam splitter reflection and transmission characteristics. The results can be seen in Figure 4.6. The experimental results indicate that for the present optical design, the absolute light throughput efficiency is about 5% or so, which when multiplied with the quantum efficiency of the tube (Figure 3.1, Chapter 3) reduced to about 1%. This product has been plotted on a relative scale as Curve 'a' in Figure 4.7 and gives the first information about the spectral response of the equipment. The theoretical estimate of the light throughput is somewhat less than the experimental value. It was expected so, for the calculations referred to the light through the optical axis only, where the substrate thickness is maximum; contribution of multiple reflections was also neglected.

The actual spectral response curve for transformed spectra is obtained by correcting the curve 'a' in Figure 4.7 for increasing incoherent light component of interferograms with decreasing input wavelengths (see Section 2.4.3 and Figure 2.6 in Chapter 2). It is

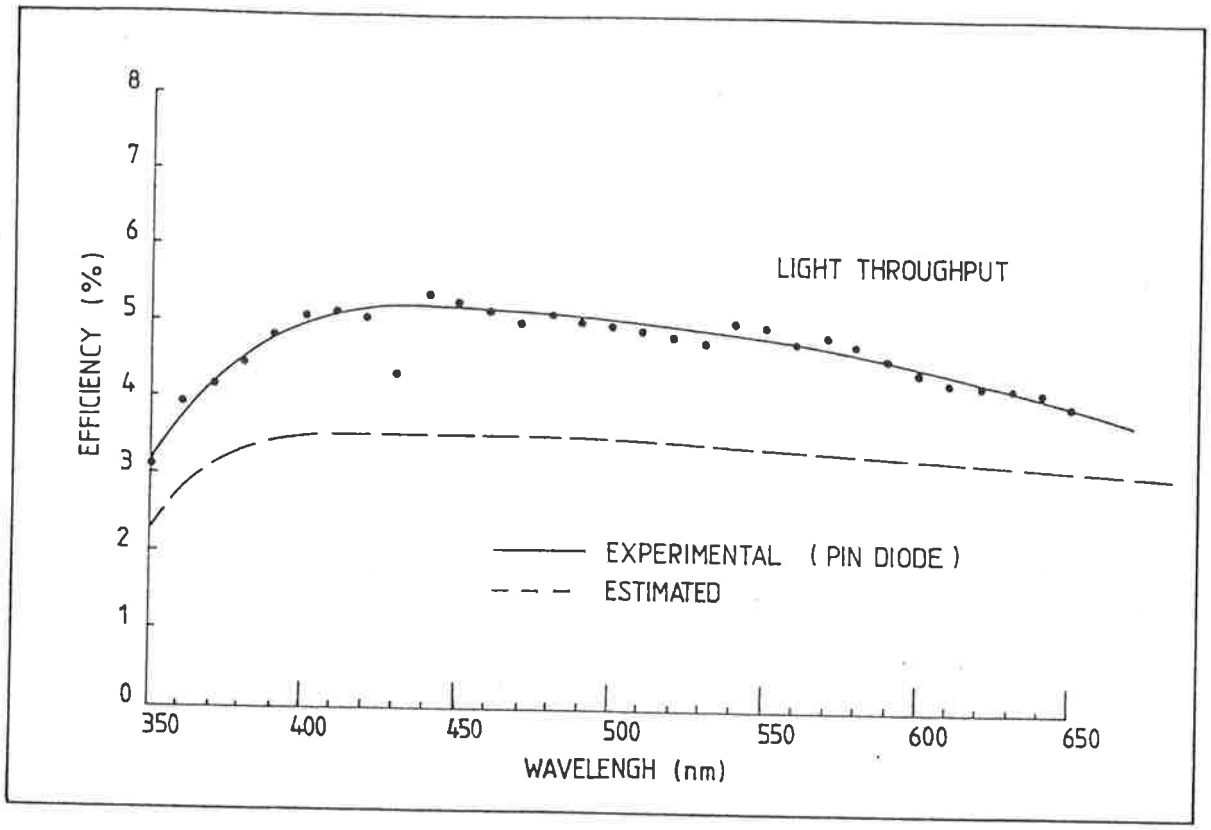

FIGURE 4.6: Light throughput efficiency of the optical system as obtained experimentally using a PIN diode (continuous line) and estimated for light transmission only along the optical axis (broken line).

plotted in Figure 4.7 as curve 'b'.

Confirmatory test of calibration is done using a standard tungsten lamp light calibrated by the CSIRO Division of Standards. Results of one such experiment are shown in Figure 4.8 and show excellent agreement between the expected and obtained spectra.

Unless otherwise mentioned, the 3D data presented in this thesis are not corrected for the spectral response of the equipment and may be treated as relative for the purpose of comparison. A corresponding set of revised figures is, however, enclosed at the end of the thesis. These figures, corrected for the spectral response of the equipment and also for the temperature discrepancy as discussed in Section 4.6 of this Chapter, may be used for comparison with similar observations in other laboratories. The discussion and conclusions drawn in the thesis are not affected.

4.5 APPLICATION TO CONSTANT INTENSITY LIGHT SOURCES

Various types of constant intensity light sources of known input spectra were used for additional tests on the performance of the equipment.

Results using monochromatic ($\Delta\lambda \simeq 1$nm) light inputs of varying wavelengths are shown in Figure 2.5 and discussed in Section 2.4.2 of Chapter 2. The peak shift and broadening of the computed spectra are due to the extended throughput and limited scanning of the interferograms.

Figure 4.9 shows the expected and obtained spectra corresponding to several broad-band light inputs in different spectral regions. The input light was generated by placing broad-band filters in front of the standard lamp mentioned in the previous section. As shown, the computed and expected values are in good agreement with each other.

Scintillators of two different types were also used. Figure 4.10(a) is the measured spectrum for a low intensity solid state light source ("beta light") supplied by D.A. Pitman Ltd., Surrey. The radioactive content of this light source is 1μCi C-14 which is dispersed in a plastic

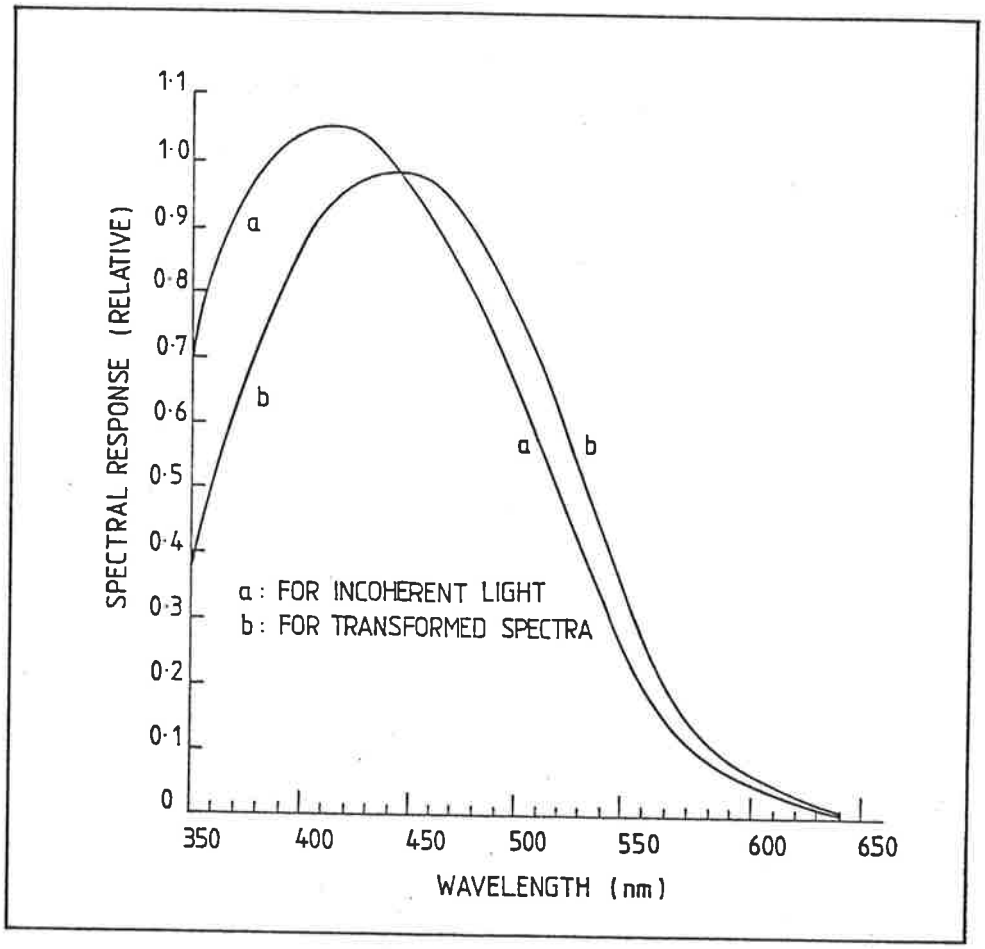

FIGURE 4.7: Relative spectral response of the equipment for incoherent light (curve a) and computed spectra (curve b).

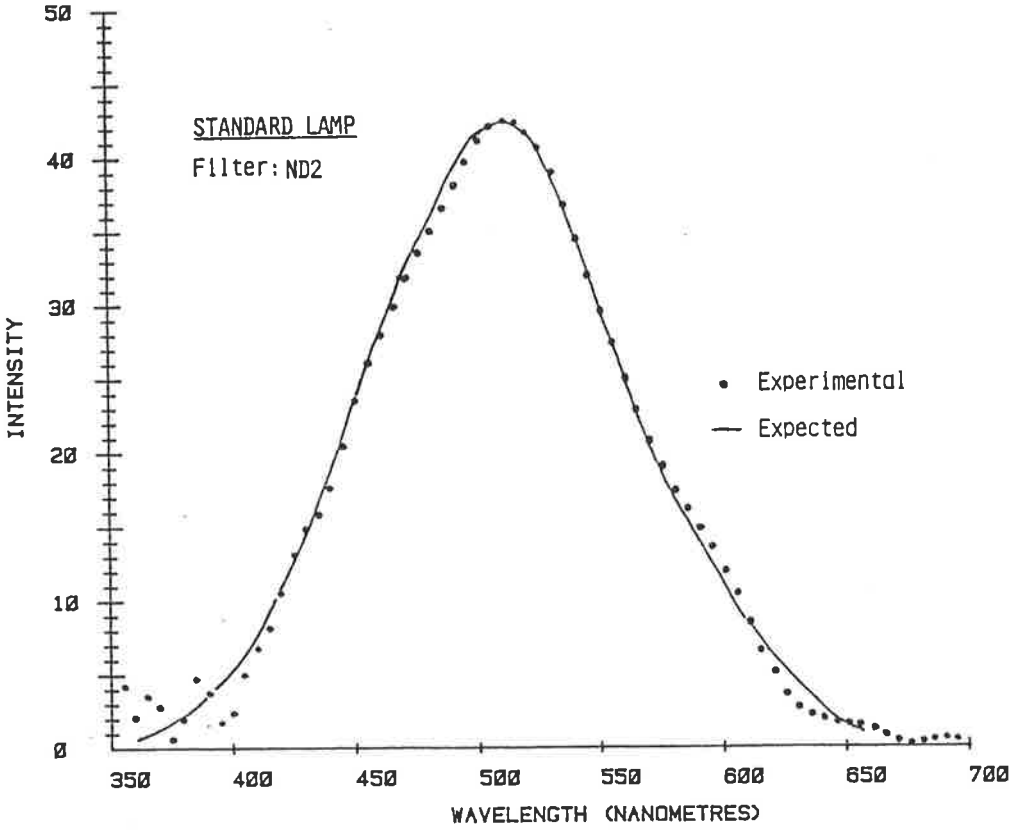

FIGURE 4.8: Computed spectrum for a standard incondescent lamp. The continuous curve is the expected spectrum.

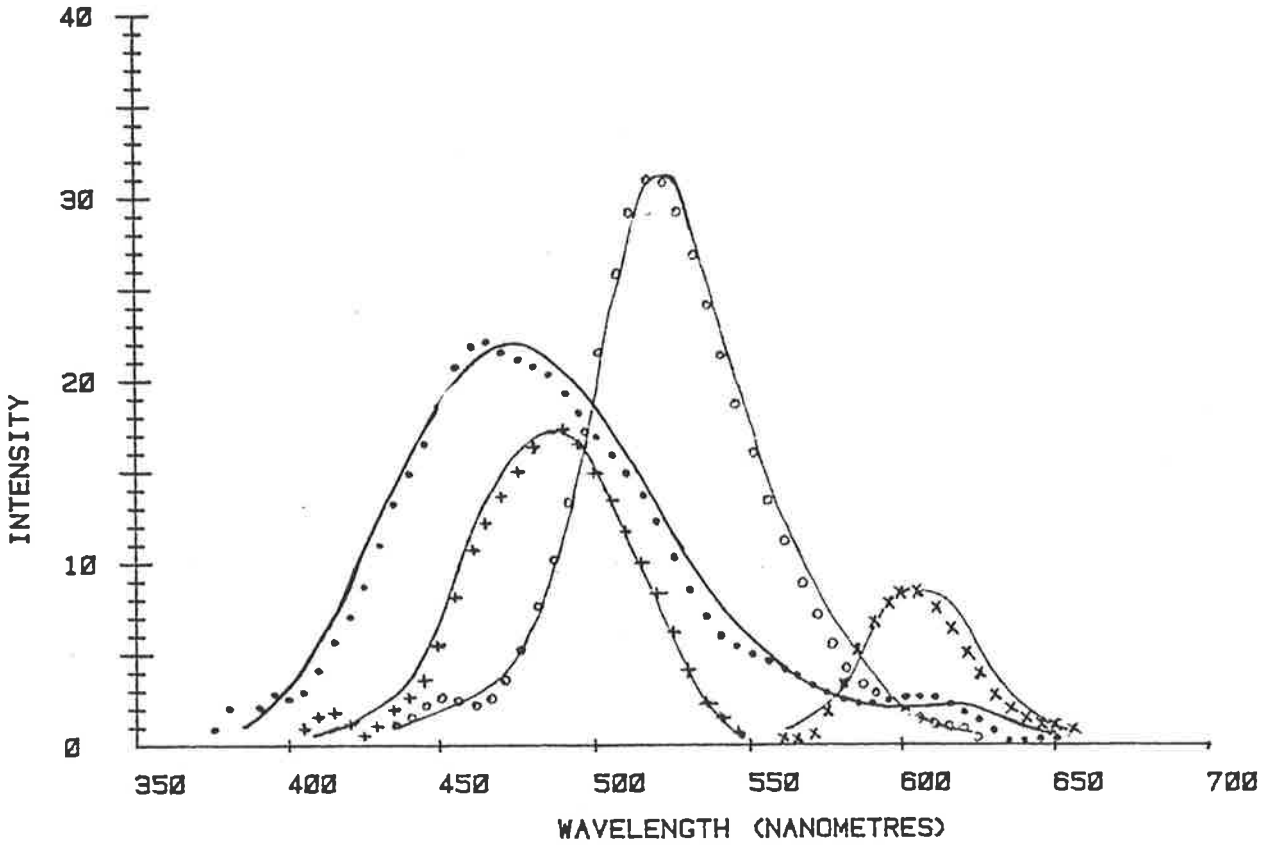

FIGURE 4.9: Expected and obtained spectra for broad band light inputs produced by placing filters of known spectral response in front of a standard lamp.

scintillator NE120. The emission spectrum for this scintillator, as reported by Facey (1966), showed a main peak at 424 nm and a smaller peak at 445 nm with a tailing towards a long wavelength side. These features are apparent in the computed spectra and compare well with the Figure 4.10 (insert) which is after the above mentioned reference.

Silver activated zinc sulphide is a well known scintillation phosphor. Its spectrum has been reported by several authors as broad-band peaking near 450 nm (see e.g. Curran, 1949; van Gool 1958; Birks 1964). The spectrum computed for a two sided interferogram corresponding to Am-241 alpha induced scintillations in a commercially available ZnS(Ag) screen is shown in Figure 4.10(b). The broad band peaks at 445 nm; a small peak near 390 nm is also suggestive. The insert shows the reported spectrum after van Gool.

Spectra presented in Figure 4.10 are not corrected for the spectral response of the equipment. In case of the solid state light, the overall change in the spectral response is about 10% within the main region of interest (400-470 nm). The ZnS(Ag) spectra may shift by several nm depending upon the art of preparation (van Gool, 1958).

4.6 THERMOLUMINESCENCE DOSIMETERS

Prior to any application to relatively less reported samples, it was thought most appropriate to observe the emission spectra for some of the popular dosimeter phosphors and compare them with the reported results.

Figures 4.11(a-c) show the emission spectra for $CaSO_4$:Dy, TLD 200 and TLD 100 respectively. These phosphors were supplied by Harshaw Chemical Company, Ohio, in 100 μm grain fraction.

The two spectral peaks at 485 and 580 nm as observed for $CaSO_4$:Dy

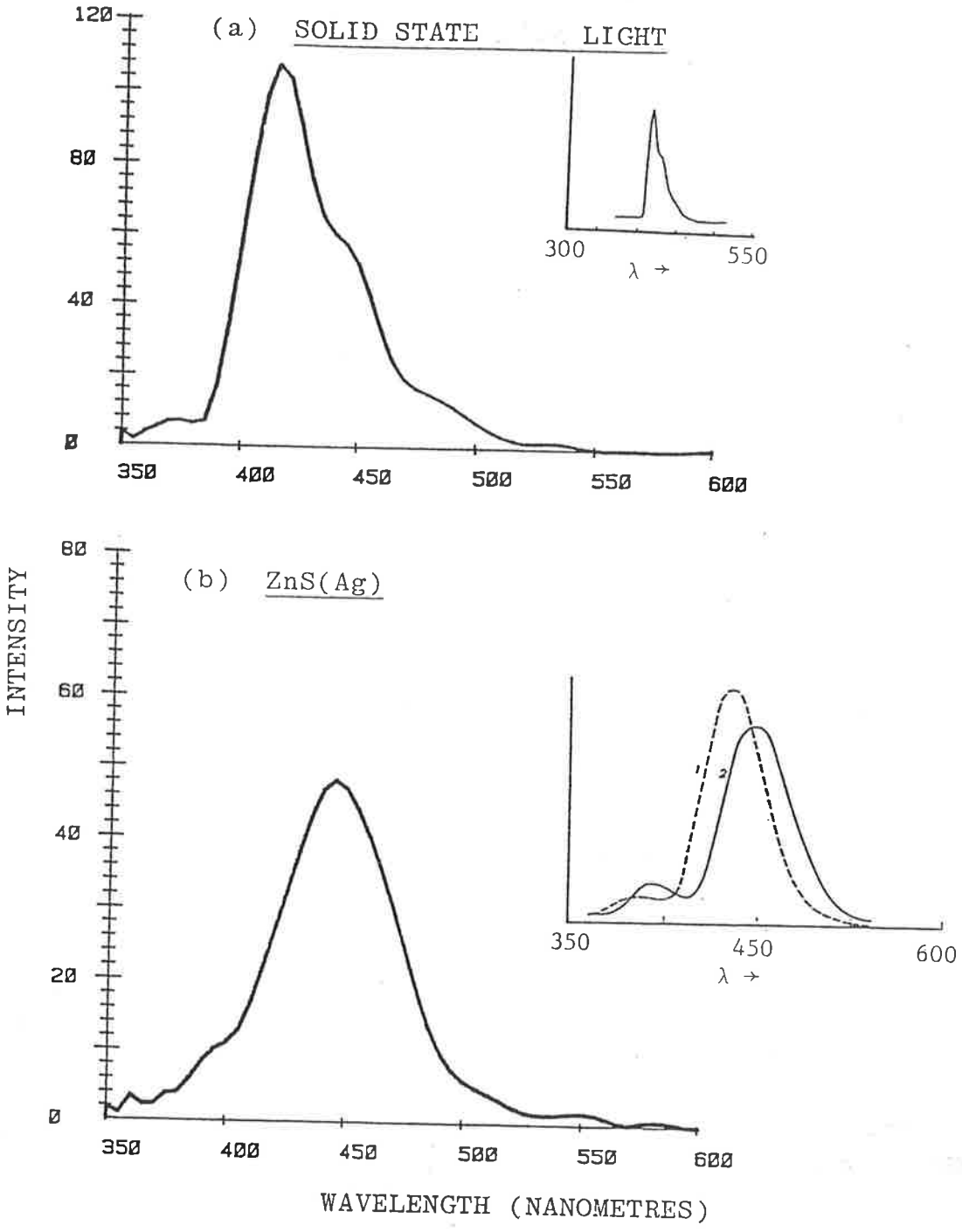

FIGURE 4.10: (a) Scintillation emission from a commercially available solid state light source (D.A.Pitman, Surrey). The insert shows the emission spectrum for a similar phosphor (after R.A.Facey,1966).

(b) Alpha induced scintillation emission from a ZnS(Ag) screen, Insert is after vanGool (1958): two different preparations.

agree well (within 10 nm) with the values reported by others (e.g. Yamashita et al, 1971; Nambi et al, 1974; Portal, 1981; Horowitz, 1984). As suggested by Nambi et al, and Portal, the peak location does not change with temperature. Some indication of the existence of smaller peaks before the main peak and at high wavelengths is also apparent and agrees with the spectral information given by Nambi et al.

TLD-200 (CaF_2:Dy) shows peaks around 490 and 595 nm for a beta dose of 0.1 Gy. This compares well with 483.5 and 576.5 nm as reported by Binder and Cameron (1969) for Cs-137 gamma dose of 500 Gy. A shoulder near 460 nm is also apparent. Some fine structure shown by Sunta (1970) is, however, not resolved. Peaks beyond 700 nm lie outside the existing spectral range.

TLD 100 (LiF:Mg,Ti) shows a broad band spectrum with its peak at 420 nm (Figure 4.11,c). This sample was given 0.4 Gy of beta dose. The results are in close agreement with the ones reported by Townsend (1983) and Fairchild (1978a), except that the present spectrum reduces in the long wavelength region due to loss of spectral response. Features like the presence of several spectral peaks and slight shift with increasing temperature are also suggestive from the present observation as well. These details were, however, not followed any further. Corresponding glow curves obtained by summation over the raw interferogram data are shown in Figure 4.12(a-c).

The 2D glow curve corresponding to the spectrum of TLD 100 shows a series of peaks at 80, 140, 190, 215 and 240°C followed by a smaller peak near 300°C. Whereas the main glow curve features are in agreement with other observers (Fairchild et al, 1978b; Townsend et al., 1983 and Horowitz, 1984), the peak locations show a consistent shift to higher

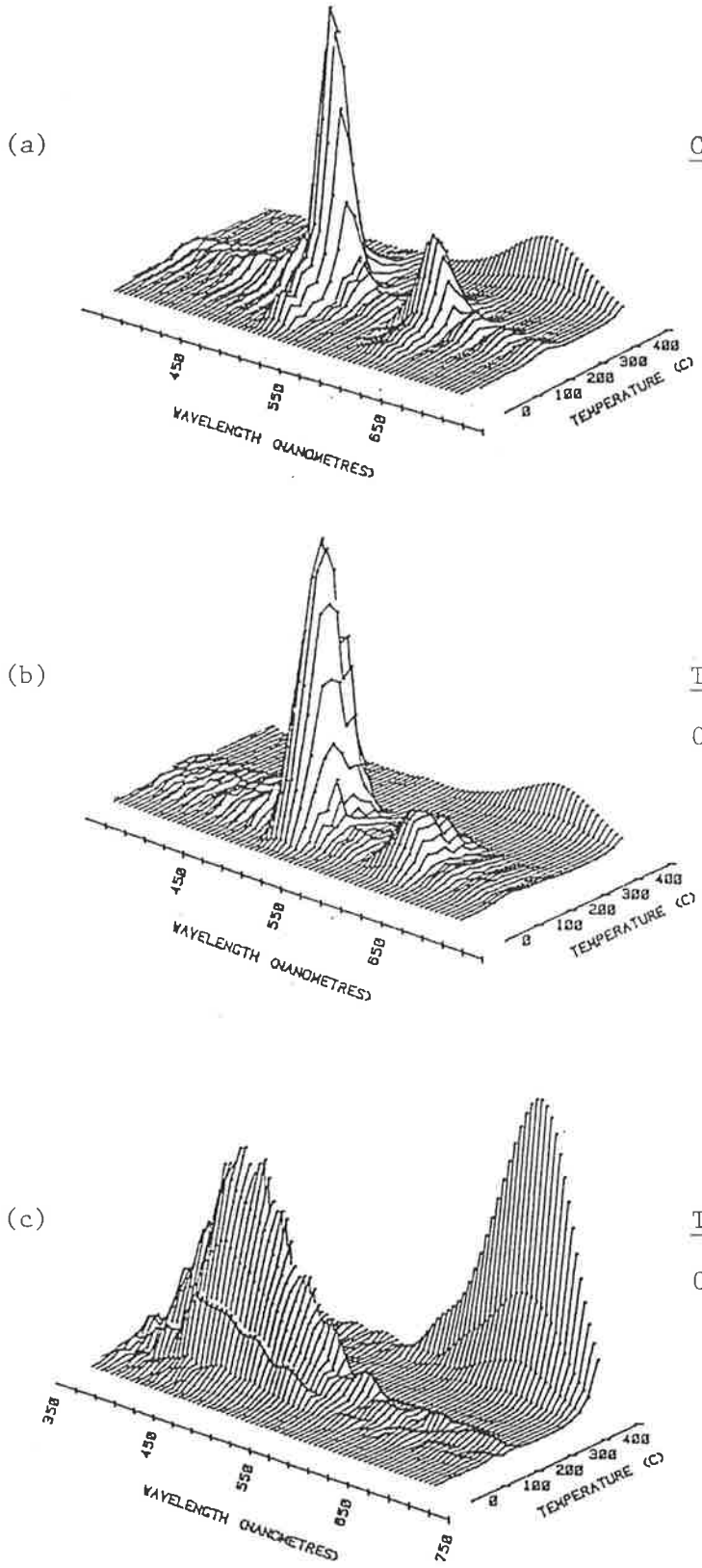

FIGURE 4.11: Beta radiation induced thermoluminescence spectra for (a) $CaSO_4$:Dy (Harshaw, Ohio) (b) TLD 200 and (c) TLD 100 dosimeter phosphors.

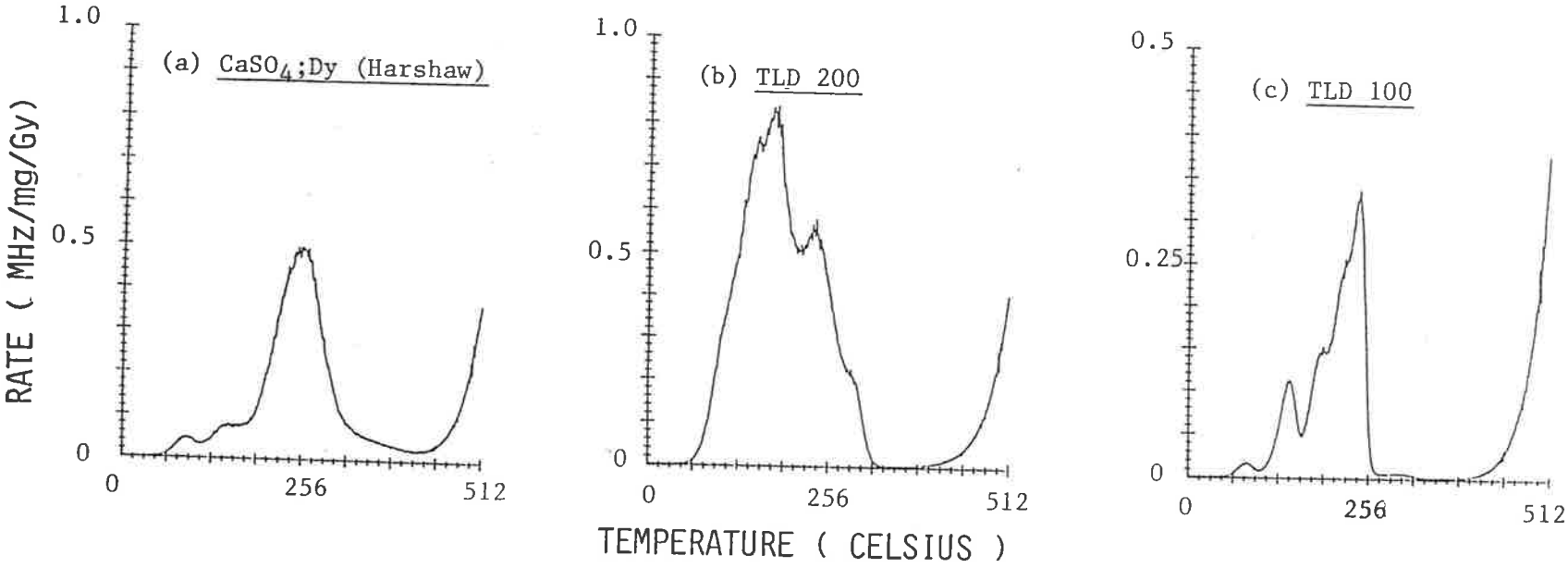

FIGURE 4.12 (a-c): The 2D TL glow curves produced by summation of raw interferogram data used for computing the spectra as shown in Figure 4.11(a-c).

temperatures. The main dosimetry peak, mostly reported to be near 200°C, appears at 240°C on this apparatus. Portal (1981) reports this peak around 225°C and the smaller high temperature peak around 275°C.

This temperature shift cannot be attributed to the effects like nature of ionization radiation, because the peak locations are consistent with the observations both for gamma and beta dose induced phosphors heated on another apparatus with a similar heating strip. Glow peaks for TLD-100 are suggested to follow first order kinetics (Fairchild et al., 1978b; McKeever, 1980). Peak shifts due to differences in initial trap concentration are also, therefore, not probable.

A similar situation arises when the 2D TL glow curves for the other two dosimeters are compared with the results reported in the references cited. For example $CaSO_4$:Dy main peak seen at 250°C in Figure 4.12(a) has been quoted to be at 220°C by Yamashita et al. (1971) and Portal (1981). Nambi (1974) reports it to be at 210°C. Horowitz (1984) mentions that the glow-curve characteristics of $CaSO_4$:Dy are dependent on details of preparation procedure and compostion of starting materials.

Similarly TLD 200 peaks in Figure 4.12(b) correspond to the temperature 140, 170, 240 and 290°C as compared to 120, 140, 200 and 240°C as shown by Binder and Cameron (1969).

Uncertainties in exact location of peak maxima are not uncommon in thermoluminescence glow curve observations. These are mostly attributed to heat losses during the glow process (Nambi, 1977). This being true, heat loss on this instrument appears to be much larger (from 10 to 20%) than displayed by the thermocouple servo error which appears to be only about 3% (Figure 3.15 Section 3.6, Chapter 3). This temperature uncertainty, therefore, applies to all TL spectra, though the wavelength peaks

show excellent agreement.

As mentioned earlier, a separate set of the Revised Figures, corrected both for the spectral response and temperature discrepancy, is enclosed at the end of the thesis.

4.7 STATUS OF THE EQUIPMENT AS A TL SPECTROMETER

Significance of TL spectral measurements has been discussed in Chapter 1 of this thesis. Several instruments based on different optical principles have so far been designed for this purpose. (For a brief review see Horowitz, 1984; McKeever, 1985). The designer mostly has to address two main problems of TL emission spectroscopy, i.e. the low intensity level and its variation with time. Methods based on optical filters are employed, sometimes with two photomultiplier tubes, one registering the filtered and the other unfiltered TL signal for reference (Nash et al., 1967). Bailiff et al (1977a) reported a 'rapid scanning' TL spectrometer based on sixteen 20 nm band width interference filters fixed on the same disc. These filters are successively interposed in the light collection system as the disc is rotated at 480 rpm during the glow-curve registration. This makes the spectral measurements possible without repetitive irradiation.

Other types of rapid scanning systems are based upon a prism or diffraction grating (Harris and Jackson, 1970; Mattern et al. 1971; McKeever et al, 1983). These systems accept only a narrow beam light input and require an exit slit in front of the detector scanning the (dispersed) spectrum in a narrow wavelength band. These requirements drastically reduce the system efficiency as a TL spectrometer where the spectral information continuously changes with the increasing temperature. Slow heating rates are generally employed to make use of short temperature scans over all wavelengths, but then the spectra can be obtained only for high radiation exposures. Low efficiency limits the

use of this type of instrument only to very sensitive thermoluminescence phosphors at radiation doses above several Grays.

Recent developments in Charge Coupling Device (CCD) arrays has made them relatively more attractive (Bakas, 1984; Imaeda et al. 1985; Wada et al., 1985). The exit slit and scan system is replaced by an array of light detecting diodes. All wavelengths in the dispersed spectrum are, therefore, registered simultaneously. This advantage is generally referred to as 'multiplexing'. $BaSO_4$:Eu thermoluminescence spectrum with radiation dose as low as 1 Gy has been reported using a CCD array (Imaeda et al., 1985).

Spectrometers, based on interference filters, make use of "throughput advantage" i.e. the spectral information can be extracted from an extended source. Bailiff et al. (1977a) displayed the usefulness of throughput advantage by reporting the spectra for minerals and radiation doses in archaeological context. They also registered the spectrum for a TL dosimeter at a radiation dose of only 0.01 Gy. The present equipment, based on Fourier transform spectroscopy, in principle, makes use of both the multiplex and throughput advantages. Data corresponding to all wavelengths of light is collected simultaneously from an extended source. These characteristics make this instrument a sensitive tool for 3D TL spectroscopy. As will be seen in the next part of the thesis on the applications, this equipment opens up a possibility of studying the thermoluminescence emission phenomena at low radiation levels and for relatively less sensitive minerals. The TL spectrum displayed in Figure 4.13 has been recorded for a beta radiation dose of only 1 mGy to 3 mgm of $CaSO_4$:Dy phosphor, heated at a rate of $5Ks^{-1}$ and sampled at twenty light output signals per degree rise in temperature.

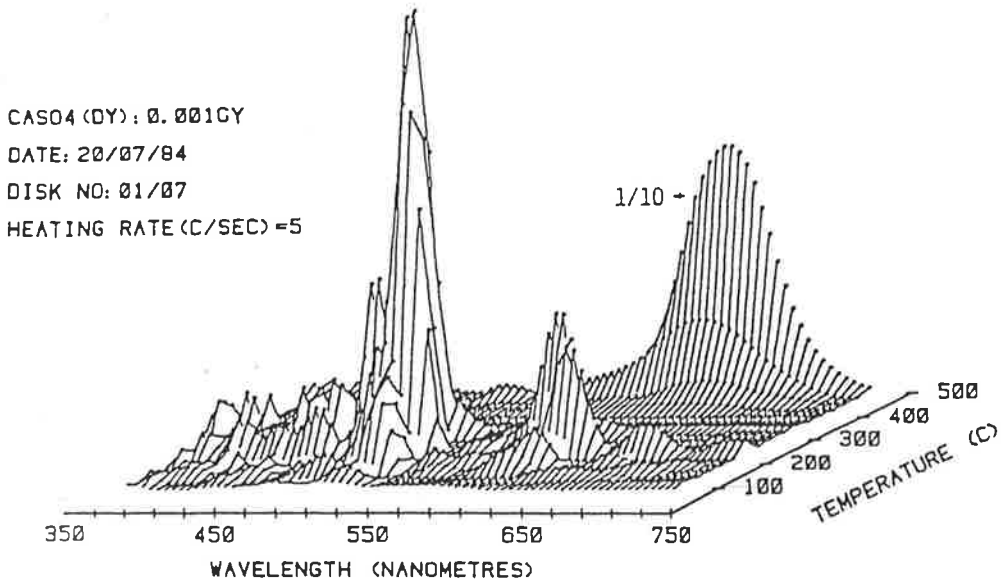

FIGURE 4.13: $CaSO_4$:Dy thermoluminescence emission for a very low beta dose (of 0.1 mGy). This figure illustrates the sensitivity of the existing equipment.

Most features commonly seen in a $CaSO_4$:Dy spectrum (as in Figure 4.11a for 0.1 Gy) are effectively resolved even at this low dose.

A limitation of the existing equipment is its narrow spectral range (350-620 nm). It can be extended on both ends by replacing the glass/acrylic optical components by those made of fused silica and the photomultiplier tube with a broad band quantum efficiency extending into red/infra red region as well.

CHAPTER FIVE

THE FELDSPARS

"...A field of unending fascination. Study of the differences can be vital for some purposes, but for other purposes they are nearly negligible - a fact not always sufficiently appreciated."

Helen D. Megaw (1974) in
'The Architecture of the Feldspar'

5.1 INTRODUCTION

Thermoluminescence emission spectra of feldspars constitutes the major portion of the rest of this thesis and it is appropriate to introduce them at this stage.

The name feldspar covers a large group of aluminosilicate minerals, subclassified both in composition and structural details. Reports on various aspects of feldspar thermoluminescence strongly suggest the significance of the subclassification. The first section of this chapter, therefore, briefly describes some features of feldspar classification. Feldspars are complex to handle in detail and the information provided here may appear rather superficial, particularly to those already familiar with the feldspar mineralogy.

The second section is about thermoluminescence in feldspars. It is confined only to the relevant aspects and is by no means complete in citation. Though some other references and details will follow in the course of discussion in the following chapters, the reader interested in recent bibliography is referred to recently published books and conference proceedings: Aitken (1985), Wagner et al. (1985) and McKeever (1985).

Feldspars used in the present study are introduced in the final section.

5.2 THE FELDSPARS: AN INTRODUCTION

The feldspars form one of the most abundant parts of several rock structures. They are present as a major constituent of a great majority of the igneous rocks and occur in many thermally and regionally metamorphic rocks as well. They are next in abundance to quartz in arenaceous sediments and common in mineral veins. Feldspars are of relatively minor significance only in the carbonate and argillaceous rocks and absent from ultra basic and some rare alkaline rocks.

This section briefly describes the feldspar composition and structure with the purpose of providing some background information about the variety of minerals used during this research. This section is based mostly on the information in Smith (1974), MacKenzie and Zussman (1974), Deer et al. (1982), Ribbe (1983a) and Brown (1984).

5.2.1 Chemical Classification

The feldspar minerals are aluminosilicates of alkaline and alkaline-earth cations and are chemically classified by the mole percentages of four end-members; namely orthoclase (Or:$KAlSi_3O_8$), albite (Ab: $NaAlSi_3O_8$), anorthite (An:$CaAl_2Si_2O_8$), and celsian (Cn:$BaAl_2Si_2O_8$).

The first three constitute a ternary system with extensive solid solutions along Or-Ab and Ab-An axes. The nomenclature on the basis of the mole percentages of the end-members is shown in Figure 5.1 which also shows the approximate location of the region of phase stability. Any melt outside the line of stability (marked as region 'Or + An') will

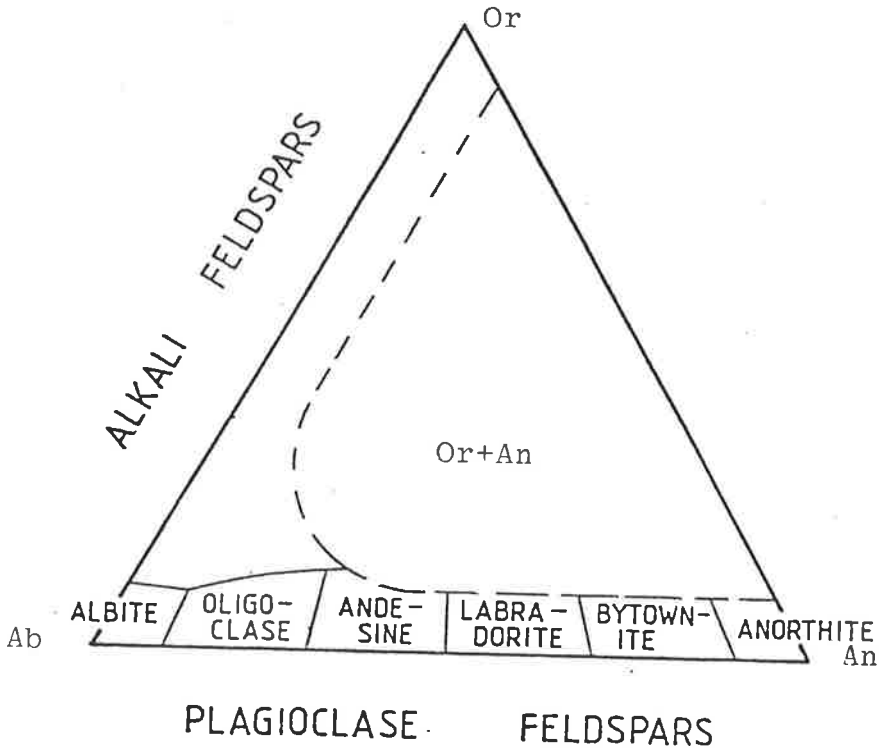

FIGURE 5.1: Feldspar nomenclature on the basis of composition. Phase stability of the ternary system is crudely represented by the broken line and any melt in Or+An region will crystallize as two solid phases.

crystallise as two solid phases i.e. a plagioclase + an alkali feldspar. Exact location of the line of stability is determined by the conditions like temperature and pressure during crystallisation (see e.g. Smith 1974, Parsons and Brown, 1984). Deer et al. (1982) suggest that, in general, all potassium feldspars may have up to 5 to 10% calcium but the sodium end members may take a little more. Similarly all plagioclases may contain up to 5 to 10% potassium in solid solution.

Barium is present in small quantities in most feldspars but the term barium feldspar applies to those which contain more than a few percent of Cn component. Feldspars with more than 90% of Cn are referred to as celsian, while those having less than 30% Cn are termed as hyalophane.

5.2.2 Structural State Classification

Structural state of feldspar is controlled mostly by the temperature of crystallisation and subsequent thermal history. Most feldspars from volcanic rocks retain the structure appropriate to their high temperature formation. Others formed either at lower temperatures or through slow cooling from elevated temperatures have crystal structure appropriate for the low temperature formation. Feldspars found in plutonic rocks are of this type. Intermediate temperature feldspars exist in between these two states.

Alkali feldspars are classified into four series on the basis of their optical properties determined by the conditions of crystallisation. Some characteristics of both high and low temperature alkali feldspar series and their end-members are shown in Figure 5.2(a,b). The cell structure change from monoclinic to triclinic for about 63% Ab molar concentration in the high temperature series is attributed to the loss of

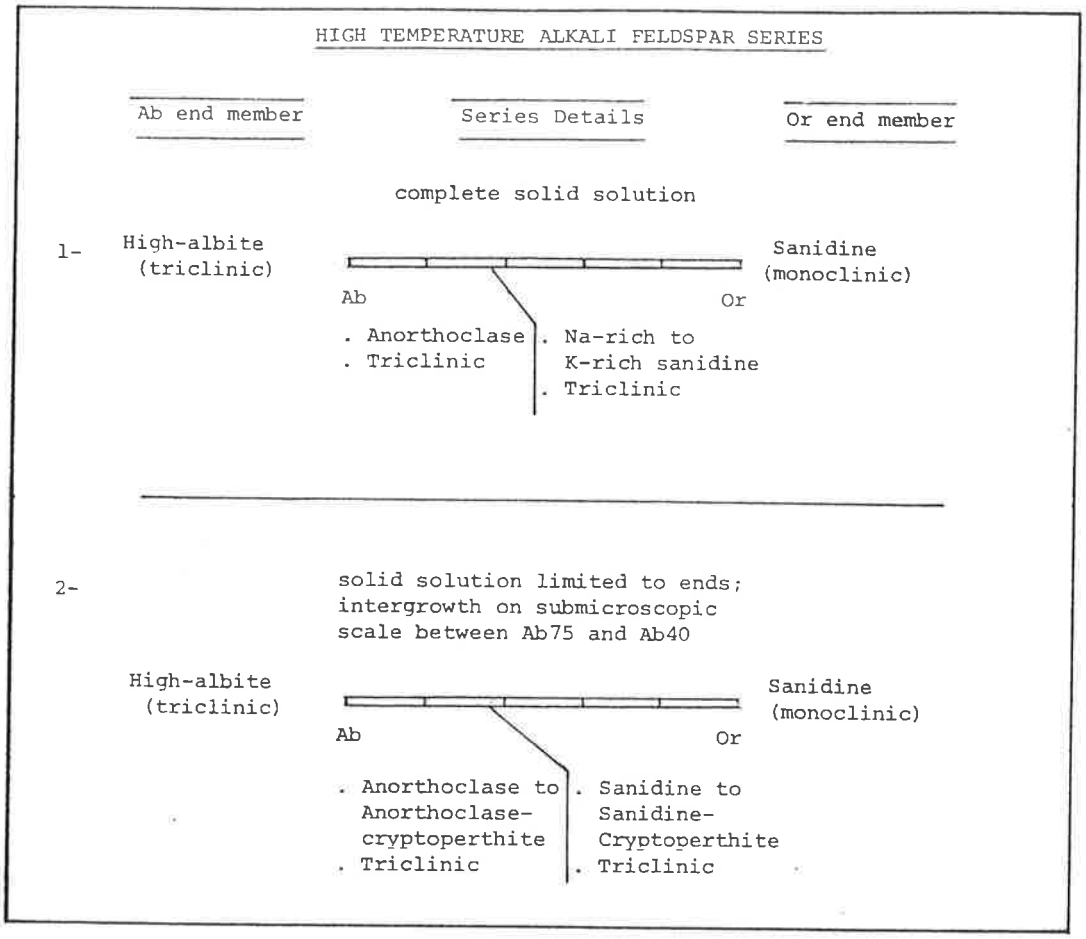

FIGURE 5.2a: High temperature alkali feldspar series and their end members. note a symmetry change near Ab63. The term cryptoperthite refers to submicroscopic intergrowths.

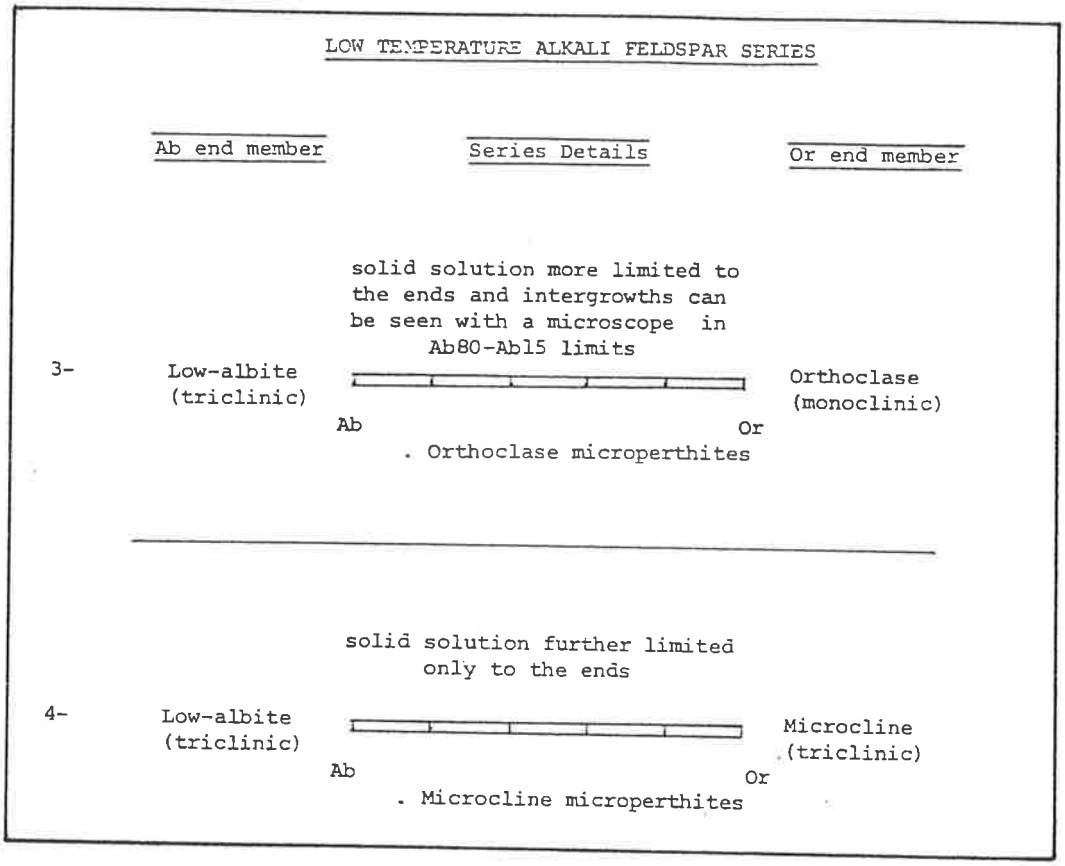

FIGURE 5.2b: Some characteristics of low temperature alkali feldspar series. Intergrowths in a microperthite can be identified using a microscope.

symmetry caused by the positioning of the smaller Na^+ cations. Exact boundaries are, however, diffused and temperature dependant.

All synthetic alkali feldspars belong to the highest temperature series, while the natural feldspars are confined only to its potassium rich end. Some alkali feldspars belonging to the low temperature series display irridescence due to lamellar intergrowths and are often named as moonstones. The term perthite is used if interpenetrating potassic and sodic phases can be seen without the aid of a microscope.

Both sodium and potassium end members formed at low temperature exhibit a state of Al,Si order in which the Al^{3+} ion shows a high preference for a specific structural site (out of the four allowed between Al and Si). This preference is lost in high temperature formation and feldspar is found to be "disordered" with complete random distribution of Al and Si. Partial order (or disorder) exists for intermediate temperatures.

A different type of fully ordered structure is observed in anorthite. The equal number of aluminium and silicon atoms alternate in the allowed lattice positions with strict regularity, which is apparently unaffected by the temperature of formation. Both anorthite and celsian triclinic cells have vector c double in length as compared to that in the case of low temperature albite.

Plagioclase series classification is complex and depends strongly upon the chemical composition. The main generalised characteristics are shown in Figure 5.2(c). The high temperature plagioclase structure, resulting in complete solid solution from the melt is retained by some volcanic rocks. Except for the boundary limits, the anorthite-like structure is common to the high and low temperature series. Deer et al.

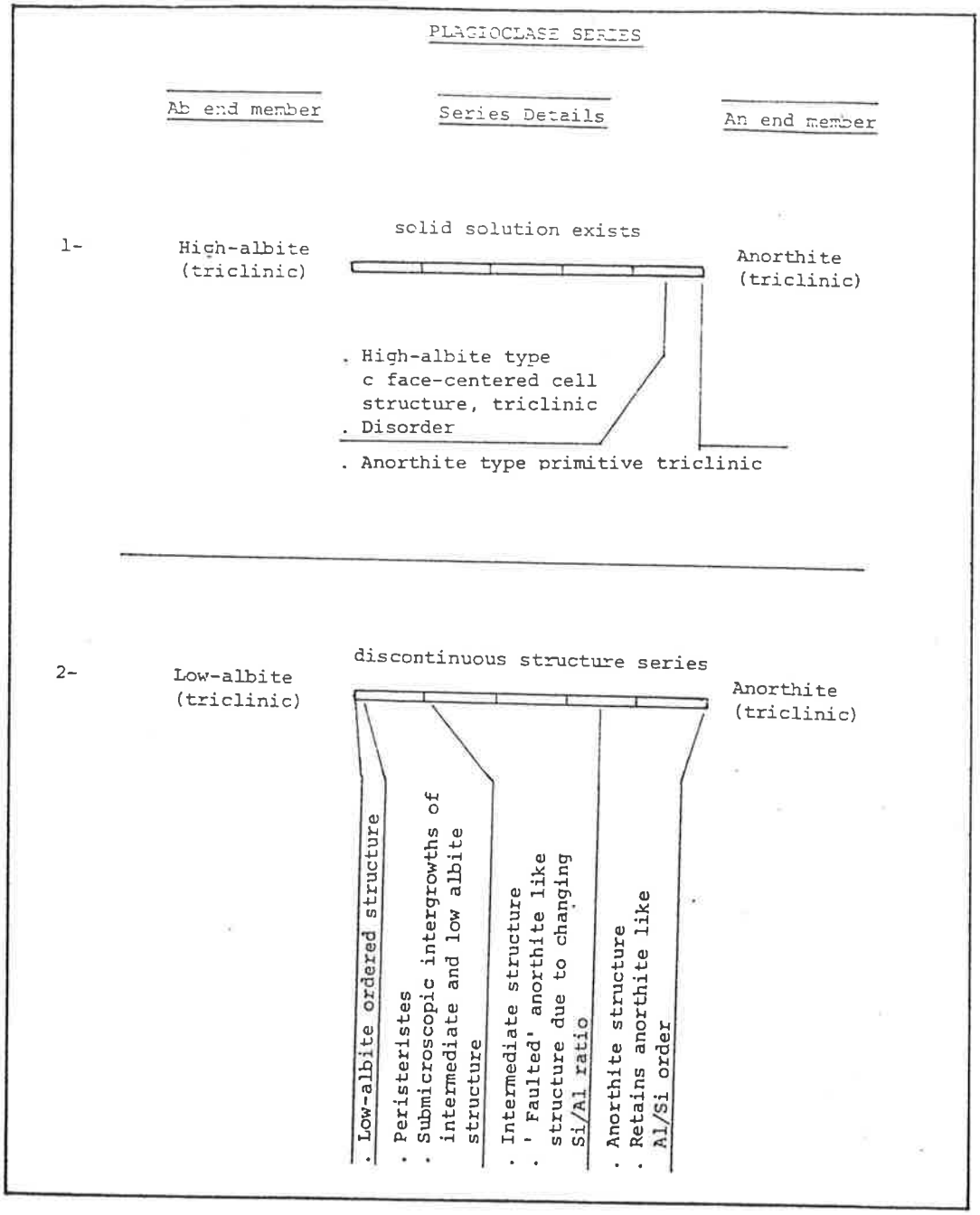

FIGURE 5.2c: Plagioclase structural classification at high and low temperature formation. The low temperature series is complex due to changing Al/Si ratio with composition.

(1982) suggest that the high temperature anorthite, in fact, extremely rapidly inverts to the low temperature anorthite structure.

As sodium replaces calcium in the anorthite structure, a corresponding replacement of Si for Al becomes necessary to preserve charge balance. The regular alternation of Si thus no longer occurs and a cell domain faulted structure evolves which is often identified through the diffused X-ray diffraction (XRD) reflections. The increasing frequency of faulted cell (or intermediate structure) extends till An22 (or Ab78). Plagioclase in Ab97-Ab78 region has submicroscopic intergrowths of both low-albite and intermediate structure feldspar.

The low temperature series is more common in most igneous rocks, metamorphic rocks and sediments.

5.2.3. Feldspar Architecture

Chemical composition of feldspar can be characterised by the general formula MT_4O_8, where 'T' are the atoms capable of tetrahedral structural co-ordination with 'O' (oxygen) atoms and 'M' is a larger cation. Typically, 4T atoms comprise (1Al + 3Si) if M is monovalent (Na,K) or (2Al + 2Si) if M is divalent (Ca,Ba).

Corner sharing AlO_4 and SiO_4 tetrahedral framework for alumino-silicates with MT_4O_8 general formula was first appreciated by Machatschki (1928). Other non-feldspar structures are now also known to follow this formula and a tetrahedral framework (see e.g. those mentioned by Ribbe, 1983b). Topology of the tetrahedral framework is, therefore, the only real criterion to uniquely determine the feldspar.

As aluminium and silicon are alike in size and bonding, quasiperfect (or disordered) structures exist where they replace each other at

random. The simplest feldspar structure, that of sanidine (disordered $KAlSi_3O_8$), was determined by Taylor (1933), who found that the four-membered rings of TO_4 tetrahedra share corners with similar rings to form crankshaft-like chains extending parallel to the a-axis (Figure 5.3).

The actual four-membered ring structure formed by the vertices T_1's and T_2's of non-equivalent tetrahedra has been shown with T-O-T linkage in Figure 5.4 (a), which is projection of the cell structure on the $(20\bar{1})$ plane. Figure 5.3(b) is the extension of the ring structure. Twofold horizontal axes of symmetry parallel to [010] (or b-axis) and a mirror plane (010) leading to C2/m sanidine structure symmetry can be noticed in the figure. M cations (not shown) are placed on the mirror plane and in large cavities made by the ring linkage structure. Depending upon their condition and composition, feldspar cell parameters deviate in detail from the sanidine structure, Megaw (1974), Smith (1974), Ribbe (1983b, 1984) Kitamura and Morimoto (1984).

Distortions in cell structure are common to almost all feldspars (see e.g. Smith 1974; Kitamura and Morimoto, 1984). These can be traced back to factors like spatial needs of different size M cations in the framework and the effect of topology on various atomic bonding requirements.

The exact location of M cations and the nature of the bonding change widely with feldspar composition. For example, large co-ordination polyhedra are associated with large size K^+ and Ba^{++} ions. Na^+ and Ca^{++}, on the contrary, are too small to fill the framework cavities and the cell structure consequently shrinks. Ca^{++} ions are placed on the alternate sides of a mean position while Na^+ displacement is irregular, distorted and depends strongly on the temperature.

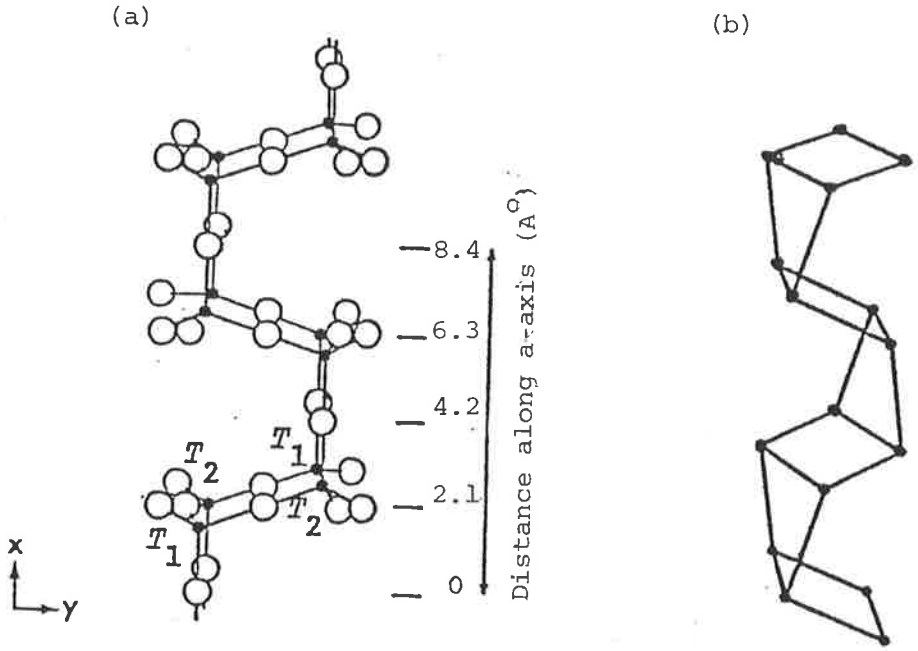

FIGURE 5.3: The double-crankshaft chain of four-membered tetrahedral rings in feldspar structure (a) after Taylor (1933), here taken from Ribbe (1983 b) and (b) a stereoscopic view. T-O-T bonds are drawn as straight lines and tetrahedral nodes shown as dots. T_1 and T_2 are two sets of non-equivalent tetrahedra (see Figure 5.4b).

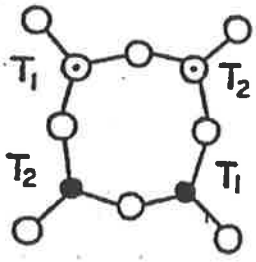

FIGURE 5.4a: The actual four-membered ring structure as projected in (20$\bar{1}$) plane. The oxygen atoms are shown blank, the dotted and darkened nodes indicate the upward and downward orientation of the tetrahedra.

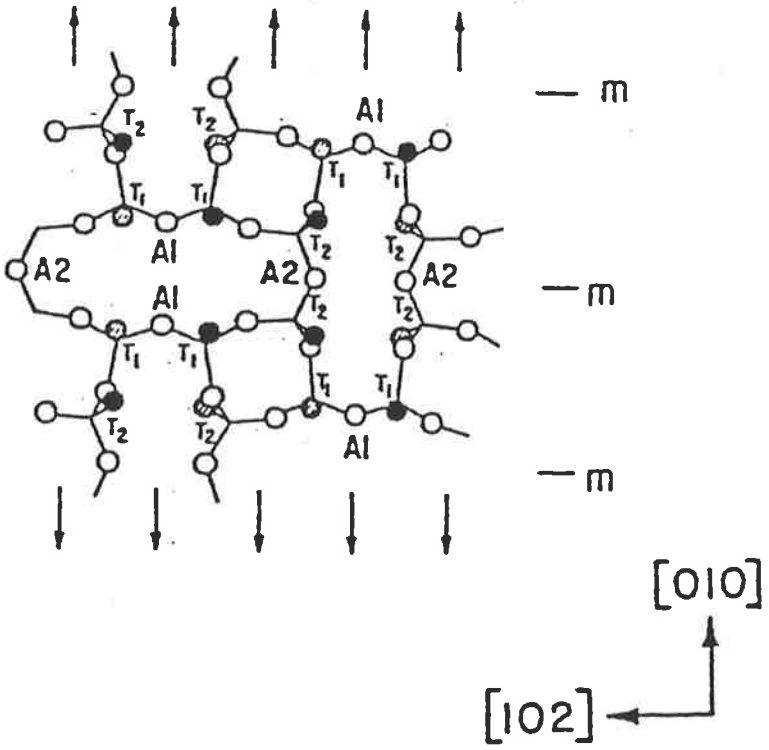

FIGURE 5.4b: Extension of the ring structure as shown in Figure 5.4a. The mirror planes parallel to (010) are marked by 'm' while the arrows point out the two fold axes of symmetry. Note that the T_1's are joined through A_1 and T_2's by A_2 oxygen sites on the mirror planes and the axes of symmetry respectively.

Smith (1974) summarises the effect of composition on the bond angles. He says that the T-O-T angles show a strong dependence on M cation size and also a weak tendency with its charge. The O-T-O angles, on the other hand, depend mainly on the M charge, while T-O distances relate with the Al/Si distribution.

5.2.4. Colours, Defects And Impurities In Feldspars

Like most other minerals, feldspars are not free from lattice defects and impurities. The extent of intake and its influence on the appearance varies widely with the factors like the environment during crystallization, composition and (occasionally) the subsequent history. The subject of feldspar colour, defects and impurities has been reviewed in Hofmeister and Rossman (1983), Smith (1974, 1983), Tullis (1983), and Gandais and Willaime (1984).

Feldspar with little impurity and defects does not absorb light in the visible portion of the spectrum and should appear clear (Hofmeister and Rossman, 1983). White, non-transparent appearance is due to the microcracks - microcracking being a dominant deformation mechanism in all feldspars (Tullis, 1983; Gandais and Williame, 1984). Smoky colour in some sanidines is attributed to mostly internal (K40) or some external (U, Th, K) radiation-induced hole centres on oxygen (O^-) in a cluster of Al^{3+} ions by producing an absorption band near 550 nm which is supported by two other bands near 380 and 450 nm associated with Fe^{3+} as an impurity. Sunlight bleaches it and ionizing radiation regenerates the colour (Speit and Lehmann, 1976; Hofmeister and Rossman, 1983). Dark feldspar inclusions are not very well understood. Hofmeister and Rossman, summarising the earlier conclusions by Smith (1974), suggest that oxides

of iron in mixed valence states, possibly with titanium and water, are thought to be responsible.

Feldspars in yellow, blue, green and red shades are also common in nature. Fe^{3+} absorption bands in the blue region lead to a yellowish tint. Fe^{2+} does not produce absorption bands in the visible region. Blue colour of amazonites (blue to green microclines, sometimes orthoclases) is reported to be due to the reduction of Pb^{2+} to Pb^{+} state. Blue sodic feldspars, with high Pb content, are relatively uncommon. Feldspars acquire pink to red shades from inclusions of hematite, a ferric oxide mineral. Oriented flakes of iron oxide sometimes give rise to preferentially scattered red colour and the feldspar is called a sunstone (Hofmeister and Rossman, 1983; Smith, 1983).

Crystal deformations including the grain scale fracture and microcracking have been discussed by Tullis (1983) and Gandais and Willaime (1984). Dislocation glide and slip, followed by partial recovery and recrystallization, is less frequent in feldspars compared with several other minerals with relatively simpler cell structure. Complex inter-atomic bondings and cell dimensions offer resistance to the propagation of dislocations and later recovery. The phenomenon, however, becomes competitive with microcracking at elevated temperatures and dominates typically above 500°C.

Impurity content of feldspars has been reviewed by Smith (1983).

5.3 THERMOLUMINESCENCE IN FELDSPARS

Historically, Wedgwood (1792) certainly reported on the thermoluminescence in a feldspar. Other significant reports include those by Hirschi (1925) and Holmquist (1926). Kohler and Leitmeier

(1932) relate the earliest observations due to Macquer (1778).

5.3.1 2D-Glow Curves

McDougall (1968) summarised contemporary reports, including his own observations, and noted a decreasing trend of natural thermoluminescence in plagioclases of increasing anorthitic content. Nishita et al. (1974) also confirmed this trend with the exception of anorthite which showed a higher signal than bytownite. Bachtiger (1967) reported a similar trend for X-ray induced TL and found enhanced thermoluminescence for turbid plagioclases indicating some correlation with H_2O or OH.

A report of a relationship between feldspar thermoluminescence and structural characteristics is that of Platanov et al. (1971). They noticed that the natural TL in K-feldspars from granitic rocks in the Ukrainian shield increased with the increasing disorder. Shcherbakov et al. (1972), extending the observation to Uman granites as well, concluded that the same argument applies to X-ray induced TL. Both these references maintain that the thermoluminescence peak in 200-220°C is associated with Al-O-Al centres. Marfunin (1979) also states the association of the oxygen hole centre with 200-220°C and Ti^{3+} centre with 280-300°C peaks, but suggests that the TL signal is commonly more intensive in microclines than in orthoclase. Sankaran et al. (1983) maintain the same view. Nishita et al. (1974) show natural TL peaks of varying shapes and peak temperatures for perthite, microcline, anorthoclase and perthite intergrowth in decreasing order of peak intensity.

Garlic et al. (1971) compared various features of lunar and terrestrial plagioclases and noticed an excessive loss of high

temperature TL during laboratory storage time (see also Garlic and Robinson, 1972). This aspect of feldspar thermoluminescence, being inexplicable on the basis of kinetic parameters, has been rightly named as 'anomalous fading' by Wintle (1973, 1977).

Guérin and Valladas (1980) report the existence of a high temperature peak in the 600-650°C region in plagioclase feldspar. Speit and Lehmann (1982) suggest that the thermal excitation of (radiation induced) holes into the valence band will possibly require higher temperature than the electrons in the conduction band. They also conclude that the nature of radiation defects in feldspars is fairly independent of the type and Al, Si disorder.

Ogelman and Kapur (1982) mention an increase in TL sensitivity of feldspars subject to weathering.

Feldspar thermoluminescence peaks are reported to follow second order or interactive TL kinetics (see e.g. Pasternack et al. 1976; Wintle and Huntley, 1980; Levy, 1982). Strickertsson (1985) determined the kinetic parameters for some natural alkali feldspars.

5.3.2 Emission Spectra

Thermoluminescence emission spectra of feldspars are far less reported as compared to their cathodo- or X-radiation induced luminescence. McDougall (1968) mentions assorted colours and shades, varying from deep blue-violet to red, as seen by various observers.

Lesnov and Serebrennikov (1972) saw a band near 570 nm in six, and an additional band near 450 nm in four out of six calcic feldspars. Ioffe and Yanchevskaya (1967) measured transmission spectra for sodic feldspars and reported three bands, the most intense being near 570 nm

and another between 380-480 nm range. The third band in the infra red region was later confirmed to be at 700 nm along with another band near 280 nm seen in connection with TL in albite (Ioffe and Yanchevskaya, 1968).

Pasternack and Levy (1978) reported that an intense emission band at 280 nm and an intermediate band near 558 nm, as observed by them in an albite from Amelia, monotonically broadened and shifted towards higher wavelengths with increasing (thermally induced) disorder. A weak band near 406 nm remained unchanged.

Lalou et al. (1972) observed the thermoluminescence emission spectrum for a lunar sample.

Marfunin (1979) assumes the possibility of emission centres to be associated with the trapping centres and suggests that the blue thermoluminescence may come from $Al-O^{-}-Al$ and Ti^{+3}, another possibility being Eu as an impurity. He attributes the peaks near 280, 580 and 750nm to Pb^{2+}, Mn^{2+} and Fe^{3+} respectively.

5.3.3. Thermoluminescence Dating

Thermoluminescence dating of feldspars is a story of successes and failures. The latest state of the art has been summarised by Aitken (1985). Factors like high thermoluminescence sensitivity and longer pre-saturation dose range make this very abundant mineral more attractive for thermoluminescence dating than the widely used quartz. But successful reports so far are mostly those related to K-feldspar dating (Mejdahl and Winther-Nielsen, 1982; Mejdahl, 1985).

Anomalous fading by an uncertain amount, over time periods of

archaeological and geological interest, is the major adverse factor leading to underestimated and untrustworthy dates (Wintle, 1973). Anomalous fading is particularly shown by high calcic plagioclases. Guérin and Valladas (1980), however, demonstrated the possibility of dating plagioclase of volcanic origin from Chaine des Puys. They state that the volcanic feldspars may show serious fading in the 300-400C range of of the glow curve, but not in the region above 600C. Thick UV filters were used to reduce the black-body radiation, which otherwise will mask the genuine signal. Earlier, Aitken et al. (1968) reported difficulties in dating plagioclase feldspars from Mount Etna and Hawaiian lavas. They noticed varying thermoluminescence signals from separates of different magnetic susceptibility and also observed spurious (non-radiation induced) thermoluminescence associated with sample grinding.

5.4 FELDSPARS IN THE PRESENT STUDIES

Twenty eight different feldspars of varying composition and locality have been studied for prompt and delayed thermoluminescence emission spectra induced by natural and artificial radiation. Identification and other available details of the individual samples are given in Table 5.1 and at the end of this Chapter. Two-dimensional glow curve information was obtained through interferogram summation. (Figure 4.2, Chapter 4).

Most of the samples have been selected from the museum collection of the Geology Department at the University of Adelaide with the courtesy and consultation of Dr. John Jones. Most composition analysis has been carried out by Dr. John Hutton using the XRF facility at the CSIRO Divison of Soils, Adelaide. Dr. Raphael Visocekas supplied two labradorite samples from Chaine des Puys region and Dr. John Hutton obtained the

synthetic feldspars.

Figure 5.5 summarises the composition distribution. The numbers in the circles are in increasing order of Ab (on Or axis) or An content and also represent the serial number assigned to the samples in the Table. An interesting feature of the figure is the high Ca and K content of feldspars along the Or and An axes respectively. Only 60% of the feldspars lie in 10% of the relevant axis. About 20% of the samples, lying between 20-30% intercept, are very likely to have crystallised in two different phases.

Albites (marked as 15 and 16) show little calcium i.e. 1.5 and 0.6% respectively. This feature is in conformity with the fact that the ordered albite-like structure can have only a small (a maximum of up to 3%) amount of calcium (Deer et al. 1982).

No Andesine (An30-50%) is included among the samples. Composition analysis of a labradorite and an anorthite was not attempted due to the shortage of the sample.

Figures 5.6(a) and (b) show the aluminium and silicon content respectively, as plotted against that expected from the idealized formula MT_4O_8. With the exception of one sample, the aluminium analysis agrees within 5% of the expected value. The data for the silicon analysis appears slightly more scattered but, with two exceptions, agrees well within 10% error limits.

Sample 28, the only barium feldspar included in the present study, showed exceptionally high silicon content. Scanning electron microscopy (SEM) and Energy Dispersive System (EDS) revealed a heterogeneous mixture of plagioclase (10%) a celsian (70%) and a quartz (20%) phase. The plagioclase appeared to be near An84. Excessive Si can, therefore, be

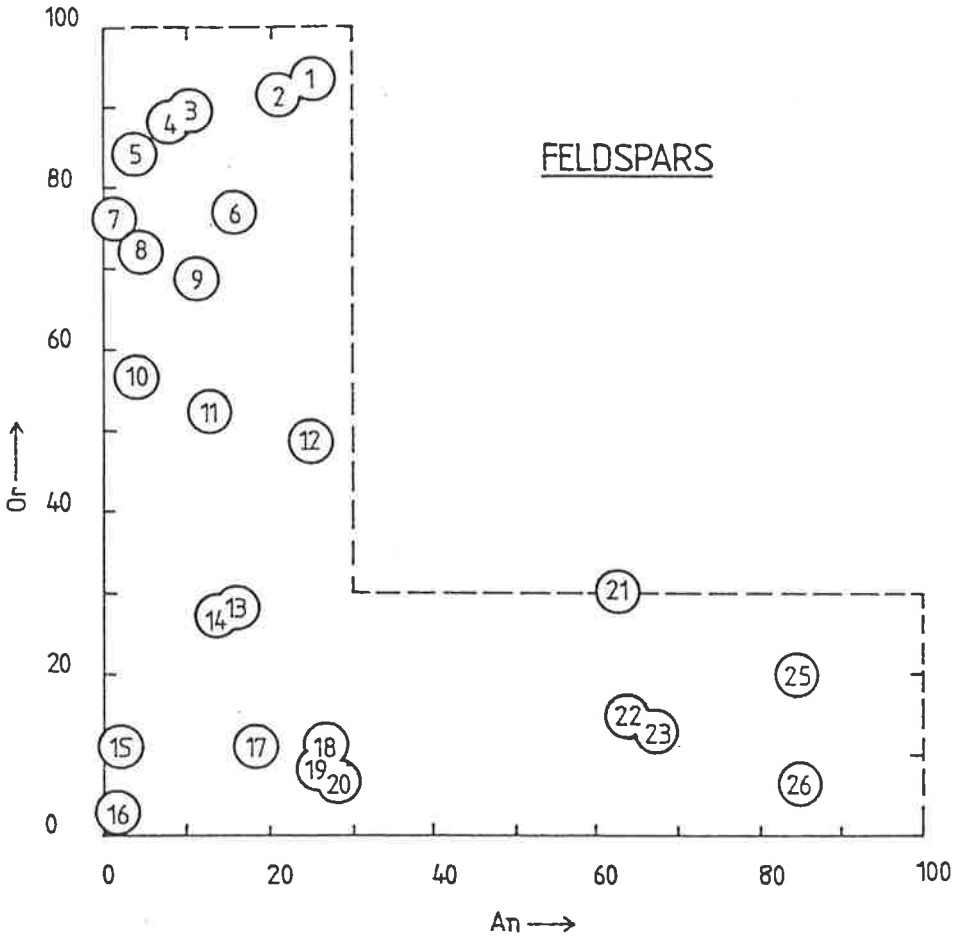

FIGURE 5.5: Composition distribution of the feldspars used in the present study. The numbers in the circles are from the highest Or molar concentration, through Ab to An. They also represent a serial number assigned to the indvidual samples in Table 5.1 .

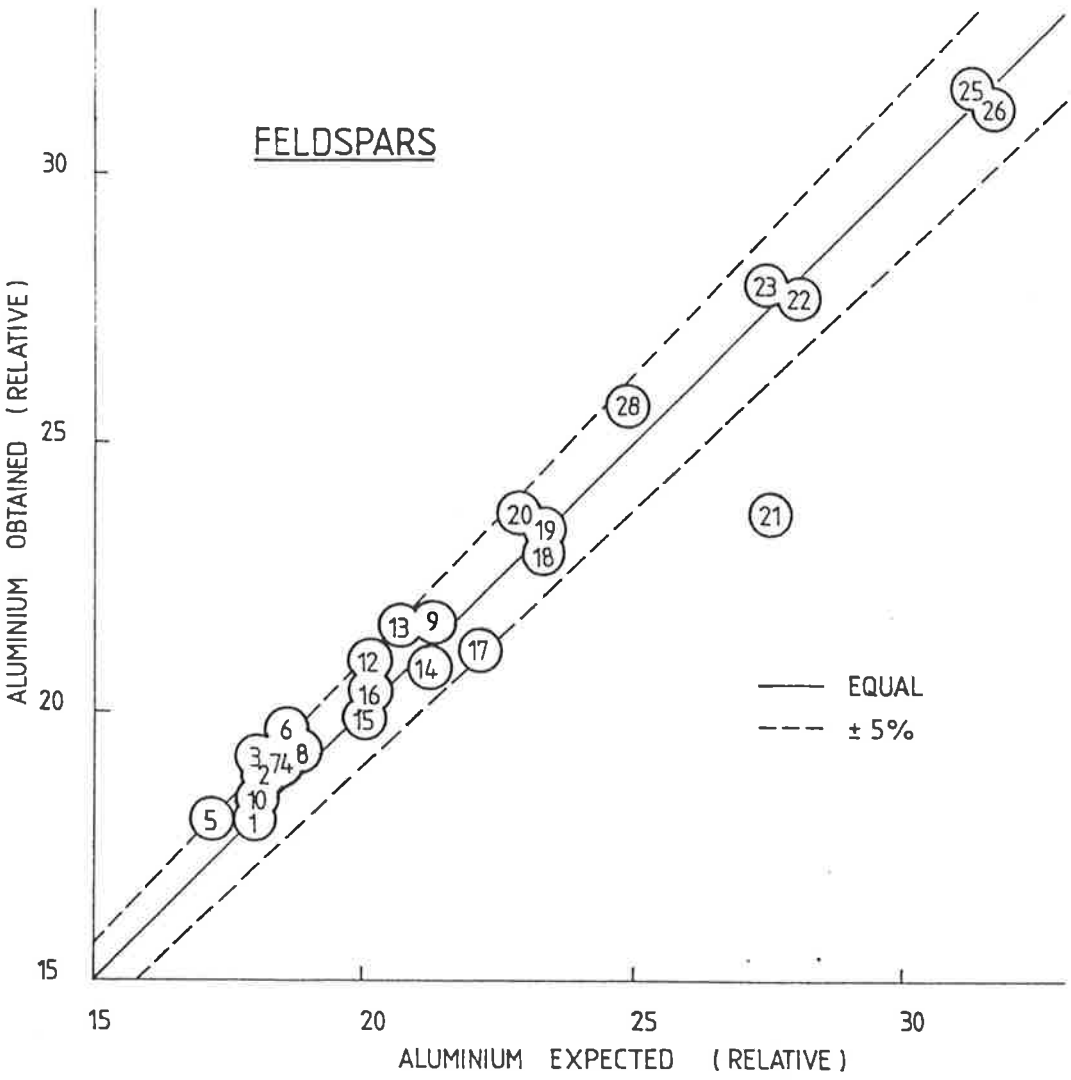

FIGURE 5.6(a): Aluminuim content of feldspar samples as obtained through XRF analysis plotted against the expected value using the idealized feldspar formula. The results are in excellent agreement with one exception explained in the text.

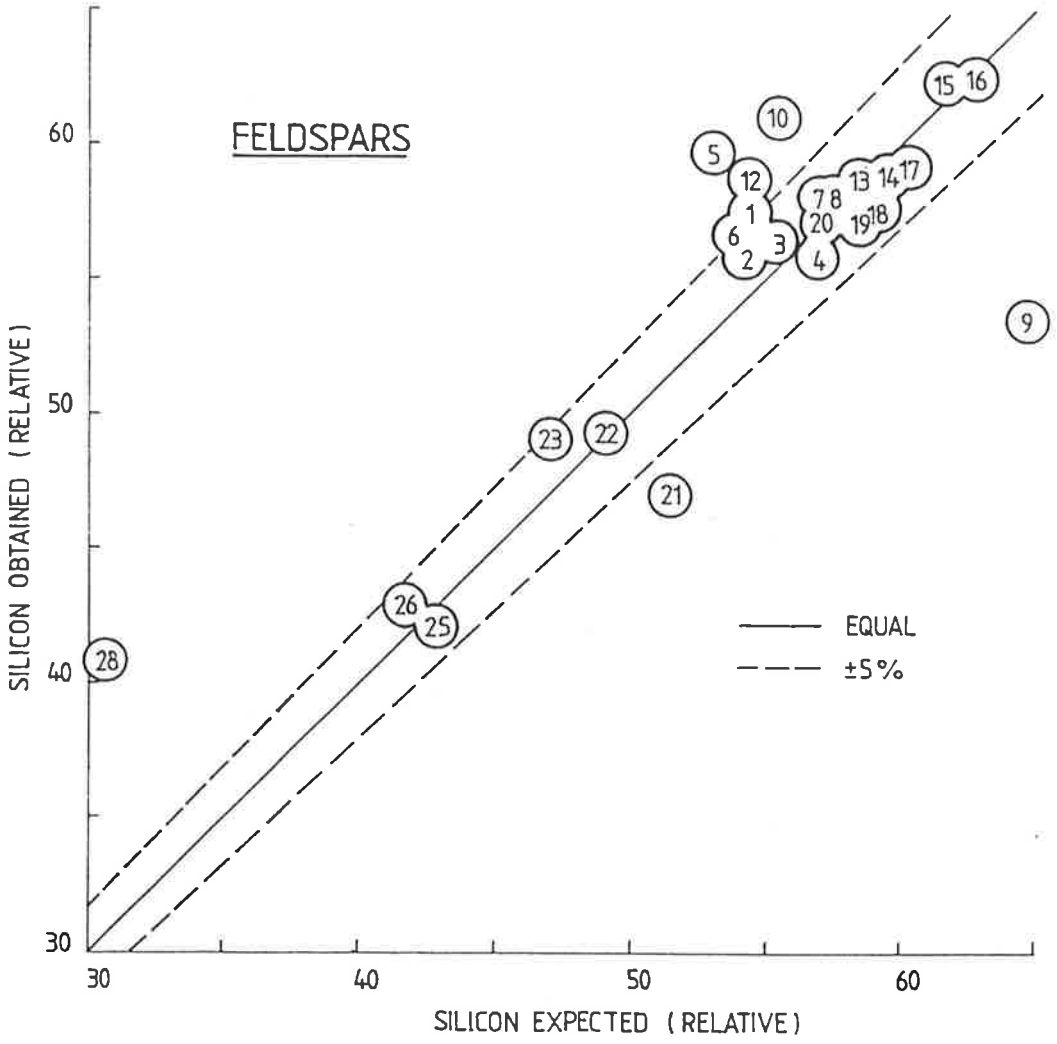

FIGURE 5.6(b): Obtained vs. expected silicon content in the feldspar samples used in the present study. See text for details and explanation.

attributed to the existence of a quartz phase. The SEM and EDS analyses are due to the courtesy of Dr. John Jones.

The low silicon content of sample 9 is presently not understood. The possible explanations include an excessive error in sodium estimate caused by the small amount of the sample available for XRF analysis and/or sodium contamination during XRF sample preparation. If the sodium estimate error is totally responsible, the corresponding aluminium estimate (Figure 5.6,a) should also have been some 10% lower than the present value.

Composition analysis identifies sample 21 as a labradorite with high potassium, iron and magnesium impurities. It reads low both on aluminium and silicon estimates. Once again, only small quantities were available for analysis. Correction for any sodium over-estimate by using silicon as a true value will only partly compensate for aluminium loss. Substitution of Al^{3+} sites by a few percent of impurity ions like Fe^{3+} is probable. Smith (1983) points out that bytownites of volcanic origin can take up to ~ 1 wt% of Fe^{3+}.

Two out of the three samples showing 5-10% higher silicon are the synthetic feldspars included in this study. It may be pointed out that an occasional deviation from the ideal MT_4O_8 formula leading to defect structures has been seen by several workers, particularly in connection with the synthetic feldspars. Goldsmith (1980), for example, synthesised an Al-deficient anorthite and Kim and Burley (1971) reported a synthetic albite with 5% excess SiO_2. Smith (1983) reviews the defect structures of feldspars.

The results reported in this thesis correspond to samples untreated for any further purification on concentration. The rock samples were

ground in a mortar and pestle and a coarse grain fraction between 90-125 μm sieved for spreading on stainless steel discs of approximately 10 mm diameter. The phosphor disc preparation procedure is common among several thermoluminescence laboratories (see e.g. Aitken, 1985; Mejdahl and Wintle, 1984). The amount of phosphor on each disc weighed between 3 and 4 mg. Deviations exist, particularly in the case of fine grain samples, and the results have been normalised for the purpose of inter-comparison. The fine grain and coarse grain samples will also have a different dose per unit mass response for a given radiation source and time (see e.g. Mejdahl, 1979). This aspect has been taken into account while comparing the results.

TABLE 5.1

FELDSPAR SAMPLES USED IN THE PRESENT STUDY: SOME DETAILS

EXPLANATIONS:

Column 1: Serial number starting from the highest Or molar concentration, through Ab to An.

Column 2: NAME: As given at the Source.

COLOUR: According to the 'Revised Standard Soil Color Charts' published by the Ministry of Agriculture and Forestry, Japan. Distributed by Frank McCarthy Colour Pty. Ltd., Melbourne (1970).

Geology Department: Geology Department, The University of Adelaide, Adelaide, S.A. 5001.

XRF JTH CSIRO: The composition analysis carried out by Dr. John Hutton using the XRF facility at the CSIRO Division of Soils, Adelaide.

JJ Geol. Dept.: The analysis provided by Dr. John Jones, Geology Department.

Expected Al, Si (Wt%): On the basis of standard feldspar formula.

(contd.)

SAMPLE No. DETAILS

1 NAME: FELDSPAR 18L IDENTIFICATION: Alkali Feldspar Sanidine
LOCATION: Broken Hill, N.S.W., Australia
FORM AS RECEIVED IN LAB.: 100 µm grains
SOURCE: Geology Department Collection
GENERAL COLOUR: Grains appear white
COMPOSITON:

K	Na	Ca	Ba	Al	Si	Fe	Ti	Mg
22.1	1.63	0.53	0.35	18.0	57.3	0.09	0.06	0

Source of analysis: XRF JTH CSIRO
Expected Al,Si (Wt%): 18, 54.9
K:Na=93:7 Na:Ca= 75:25 K:Na:Ca= 91:7:2
OTHER DETAILS:

2 NAME: FELDSPAR 241/3 IDENTIFICATION: Alkali Feldspar Orthoclase
LOCATION: Bruckhanga, South Australia
FORM AS RECEIVED IN LAB.: 100-200 µm grains
SOURCE: Geology Department Collection
GENERAL COLOUR: Light grey in bulk, 7.5Y7/1, 1-2% black grains
COMPOSITON:

K	Na	Ca	Ba	Al	Si	Fe	Ti	Mg
22.1	2.1	0.55	1.5	18.9	55.7	0.19	0.08	0.02

Source of analysis: XRF JTH CSIRO
Expected Al,Si (Wt%): 18.3, 54.3
K:Na=91:9 Na:Ca= 79:21 K:Na:Ca=89:9:2
OTHER DETAILS:

3 NAME: FELDSPAR 13802 IDENTIFICATION: Alkali Feldspar Orthoclase
LOCATION: Kingston, South Australia
FORM AS RECEIVED IN LAB.: About 500 µm grains
SOURCE: Geology Department Collection
GENERAL COLOUR: Clear to white
COMPOSITON:

K	Na	Ca	Ba	Al	Si	Fe	Ti	Mg
21.3	2.5	0.25	0.66	19.1	56.2	0.02	0.08	0.01

Source of analysis: XRF JTH CSIRO
Expected Al,Si (Wt%): 18.2, 55.5
K:Na=90:10 Na:Ca=91:9 K:Na:Ca=89:10:1
OTHER DETAILS:

4 NAME: FELDSPAR 16129 IDENTIFICATION: Alkali Feldspar Orthoclase
LOCATION: Taratap, South Australia
FORM AS RECEIVED IN LAB.: About 200µm grains
SOURCE: Geology Department Collection
GENERAL COLOUR: Light olive grey, 2.5GY7/1
COMPOSITON:

K	Na	Ca	Ba	Al	Si	Fe	Ti	Mg
21.4	2.8	0.26	0.83	19.0	55.7	0.01	0.08	0.03

Source of analysis: XRF JTH CSIRO
Expected Al,Si (Wt%): 18.7, 56.8
K:Na= 89:11 Na:Ca=91:9 K:Na:Ca=88:11:1
OTHER DETAILS: Also identified as Granadiorite

SAMPLE No. DETAILS

5 NAME:BNS 70a IDENTIFICATION:Sanidine(?)
LOCATION:Synthetic feldspar
FORM AS RECEIVED IN LAB.: Fine grain
SOURCE: JTH, CSIRO Collection
GENERAL COLOUR: White
COMPOSITON:

K	Na	Ca	Ba	Al	Si	Fe	Ti	Mg
18.6	3.5	0.14	0.03	18	59.7	0.08	0.01	0

Source of analysis: NBS Standard
Expected Al,Si (Wt%): 17.1,53.1
K:Na= 84:16 Na:Ca= 96:4 K:Na:Ca= 83:16:1
OTHER DETAILS:

6 NAME: FELDSPAR 241/1 IDENTIFICATION: Orthoclase
LOCATION: Bayard, New Mexico, U.S.A.
FORM AS RECEIVED IN LAB.: Granular 1-5µm
SOURCE: Geology Department Collection
GENERAL COLOUR: White
COMPOSITON:

K	Na	Ca	Ba	Al	Si	Fe	Ti	Mg
15.9	4.5	0.89	1.8	19.6	56.4	0.55	0.04	0.01

Source of analysis: XRF JTH CSIRO
Expected Al,Si (Wt%): 18.5, 53.8
K:Na=77:23 Na:Ca= 84:16 K:Na:Ca= 74:22:4
OTHER DETAILS:

7 NAME: FELDSAPR 4456 IDENTIFICATION: -
LOCATION: Pinnacle Arkaroola, South Australia
FORM AS RECEIVED IN LAB.: Rock pieces 2-3cm
SOURCE: Geology Department Collection
GENERAL COLOUR: White to light grey, 2.5Y8/1
COMPOSITON:

K	Na	Ca	Ba	Al	Si	Fe	Ti	Mg
17.4	5.4	0.01	0.11	19.0	57.9	0.06	0.06	0.01

Source of analysis: XRF JTH CSIRO
Expected Al,Si (Wt%): 18.4, 57.4
K:Na=76:24 Na:Ca= 100:0 K:Na:Ca= 76:24:0
OTHER DETAILS:

8 NAME: FELDSPAR 5785 IDENTIFICATION: Orthoclase microperthite
LOCATION: Wirrega, South Australia
FORM AS RECEIVED IN LAB.: Granular about 500µm
SOURCE: Geology Department Collection
GENERAL COLOUR: Dull Ogange
COMPOSITON:

K	Na	Ca	Ba	Al	Si	Fe	Ti	Mg
16.2	6.1	0.27	0.11	19.1	57.9	0.2	0.06	0.02

Source of analysis: XRF JTH CSIRO
Expected Al,Si (Wt%): 18.7, 57.6
K:Na=73:27 Na:Ca= 96:4 K:Na:Ca=72:27:1
OTHER DETAILS:

SAMPLE No. DETAILS

9 NAME: FELDSPAR M4600A IDENTIFICATION: Sodic Sanidine
LOCATION: Mount Soma, Itali
FORM AS RECEIVED IN LAB.: Grains 100μm
SOURCE: Geology Department Collection
GENERAL COLOUR: Light Grey 5Y8/2
COMPOSITON:

K	Na	Ca	Ba	Al	Si	Fe	Ti	Mg
16.2	7.5	1.0	0.04	21.6	53.9	0.19	0.04	0.02

Source of analysis: XRF JTH CSIRO
Expected Al,Si (Wt%): 21.3, 63.7
K:Na=69:31 Na:Ca= 88:12 K:Na:Ca= 66:30:4
OTHER DETAILS:

10 NAME: FELDSPAR G31 IDENTIFICATION: Sanidine
LOCATION: Slieve Gullion, Northern Ireland
FORM AS RECEIVED IN LAB.: Grains 100-200μm
SOURCE: Geology Department Collection
GENERAL COLOUR: Light Yellow, 5Y7/3
COMPOSITON:

K	Na	Ca	Ba	Al	Si	Fe	Ti	Mg
11.1	8.5	0.35	0.05	18.3	61.2	0.53	0.04	0.02

Source of analysis: XRF JTH CSIRO
Expected Al,Si (Wt%): 18.1, 55.4
K:Na= 57:43 Na:Ca= 96:4 K:Na:Ca= 56:42:2
OTHER DETAILS:

11 NAME: FELDSPAR 241/2 IDENTIFICATION: Moonstone
LOCATION: Wisconsin, U.S.A.
FORM AS RECEIVED IN LAB.: Grains 100μm
SOURCE: Geology Department Collection
GENERAL COLOUR: Light Grey, 7.5Y7/2
COMPOSITON:

K	Na	Ca	Ba	Al	Si	Fe	Ti	Mg
48.8	44.7	6.5	-	-	-	-	-	-

Source of analysis: JJ Geol. Dept.
Expected Al,Si (Wt%): -
K:Na= 52:48 Na:Ca= 87:13 K:Na:Ca= 49:45:6
OTHER DETAILS:

12 NAME: NBS 99a IDENTIFICATION: Sodic Sanidine (?)
LOCATION: Synthetic Feldspar
FORM AS RECEIVED IN LAB.: Fine Grains
SOURCE: JTH CSIRO Collection
GENERAL COLOUR: White
COMPOSITON:

K	Na	Ca	Ba	Al	Si	Fe	Ti	Mg
8.3	8.8	2.9	0.44	20.9	58.6	0.07	0	0.02

Source of analysis: BNS Standard, Washington D.C.
Expected Al,Si (Wt%): 20.2, 54.5
K:Na= 48:52 Na:Ca= 75:25 K:Na:Ca= 41:44:15
OTHER DETAILS:

SAMPLE No.	DETAILS

13 NAME: FELDSPAR 241/12 IDENTIFICATION: Anorthoclase
LOCATION: Mount Anakie, Victoria, Australia
FORM AS RECEIVED IN LAB.: Rock pieces 1-2cm
SOURCE: Geology Department Collection
GENERAL COLOUR: Clear
COMPOSITON:

K	Na	Ca	Ba	Al	Si	Fe	Ti	Mg
4.8	12.3	2.2	0.31	21.6	58.7	0.16	0.02	0.01

Source of analysis: XRF JTH CSIRO
Expected Al,Si (Wt%): 20.8, 58.5
K:Na= 28:72 Na:Ca= 85:15 K:Na:Ca= 25:64:11
OTHER DETAILS:

14 NAME: FELDSPAR 241/4 IDENTIFICATION: Anorthoclase
LOCATION: Mount Anakie, Victoria, Australia
FORM AS RECEIVED IN LAB.: Fine grains
SOURCE: Geology Department Collection
GENERAL COLOUR: White
COMPOSITON:

K	Na	Ca	Ba	Al	Si	Fe	Ti	Mg
4.8	12.6	2.2	0.4	20.8	58.8	0.25	0.11	0.09

Source of analysis: XRF JTH CSIRO
Expected Al,Si (Wt%): 21.2,59.8
K:Na=28:72 Na:Ca=85:15 K:Na:Ca=24:65:11
OTHER DETAILS:

15 NAME: FELDSPAR 16949 IDENTIFICATION: Albite
LOCATION: Sitting Bull Locality
FORM AS RECEIVED IN LAB.: Rock piece
SOURCE: Geology Department Collection
GENERAL COLOUR: Greyish white, N8/0
COMPOSITON:

K	Na	Ca	Ba	Al	Si	Fe	Ti	Mg
2.0	15.6	0.24	0.01	19.9	62.2	0.06	0.01	0.02

Source of analysis: XRF JTH CSIRO
Expected Al,Si (Wt%): 20.0, 61.9
K:Na= 11:89 Na:Ca=98:2 K:Na:Ca= 11:87:2
OTHER DETAILS:

16 NAME: FELDSPAR 16955 IDENTIFICATION: Albite
LOCATION: Amelia Court House, Virginia, U.S.A.
FORM AS RECEIVED IN LAB.: Rock piece
SOURCE: Geology Department Collection
GENERAL COLOUR: White
COMPOSITON:

K	Na	Ca	Ba	Al	Si	Fe	Ti	Mg
0.45	16.8	0.11	0	20.3	62.3	0.1	0.01	0

Source of analysis: JJ Geol. Dept.
Expected Al,Si (Wt%): 20.2,62.7
K:Na= 3:97 Na:Ca= 99:1 K:Na:Ca= 2:97:1
OTHER DETAILS:

SAMPLE No. DETAILS

17 NAME: FELDSPAR 19920 IDENTIFICATION: Oligoclase
LOCATION: Arendal , Norway
FORM AS RECEIVED IN LAB.: Rock piece
SOURCE: Geology Department Collection
GENERAL COLOUR: Olive grey to dark grey
COMPOSITON:

K	Na	Ca	Ba	Al	Si	Fe	Ti	Mg
1.8	14.1	3.2	0.03	21.1	59.0	0.61	0.03	0.2

Source of analysis: XRF JTH CSIRO
Expected Al,Si (Wt%): 22.17, 60.12
K:Na= 11;89 Na:Ca= 81:19 K:Na:Ca= 9:74:17
OTHER DETAILS:

18 NAME: FELDSPAR 307 IDENTIFICATION: Oligoclase
LOCATION: Sweden
FORM AS RECEIVED IN LAB.: Rock piece
SOURCE: Geology Department Collection
GENERAL COLOUR: Greyish white
COMPOSITON:

K	Na	Ca	Ba	Al	Si	Fe	Ti	Mg
1.1	13.6	4.9	0.01	22.9	57.4	0.19	0.01	0.02

Source of analysis: XRF JTH CSIRO
Expected Al,Si (Wt%): 23.3, 59.1
K:Na= 7:93 Na:Ca= 73:27 K:Na:Ca= 7:69:24
OTHER DETAILS:

19 NAME: FELDSPAR 19752 IDENTIFICATION: Oligoclase
LOCATION: Renfrew Co., Ontario,Canada
FORM AS RECEIVED IN LAB.: Rock piece
SOURCE: Geology Department Collection
GENERAL COLOUR: White
COMPOSITON:

K	Na	Ca	Ba	Al	Si	Fe	Ti	Mg
0.66	13.8	5.0	0.03	23.3	57.2	0.05	0.01	0.03

Source of analysis: XRF JTH CSIRO
Expected Al,Si (Wt%): 23.4, 58.9
K:Na= 5:95 Na:Ca= 73:27 K:Na:Ca= 3:71:26
OTHER DETAILS:

20 NAME: FELDSPAR 16947 IDENTIFICATION: Oligoclase
LOCATION: Mitchell Co., North Carolina, U.S.A.
FORM AS RECEIVED IN LAB.: Rock piece
SOURCE: Geology Department Collection
GENERAL COLOUR: White
COMPOSITON:

K	Na	Ca	Ba	Al	Si	Fe	Ti	Mg
0.5	13.3	5.2	0.03	23.6	57.2	0.15	0.01	0.01

Source of analysis: XRF JTH CSIRO
Expected Al,Si (Wt%): 23.0, 57.1
K:Na= 4:96 Na:Ca= 72:28 K:Na:Ca= 3:70:27
OTHER DETAILS:

SAMPLE No.	DETAILS

21 NAME: LABRADORITE C.F.R. IDENTIFICATION: Labradorite
LOCATION: Chaine des Puys, France
FORM AS RECEIVED IN LAB.: Grains 100µm
SOURCE: Laboratoire de Luminescence, Paris
GENERAL COLOUR: Grey, 5Y6/1
COMPOSITON:

K	Na	Ca	Ba	Al	Si	Fe	Ti	Mg
3.3	7.5	12.3	0.19	23.5	47.1	3.2	0.55	2.5

Source of analysis: XRF JTH CSIRO
Expected Al,Si (Wt%): 27.6, 51.7
K:Na= 30:70 Na:Ca= 38:62 K:Na:Ca= 14:33:53
OTHER DETAILS:

22 NAME: FELDSPAR 18568 IDENTIFICATION: Labradorite
LOCATION: Labrador
FORM AS RECEIVED IN LAB.: Rock piece
SOURCE: Geology Department Collection
GENERAL COLOUR: Light olive grey 5GY7/1, dark grey inclusions
COMPOSITON:

K	Na	Ca	Ba	Al	Si	Fe	Ti	Mg
0.94	7.7	13.5	0.08	27.8	49.2	0.7	0.09	0.06

Source of analysis: XRF JTH CSIRO
Expected Al,Si (Wt%): 27.9, 49.2
K:Na= 11:89 Na:Ca= 36:64 K:Na:Ca=4:35:61
OTHER DETAILS: 2-5mm dark grey inclusions covering 40-50% of section area.

23 NAME: FELDSPAR 18681 IDENTIFICATION: Labradorite
LOCATION: St. Paul Island, Canada
FORM AS RECEIVED IN LAB.: Rock piece
SOURCE: Gelogy Department Collection
GENERAL COLOUR: Olive grey 2.5GY6/1 with dark grey inclusions N3/0
COMPOSITON:

K	Na	Ca	Ba	Al	Si	Fe	Ti	Mg
0.78	7.0	13.9	0.06	27.7	49.1	1.2	0.18	0.13

Source of analysis: XRF JTH CSIRO
Expected Al,Si (Wt%): 27.6, 47.0
K:Na= 10:90 Na:Ca= 33:67 K:Na:Ca= 4:32:64
OTHER DETAILS:

24 NAME: LABRADORITE OXFORD IDENTIFICATION: Labradorite
LOCATION: Chaine des Puys, France
FORM AS RECEIVED IN LAB.: Grains 100µm
SOURCE: Laboratoire de Luminescence, Paris
GENERAL COLOUR: White with 10-20% dark grains
COMPOSITON: NOT AVAILABLE

K	Na	Ca	Ba	Al	Si	Fe	Ti	Mg
-	-	-	-	-	-	-	-	-

Source of analysis:
Expected Al,Si (Wt%):
K:Na= Na:Ca= K:Na:Ca=
OTHER DETAILS:

SAMPLE NO.	DETAILS

25 NAME: FELDSPAR 303 IDENTIFICATION: Bytownite
LOCATION: Silesia, Germany
FORM AS RECEIVED IN LAB.: Rock piece
SOURCE: Geology Department Collection
GENERAL COLOUR: Greyish olive 5Y6/2, 30% dark N3/0 inclusions
COMPOSITON:

K	Na	Ca	Ba	Al	Si	Fe	Ti	Mg
0.74	3.7	19.7	0.06	31.4	42.1	1.1	0.1	1.1

Source of analysis: XRF JTH CSIRO
Expected Al,Si (Wt%): 31.4, 42.9
K:Na= 17:83 Na:Ca= 16:84 K:Na:Ca= 3:16:81
OTHER DETAILS:

26 NAME: FELDSPAR 19049 IDENTIFICATION: Bytownite
LOCATION: Crystal Bay, Minnesota, U.S.A.
FORM AS RECEIVED IN LAB.: Rock piece
SOURCE: Geology Department Collection
GENERAL COLOUR: Olive grey, dark inclusions not uniformly scattered
COMPOSITON:

K	Na	Ca	Ba	Al	Si	Fe	Ti	Mg
0.12	3.6	20.1	0.01	31.2	43.1	1.5	0.05	0.41

Source of analysis: XRF JTH CSIRO
Expected Al,Si (Wt%): 31.4, 41.7
K:Na= 3:97 Na:Ca= 15:85 K:Na:Ca= 1:15:84
OTHER DETAILS:

27 NAME: FELDSPAR 18446 IDENTIFICATION: Anorthite
LOCATION: Myakejina, Japan
FORM AS RECEIVED IN LAB.: Small sample, lose crystals 2-3mm
SOURCE: Geology Department Collection
GENERAL COLOUR: Clear
COMPOSITON: NOT AVAILABLE

K	Na	Ca	Ba	Al	Si	Fe	Ti	Mg
-	-	-	-	-	-	-	-	-

Source of analysis:
Expected Al,Si (Wt%):
K:Na= Na:Ca= K:Na:Ca=
OTHER DETAILS: Blackened exterior as the sample recovered out of volcanic ash.

28 NAME: FELDSPAR 4487 IDENTIFICATION: Barium Feldspar
LOCATION: Broken Hill, New South Wales, Australia
FORM AS RECEIVED IN LAB.: Fine grains
SOURCE: Geology Department Collection
GENERAL COLOUR: White
COMPOSITON:

K	Na	Ca	Ba	Al	Si	Fe	Ti	Mg
0.94	1.3	11.4	18.9	25.8	41.6	0.03	0.05	0

Source of analysis: XRF JTH CSIRO
Expected Al,Si (Wt%): 24.9, 30.5
K:Na= 42:58 Na:Ca= 10:90 K:Na:Ca= 7:9:84
OTHER DETAILS:

CHAPTER SIX

THERMOLUMINESCENCE IN Na-K FELDSPARS

"So it may be that feldspar is really the Cinderella of the standard techniques. Its thermoluminescence is 10-50 times brighter than that of quartz, and its dose range is substantially greater..."

Martin Aitken
Thermoluminescence Dating

6.1 INTRODUCTION

The subject matter in the present and the following chapter mostly handles the overall features in various compositional groups of feldspars described in Section 5.4 of Chapter Five. Attempts have been made to work out some systematics in the thermoluminescence character. Emission spectrum of the celsian is discussed in Chapter Eight.

Results for sixteen samples on the Na-K axis have been reported in this chapter. These have been subsectioned for ease in discussion. The end members have been reported first in Section 6.2, followed by a separate section for intermediate composition feldspars. Synthetic feldspars are handled in Section 6.4. Emission bands have also been discussed in the light of information available from other references.

The terms ATL and NTL have been used to represent the natural and laboratory beta radiation-induced (artificial) thermoluminescence in the samples. Unless otherwise stated, the 2D-TL glow curves presented in this and the following chapters have been plotted using the raw interferogram data as described in Chapter Four.

6.2 THE END MEMBERS

Thermoluminescence emission spectra of four high potassic feldspars with about 90% Or and an albite with 97% Ab are reported and discussed in this section.

6.2.1 High Potassic Feldspars

Figure 6.1, plotted for sample #3, a high potassic feldspar from Kingston, South Australia, represents typical natural and artificial thermoluminescence spectra for members of this group.

For natural thermoluminescence (Figure 6.1a), an emission band near 400 nm with a FWHM of about 60 nm extends throughout the glow curve. The intensity peaks between 350-375C, which is followed by another high temperature peak still in emerging state at the terminating temperature of 500C. Up to about 300C, the 2D-ATL signal probably comprises more than one trapping centre of decreasing population with increasing depth. A definite peak appears at 345C followed by the high temperature signal above 500C. A slight decrease was noticed in the high temperature signal after successive glowing of this (and some other) sample(s). This can be attributed to a small but significant partly drained residue from the high natural thermoluminescence signal at the terminating temperature.

An interesting aspect of the emission spectrum is the low temperature broad-band signal. It can be seen from Figures 6.1(b) that the emission band near 200C extends in its FWHM from about 385 nm to 525 nm with its peak at 420 nm. It shrinks with increasing temperature and the peak shifts towards lower wavelengths till the 400 nm emission band characteristics as seen in NTL are restored from about 300C onwards. The

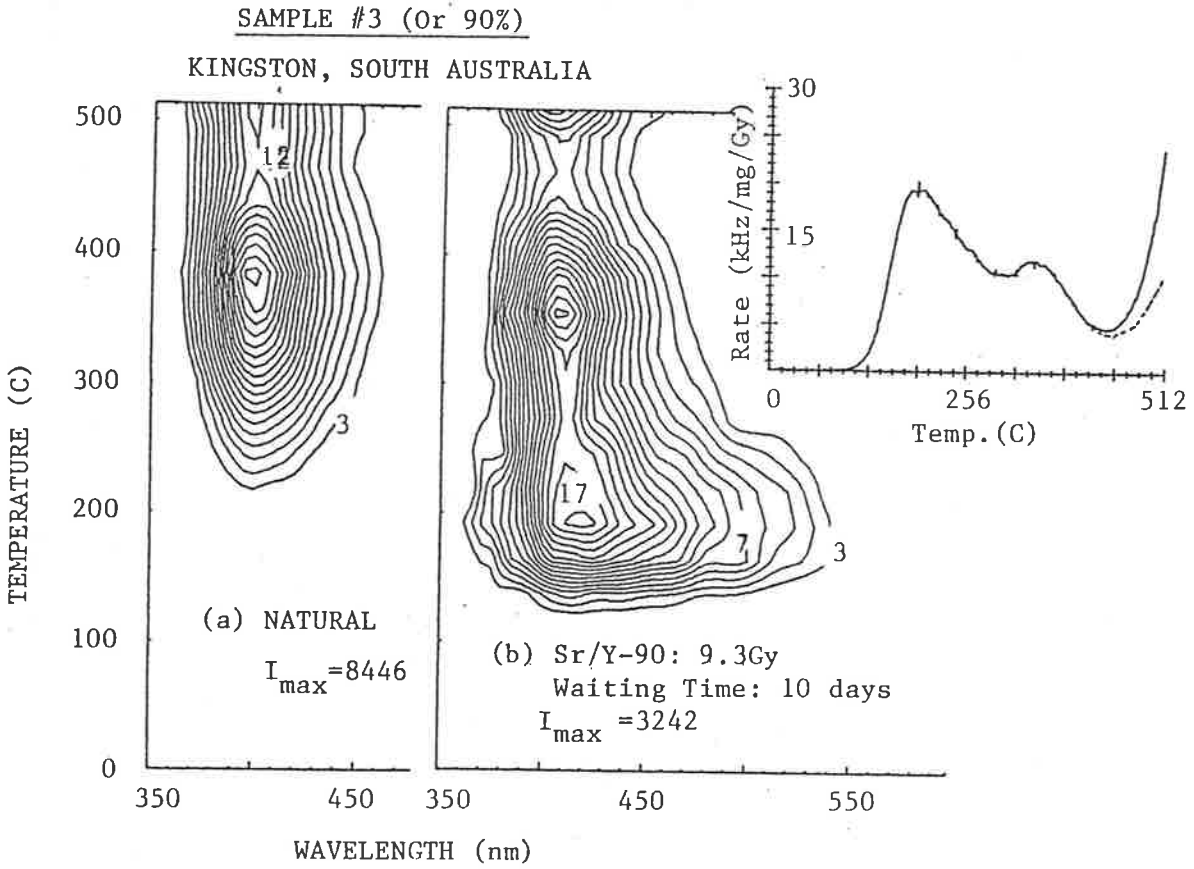

FIGURE 6.1: (a) Natural and (b) laboratory radiation induced thermoluminescence in a high potassic feldspar from Kingston, South Australia. The insert in (b) shows the corresponding 2D TL glow curve where the broken line represents the TL signal corrected for the black body emission. I_{max} is the maximum intensity corresponding to the contour #20.

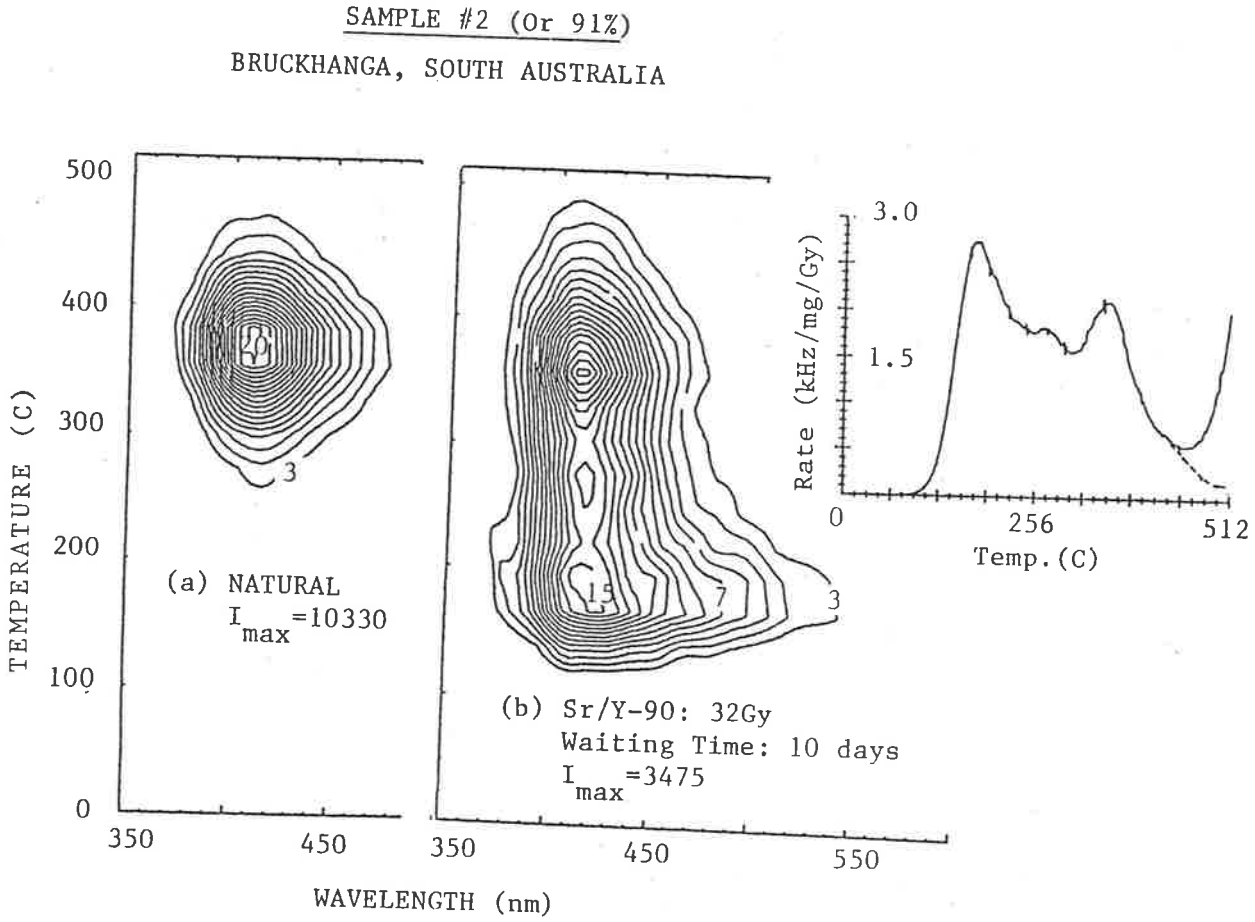

FIGURE 6.2: Thermoluminescence behaviour of a high potassic feldspar from Bruckhanga, South Australia, differs from the other three samples used in the present study through little signal above 500C. (a) Natural and (b) laboratory radiation induced TL signal. The insert shows the corresponding 2D TL glow curve. I_{max} refers to the max intensity for contour #20.

shrinking tail nature and the gradual shift of the emission peak suggest that the broad band may actually be due to some additional centres with characteristic higher wavelength emission and preferential recombination at lower temperatures.

One of the four high potassic feldspar samples showed very little TL signal above 500C (Figure 6.2a). An additional peak which could only be suggested in the other three samples, distinctly appeared near 280C in the ATL (Figure 6.2b). The sample showed less natural TL and four to five times lower TL sensitivity. The wavelength bands in the emission spectrum, however, appeared similar to those seen in other high potassic feldspars.

6.2.2 The Sodic End Member

Figure 6.3(a,b) shows thermoluminescence behaviour for sample #16, an albite from Amelia Court House, Virginia, U.S.A. As can be seen through Figure 5.5 of Chapter 5, this sample has the lowest K content among the feldspars on the Na-K axis. Both the natural and ATL spectra show two main emission bands around 400 and 530 nm. The natural thermoluminescence signal (Figure 6.3a) peaks near 350C and readily extends above 500C. The 530 nm band with its FWHM of about 90 nm dominates the lower temperature signal, but the relative height of the 400 nm peak continuously increases till the high temperature signal above 500C is mainly due to the 400 nm band. In detail, the 400 nm band in albite comprises more than one component and appears broader than that in the case of high potassic feldspars.

The 135C initial peak of the laboratory radiation induced TL is followed by two others at 220 and 300C and a high temperature signal

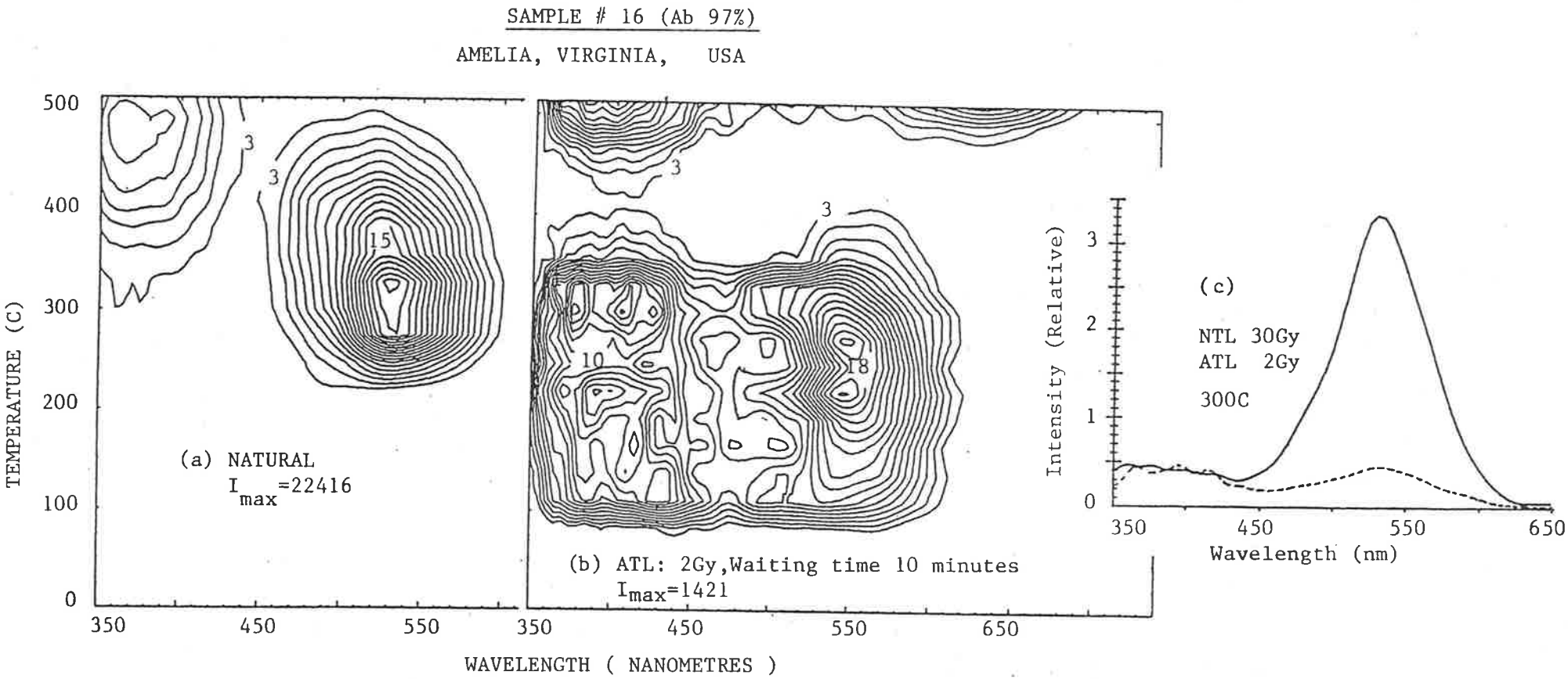

FIGURE 6.3: Thermoluminescence behaviour of the sodic end member, an ordered albite from Amelià, Viginia. Two main emission bands near 400nm and 530nm as seen for natural (a) and laboratory radiation induced TL (b) differ in relative heights at a given temperature (c). Figure (c) has been plotted scaling the signal for the same height in the 400nm region, and also shows that this band most probably comprises more than one emission centre.

above 500C. Main features of the 530 and 400 nm emission bands are the same as for the natural TL, the only major exception being a marked difference in the relative intensities for a given temperature. Some additional smaller peaks appear in the region for ATL spectrum. They extend up to about 300C or so. Also the Amelia albite is two to three times more TL sensitive than most high potassic end members.

It is interesting to note that another sample #15, from Sitting Bull locality, and labelled as an albite shows different TL characteristics from those of the Amelia albite. This sample, with 11% Or, resembled in its TL behaviour, and has been bracketed with, the intermediate composition potassic feldspars.

6.2.3 Some Discussion about the Emission Bands

Few and very scattered references are available on thermoluminescence emission spectra of feldspars. Most of these have already been cited in Chapter Five in connection with a brief review of the 3D TL in feldspars. This section is an attempt to understand the nature of the emission bands in the light of the previously reported findings and the present results.

6.2.3.1 The 550 nm Emission Band

A comparison of relative intensities of the two main emission bands in natural and laboratory induced thermoluminescence leads to some interesting facts about TL in the high sodic end member. As shown in Figure 6.3c, for 300C thermoluminescence signal, the relative heights change from 1:7 to 3:2 for NTL and 2.0 Gy ATL respectively. Two different mechanisms therefore control these bands and the one at 530 nm

may well be linked with some radiation defect. This conclusion is based on the fact that on comparison of TL intensities, the natural radiation dose appears to be about fifteen times higher than the laboratory dose.

The argument is further supported by the findings of the other workers as well. The albite sample #16 originated from the Amelia Court House, Virginia. An albite from the same locality, along with some other samples, was used by Pasternack (1978, see also Paasternack et al. 1976, 1978) for observing the thermoluminescence spectra from room temperature to about 350C in the range 200 nm to 650 nm. Pasternack could just see the natural TL in the Amelia albite at the sensitivity limit of his apparatus and reported a single radiation band at 560 nm. The other radiation band at 400 nm, which appears to be about seven times smaller in height than the 560 nm band in this temperature region on our equipment, was obviously not observed by him. Three emission bands, however, appeared in decreasing order of intensity at 280, 560 and 395 nm range when the sample was given a gamma radiation dose of 10^4Gy. Pasternack used a dispersive type 3DTL equipment and the second order of 280 nm emission overlapped the 560 nm signal. The present results would therefore be better compared with his observations made by interposing a Corning 0-52 UV filter. The two emission bands were then seen in a ratio of 1:16 which indicates an increase in the 560 nm band height with the increased radiation dose.

An earlier report from Ioffe and Yanchevskaya (1968) on X-ray induced luminescence in single crystals of albite mentions four emission bands with peaks near 280, 400, 550 and above 700 nm. They add that the relative intensities of both the ultraviolet and the 550 nm bands varied from sample to sample depending upon the irradiation.

The radiation defects observed in feldspars have been reported by several authors (see e.g. Speit and Lehmann, 1982: Matyash et al. 1982 and Lehmann, 1984). Work by Speit and Lehmann is of more significance here, as it includes a table on characteristic TL emission assigned to various fully or partly identified radiation defects seen in fifteen different feldspars. They did not see a radiation-induced TL emission band in the 530-560 nm region for their albite sample from Norway. A band in the 530-540 nm region has, however, been reported for seven other feldspars of varying composition and localities. This band has been associated with a hole centre on oxygen with Si as one neighbour and another unidentified neighbour which has to be a small divalent atom at the 'T' sites in the feldspar structure (see Chapter Five for the feldspar structure).

Alternative possibilities of 530 nm band association with some impurity like Mn^{2+} or surface defects have also been reported by several authors. Although detailed discussion of this aspect is postponed until the next chapter on thermoluminescence in plagioclase feldspars, yet it is worth pointing out at this stage that the actual emission band seen in a sample may be due to the composite effect of more than one possibility and such classification is not investigated during the present studies.

6.2.3.2 The 400 nm Emission

The 400 nm emission band as seen in both potassic and sodic end members has not been identified as a radiation induced defect by Speit and Lehmann (1982).

The fact that all the high potassic feldspars in the present study belong to the high temperature disordered series while the sodic end

member is an ordered albite, suggests that the 400 nm emission may not be (at least strongly) related to the degree of order of feldspar. It may, however, be recalled comparing Figures 6.1 and 6.3 that the emission from the sodic end member differs in detail from that of high potassic feldspars. Pasternack and Levy (1978) reported that the thermally induced disorder in albites changed the 280 and 560 nm band parameters resulting in peak broadening and shift to higher wavelengths while the 400 nm band parameters remained unchanged. Pasternack did not notice a monotonic change in the absolute intensity of the 400 nm band with increasing disorder. A systematic increase in the ratios of integrated intensities of 400 and 560 nm bands was, however, observed.

Summarising the thermoluminescence study of lunar samples, McKeever (1985) points out the association of 420-440 nm with potassic feldspar phase. A possible correlation with the presence of phosphate points towards a promising direction for further investigation. Phosphorus as an impurity tends to associate with the end members in feldspars (Smith, 1974). Mason et al. 1982 (see also Mason, 1982) noticed higher P content in lamellae of microcline perthites in K-feldspars.

A suggestion by Marfunin (1979) that the 400 nm emission band may be related to Eu^{2+} defect in feldspars has been discussed in Chapter 7 on thermoluminescence in plagioclase feldspars.

6.2.3.3 The 450-470 nm Emission

An emission band associated with $Al\text{-}O^{-}\text{-}Al$ defect has been proposed to be responsible for emission in this wavelength region (Speit and Lehmann, 1982; Marfunin, 1979). According to a review by Lehmann (1984) it is a commonly known radiation defect in feldspars. As is clear

from Figures 6.1-6.3, both albite and high potassic feldspar groups show some emission in this region, particularly for the lower temperature signal. The reason that the 470 nm emission is not seen much above 220C perhaps relates to the fact that the same band acts as a trapping centre in this temperature region. It has surely been lost by thermal decay for natural TL.

6.2.3.4 The UV and Infrared Emission

Emission bands at 280 nm and 750 nm have been reported for high sodic feldspars (see e.g. Ioffe and Yanchevskaya, 1968; Pasternack and Levy, 1978). Their absence from other types of feldspars may only be due to the lack of experimental observation. These bands were not seen on our equipment due to its limited spectral response and details can be seen in the references cited above.

6.3 INTERMEDIATE POTASSIC FELDSPARS

The nine alkali feldspar samples with intermediate potassic composition vary in their TL signal when seen in detail, yet several common and interesting features throw light on their overall behaviour. All of them differ significantly as a group from both the end members. For convenience in data handling and explanation, the results are presented in two groups made on a compositional basis.

6.3.1 Alkali Feldspars with 50-80% Or Content

Six alkali feldspars in the present study belong to this group and representative emission spectra for NTL and ATL of sample #9, a high temperature sanidine from Mount Soma, Italy, with about 70% Or are shown

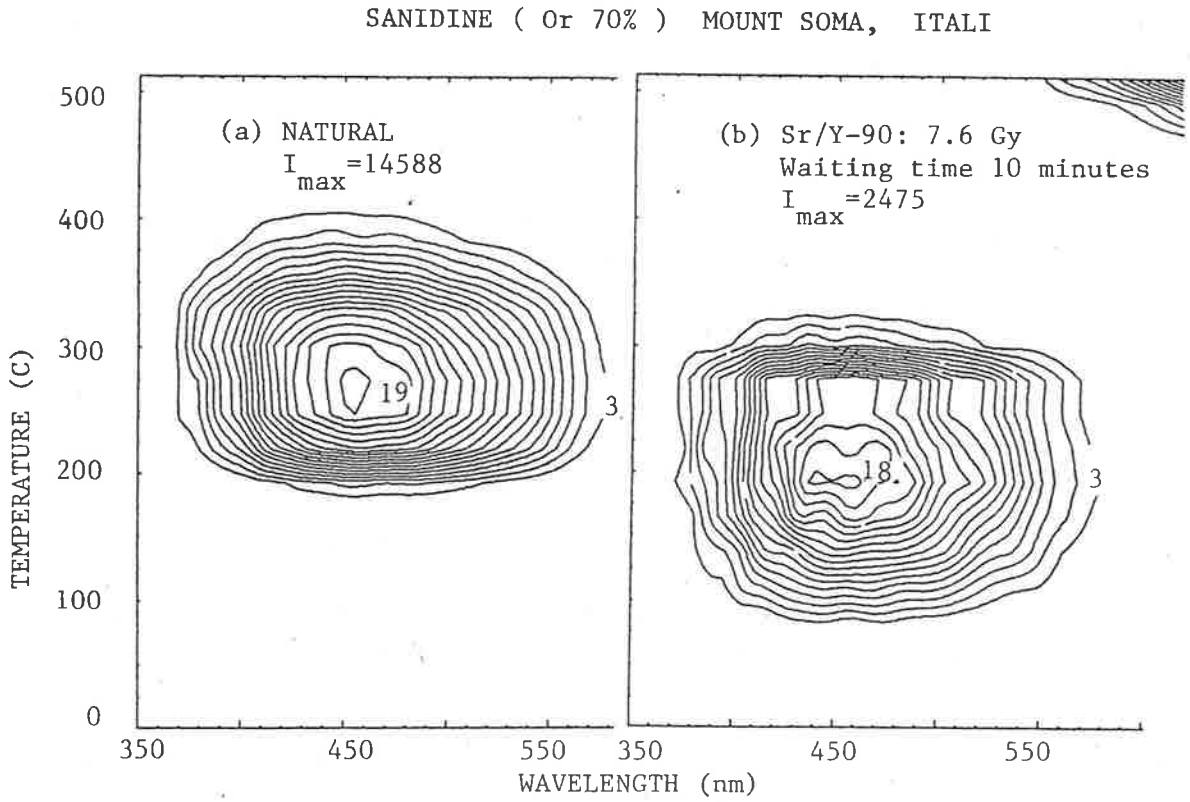

FIGURE 6.4: The broad band themoluminescence emission spectrum for a sanidine from Mount Soma, Itali. The figure represents the general TL behaviour of Na-K feldspars in 50-80% Or region.

in Figure 6.4 (a,b). The emission spectrum appears to be broad band with FWHM from about 400 nm to about 550 nm peaking in the 430-450 nm region. It is likely to be due to the composite effect of various emission bands already described in connection with the end members.

The major difference is noticed for the trapping centre characteristics. The 345C peak seen in all high potassic feldspars, and the 300C peak in high sodium feldspar are either absent or appear very little in intermediate composition samples. Even for the low temperature signal, the samples show TL sensitivity between one to two orders of magnitude less than that of the end members. The previous history of exposure to natural radiation and sunlight is not known, yet the poor NTL in most samples may well be attributed to the lack of any substantial TL peaks above 250C or so. Unlike most end members, the intermediate composition feldspars tend not to show the TL signal extending above 500C.

6.3.2. Feldspars with Mixed TL Features

As has been described in Chapter 5, feldspars crystallized at lower temperatures or through slow cooling possess mixed phases and may, therefore, exhibit mixed composition dependant thermoluminescence behaviour.

Such character has been readily shown by sample #11 from Wisconsin, U.S.A., identified as a moonstone with fine lamellar intergrowths of end member phases. Natural thermoluminescence of this member has been plotted in Figure 6.5, which can be compared with Figures 6.1a, 6.3a and 6.4a showing the NTL spectrum for a high potassic, high sodic and intermediate composition feldspars respectively.

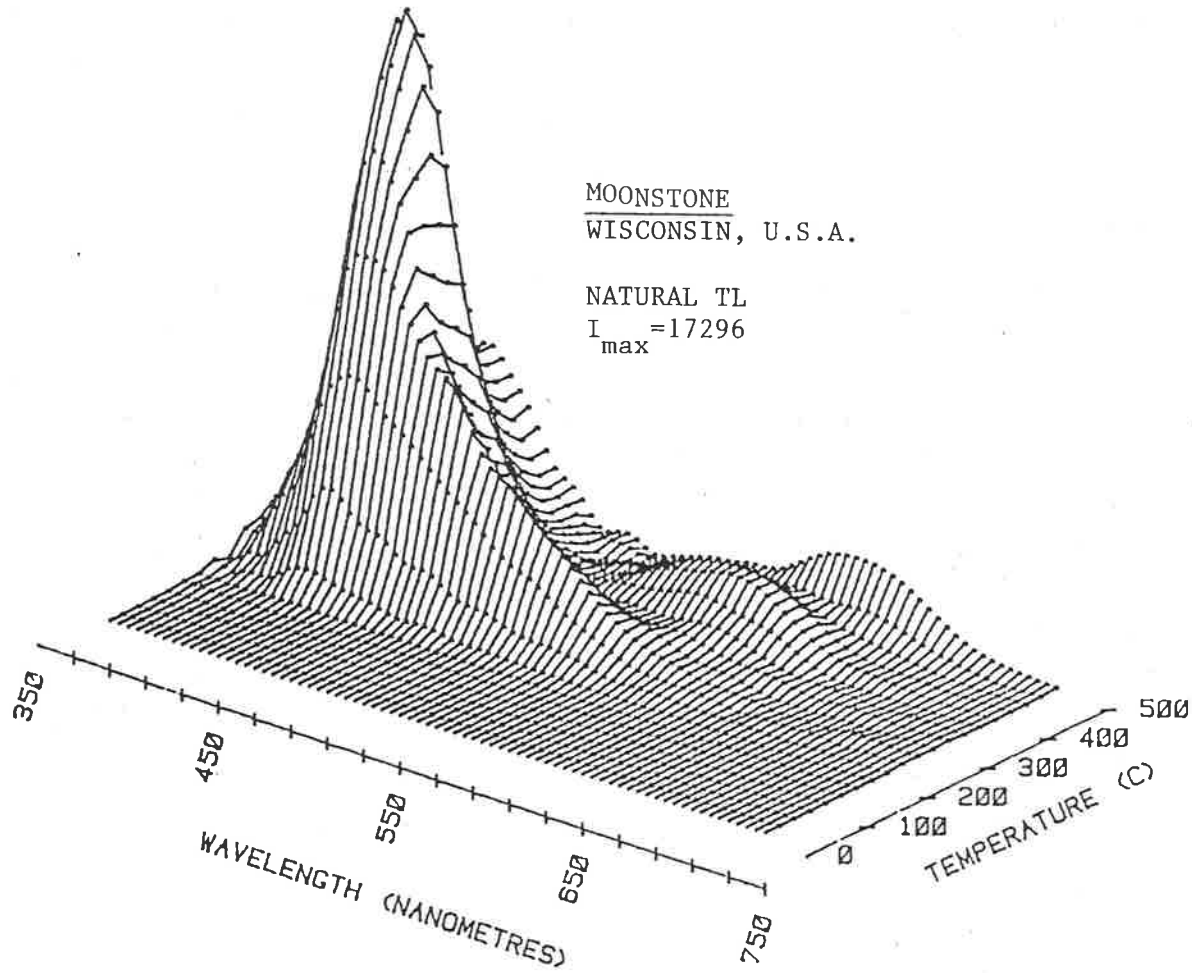

FIGURE 6.5: Natural TL emission from a moonstone. Mixed thermoluminescence emission characteristics of the end members and intermediate composition Na-K feldspars are evident from the figure.

It is interesting to note that the other two samples, #8 and #10, showing mixed spectral behaviour to a lesser degree, have been optically identified as high temperature orthoclase and sanidine respectively. Some discussion on this subject will continue in a following section.

6.3.3 Alkali Feldspars with Low Or Content (10-30%)

The three low potassic feldspars include two triclinic anorthoclase samples, with about 27% Or originating from the same main site of Mount Anakie in Victoria (Australia), and an ordered feldspar with about 11% Or, labelled as an albite from the Sitting Bull locality. The Or content of the anorthoclase samples indicates their vicinity to the line of change of structural symmetry as discussed in Chapter Five.

It can be seen through the group representative Figure 6.6 for one of the anorthoclase samples that, despite the change in symmetry, the general features of thermoluminescence emission spectrum of feldspars with low Or content do not differ from those of the other intermediate composition feldspars.

6.3.4 Some Discussion

Poor high temperature signal in intermediate composition feldspars (Figure 6.7) indicates the absence of some trapping and/or emission centres which are exclusive to the end members. The exact nature of these centres could not be identified. One such trapping centre could possibly be Ti^{3+} with its characteristic temperature peak in the 280-300C region (Marfunin, 1979). A peak in this region is readily seen for the high sodic end member but also suggested for the high potassic

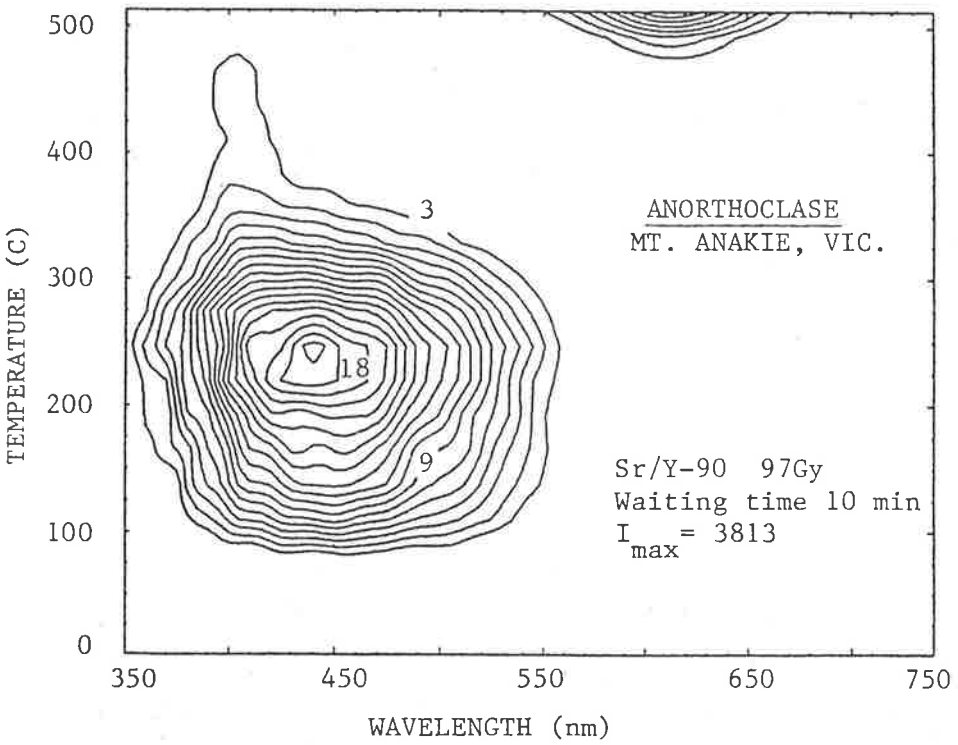

FIGURE 6.6: Laboratory radiation induced thermoluminescence in an anorthoclase from Mount Anakie, Victoria Australia. The TL features represent the alkali feldspars in 10-30% Or region.

feldspars. Ti^{3+} impurity correlation with the end members is not quite established. A review on some trace and minor elements by Smith (1983) suggests that the Ti content in feldspars partly depends upon the Ti content of the parent magma. Smith also points out the error limitations of Ti estimates using electron probe analysis technique. One positive report from the ion probe analysis of lunar feldspars (Steele et al., 1980) shows only a weak correlation between Na and Ti.

It is interesting to note that the occasional higher TL sensitivity in the intermediate composition region (Figure 6.7) relates to the degree of mixed TL spectral character shown by a few samples. As mentioned earlier, the mixed behaviour most probably indicates the presence of the end member phase, but the fact that the mixed phase character is also revealed by feldspar samples which are classified as sanidine and orthoclase on the basis of their cell structure analysis using X-ray diffraction technique, requires explanation.

Relatively recent studies on perthitic intergrowths in potassic feldspars show that the XRD or optical behaviour of a potassic feldspar may not be a true indicator of the degree of ordering in the feldspar (see e.g. Eggleton and Buseck, 1980; Ribbe, 1983c). The ordering of feldspars is primarily related to the migration of Al to specific positions in the cell structure which takes place in an attempt to lower the free energy by balancing the local electrostatic charge distribution. In monoclinic high temperature potassic feldspars, which are formed if the rock is quenched near 1000C or so, the Al migration may take place with slow annealing at ambient temperatures over geological times. The ordered structure originates as distorted nucleations within the monoclinic matrix while the energy release accumulates as strain in

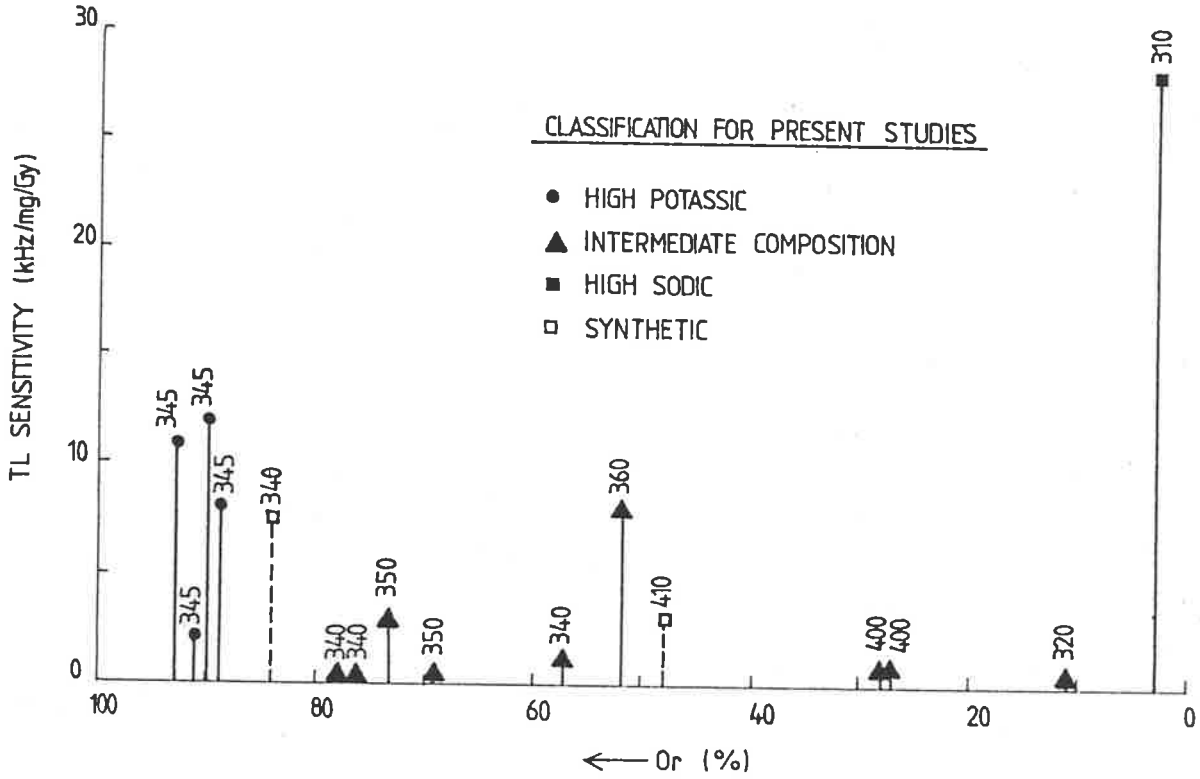

FIGURE 6.7: The TL sensitivity of Na-K feldspars used in the present study. The 2D TL maximmum in the 300-450C region has been indicated by numbers beside the points for individual samples.

the lattice structure. Ribbe (1983c) points out that the distorted structure, which is in fact a highly ordered triclinic intergrowth, cannot be recognised till it grows to a size of 50-100 nm for coherent diffraction technique or 500-1000 nm for optical observation.

On the basis of their study of the development of such triclinic domains within the basic monoclinic topology of the original feldspar structure by using high resolution transmission electron microscope and conventional X-ray techniques, Eggleton and Buseck (1980) suggest that the discrete triclinic reflections start appearing in the X-ray patterns (indicating the presence of low microcline) only when, depending upon the situation of the feldspar, a balance point between the strain energy and the energy released is passed. Ribbe (1983c) points out that a K-feldspar may be severely strained thereby hiding its true degree of order and also suggests the nucleation mechanism (not described here in detail) as the possible cause for the existence of low ordered albite in monoclinic orthoclases and in some partly ordered intermediate microclines. The lamellar nucleation in Ab- and Or-rich phases during alkali feldspar exsolution has also been reported in relation with strains in feldspars (Yund, 1984).

Whereas these references are quoted to suggest an explanation for the TL behaviour of only a few samples, it may be emphasized that the difference in sensitivity can make thermoluminescence a simple but powerful tool for estimating levels of mixed phases in potassic feldspars which is a field of growing interest from various academic and applied aspects of feldspar mineralogy (the interested reader is referred to Ribbe, 1983a and Brown, 1984).

6.4 THERMOLUMINESCENCE IN SYNTHETIC FELDSPARS

Most synthetic feldspars are prepared by homogenising the constituents at a high temperature (Deer et al., 1982). The structural state of potassic feldspars is, however, strongly controlled by the subsequent cooling conditions as well, and these conditons being unknown, the synthetic feldspars are being handled in the present separate section.

Both of the synthetic feldspars used in the present study showed mixed TL behaviour which was more prominent in sample #12 (Feldspar 99a, Or ≈ 41%). As can be seen from Figure 6.8 the emission band characteristics as described in the case of other mixed phase feldspars are clearly displayed by this sample as well.

Synthetic feldspar sample #5 (Feldspar 70a, Or ≈ 84%) dominantly showed the intermediate composition broadband structure, yet the 400 nm high temperature extension could also be noticed.

Diffusion in potassic feldspars for later formation of two phase structure has been studied by several mineralogists, an attractive aspect of the study being that the natural phenomena can be duplicated in laboratory time (Ribbe, 1983d). Yund (1983a, 1984) provides a review on the microstructure intergrowths in potassic feldspars and suggests that the two-phase texture can be seen after a couple of hours of heating above 500C. The present observations strongly suggest thermoluminescence as a tool for estimating the extent of such intergrowths.

It may be recalled from Chapter Five, that both the synthetic feldspars showed silicon content higher by about 10% than what is expected by an ideal formula for feldspars. Synthetic feldspars with high silicon content have been reported by several authors. These

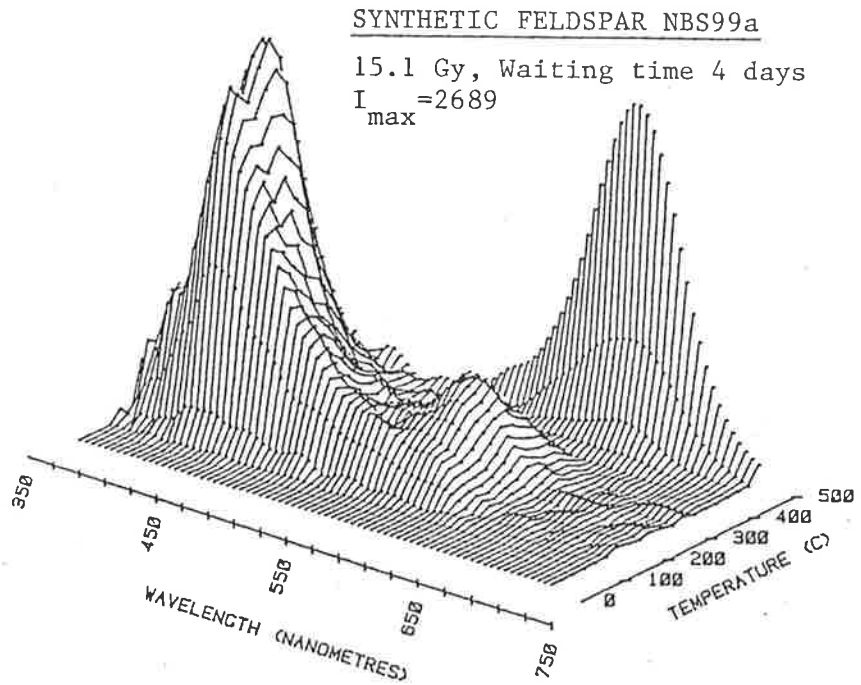

FIGURE 6.8: Thermoluminescence emission from a synthetic feldspar sample BNS99a. The spectrum was recorded four days after 15.1 Gy of beta irradiation. Natural thermoluminescence was earlier drained.

feldspars are also noted for later exsolution of excessive silicon as quartz (see e.g. Smith 1974, 1983).

The presence of a quartz-like phase was noticed in these samples by the indication of a characteristic peak near 110C. As shown in Figure 6.9, this peak did not sensitise with repeated irradiation and glow, indicating perhaps the later low temperature exsolution of quartz, rather than some separate SiO_2 fusion from the initial constitutions. (For temperature sensitisation of 110C peak in quartz, see Section 8.2, Chapter Eight.)

6.5 2D-TL INTENSITY IN K-Na FELDSPARS: COMPARISON OF OBSERVATIONS

The 2D TL observations as summarised in this chapter can be partly compared with the scattered reports by other authors. Nishita et al. (1974) reported on the natural thermoluminescence of several minerals including an albite, perthite, microcline, anorthoclase and a perthite intergrowth. The NTL peak intensity was seen to decrease roughly in the ratio of 30:8:5:4:2 respectively. Glow peaks in the two perthites were seen at about 250C followed by another peak at 340C. The albite showed an overlapping signal with peaks near 200, 320 and 410C. The broad band nature of the signal makes it hard to locate the peak temperatures in other samples but anorthoclase, microcline, albite and perthite showed a high temperature signal extending above the 500C limit. These observations are generally in agreement with the present ones.

The present observations are also in conformity with Tarashchan (1978) that thermoluminescence is commonly more intense in (high temperature crystallized) orthoclases. Marfunin (1979) and Sankaran et al. (1983) also maintain the same view.

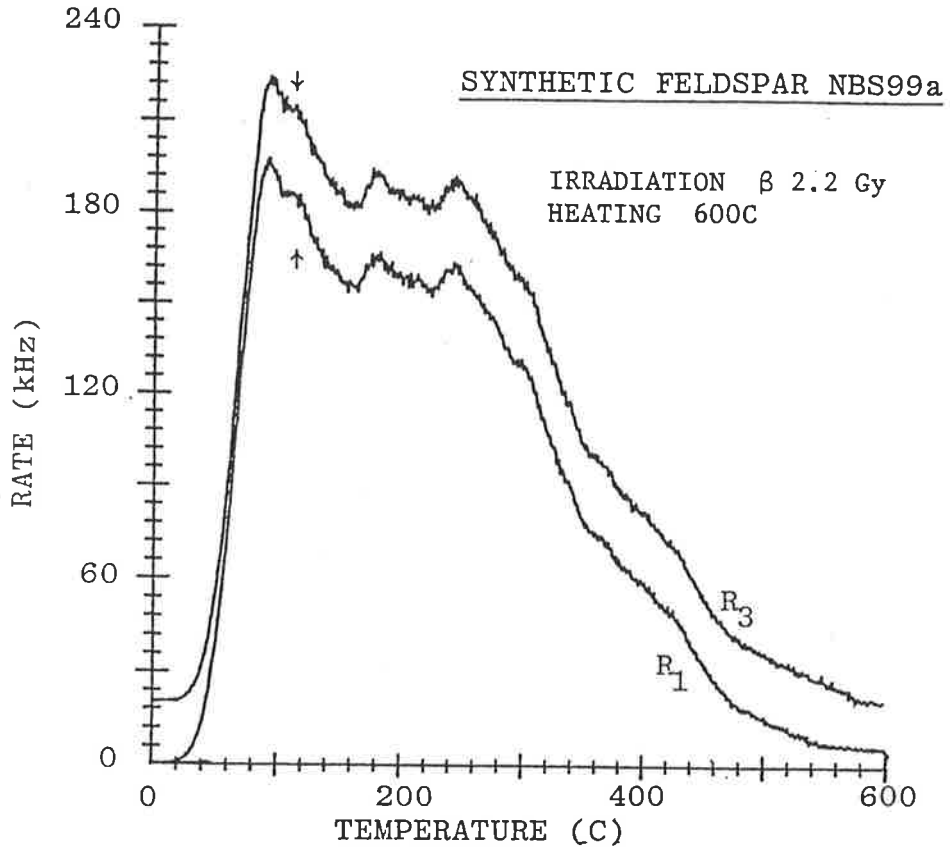

FIGURE 6.9: Glow curves for synthetic feldspar NBS99a as recorded on the 2D TL equipment. Note a peak near 110C which does not sensitise with repeated irradiation and glow. The curves represent the first (R_1) and the third (R_3) irradiation (2.2 Gy) and heating (600C) cycle after draining the natural TL.

Reports by Platanov et al. (1971) and Scherbakov et al. (1972) seem to contradict the findings of Tarashchan, Marfunin, Sankaran et al. and the author. They propose a strong inverse relationship between the triclinicity of the potassic feldspar and its thermoluminescence. [Normalized between unity and zero for the states of extreme order (like maximum microcline) and disorder (like high temperature sanidine) respectively, the triclinicity is an indicator of the structural state of potassic feldspar (Smith 1974).] Like several other workers, Platanov et al. conclude that Al-$\bar{O}$-Al centres play a major role in thermoluminescence. The original work is in the Russian language and citation is based on the translated abstracts. At the time of writing, a full translation is not available and this makes comparisons somewhat harder.

Correlation between thermally induced disorder in albites and their thermoluminescence emission spectra has been studied by Pasternack (1978). His results show a moderate (but not strictly monotonic) decrease in TL sensitivity for 280 nm and 560 nm emission bands which is partly compensated for by the 400 nm band intensity change in the opposite direction. The ultimate 2D TL behaviour may, therefore, depend upon the spectral response of the equipment as well.

The thermoluminescence reports by various authors cited in this chapter most probably take the structural information from the X-ray diffraction technique. Recently recognised limitations of this method have already been pointed out. The usefulness of the XRD analysis is not denied, yet it is likely that some thermoluminescence characteristics may be better related to the feldspar textures revealed through transmision electron microscopy.

The present study leads to a compositional rather than a structural

correlation. The thermoluminescence signal apears to be higher for both the potassic and sodic end members and drops by one to two orders of magnitude for the intermediate composition alkali feldspars. Anomalies exist but they most probably represent the presence of high potassic and sodic intergrowths. Hence, as far as the present study suggests, the encouraging remarks by Martin Aitken reproduced at the beginning of this chapter, fit the feldspars localized at the extreme ends of the Na-K line. Another promising possibility of dating plagioclases through high temperature peaks is discussed in the following chapter.

The TL characteristics of the feldspar samples reported here could not be convincingly correlated with the observations like colour, place of origin and impurity content as obtained by XRF. But it is worth pointing out here that, as far as the TL behaviour is concerned, the impurity estimates using XRF analysis may well be fairly non-representative. The above statement, therefore, does not deny or prove the role of an impurity or structural defect controlling the TL behaviour. The same argument, of course, applies to the plagioclase feldspars discussed in Chapter Seven.

CHAPTER SEVEN

THERMOLUMINESCENCE IN PLAGIOCLASE FELDSPARS

"...if a lump, of the size of a small bean... be laid upon the heater, the light proceeds gradually upwards from the part in contact with the heater till the whole mass is thoroughly illuminated, if the same piece be heated a second time, it is much less luminous...."

Thomas Wedgwood (1792)
from a report on the thermoluminescence
in red feldspar from Saxony.

7.1 INTRODUCTION

The first two sections of this chapter deal with the thermoluminescence sensitivity and the emission bands as seen in plagioclase feldspars. The observations are based on twelve different samples of varying composition and localities, and the results concentrate upon the general features rather than the individual sample details, except in the case of a labradorite from Chain des Puys region, which has been described in the last section for its mixed thermoluminescence behaviour. Anomalous fading as seen in some of the samples in the present studies is also reported. Some suggestions for further extension of the work are included at appropriate places during the discussion of results. In so far as most of the emission bands have been partly discussed in connection with the Na-K feldspars as well, this chapter may be regarded as a continuation of what has earlier been described in Chapter Six.

7.2 THE TL INTENSITY

The most interesting feature of plagioclase thermoluminescence is

its inverse correlation with the calcic content (Figure 7.1). Similar behaviour was suggested by McDougall, 1968, and Nishita et al., 1974. These results indicate that on the plagioclase axis in feldspars, the TL sensitivity is strongly associated with either a lattice defect or some impurity affiliated to the composition.

For a given composition bracket a large spread in the TL sensitivity of the samples can be noticed which can only partly be explained due to any (up to about 5%) error in the Ab:An ratio estimates.

7.3 THE EMISSION SPECTRA

The salient features of the emission spectrum of albites have been discussed in Section 6.2 of the previous chapter. The spectra for some other representative samples from along the plagioclase axis are shown in Figure 7.2 (a-c). Some interesting characteristics are discussed in the following sections.

7.3.1 The 550 nm Emission Band

The relative height of the 550 nm emission band in the emission spectra appears to be decreasing on increasing anorthite content till, for highest calcic feldspars it reduces only to not more than a shoulder to the other lower wavelength emission bands. This emission band is preferentially filled at the lower temperatures. At the same time the TL sensitivity of the 400 nm peak decreases dramatically with increasing An content.

It was mentioned in the previous chapter that the 550 nm emission band may be associated with a radiation induced hole centre on oxygen with Si as one neighbour and another unidentified neighbour which has to

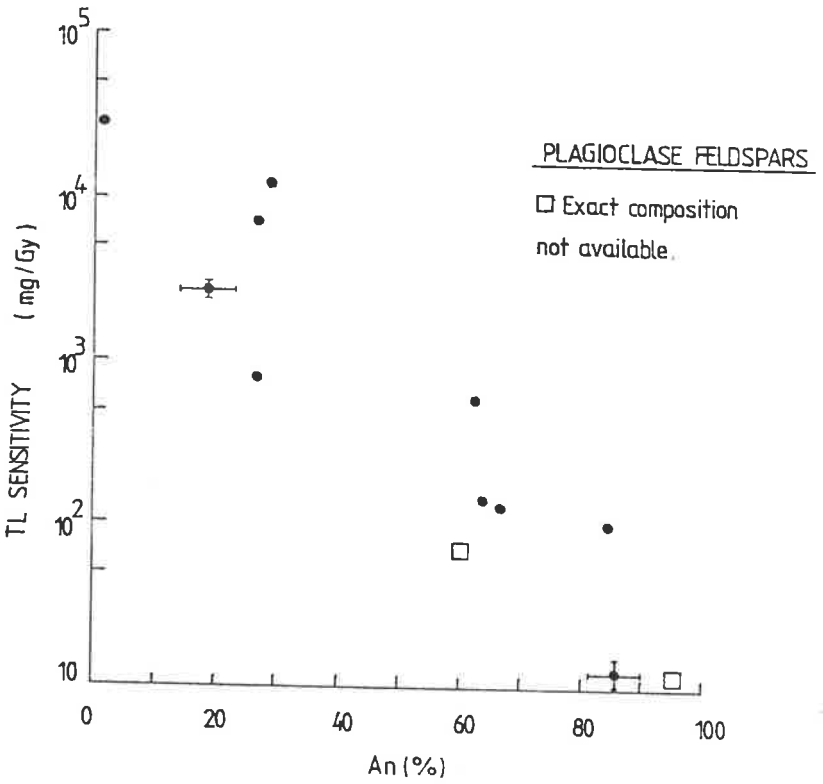

FIGURE 7.1: TL sensitivity vs. anorthite content in plagioclase feldspar samples used in the present study. Note the logarithimic nature of the sensitivity scale. For the cases where the exact composition was not known, the points have been plotted against the average value of the composition bracket.

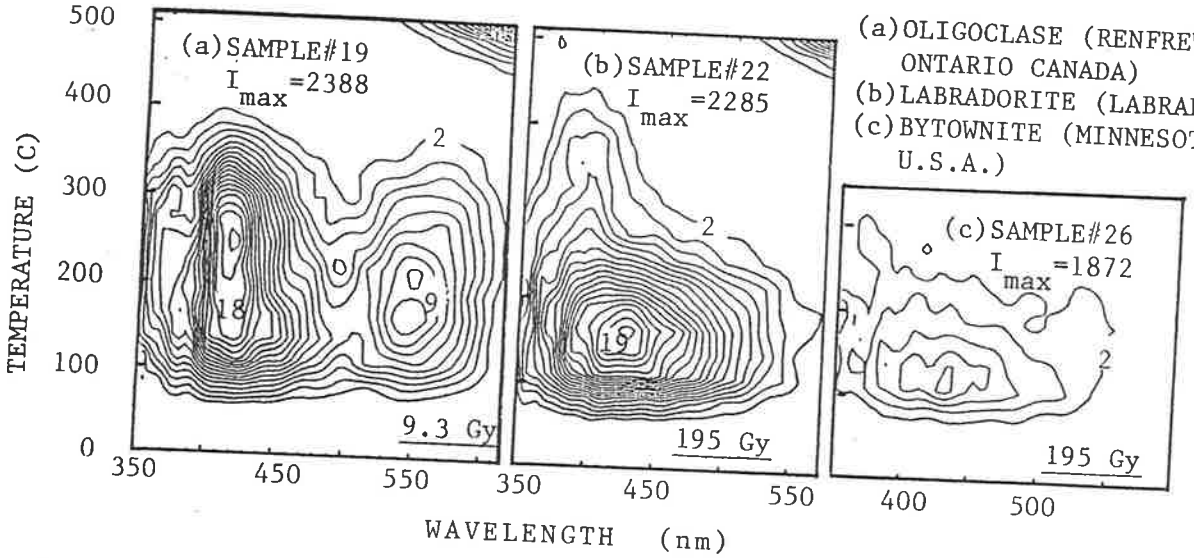

FIGURE7.2: Laboratory radiation induced thermoluminescence emission spectra in plagioclase feldspar of varying composition. The main features represent the overall behaviuor of the high sodic and high calcic feldspars. I_{max} corresponds the intensity for contour number 20.

be a small divalent atom at the 'T' sites in the feldspar structure. The alternate possibility of its association with an electron trap on Mn as an impurity is further discussed in this section.

Marfunin (1979) with reference to Tarashchan (1978) attributes the TL emission near 580 nm to Mn^{2+}. McKeever (1985) referring to the work of Geake et al. (1977), Telfer and Wakter (1978) and other workers on cathodoluminescence of terrestrial and lunar samples suggests the association of 560 nm peak with Mn^{2+} replacing the Ca^{2+} in the plagioclase feldspars. Huntley (private communication) also relates the 560 nm emission to Mn. Neither of these references attributes this defect to radiation.

The reason for the higher relative intensity of the 560 nm band in high sodic feldspars is not understood. Mn as an impurity in feldspar against Or and An content has been discussed by Smith (1974). Reviewing the reports by several authors, he suggests a correlation with Ca in the feldspar and that Mn substitution is expected more in a plagiolcase feldspar than a potassic feldspar type structure. Smith also stresses the inaccuracy of the available data and the need for further systematic studies (1974, 1983).

The less sensitive high calcic feldspars have been studied at a radiation dose of about 200 Gy, as compared to about 2Gy for the albite sample. Any radiation-induced TL emission centres should therefore have shown up with relatively higher intensity in high calcic feldspars. Neither of the above mentioned expected trends tallies with the experimental observations. It is worth mentioning that the colour of non-radiation induced 'spurious TL' has also been reported in this wavelength region (Fleming, 1979).

7.3.2 The 400 nm Emission Band

The 400 nm emission band seen in high sodic plagioclases appears to be broader than the one in high potassic feldspars. Figure 6.3c for an albite and Figure 7.3 for an oligoclase indicate that the emission in fact comprises more than one overlapping band.

Eu^{2+} can be one of the possible emission centres (Marfunin, 1979). Impurity analysis of a variety of feldspars from different localities has been given by Smith (1974) indicating a general (though not very strong) trend of higher Eu content with increasing sodium over calcium. Smith (1983) suggests the Eu intake as an impurity is also strongly determined by the initial Eu in the parent magma and by the reducing environmental conditons (oxygen fugacity). If associated with the Eu centre, the 400 nm emission band should show higher in lunar feldspar samples with anomalously higher Eu impurity. Observations by workers like Lalou et al. (1972) and Durrani et al (1973) show that the main emission is in the 420--440 nm region, with another emission peak near 560 nm. McKeever (1985) also notes the dominant blue peak in the thermoluminescence curve, but also points out that the detailed mineral analysis indicates the association of the blue emission with a potassium feldspar phase.

7.3.3 The Broad Band Emission of High Calcic Feldspars

The seven high calcic feldspars included in the present study showed broad band spectra with peak in the 430-470 nm region and extending on both sides with a FWHM of up to 150 nm. In each case the spectra comprised several overlapping emission bands, and particularly for some labradorites, a small 400 nm tail extending to high temperatures could

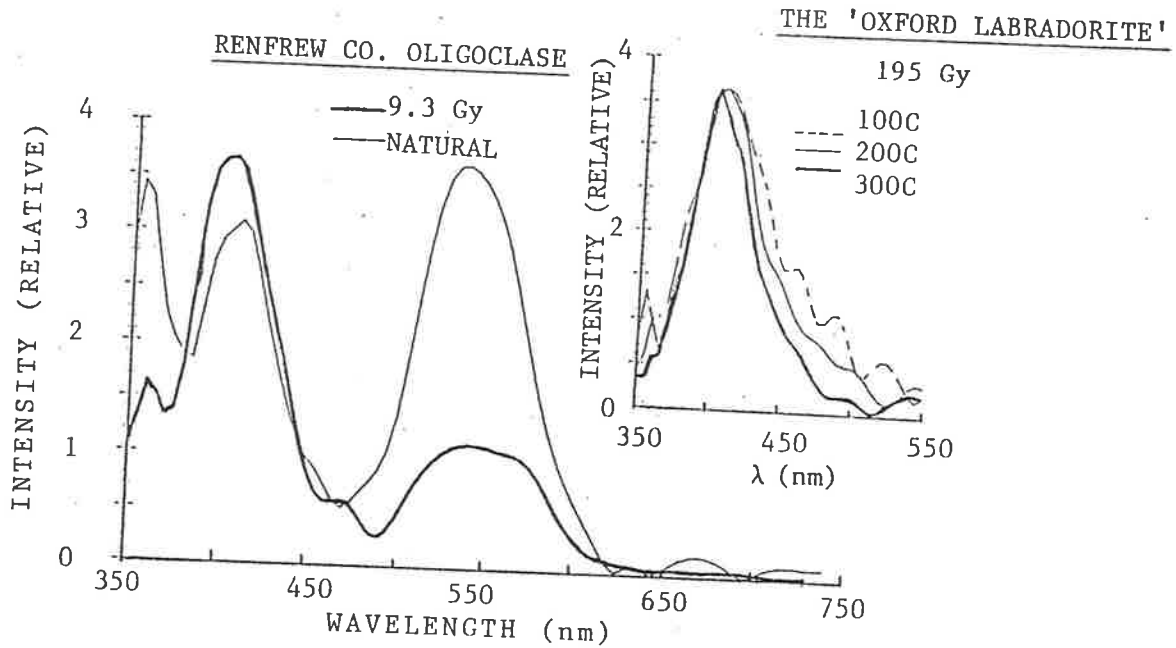

FIGURE 7.3: The thermoluminescence emission spectra at 300C for the oligoclase sample shown in Figure 7.2. These results normalized for the peak values, have been replotted to emphasise that (a) the 400nm band comprises more than one emission centre.and (b) the relative intensity of 550nm band appears to be different in natural and lab radiation induced (also see Chapter Six for discussion on 550nm band). The insert is the emission spectrum for labradorite sample #24 for induced radiation dose of 195Gy. A labradorite from the same origin was used by Wintle (1977) and Visocekas (1985) to study the anomalous fading.

also be observed. The TL spectral character of high calcic feldspars, therefore, resembles that of intermediate potassic feldspars and several explanations given in Section 6.3 (Chapter Six) may apply to these samples as well.

It can also be recalled from Section 6.2.3.3 of the previous chapter that the Al-O-Al defect emission centre in the 450-470 nm region may also take part in thermoluminescence as a trapping centre responsible for peak near 220C. Absence of appreciable numbers of emission centres may, therefore, be a possible explanation of the diminishing high temperature peaks in the high calcic feldspars (Figure 7.4).

7.4 THE ANOMALOUS FADING

As mentioned earlier in Chapter Five, anomalous fading is the name given to the loss of thermoluminescence signal, which cannot be predicted by the kinetic models. Anomalous fading is one of the widely mentioned TL characteristics of feldspars and perhaps introduces the most significant set-back in their acceptance as a mineral for routine thermoluminescence dating. Since its observation in lunar samples (Garlick and Robinson, 1972) and basaltic lavas of granitic origin (Wintle, 1973) several attempts have been made for the better understanding of the phenomenon.

During a systematic study Wintle (1977) reported from 10-40% fading in TL signal above 300C for feldspars like a sanidine, labradorite, andesine and bytownite. Mejdahl (1985) reported from zero to 50% fading in plagioclase feldspar extracts from archaeological samples. The results for potassium feldspars fall into two groups; less than 10% and between 20 and 35% fading. Guerin and Valladas (1980) reported that the

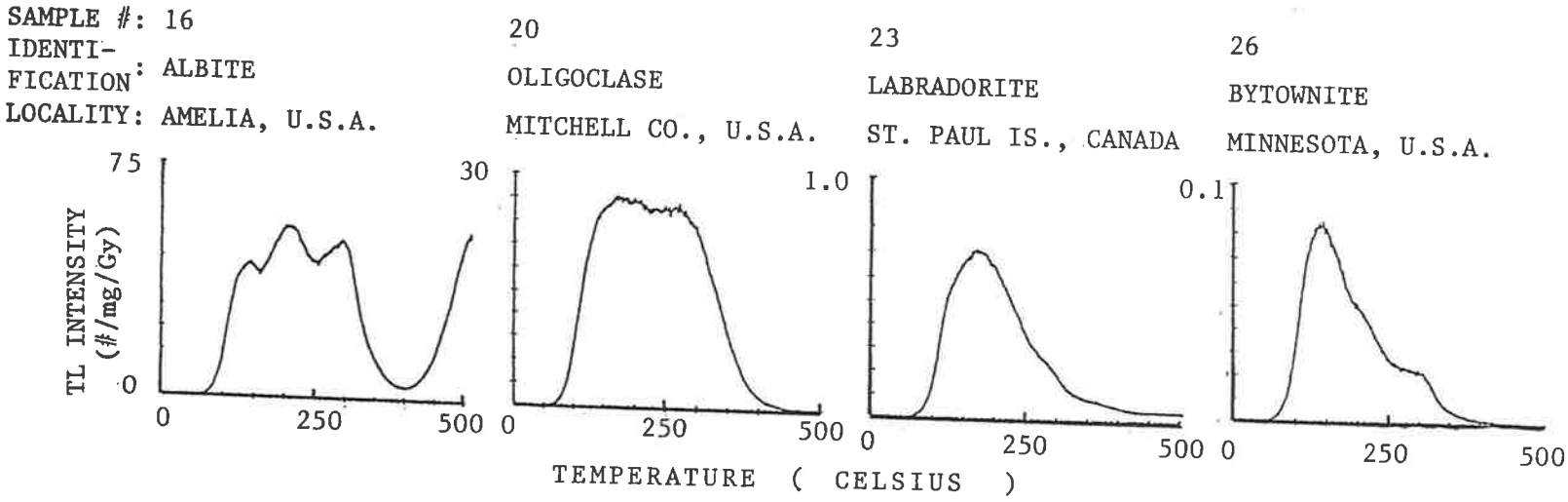

FIGURE 7.4: Glow curves recorded on the 2D TL equipment for an albite, oligoclase, labradorite and bytownite. In addition to the overall intensity, the relative heights of high temperature peaks also decrease for high calcic feldspars.

high temperature peaks (above 500C) do not significantly fade and can be used to obtain reasonable dates. Akber and Prescott (1985) observed a trend in the Ca content of the Plagioclases and anomalous fading. Hasan et al. (1986) suggested stronger fading in ordered feldspars compared to the disordered feldspars.

The most popular explanation of anomalous fading is the signal loss due to quantum mechanical tunnelling as the wave function of the trapped charge and the luminescence centre overlap (Visocekas et al., 1976; Visocekas 1979, 1985).

The model successfully explains the logarithmic time dependence of anomalous fading in plagioclase feldspars. In a recent study of anomalous fading in a labradorite sample, Visocekas observed that the anomalous fading is accompanied by the emission in the red-infra-red region between 630 and 890 nm range as the lower cut-off of the filter and the upper limit of the photomultiplier spectral response used during the experiment. The actual TL glow curve emission was, however, broad band in the UV-blue green region. Using an Sr/Y-90 beta radiation source Visocekas observed 14% and 25% fading per decade of time after a radiation dose of 900 Gy and (a saturation dose of) 24,000 Gy respectively.

All of the five high calcic feldspars tested for anomalous fading over about two weeks in the present studies showed anomalous fading to a varying degree. The results indicate that the anomalous TL loss is fairly independent of the glow peak temperature. Also, with the existing results of the emission spectra, it is hard to say that the fading is related to the preferential quenching of the signal from a specific emission band in the high calcic phase.

The labradorite sample #24 tested in the present study is the same as used by Visocekas (1985) and earlier by Wintle (1977). Our findings confirm the broad band spectrum extending from UV-blue to green region (Figure 7.3, insert). The red to infra-red emission could not, of course, be seen with the present equipment.

Hasan et al. (1986) argued that order/disorder dependent re-orientation of bonds of Mn as an impurity in plagioclase feldspars may lead to extensive fading in the ordered state. It is interesting to note that the Mn substitution in Ca sites in $CaCO_3$:Mn does produce TL emission in the red region (Medlin, 1968). Geake et al. (1971) mention that the higher field strength experienced by Mn in a feldspar matrix compared to a $CaCO_3$ matrix will move the emission to the blue-green region.

Marfunin (1979) related the emission in the red region to Fe^{3+} as an impurity in feldspars. A broad correlation does exist in the anomalous fading and the iron content found through XRF analysis of the present samples (Table 7.1). Iron is preferentially taken by high calcic feldspar, though its absolute content is determined by the iron in the parent magma (Smith, 1983). The reducing environments result in the higher iron intake as Fe^{2+} against Fe^{3+} in lunar feldspars compared to the terrestrial ones. Further investigations on both Fe^{3+} and Mn^{2+} content of feldspars and their correlation with the anomalous fading is therefore suggested.

No investigations of the correlation between the optical properties of the samples and anomalous fading were carried out as a part of the present studies. The albite sample #16 from Amelia is essentially an ordered sample and showed little anomalous fading.

Radiation dose dependant anomalous fading rates (Visocekas, 1985)

TABLE 7.1

Sample #	An%	Locality	Fe Content	Anomalous Fading (%)
22	64	Labrador 0.7	20	
23	67	St. Paul Island, Canada	1.2	32
24	-	Chaine Des Puys, France	-	50
21	62	Chaine Des Puys, France	3.26	58

Anomalous fading in the labradorites from different places of origin. Uncertainties in the values in columns 2 and 5 are between 2-5%. The anomalous fading in column 5 refers to the percentage of the total signal lost during 10 days of storage at room temperature. The loss for signal has been estimated around 300C.

suggest the involvement of radiation induced defects in the process.

7.5 A SAMPLE WITH MIXED TL SIGNAL

Sample #21, compositionally identified as a labradorite, showed mixed thermoluminescence behaviour. In addition to the characteristic high calcic broad band emission, a substantial component of high sodic plagioclase (and/or high potassic feldspar) emission can be recognised as the 400 nm signal extending through to the high temperature peak above 500C (Figure 7.5). This sample originated from the Chaine des Puys region in France (R. Visocekas, private communication) and the XRF analysis shows significant potassium content (see Table 5.1, Chapter Five).

Consistent with the results quoted earlier, the fading at high temperature appears to be relatively less significant (Figure 7.6). It is interesting to note that a plagioclase sample from the same region was used by Guérin and Valladas (1980) to demonstrate the possibility of dating plagioclase feldspars using the high temperature thermoluminescence signal.

The sample has high iron content and, among the labradorites used in the present studies, showed the maximum fading rate of temperature peaks in 300C region (Table 7.1).

The marked sensitivity difference can make thermoluminescence a very effective but simple tool in recognising the presence of small amounts of low sodic phases in high calcic feldspars. The two phase textures do exist in plagioclase feldspars and owing to their submicroscopic nature, generally offer difficulties in recognition through bulk analysis (Ribbe, 1983d).

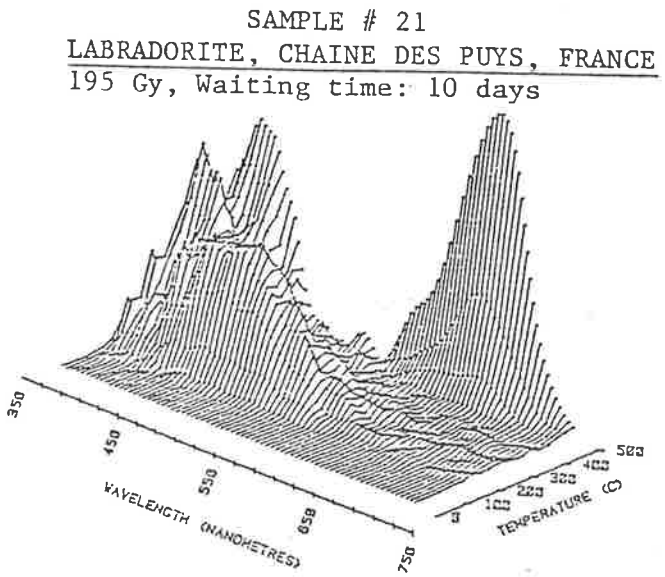

FIGURE 7.5: Thermoluminescence emission spectrum for sample #21, labelled as labradorite, shows a significant component similar to a high sodic and/or high potassic phase (see text).

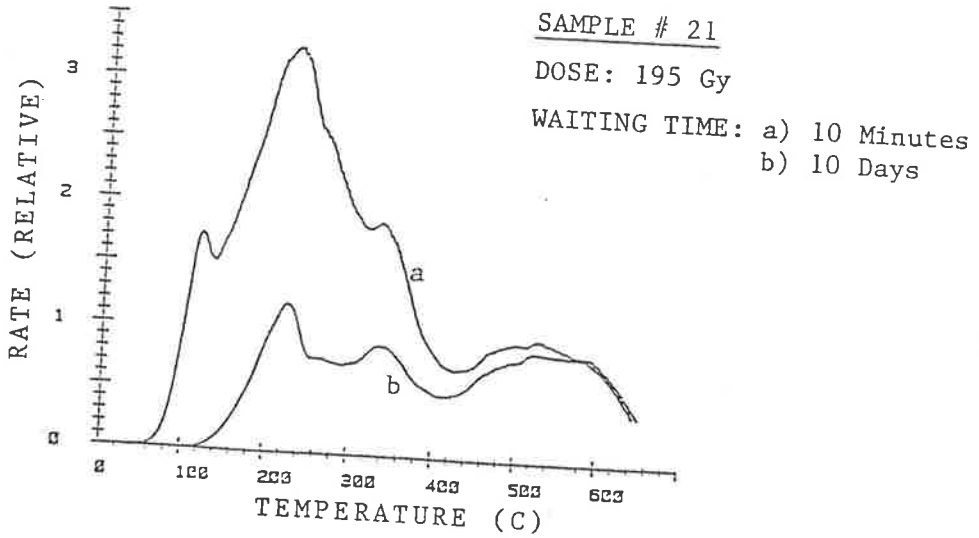

FIGURE 7.6: The 2D TL glow curves for the sample mentioned in Figure 7.5 . The high temperature peak shows lesser anomalous fading.

CHAPTER EIGHT

SOME OTHER APPLICATIONS

8.1 INTRODUCTION

In addition to its major application to the study of thermoluminescence in feldspars, the equipment was also used for other related problems. Two of these applications, relating to 110C TL peak sensitization in quartz and to fine grain dating of the Pacific Island pottery, are discussed in the following two sections. The last section describes thermoluminescence in a barium feldspar from Broken Hill, Australia.

8.2 THE 110C EMISSION FROM HIGH FIRED QUARTZ

The pre-dose effect upon the 110C peak in high fired quartz as earlier described by Fleming (1973) may be regarded as an increment in TL sensitivity in proportion to the induced radiation dose upon subsequent heating above 500C. The sensitivity estimates may, therefore, be used as an index to measure the radiation dose as received by a sample in its natural environment over archaeological/geological time. The basic principles and advantages of the pre-dose dating method have been described in detail by authors like Aitken (1985) and McKeever (1985). Recent successful applications include dating of high fired porcelain and ceramic artifacts (Stoneham, 1983; Robertson and Prescott, 1986). Its use in environmental and accident dosimetry has also been suggested by Haskell et al. (1985).

Considerable interest exists in a better understanding of the nature

of the traps responsible for the phenomenon. A model proposed by Zimmerman (1971b) is based upon the temperature dependant transfer of charge from a reservoir (R) non-luminescent trapping site to a luminescent (L) site (Figure 8.1a). Trapping at R is therefore greater than L because of a larger capture cross-section and/or a larger concentration of available traps. The number of populated R sites is proportional to the pre-dose.

A recent report by McKeever et al. (1985) stimulated the present studies. Combining experimental observations using electron spin resonance (ESR) and thermoluminescence, McKeever et al. proposed the existence of two luminescence centres active at 110°C (Figure 8.1 b). They noticed that the effect was not due to the recombination taking place at the Al-hole sites and the enhancement may rather be due to the electron recombination with the holes at an unknown defect centre. An interesting supporting argument to the findings of McKeever et al. came from the previously reported information on the thermoluminescence emission of quartz. Jani et al., (1983) while studying the nature of high temperature thermoluminescence in quartz proposed that the emission is in the 470 nm region and the recombination at the Al-hole centres is responsible for it. It is therefore reasonable to assume that the 110C TL emission would be in the same wavelength region, provided the same defect acts as the luminescence centre. Zimmerman (1971b), on the other hand, reported that 110C peak is 'predominantly emitted at 380 nm with a weaker emission near 470 nm. These findings lead McKeever et al. to predict that the 380 nm emission may be related to the luminescence centre at the unknown site. This prediction being true, the pre-dose effect should show an increasing ratio of 380/470 nm emission at 110 C.

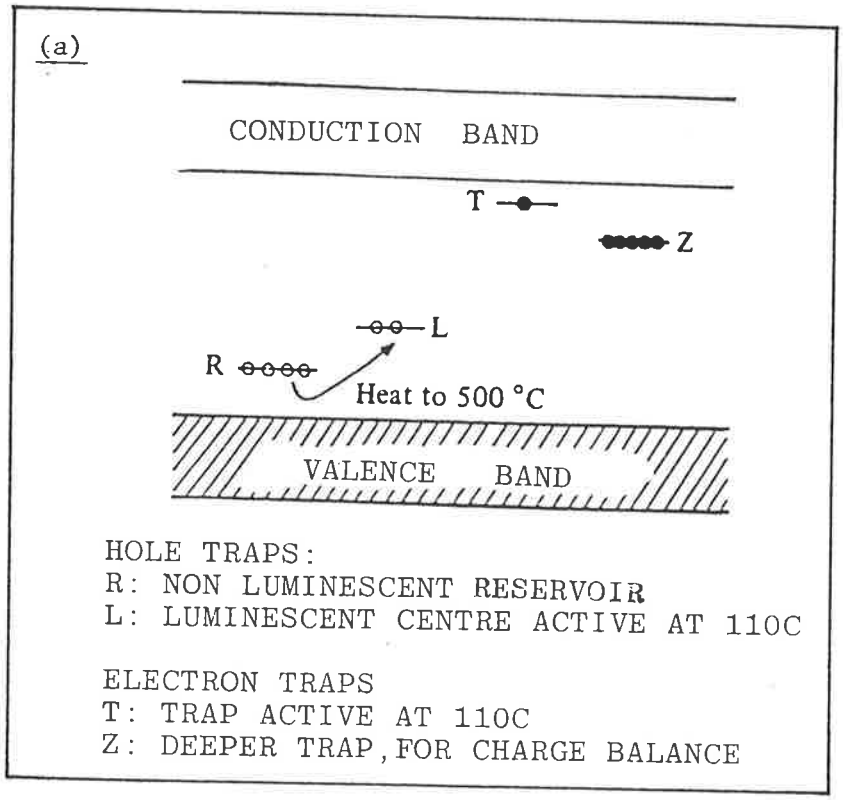

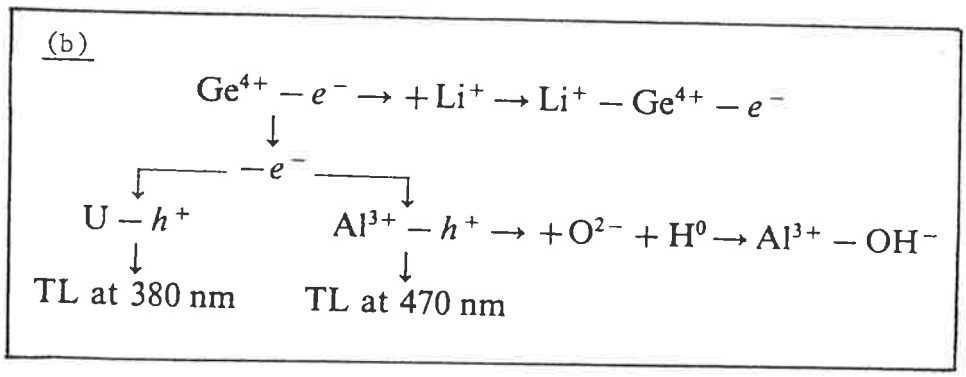

FIGURE 8.1: (a) An illustration of Zimmerman's model for the pre-dose effect upon 110C TL peak in quartz. Figure after McKeever (1985).

(b) The hole traps active at 110C emission in quartz. Recombination at the unknown luminescence centre U-$h^{\pm}$ with TL emission at 380nm is expected to be responsible for the pre-dose effect (McKeever et al.,1985).

Our findings about three different pottery samples from Thailand are shown in Figure 8.2. The samples were in the form of 200 μm thick slices of area about $1cm^2$. Beta dose between repeated heating cycles has been inserted in the Figures. Samples labelled as Kiln 51 and Kiln 61 are high fired unglazed stoneware sherds found in the respective kilns in the Ban Ko Noi region in Thailand and excavated in 1982 and 1983 respectively, while T782 is an earthenware sherd collected from the excavation of a habitation site at Ban Wang Samrong in 1982. It is probably a part of a domestic pottery vessel and was fired to a lower temperature than the other two.

The 110°C peak sensitization is readily observed for high fired pottery samples, and Figures 8.3 (a,b) show that, out of the two broad bands near 380 nm and 480 nm, the sensitisation is attributed only to the former band. Some desensitisation is observed for the low fired T782 sample and the proportional heights of the two broad bands remain unaltered during repeated glow.

In addition to the samples from the Thailand pottery, we also observed the sensitization effect in 90-125 μm quartz grains from Wokewine site. Wokewine is in the South East of South Australia. The results are shown in Figure 8.3. A portion of the sample which was annealed in air at 850°C for two hours and then allowed to cool showed 400 nm emission band sensitization.

Our results are, therefore, in conformity with the predicitons of McKeever et al. that the pre-dose is contributed by the luminescence centre leading to the TL signal near 380 nm, while the other centre with 470 nm emission does not play a significant role in the phenomenon. A comparison of Figures 8.2(c) and 8.3(b) shows that the mere presence of

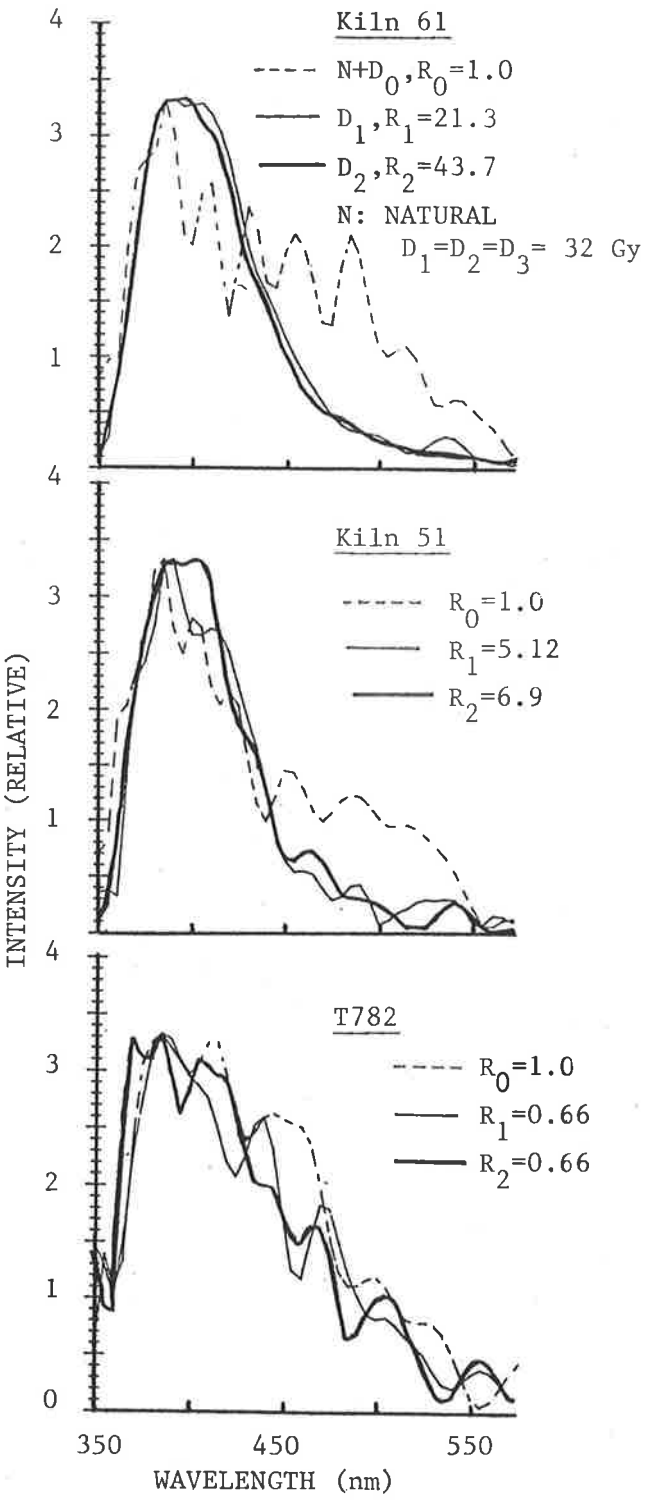

FIGURE 8.2: 110C TL emission from chips of pottery samples recovered from different archaeological sites in Thailand. The figures have been plotted for repeated irradiation and glow and R_0, R_1 and R_2 give the scaling factors for the respective glow curve intensities.

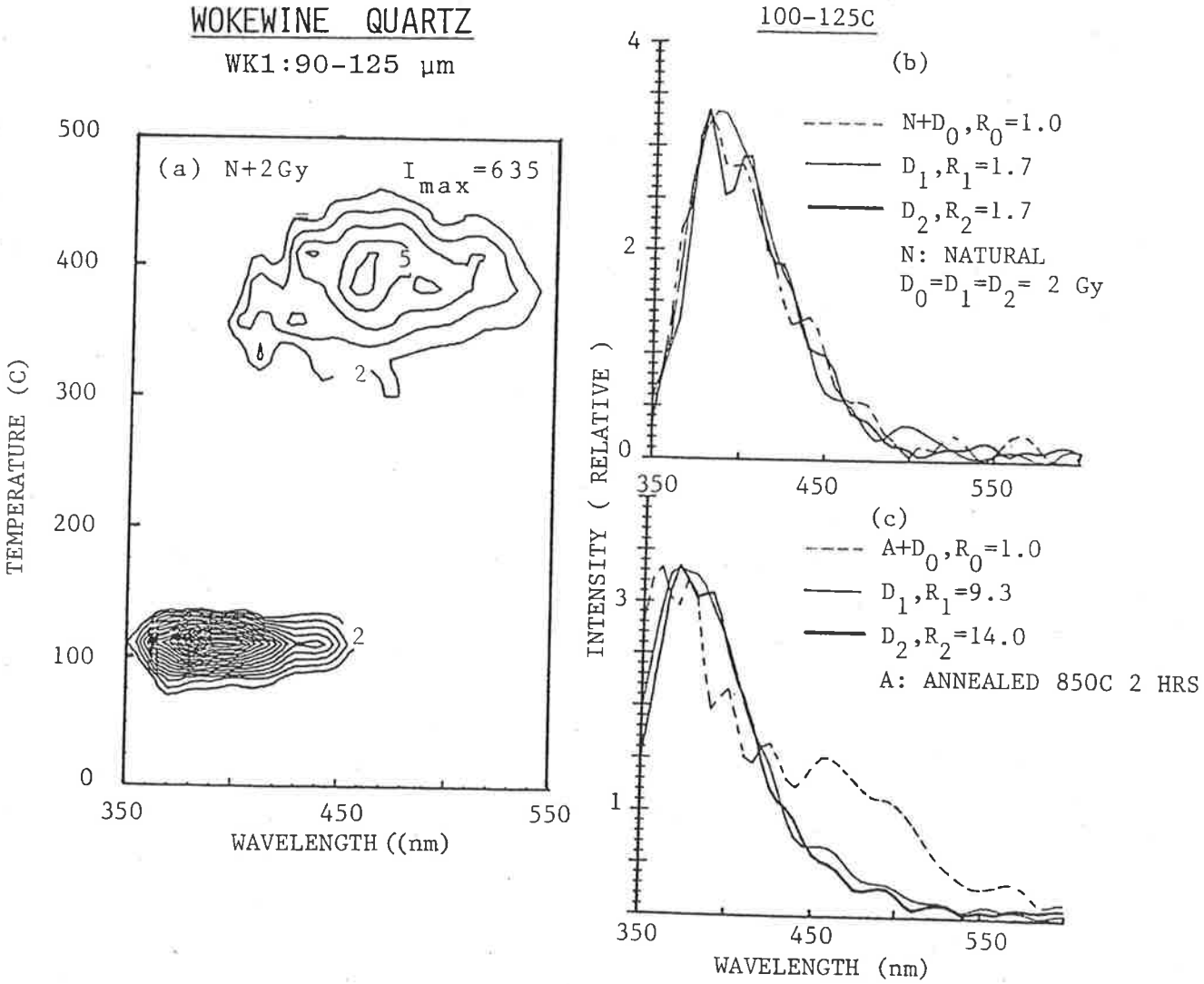

FIGURE 8.3: TL emission from a quartz sample from Wokewine, Flinders Ranges, South australia. (a) Natural + 2 Gy, and 110C emission for repeated irradiation and glow (2 Gy- 500C) for sample (b) as received and (c) annealed in air at 850C for two hours. R's are the scaling factors as in Figure 8.2. I_{max} in this and the following figures refers to the maximum intensity corresponding to contour number 20.

380 nm band or the absence of 470 nm band is insufficient to ensure pre-dose sensitisation. The high temperature emission band peaks near 470 nm (Figure 8.3a) agree well with a recent report by Jani et al. (1983, also see McKeever 1984).

8.3 THE PACIFIC ISLAND POTTERY

Attempts to obtain fine grain dates for pottery samples from the Pacific Islands have met with only mixed success. According to Prescott et al. (1982), variations in the geological structure of the region seem to play a key role in the thermoluminescence behaviour of the material from which the pottery is made.

The islands lying westward of the Philippines and New Caledonia (dot dashed line in Figure 8.4) are continental in origin and pottery from these islands is mainly datable. A band, about 1000 km wide of andesitic rocks of volcanic origin extends northward and eastward from this. Beyond the 'andesite line' shown dotted on Figure 8.4, the islands are based on basaltic oceanic volcanoes and coral built on volcanic bases (Dickinson and Shutler, 1979). The last two regions are expected to be low in TL sensitive minerals like quartz and potassic feldspar and high in calcite and plagioclases.

Historically, the problems associated with the thermoluminescence dating of the Pacific Island pottery led to the beginning of the present project. The results presented in the previous chapters on TL in feldspars provide a general answer to the main problem, i.e. the TL sensitivity depends strongly upon the feldspar composition, and, in addition to their poor TL response, the high calcic feldspars have a tendency to fade anomalously. Only a few of the Pacific Island pottery

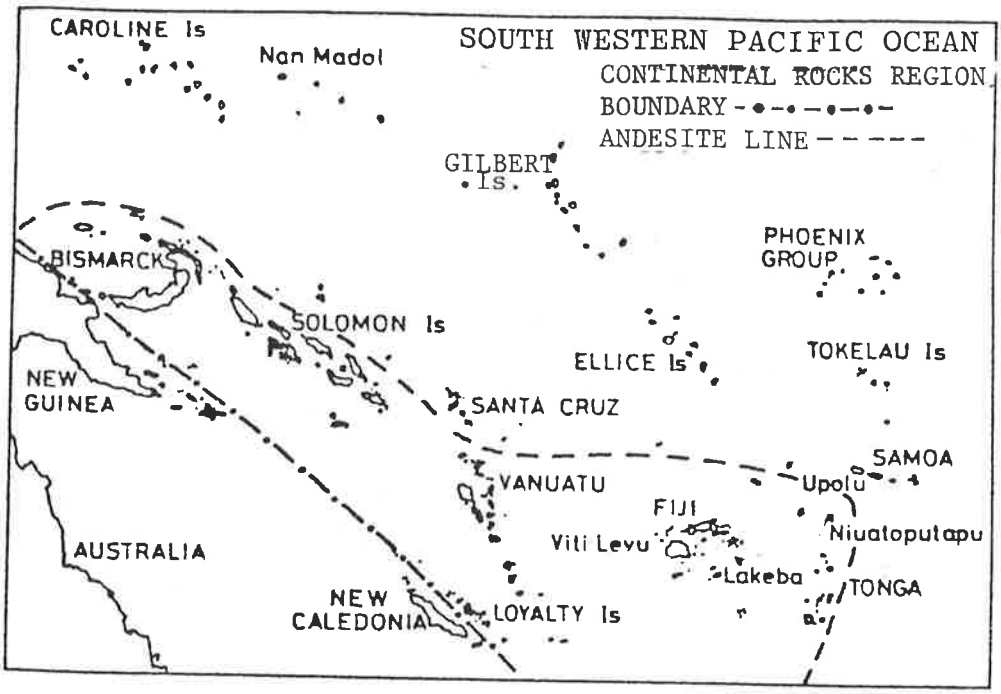

FIGURE 8.4: A map of South Western part of the Pacific Ocean. The dash-dot line shows the approximate boundary of the continental rocks. The andesite line is indicated by dashes.

samples were, however, tried as part of this research work, but in several ways the results are interesting and illustrate the nature of the problem.

As mentioned above, Prescott et al. (1982) faced problems like low natural TL and spurious TL signal. Yet the antiquity of several samples from specific sites was established within reasonable limits of the age predicted by other methods. Viti Levu, being one of the 'successful' sites appears interesting as the island lies within the so-called andesitic region which is expected to be low in TL sensitive minerals and hence poor in natural thermoluminescence. The successful results, in fact, come from a small pocket of different geological structure described by Dickinson and Shutler (1979) as having rocks of volcanic plutonic origin. One of the samples from the Yanuca site (VL/16/81/3/3/9), however, offered difficulties in dating. It showed little TL signal which saturated quickly.

The thermoluminescence emission spectra of this undatable, and other two datable samples are shown in Figure 8.5. The main features of the emission band near 380 nm are similar, but the change in the overall TL sensitivity is evident. The major contrast is the existence of an emission band near 540 nm in the non-datable pottery sample.

The multi-mineral nature of the fine grain samples and the present limited variety of the minerals for which the TL emission spectra has been seen on this equipment make it difficult to interpret the results in any great detail. Yet a band similar to this may be attributed to calcite. The XRF analysis based on carbonate loss during fused sample preparations also indicates the presence of about 8% calcite in this sherd.

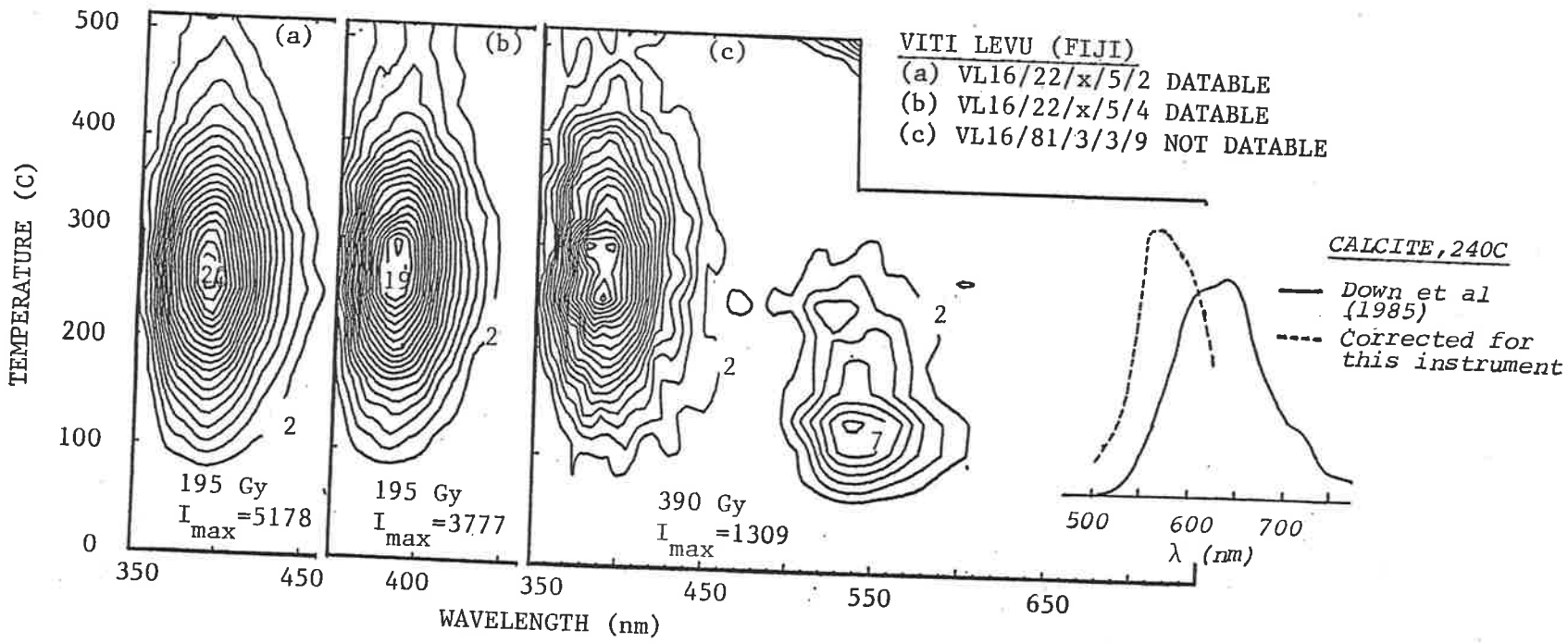

FIGURE 8.5: TL emission spectra for fine grains extracted from two datable and one undatable pottery sample from Viti Levu, Fiji. The insert in (c) shows the calcite emission spectrum as reported in Down et al. (1985) and corrected for our instrument response.

It is worth mentioning that the emission peak of the calcite is in the red region (insert Figure 8.5c) and only a small fraction of it is detectable due to the poor spectral response of our equipment in this region. Calcite shows a strong low temperature peak near 75C which may quickly fade leaving behind only the higher temperature components extending up to 100C or so. Another small peak near 200C suggestive in 550 nm band is also a characteristic of calcite (see e.g. Medlin, 1968; Down et al., 1985). Higher radiation dose revealed a definite 200C peak and overall stronger emission band.

We therefore conclude that the sample in question contains substantial amounts of calcite and the TL signal, being mostly in the red region, will be detected with poor efficiency by the conventional 2D-TL equipment commonly used for dating.

Thermoluminescence emission spectra from two other sites are shown in Figures 8.6 and 8.7. These sites lie towards the north west beyond the top left hand corner of the map shown in Figure 8.4 and come in the oceanic region of coral built islands on volcanic bases. Samples from the Yap (9.31N, 138.06E) and the Palau Islands (7.30N, 134.3E) were tested for datability. Yap itself has an unusual geology which suggested that it might be an exception like Viti Levu. No actual dates were attempted by Robertson (private communication) but she rated samples AH-228, AH-233 and AH-267 as "promising", "possible" and "doubtful" respectively. This is borne out by the spectral data. Broad similarities of the AH-228 and AH-233 may indicate that the same type of soil is responsible for the TL signal in each case, though its content may vary from one to another sample. Marked difference in the emission spectrum of sample AH-267 is probably due to the absence of the TL

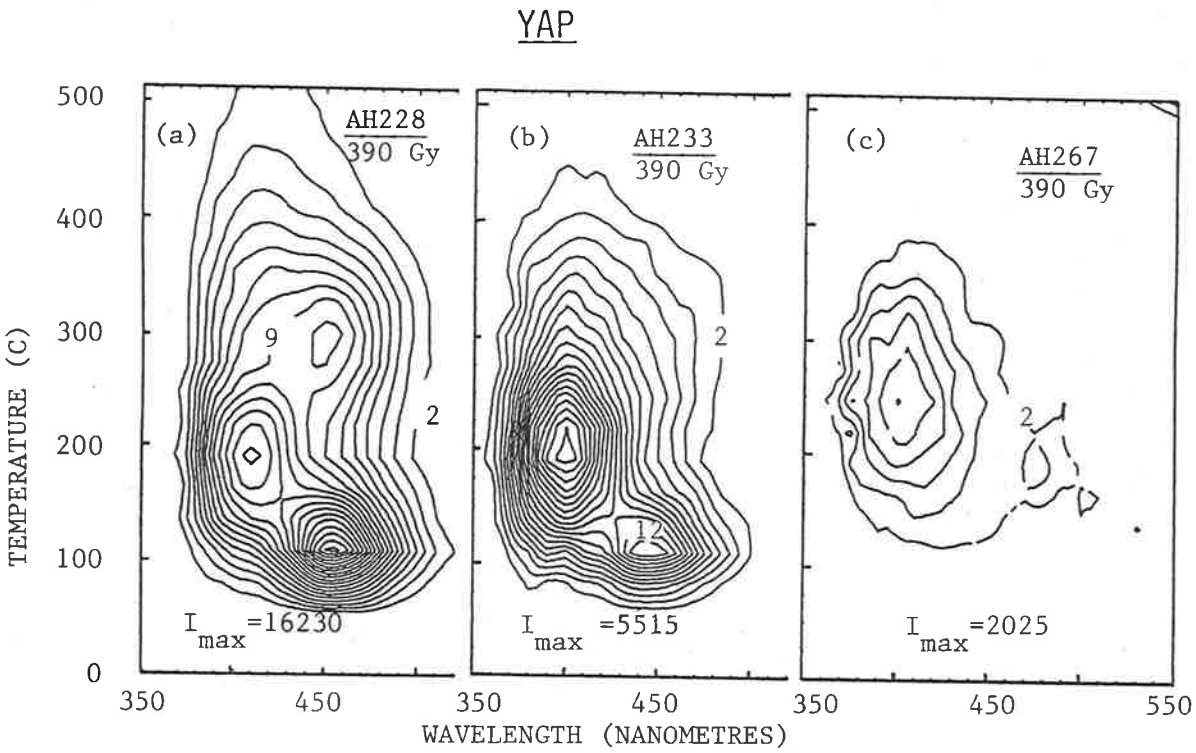

FIGURE 8.6: Thermoluminescence emission spectra for three different archaeological samples from Yap. The samples have been rated as (a) promising (b) possible and (c) doubtful for the purpose of TL dating. I_{max} in each case corresponds to contour number 20.

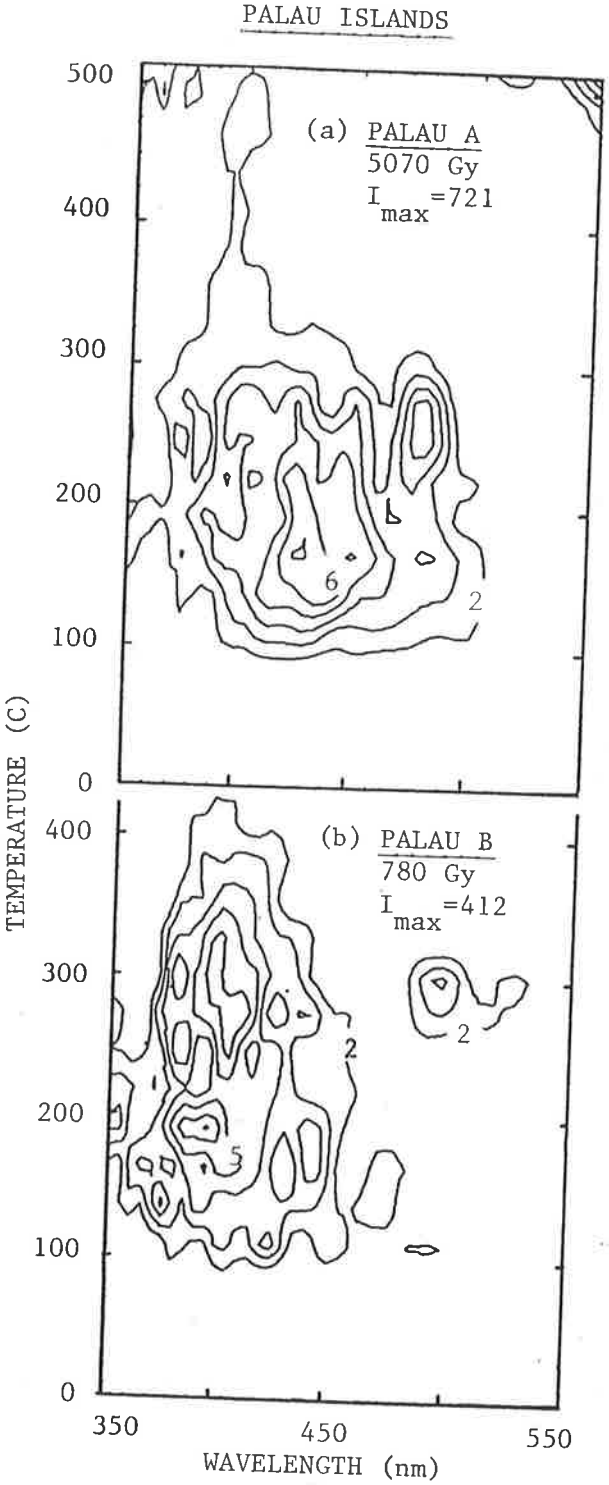

FIGURE 8.7: Emission spectra for two pottery samples from Palau Islands. The island represents the general soil features of oceanic basaltic region of volcanic origin.

sensitive component and indicates a different pottery fabric. Unfortunately, the question of classification between the indigenous and possible Filipino imported pottery could not be answered during the present limited study, as no sample from the contemporary Filipino pottery was run to make any comparisons. Yet comparison of the TL emission spectra from the pottery samples of three different islands (Figures 8.5-8.7) strongly suggests the possibility of such applications.

Pottery samples from the neighbouring Palau Islands which represent the general soil features of the region were the least sensitive to TL (Figure 8.7).

Sample discs used in the Pacific Island pottery studies were kindly provided by Dr. Gillian Robertson.

8.4 THE BROKEN HILL CELSIAN

To the best of the author's knowledge, the thermoluminescence in the relatively rare barium end member of the feldspar family has not so far been reported in the literature. Unfortunately, the mixed mineral behaviour of the present sample makes the data of somewhat limited significance. As mentioned in Chapter 5, deviation in silicon content seen through the XRF analysis from that expected through the idealised feldspar formula suggested the presence of a silica phase in appreciable percentage. Later investigations through energy dispersive system (EDS) analysis and electron microscopy confirmed the existence of a mixture of barium and plagioclase feldspar phases with quartz. Natural and laboratory radiation induced TL spectra are shown in Figure 8.8.

We expect that the 10% plagioclase phase with 84% anorthitic content will not contribute significantly due to its poor sensitivity (see

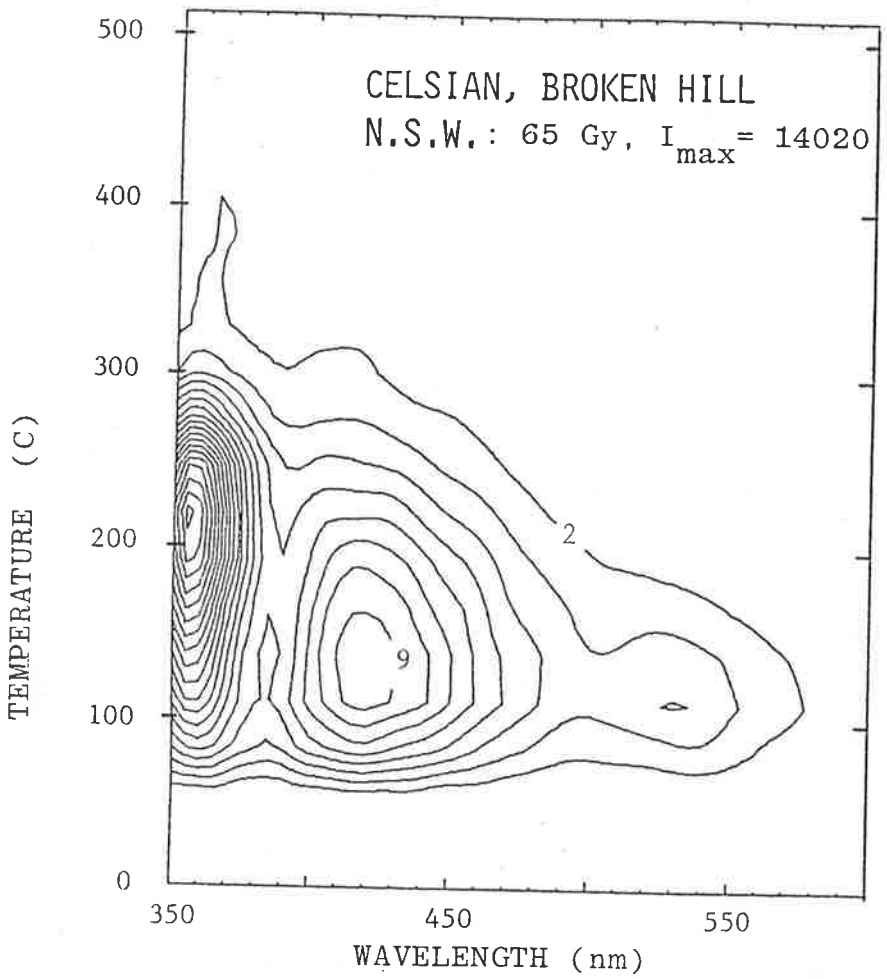

FIGURE 8.8: Thermoluminescence emission spectrum for a Barium feldspar sample from Broken Hill, New South Wales, Australia.

Chapter Seven). About 20% quartz is expected to show a low temperature peak near 110C in the 380 nm and/or 470 nm region and a high temperature signal around 470 nm.

The experimental results show the presence of a strong emission band near 360 nm, and another band around 430 nm or so. A weaker low temperature 530 nm band, as seen in several other plagioclase feldspars is also observed. In the light of our experience with some other quartz samples (see e.g. Figure 8.3a), we expect a very much stronger 110°C peak than the high temperature signal for post irradiation waiting time of ten minutes. The higher temperature signal may, therefore, well be due to the barium feldspar phase.

Owing to the similarities in potassium and barium ionic size and bondings in the feldspar structure, it is interesting to speculate on the possibility of some resemblence between the high potassic and barium feldspar emission spectra. The strong signal near 360 nm, may thus be the counterpart of 400 nm emission from high potassic feldspar. The present result, however, mostly suggests the need for further investigations.

CHAPTER NINE

THE LAST CHAPTER

It is appropriate to summarise briefly the findings and to point out some directions for further investigations.

Some broad based systematics evolved despite the complex nature of the feldspar system. Main emission bands were seen around 400 nm and 530 nm. The plagioclase feldspars showed more than one emission band in the 400 nm region. Feldspars of intermediate potassic and high calcic composition generally exhibit broad band spectra peaking in the 430-450 nm region.

A striking feature is a systematic trend of TL sensitivity over the plagioclase axis. The sensitivity which decreased over several orders of magnitude, in fact helped correcting the initially labelled classification of some of the samples supplied for the present study. The exact composition was later confirmed through the XRF analysis. It is realized that the poor sensitivity and the effects like anomalous fading may cause difficulties in dating high calcic feldspars.

A good proportion of the present effort went into the development of the equipment itself for reliable and reproducible operation for the type of research work it was intended to be used for. The chapters related to the applications are, in a way, the first serious attempt to demonstrate its capabilities and status. There is no end to further developments and some of the suggestions pointed out at various stages of equipment description in Chapters Three and Four have, in fact, already made

considerable progress for implementation during the time taken for writing up this thesis.

Plans for extending the equipment spectral response in the red/infra-red and the ultraviolet region are under way and make a part of the Ph.D. project of Phil Fox. The proposed EMI 9558QB photomultiplier tube has a better response in the red region, compared with the existing EMI 9635QA tube with its diminishing quantum efficiency above 620 nm or so.

An interesting extension of the existing research work with the new photomultiplier tube in the equipment will be to investigate further the phenomenon of anomalous fading with its expected red emission and to establish its relationship, if any, with the structural state, or iron as an impurity in the feldspar. Existing laboratory facilities can be used to separate grain fractions of varying magnetic susceptibility in a given sample, thereby providing a range of varying iron content in a feldspar of the same origin.

The 530 nm emission band seen in plagioclase feldspars requires further investigations. Mn^{2+} replacement of the Ca^{2+} ion in calcite gives rise to red emission, while a similar replacement in a calcic feldspar is expected to generate a yellow-green emission band. Mn^{2+} as an impurity has more affiliation for high calcic feldspars, yet the 530 nm emission is seen more readily in high sodic feldspars used in the present study. An alternate possibility of the band association with a radiation defect is also proposed. This has been used to explain the difference in the relative intensities of 530 and 400 nm emission bands for the high natural and a lower laboratory radiation induced TL in a number of high sodic plagioclase feldspars. Further experimental

observation is required to observe changes in the relative heights of these bands as a function of radiation dose. Recently, an oligoclase sample observed by Huntley (private communication) showed only one band near 450 nm, while the albite showed both the 400 and 550 nm bands and a transition between them with increasing temperature. It is also important to mention that the (non-radiation induced) spurious TL emission is also thought to be around 550 nm.

Recently published volumes on the latest state of the art in feldspars (Ribbe, 1983; Brown, 1984) helped understanding and explaining TL observations reported in this thesis. These volumes do not mention any significant contribution of thermoluminescence as a technique applied to some aspects of feldspar mineralogy. This area is, therefore, open for research. An interesting starting point could be to study the thermoluminescence in strained potassic feldspars with end-member characters unrevealed by the conventional XRD analysis for the cell structure. These investigations are suggested on the basis of the appearance of some end-member TL emission spectral behaviour in the intermediate compositional feldspars optically labelled as sanidine or orthoclase.

Thermoluminescence emission spectrometry of multi-mineral fine grains from the Pacific Island pottery made only a small part of the present research. It helped in understanding that the different behaviour of one sample from the Viti Levu Island may be attributed to the high calcite content. Moreover, it also revealed wide broad scale differences in the emission spectra patterns of pottery samples made of soils from different localities. This aspect may prove to be of interest in archaeological context to identify, for example, indigenous and

imported artefacts and for other applications where such soil identification is of some relevance.

Quartz is a mineral of prime significance in thermoluminescence dating. It has been studied only with reference to the pre dose effect on the 110C peak to confirm that the sensitization is attributed to a luminescence centre near 380 nm. Further extensive study on the overall spectrum is highly desirable. This may also include the effect of bleaching on the luminescence centres and comparison of the emission spectra from magnetic and non-magnetic grain fractions of quartz.

Thermoluminescence emission spectrum of a feldspar sample identified as a labradorite from Chain des Puys region in France, certainly showed the presence of a small amount of more TL sensitive potassic phase in it. The presence of such a phase probably helped Guerin and Valladas (1980) with dating a "plagioclase" sample from this area. Heating above 500C and extensive filtering of the black body radiation was, however, required. Feldspar systems with such mixed plagioclase and potassic composition do, though less frequently, exist in nature and further research on their identification using thermoluminescence will make an interesting project.

Growth of any radiation induced thermoluminescence emission centres detected with a different efficiency, or lying outside the filtered domains of the commonly used thermoluminescence equipment requires further attention to investigate its effects on estimates of the equivalent radiation dose and plateau for thermoluminescence dating applications. One such centre at 530 nm has actually been suggested for the plagioclase feldspars.

Some modifications to the equipment itself would improve its

operation. Replacement of the photomultiplier tube and the existing optical components has already been discussed in Section 4.7 of Chapter Four. An improved absolute calibration of the oven would be helpful in kinetic studies. It would be desirable to evaporate grid-like patterns of total reflection film on quartz substrate and use them as neutral density filters. Spectral response of such filters is expected to be linear, and dependant upon the grid mesh size instead of the film thickness. These can be prepared using the thin film deposition facilities available in the Department.

Paragraphs above show a glimpse of the further research and development possibilities. The author is confident that it is not the last chapter on the thermoluminescence emission studies using the Fourier transform spectrometer in the Physics Department at the University of Adelaide.

BIBLIOGRAPHY

Aitken, M.J., Fleming, S.J., Doell, R.R. and Tanguy, J.C. (1968) 'Thermoluminescent study of lavas from Mt. Etna and other historic flows: preliminary results' in 'Thermoluminescence of Geological Materials', Ed. D.J. McDougall, Academic Press, London pp. 359-366.

Aitken, M.J. (1974) 'Physics and Archaeology', Oxford University Press, London.

Aitken, M.J. (1985) 'Thermoluminescence Dating', Academic Press, Orlando.

Akber and Prescott (1985) 'Thermoluminescence in some feldspars: early results from studies of spectra': Nuclear Tracks 10 575-580.

Bachtiger, K. (1967) 'Die Thermolumineszenze einiger skandinavischer und nordamerikanischer plagioklase. (Teil V der Laboratoriumsuntersunchungen an Plagioklasen)': SMPM 47 365-384 (not directly seen, as mentioned by Smith, 1974).

Bailiff, I.K., Morris, D.A. and Aitken, M.J. (1977a) 'A rapid scanning interference spectrometer: application to low-level thermoluminescence emission': Journal of Physics E 10 1156-1160.

Bailiff, I.K., Bowman, S.G.E., Mobbs, S.F. and Aitken, M.J. (1977b) 'The phototransfer technique and its use in thermoluminescence dating': J. Electrostat 3 269-280.

Bakas, G.V. (1984) 'A new optical multichannel analyser using a charge coupled device as detector for thermoluminescence emission measurements': Radiation Protection Dosimetry 9 301-305.

Basedow, R.W., Cocks, T.D. (1979) 'Piezoelectric Ceramic Displacement Characteristics at Low Frequencies and their consequences in Fabry-Perot Interferometry': a Mawson Institute for Antarctic Research report, Adelaide.

Becker, K. (1973) 'Solid State Dosimetry', CRC Press, Boca Raton, Florida.

Becker, K. (1974) 'The discovery of thermoluminescence': Health Physics 27 321.

Bell, R.J. (1972) 'Introductory Fourier Transform Spectroscopy', Academic Press, New York.

Binder, W. and Cameron, J.R. (1969) 'Dosimetric Properties of CaF_2:Dy': Health Physics 17 613-618.

Birch, J.R., Ed. (1984): 'Fourier Transform Spectroscopy - Proceedings of the International Conference, Durham, 5-9 September 1983', published as a special issue of Infrared Physics Vol. 24 Nos. 2,3.

Birks, J.B. (1964) 'The Theory and Practice of Scintillation Counting', Pergamon Press, New York.

Boyle, R. (1664) 'Experiments and considerations touching colours': London pp 413-423 (not seen, taken from Harvey, 1957).

Brown, W.L., Ed. (1984) 'Feldspars and Feldspathoids - Structures, Properties and Occurrences', D. Riedel Publishing Company, Dordrecht.

Chamberlain, J. (1979) 'The Principles of Interferometric Spectroscopy', Editors G.W. Chantry and N.W.B. Stone, John Wiley and Sons, Chichester.

Chantry, G.W. and Fleming, J.W. (1976) 'Resolution limits in Fourier transform spectrometry': Infrared Physics 16 655-660.

Chantry, G.W. (1979) 'Modern Aspects of Microwave Spectroscopy', Academic Press, London.

Chen, R. and Kirsh, Y. (1981) 'Analysis of Thermally Stimulated Processes', Pergamon Press, Oxford.

Connes, P. (1984) 'Early History of Fourier Transform Spectroscopy': Infrared Physics 24 69-93.

Curran, S.C. (1953) 'Luminescence and the Scintillation Counters', Butterworth Scientific Publications, London.

Deer, W.A., Howie, R.A., and Zussman, J. (1982) 'An Introduction to the Rock-forming Minerals', Longman Group Limited, Essex.

Dickinson, W.R. and Shutler Jr., R. (1979) 'Petrography of sand tempers in Pacific Islands potsherds': Geological Society of America Bulletin Part II 90 1644-1701.

Down, S.J., Flower, R., Strain, J.A. and Townsend, P.D. (1985) 'Thermoluminescence emission spectra of calcite and iceland spar': Nuclear Tracks 10 581-589.

Durrani, S.A., Prachyabrued, W., Hwang, F.S.W., Edgington, J.A. and Blair, I.M. (1973) 'Thermoluminescence of some Apollo 14 and 16 fines and rock samples', Proceedings 4th Lunar Science Conference Eds. R. Brett, W.C. Phinney and D.W. Strangway, Pergamon Press, New York pp 2465-2479.

Eggleton, R.A. and Buseck P.R. (1980) 'The orthoclase-microcline inversion: a high resolution transmission electron microscope study and strain analysis': Contrib. Mineral. Petrol. 74 123-133.

Eley, D.D. and Wilkinson, P.R. (1959) 'Kinetics of oxidation of aluminium films' in 'Structure and Properties of Thin Films', Eds. Neugebauer, C.A., Newkirk, J.B., and Virmilyea, D.A.: John Wiley and Sons, Inc. New York.

Facey, R.A. (1966) 'A substandard light source of very low intensity': Journal of Scientific Instruments 43 658-659.

Fairchild, R.G., Mattern, P.L., Lengweiler, K., and Levy, P.W. (1978a) 'Thermoluminescence of LiF TLD-100: Emission spectra measurements': Journal of Applied Physics 49 4512-4522.

Fairchild, R.G., Mattern, P.L., Lengweiler, K. and Levy, P.W. (1978b) 'Thermoluminescence of LiF TLD-100: glow curve kinetics': Journal of Applied Physics 49 4523-4533.

Fellgett, P.B. (1951) Ph.D Thesis, University of Cambridge, England. Not seen, referred to by Bell (1972), Chamberlain (1979) and others.

Fleming, S.J. (1968) 'The colour of spurious thermoluminescence in dosimetry phosphors', in Proc. 2nd Int. Conf. Luminescence Dosimetry, Eds. J.A. Auxier, K. Becker, and E.M. Robinson. Springfield, Va. pp 266-280.

Fleming, S.J. (1970) 'Thermoluminescent dating: refinement of the quartz inclusion method': Archaeometry 12 133-145.

Fleming, S.J. (1973) 'The pre-dose technique: A new thermoluminescent dating method': Archaeometry 15 13-30.

Fleming, S.J. (1979) 'Thermoluminescence Techniques in Archaeology', Clarendon Press, Oxford.

Forman, M.L., Steel, W.H. and Vanasse, G.A. (1966) 'Correction of asymmetric interferograms obtained in Fourier spectroscopy': Journal of the Optical Society of America 56 59-63.

Gandais, M. and Willaime, C. (1984) 'Mechanical properties of feldspars' in 'Feldspars and Feldspathoids - Structures, Properties and Occurrences', Ed. W.L. Brown, D. Reidel Publishing Company, Dordrecht pp.207-246.

Garlick, G.F.J. and Gibson, A.F. (1948) 'The electron trap mechanism of luminescence in sulphide and silicate phosphors': Proc. Phys. Soc. 60 574-590.

Garlick, G.F.J., Lamb, W.E., and Steigmann, G.A. (1971) 'Thermoluminescence of lunar samples and terrestrial plagioclases': Proceedings of the Second Lunar Science Conference, Ed. A.A. Levinson, M.I.T. Press, pp. 2277-2283.

Garlick G.F.J. and Robinson, I. (1972) 'The thermoluminescence of lunar samples' in 'The Moon', Eds. S.K. Runcorn and H.C. Urey, D. Reidel Publishing Co., Dordrecht, pp. 324-329.

Gasiot, J., Bräunlich, D., Fillard, J.P. (1982) 'Laser heating in thermoluminescence dosimetry': Journal of Applied Physics 53 5200-5209.

Geake, J.E., Walker, G., Mills. A.A. and Garlick, G.F.J. (1971) 'Luminescence of Apollo lunar samples' in Proceedings 2nd Lunar Science Conference, Ed. A.A. Levinson, the MIT Press, Massachusetts, pp 2265-2275.

Geake, J.E., Walker, G., Telfer, D.J., and Mills, A.A. (1977) 'The cause and significance of luminescence in lunar plagioclase': Phil. Trans. Roy. Soc. Lond. A 285 403-408.

Gebbie, H.A. (1984) 'Fourier transform spectroscopy - recollections of the period 1955-1960': Infrared Physics 24 105-109.

Göksu, H.Y. and Fremlin, J.H. (1972) 'Thermoluminescence from unirradiated flints: regeneration thermoluminescence': Archaeometry 12, 67-72.

Goldsmith, J.R. (1980) 'The melting and breakdown reactions of anorthite at high pressure and temperatures': Am. Mineral. 65 272-284.

Grew, N. (1681) Museum Regalis Societatis, London, 158 (not seen, taken from Harvey, 1957.)

Griffiths, P.R. (1975) 'Chemical Infrared Fourier Transform Spectroscopy', Wiley Interscience, New York

Guelachvili, G. (1981) 'Distortions in Fourier Spectra and Diagnosis' in 'Spectrometric Techniques' Volume 2, Editor G.A. Vanasse, Academic Press, New York.

Guérin, G. and Valladas, G. (1980) 'TL dating of volcanic plagioclases': Nature 286 697-699.

Halperin, A. and Braner, A.A. (1960) 'Evaluation of thermal activation energies from glow curves': Phys. Rev. 117 408-415.

Harris, A.M. and Jackson, J.H., (1970) 'A rapid scanning spectrometer for the region 200-850 nm: application of thermoluminescent emission spectra': Journal of Physics E 3 374-376.

Harvey, E.N. (1957) 'A History of Luminescence from the Earliest Times until 1900', J.H. Furst Co., Baltimore.

Hasan, F.A., Keek, D.B., Hartmetz, C. and Sears, W.G.D. (1986) 'Anomalous fading of thermoluminescence in meteorites': Journal of Luminescence 34 327-335.

Haskell, E.H., Kaipa, P.L. and Wrenn, M.E. (1985) 'Environmental and accident dosimetry using the pre-dose TL technique': Nuclear Tracks 10 513-516.

Hernandez, G. (1978) 'Piezoelectric scanning of Fabry-Perot spectrometers: nonlinearities': Applied Optics 17 3088-3095.

Hirschi, H. (1925) 'Thermolumineszenz der kalifeldspäte': Schweiz Mineral Petrogr. Mitt. 5 427-428 (not seen, extracted from Pasternack, 1978).

Hofmeister, A.M. and Rossman, G.R. (1983) 'Color in feldspars' in 'Feldspar Minerology', Ed. P.H. Ribbe, Bookcrafters Inc., Michigan: pp 271-280.

Holland, L. (1966) 'Vacuum Deposition of Thin Films', Chapman and Hall Ltd., London - Ch. 11 pp 320-357 is on Evaporated Aluminium Films.

Holmquist, P.J. (1926) 'Meddelande rörande thermoluminescens hos kalifaltspat': Geol. Foren. Stockholm, Forh. 48 611-613 (not seen, extracted from Pasternack, 1978).

Horowitz, Y.S. (1984) 'Thermoluminescence and Thermoluminescent Dosimetry', CRC Press Inc., Boca Raton.

Huntley, D.J., Godfrey-Smith, D.I. and Thewalt, M.L.W. (1985) 'Optical dating of sediments': Nature 313 105-107.

Imaeda, K., Kitajima, T., Kuga, K., Miono, S., Misaki, A., Nakamura, M., Ninagawa, K., Okamoto, Y., Saavedra, O., Saito, T., Takahashi, N., Takano, Y., Tomiyama, T., Wada,T., Yamamoto, I. and Yamashita, Y. (1985) 'Spatial distribution readout system of thermoluminescence sheets': Nuclear Instruments and Methods in Physics Research A 241 567-571.

Ioffe, V.A. and Yanchevskaya, I.S. (1967) 'Study of the thermoluminescence and electron paramagnetic resonance of irradiated aluminium silicates': Optics and Spectroscopy 23, 265-266.

Ioffe, V.A. and Yanchevskaya, I.S. (1968) 'Electron paramagnetic resonance and thermoluminescence of irradiated single crystals of the aluminosilicates $NaAlSi_3O_8$ and $LiAlSiO_4$': Soviet Physics - Solid State 10 370-374.

Jacquinot, P. (1954) 'The luminosity of spectrometers with prisms, gratings or Fabry-Perot etalons': Journal of Optical Society of America 44 761-765.

Jani, M.G., Halliburton, L.E. and Kohnke, E.E. (1983) 'Point defects in crystalline SiO_2: thermally stimulated luminescence above room temperature': J. Applied Physics 54 6321-6328.

Jensen, H.E. and Prescott, J.R. (1982) 'A Fourier transform spectrometer for the measurement of thermoluminescence emission spectra': PACT 6 542-548.

Jensen, H.E. (1982) 'Physical Measurements Associated with Thermoluminescence Dating', Ph.D. Thesis, the University of Adelaide, Adelaide, Australia.

Kim, K., and Burley, B.J. (1971) 'Phase equilibria in the system $NaAlSi_3O_8$-$NaAlSiO_4$-H_2O with special emphasis on the stability of analcite': Canadian Journal of Earth Science 8 311-337.

Kitamura, M. and Morimoto, N. (1984) 'The modulated structure of the intermediate plagioclases and its change with composition' in 'Feldspars and Feldspathoids - Structures, Properties and Occurrences', Ed. W.L. Brown, D. Riedel Publishing Company, Dordrecht: pp 95-119.

Kohler, A. and Leitmeier, H. (1932) 'Beobachtungen uber Thermolumineszenz und Mineralien': Anz. Akad. Wiss., Wien 18 163-168 (not seen, extracted from Pasternack, 1978).

Lalou, C., Valladas, G., Brito, U., Henni, A., Ceva, T., Visocekas, R. (1972) 'Spectral emission of natural and artificially induced thermoluminescence in Apollo 14 lunar sample 14163,147' Proceedings of the Third Lunar Science Conference, Ed. D.R. Criswell, pp. 3009-3020.

Lehmann, G. (1984) 'Spectroscopy of Feldspars' in 'Feldspars and Feldspathoids', Ed. W.L. Brown, D. Reidel Publishing Company, Netherlands, pp 121-162.

Lesnov, F.P. and Serebrennikov, A.I. (1972) 'Thermally induced luminescence in plagioclases from heterogeneous gabbroic rocks of the Anadym-Koryak fold system': Geol. Geofiz. 4 41-47.

Levy, P.W. (1982) 'Thermoluminescence and optical bleaching in minerals exhibiting second order kinetics and other charge retrapping characteristics': PACT Journal 6 224-242.

McDougall, D.J. (1968) 'Natural Thermoluminescence of Igneous Rocks and Associated Ore Deposits' in 'Thermoluminescence of Geological Materials', Ed. D.J. McDougall, Academic Press, London: pp.527-544.

McKeever, S.W.S. (1980) 'Thermoluminescence in lithium fluoride; analysis of the glow curves': Nucl. Instruments and Methods 175 19-20.

McKeever, S.W.S. (1984) 'Thermoluminescence in quartz and silica': Radiation Protection Dosimetry 8 81-98.

McKeever, S.W.S. (1985) 'Thermoluminescence of Solids', Cambridge University Press, New York.

McKeever, S.W.S., Ahmed, K., Chandler, P.J., Strain, J.A., Rendell, H.M. and Townsend, P.D. (1983) 'Analysis of emission spectra of meteorites during thermoluminescence measurements': PACT Journal 9 187-204.

McKeever, S.W.S., Chen, C.Y. and Halliburton, L.E. (1985) 'Point defects and the pre-dose effect in natural quartz': Nuclear Tracks 10 489-495.

MacKenzie, W.S. and Zussman, J., Eds. (1974) 'The Feldspars', Manchester University Press, Manchester.

Machatschki, F. (1928) 'The structure and constitution of feldspars': Centr. Mineral. Abt. A, 97-104: (not seen, taken from Ribbe, 1983b).

Macquer, J.P. (1778) 'Dictionaire de Chymie Volume 3', Paris (as mentioned by Köhler and Leitmeier, 1934).

Marfunin, A.S. (1979) 'Spectroscopy, Luminescence and Radiation Centers in Minerals', Springer-Verlag, Berlin, Heidelberg.

Mason, R.A. (1982) 'Trace element distributions between the perthite phases of alkali feldspars from pegmatites': Mineral. Mag. 45 101-106.

Mason, R.A., Smith, J.V., Dawson, J.B. and Treves, S.B. (1982) 'A reconnaissance of trace elements in anorthoclase megacrysts': Mineral Mag. 46 7-11.

Mattern, P.L., Lengweiler, K., and Levy, P.W. (1971) 'Apparatus for the simultaneous determination of thermoluminescent intensity and spectral distribution': Modern Geology, 2 293-294.

Matyash, I.V., Bagmut, N.N., Litovchenko, A.S. and Broshko, V.Y. (1982) 'Electron paramagnetic resonance study of new paramagnetic centres in microcline-perthites from pegmatites': Physics and Chemistry of Minerals 8 149-152.

Medlin, W.L. (1968) 'Nature of Traps and Emission Centres in Thermoluminescent Rock Materials': Ch. 4.1 in 'Thermoluminescence of Geological Materials', Ed. D.J. McDougall, Academic Press, London pp. 193-223.

Megaw, H.D. (1974) 'The architecture of the feldspars' in 'The Feldspars', Eds. W.S. MacKenzie and J.Zussman, Manchester University Press, Manchester pp. 2-24.

Mejdahl, V. (1979) 'Thermoluminescence dating, beta dose attenuation in quartz grains' Archaeometry 21 61-72.

Mejdahl, V. (1982) 'An automated procedure of thermoluminescence dating of pottery and burnt stones': PACT 7 83-96.

Mejdahl and Winther-Nielsen, M. (1982) 'TL dating based on feldspar inclusions': PACT Journal 6 426-437.

Mejdahl, V., and Wintle, A.G. (1984) 'Thermoluminescence applied to age determination in archaeology and geology' in 'Thermoluminescence and Thermoluminescent Dosimetry', Ed. Y.S. Horowitz, CRC Press, Boca Raton, pp 133-190.

Mejdahl, V. (1985) 'A survey of archaeological samples dated in 1984', Report Risø-M-2541.

Michelson, A.A. (1891) 'On the application of interference-methods to spectroscopic measurements - I': Philosophical Magazine 31 (5th series), 338-346.

Michelson, A.A. (1892) 'On the application of interference methods to spectroscopic measurements - II': Philosophical Magazine, 34 (5th series) 280-299.

Michelson, A.A. (1927) 'Studies in Optics', the University of Chicago Press, Chicago, Phoenix Edition, 3rd impression in 1962.

Morse, H.W. (1905) Astrophys. J. 21 410 (not seen, as mentioned by McKeever, 1985).

Nambi, K.S.V. (1977) 'Thermoluminescence: its Understanding and Applications' INF IEA54 CPRD AMDI Inst. de Energia Atomica, Saõ-Paulo, Brasil.

Nambi, K.S.V., Bapal, V.N. and Ganguly, A.K. (1974) 'Thermoluminescence of $CaSO_4$ doped with rare earths': Journal of Physics C 7 4403-4415.

Nash, A.E., Johnson, T.L., Attix, F.H., and Schylman, J.H. (1967) 'Spurious thermoluminescence of CaF_2:Mn and LiF (TLD-100)': in Proc. Int. Conf. Luminescence Dosimetry, USAEC Conf.-650637 NMS, Springfield, Va., p244.

Nishita, H., Hamilton, M. and Haug, R.M. (1974) 'Natural thermoluminescence of soils, minerals, and certain rocks', Soil Science 117 211-219.

Norton, H.R. and Beer, R. (1976) 'New apodizing functions for Fourier spectrometry': Journal of Optical Society of America 66 259-264.

Ogelman, Y.G. and Kapur, S. (1982) 'Thermoluminescence reveals weathering states in basaltic rocks': Nature 296 231-232.

Park, J.H., (1982) 'Effect of interferogram smearing on atmospheric limb sounding by Fourier Transform Spectroscopy': Applied Optics 21 1356-1366.

Park, J.H. (1983) 'Analysis method for Fourier Transform Spectroscopy': Applied Optics 22 835-849.

Parsons, I. and Brown, W.L. (1984) 'Feldspars and the thermal history of igneous rocks' in 'Feldspars and Feldspathoids - Structures, Properties and Occurrences', Ed. W.L. Brown, D. Reidel Publishing Company, Dordrecht, pp 318-372.

Pasternack, E.S., Gaines, A.M. and Levy, P.W. (1976) 'Thermoluminescence of ordered and disordered albites': Geological Abstracts with Programs 8 1044.

Pasternack, E.S. (1978) 'Thermoluminescence of ordered and thermally disordered albites', Ph.D Thesis, University of Pennsylvania, Philadelphia, U.S.A.

Pasternack, E.S. and Levy, P.W. (1978) 'Changes in thermoluminescence emission spectrum accompanying thermal disorder in Amelia albite': Geological Abstracts with Programs 10 468.

Platanov, A.N., Rokachuck, T.A., Tarashchan, A.N. and Shcherbakov, I.B. (1971) 'Relation of feldspar thermoluminescence to structural characteristics'. Chemical Abstracts 75 101 (# 119956e), original reference in Russian language Geol. Zh. 31 (1971) 92-95.

Portal, G. (1981) 'Preparation and Properties of Principal TL Products' in 'Applied Thermoluminescence Dosimetry', Eds. M. Oberhofer and A. Scharmann, ECSC, Brussels.

Prescott, J.R., Robertson, G.B., Green, R.C. (1982) 'Thermoluminescence dating of Pacific Island pottery - successes and failures': Archaeology in Oceania 17 142-147.

Randall, J.T., Wilkins, M.H.F. (1945a) 'Phosphorescence and electron traps. I. The study of trap distributions': Proc. Roy. Soc. London A184 366-389.

Randall, J.T., Wilkins, M.H.F. (1945b) 'Phosphorescence and electron traps. II. The interpretation of long period phosphorescence': Proc. Roy. Soc. London 184 390-433.

Rayleigh, L. (1892) 'On the interference bands of approximately homogeneous light': in a letter to Prof. A. Michelson: Philosphical Magazine, 34 (5th series) 407-411.

Ribbe, P.H. Ed. (1983a) 'Feldspar Mineralogy', Bookcrafters Inc., Michigan.

Ribbe, P.H. (1983b) 'The Chemistry, structure and nomenclature of feldspars' in 'Feldspar Mineralogy', Ed. P.H. Ribbe, Bookcrafters Inc., Michigan, pp 1-19.

Ribbe, P.H. (1983c) 'Aluminium-silicon order in feldspars; domain textures and diffraction patterns' in 'Feldspar Mineralogy', Ed. P.H. Ribbe, Bookcrafters, Michigan, pp 21-55.

Ribbe, P.H. (1983d) 'Exsolution textures in ternary and plagioclase feldspars; interference colors' in 'Feldspar Mineralogy', Ed. P.H. Ribbe, Bookcrafters, Michigan, pp.241-270.

Ribbe, P.H. (1984) 'Average structures of alkali and plagioclase feldspars: systematics and application' in 'Feldspars and Feldspathoids - Structures, Properties and Occurrences', Ed. W.L. Brown, D. Reidel Publishing Company, Dordrecht, pp 1-55.

Robertson, G.B. and Prescott, J.R. (1986) 'Thermoluminescence dating - a key element in the Thai ceramic archaeological project?': Second Australian Archaeometry Conference, Canberra 11-14 Feb, 1985 (proceedings to appear.)

Rose, A. (1963) 'Concepts in Photoconductivity and Allied Problems', Interscience, New York.

Rubens, H. and Hollnagel, H. (1910) 'Measurement in the extreme infra-red spectrum': Philosophical Magazine 19 (6th series) 761-782.

Sankaran, A.V., Nambi, K.S.V. and Sunta, C.M. (1982) 'Current Status of Thermoluminescence Studies in Minerals and Rocks': Bhabha Atomic Research Centre Report # BARC-1156.

Sankaran, A.V., Nambi, K.S.V. and Sunta, C.M. (1983) 'Progress of thermoluminescence research on geological materials', Proceedings of Indian National Science Academy 49 18-112.

Shcherbakov, I.B., Platanov, A.N., Tarashchan, A.N. and Povarennykh, A.S. (1972) 'Thermoluminescence of potassic feldspars from some granitic rocks of the Ukrainian Shield', Chemical Abstracts 76 153 (# 74804f) - original reference in Russian language Geol. Zh. 3 (1971) 20-27.

Shockley, W. and Read Jr., W.T. (1952) 'Statistics of the recombination of holes and electrons': Physical Review 87 835-842.

Singhvi, A.K. and Wagner, G.A. (1985) 'Thermoluminescence Dating and its Applications to Young Sedimentary Deposits': Max-Planck-Institut für Kernphysik, Heidelberg, Report # MPI H 19B5-V 17.

Sippel, R.F. and Spencer, A.B. (1970) 'Luminescence petrography and properties of lunar crystalline rocks and breccias', Proc. Apollo 11 Lunar Sci. Conf., Ed. A.A. Levinson, M.I.T. press, 2413-2426.

Smith, J.V. (1974) 'Feldspar Minerals', Springer-Verlag, Berlin.

Smith, J.V. (1983) 'Some chemical properties of feldspars' in 'Feldspar Mineralogy', Ed. P.H. Ribbe, Bookcrafters Inc., Michigan, pp 281-296.

Smith, B.W. (1983a) 'New Applications of Thermoluminescence Dating', Ph.D. Thesis, the University of Adelaide.

Speit, B. and Lehmann, G. (1976) 'Hole centers in the feldspar sanidine': Phys. Stat. Sol. A36 471-481.

Speit, B. and Lehmann, G. (1982) 'Radiation defects in feldspars': Physics and Chemistry of Minerals 8 77-82.

Steel, W.H. (1964) 'Interferometers without collimation for Fourier spectroscopy': Journal of Optical Society of America 54 151-156.

Steel, W.H. (1983) 'Interferometry', 2nd Edition, Cambridge University Press, Cambridge.

Steele, I.M., Hutcheon, I.D. and Smith, J.V. (1980) 'Ion microprobe analysis and petrogenetic interpretations of Li, Mg, Ti, K, Sr and Ba in lunar plagioclase': Geochim. Cosmochim. Acta. Suppl. 14 571-590.

Strickertsson, K. (1985) 'The thermoluminescence of potassium feldspars - glow curve characteristics and initial rise measurements': Nuclear Tracks 10 613-617.

Stoneham, D. (1983) 'Porcelain dating': PACT 9 227-239.

Sunta, C. (1970) 'Thermoluminescence spectrum of gamma-irradiated natural calcium fluoride': Journal of Physics C3 1978-1983.

Tarashchan, A.N. (1978) 'Luminescence of minerals', Kiev, Naukova dumka.

Taylor, W.H. (1933) 'The structure of sanidine and other feldspars': Z. Kristallogr 85 425-442.

Telfer, D.J. and Walker, G. (1978) 'Ligand field bands of Mn^{2+} and Fe^{3+} luminescence centres and their site occupancy in plagioclase feldspars': Mod. Geol. 6 199-210.

Tittel, H.O., Thiel, E., Trakowski, W. Schneider, M. and Heinrich, W. (1984) 'A Fourier spectrometer for visible light': Infrared Physics 24 323-328.

Tolansky, S. (1973) 'An Introduction to Interferometry', 2nd Edition, Longman Group Ltd., London.

Townsend, P.D., Ahmed, K., Chandler, P.J., McKeever, S.W.S. and Whitlow, H.J. (1983) 'Measurement of the emission spectra of LiF during thermoluminescence': Radiation Effects 72 245-257.

Tullis, J. (1983) 'Deformation of feldspars', in 'Feldspar Mineralogy', Ed. P.H. Ribbe, Bookcrafters Inc., Michigan: pp.297-323.

van Gool, W. (1958) 'Fluorescence and photoconduction of silver activated cadmium sulphide': Philips Research Reports 13 157-166.

Visocekas, R. (1979) 'Miscellaneous aspects of artificial TL of calcite: emission spectra, athermal detrapping and anomalous fading': PACT 3 258-265.

Visocekas, R. (1985) 'Tunnelling radiative recombination in labradorite: its association with anomalous fading of thermo-luminescence': Nuclear Tracks 10 521-529.

Visocekas, R., Ceva, T., Marti, C., Lefaucheux, F. and Robert, M.C. (1976) 'Tunnelling processes in afterglow of calcite': Phys. Stat. Solidi (a) 35 315-327.

Wada, T., Yamamoto, J., Takahashi, N. and Misaki, A. (1985) 'Readout Technique of Thermoluminescence Calorimeter for Large Cascade Detectors': Institute of Cosmic Ray Research, University of Tokyo, ICR-127-85-8.

Wagner, G.A., Aitken, M.J., Singhvi, A.K., Mangini, A., Mejdahl, V., Pernicka, E., and Durrani, S.A. Eds. (1985) 'Proceedings of the 4th international specialist seminar on thermoluminescence and electron spin resonance dating': published as a special issue of 'Nuclear Tracks and Radiation Measurements', Volume 10, Number 4-6.

Wedgwood, T. (1792) 'Experiments and observations on the production of light from different bodies, by heat and by attrition': Philosophical Transactions, Royal Society of London 82 28-47.

Williams, F.E. (1949) 'Review of the interpretations of luminescence phenomena': Journal of the Optical Society of America 39 648-654.

Wintle, A.G. (1973) 'Anomalous fading of thermoluminescence in mineral samples': Nature 245 143-144.

Wintle, A.G. (1977) 'Detailed study of a thermoluminescent mineral exhibiting anomalous fading': Journal of Luminescence 15 385-393.

Wintle, A.G. and Huntley, D.J. (1980) 'Thermoluminescence dating of ocean sediments': Canadian Journal of Earth Science 17 348-360.

Yamashita, T., Nada, N., Onishi, H. and Kitamura, S. (1971) 'Calcium sulphate activated by thalium or dysprosium for thermoluminescence dosimetry': Health Physics 21 295-300.

Yund, R.A. (1983a) 'Microstructure, kinetics and mechanisms of alkali feldspar exsolution' in 'Feldspar Mineralogy', Ed. P.H. Ribbe, Bookcrafters, Michigan, pp.177-202.

Yund, R.A. (1983b) 'Diffusion in feldspars' in 'Feldspar Mineralogy', Ed. P.H. Ribbe, Bookcrafters, Michigan, pp. 203-222.

Yund, R.A. (1984) 'Alkali feldspar exsolution: kinetics and dependence on alkali interdiffusion' in 'Feldspars and Feldspathoids', Ed. W.L. Brown, D. Reidel Publishing Company, Netherlands, pp.281-315.

Zimmerman, D.W. (1971a) 'Thermoluminescence dating using fine grains from pottery': Archaeometry 13 29-52.

Zimmerman, D.W. (1971b) 'The radiation-induced increase of the 100°C thermoluminescence sensitivity of fired quartz': Journal of Physics C 4 3265-3277.

Zimmerman, D.W. (1979) 'Thermoluminescence dating using zircon grains': PACT 3 458-465.

APPENDIX

THICK SOURCE ALPHA COUNTING USING FUSED GLASS DISCS: CORRECTIONS FOR LOSS OF RADON AND POLONIUM

Reprinted from

THE NUCLEAR INSTRUMENTS AND METHODS
IN PHYSICS RESEARCH A234 (1985)394

Akber, R.A., Hutton, J.T. & Prescott, J.R. (1984) Thick source alpha counting using fused glass discs: corrections for loss of radon and polonium.
Nuclear Instruments and Methods in Physics Research Section A, v. 234(2), pp. 394-397

REVISED FIGURES

As mentioned in Chapter Four, a set of Revised Figures, corrected for the spectral response of the equipment (Figure 4.7) and 15% temperature discrepancy due to heat losses (Section 4.6), is included to facilitate comparison. The corresponding figures incorporated in the main text may be treated as relative, though the discussion and the conclusion drawn from them equally apply to the revised figures as well.

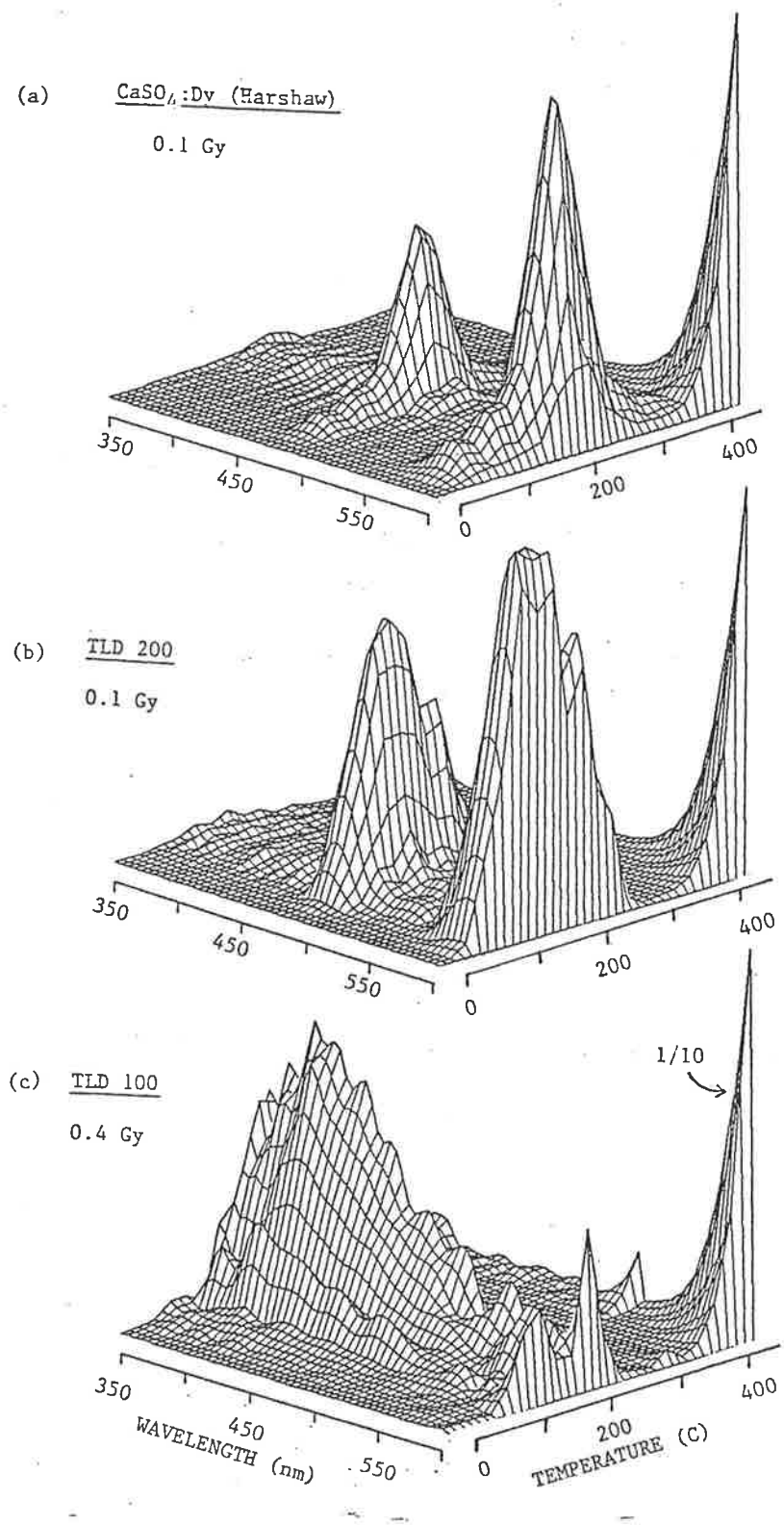

REVISED FIGURE 4.11: Beta radiation induced thermoluminescence spectra for (a) $CaSO_4$:Dy (Harshaw, Ohio) (b) TLD 200 and (c) TLD 100 dosimeter phosphors.

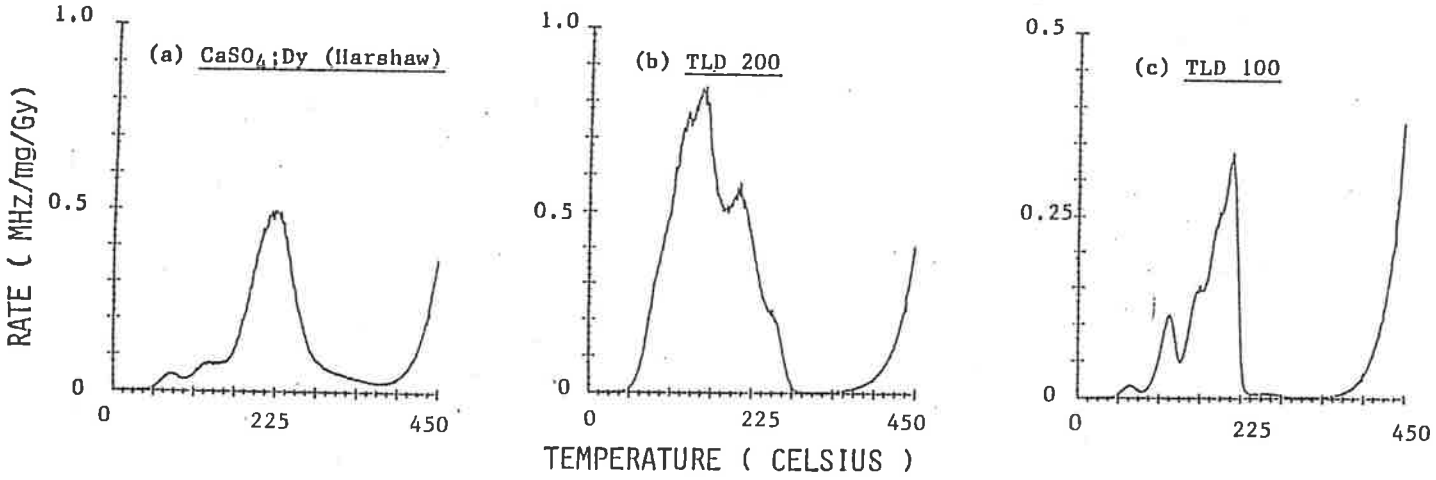

REVISED FIGURE 4.12 (a-c): The 2D TL glow curves produced by summation of raw interferogram data used for computing the spectra as shown in Figure 4.11(a-c).

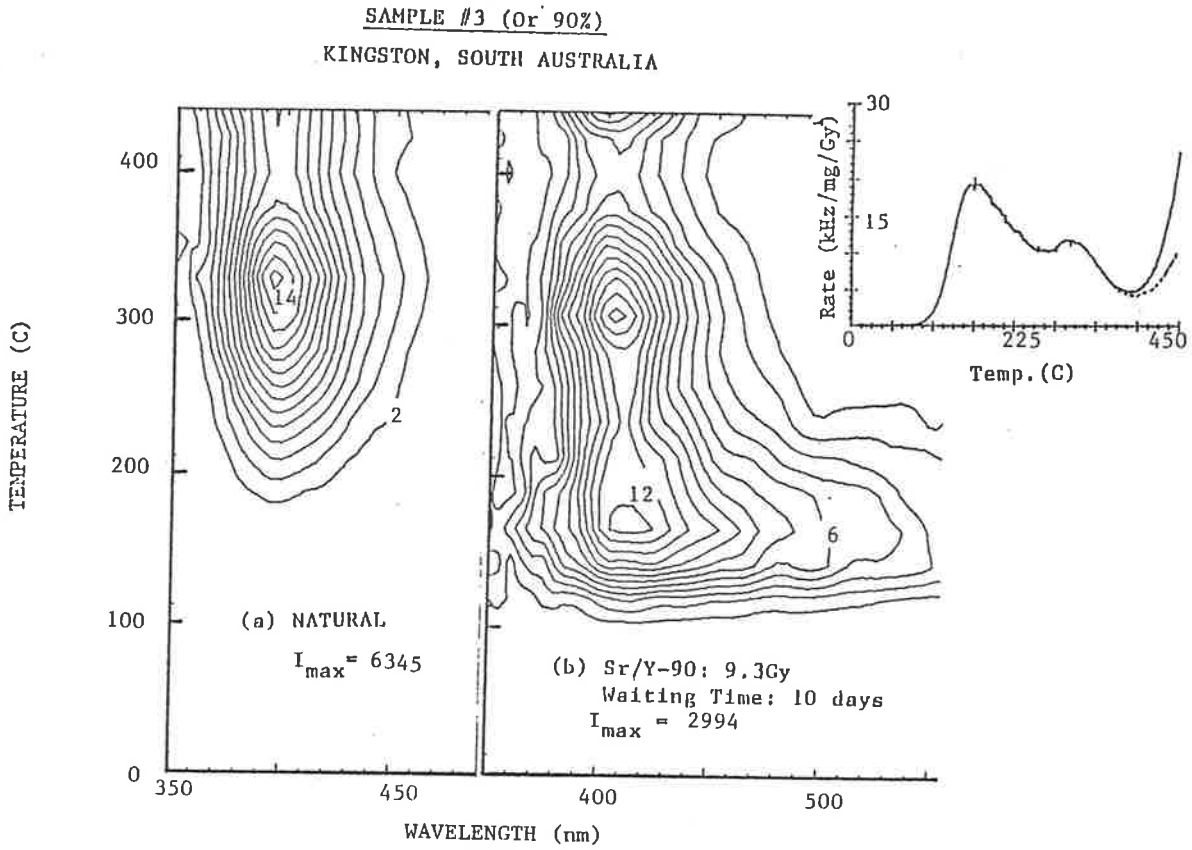

REVISED FIGURE 6.1: (a) Natural and (b) laboratory radiation induced thermoluminescence in a high potassic feldspar from Kingston, South Australia. The insert in (b) shows the corresponding 2D TL glow curve where the broken line represents the TL signal corrected for the black body emission. I_{max} is the maximum intensity corresponding to the contour # 15.

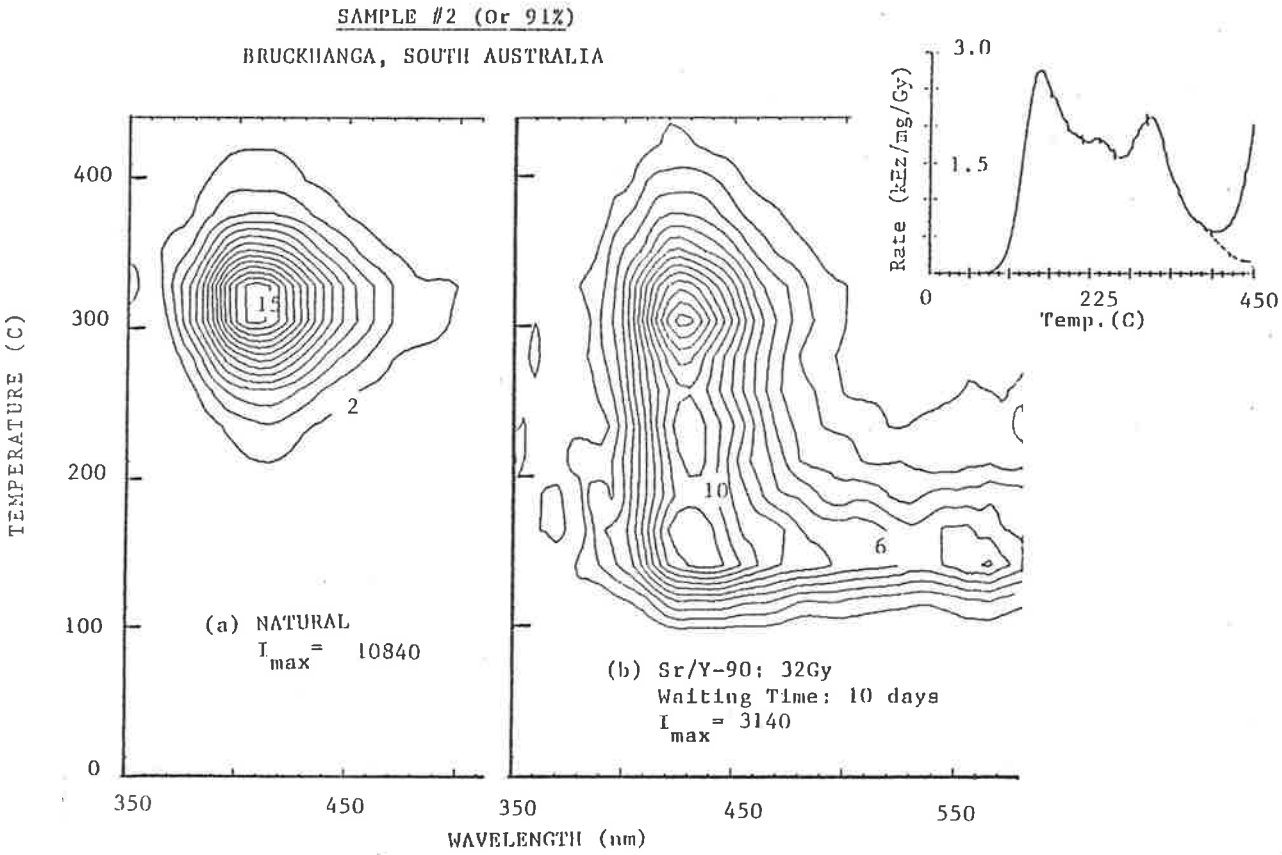

REVISED FIGURE 6.2: Thermoluminescence behaviour of a high potassic feldspar from Bruckhanga, South Australia, differs from the other three samples used in the present study through little signal above 450C. (a) Natural and (b) laboratory radiation induced TL signal. The insert shows the corresponding 2D TL glow curve. I_{max} refers to the max intensity for contour # 15.

SAMPLE # 16 (Ab 97%)

AMELIA, VIRGINIA, USA

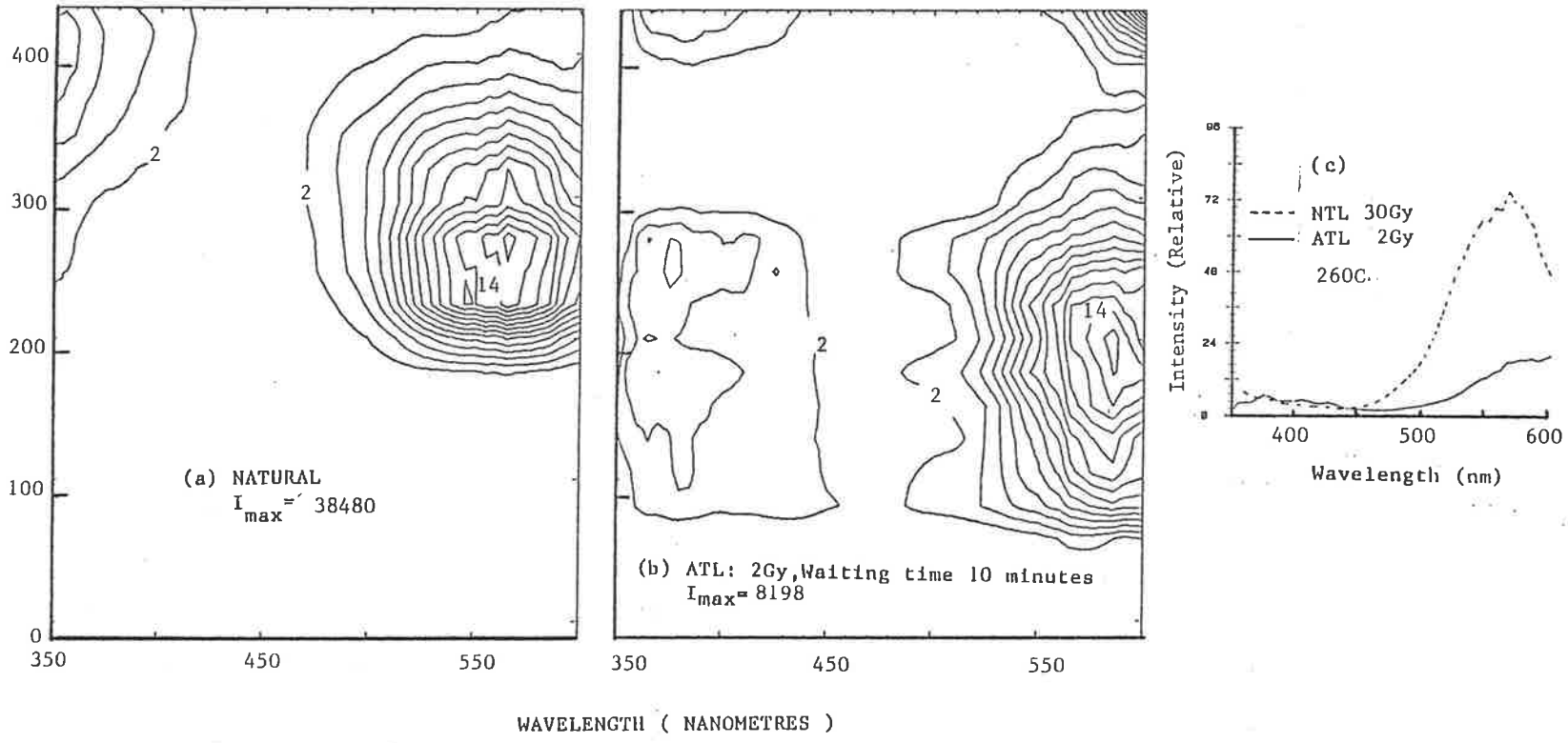

WAVELENGTH (NANOMETRES)

REVISED FIGURE 6.3: Thermoluminescence behaviour of the sodic end member, an ordered albite from Amelia, Viginia. Two main emission bands near 400nm and 530nm as seen for natural (a) and laboratory radiation induced TL (b) differ in relative heights at a given temperature (c). Figure (c) has been plotted scaling the signal for the same height in the 400nm region, and also shows that this band most probably comprises more than one emission centre.

SANIDINE (Or 70%) MOUNT SOMA, ITALI

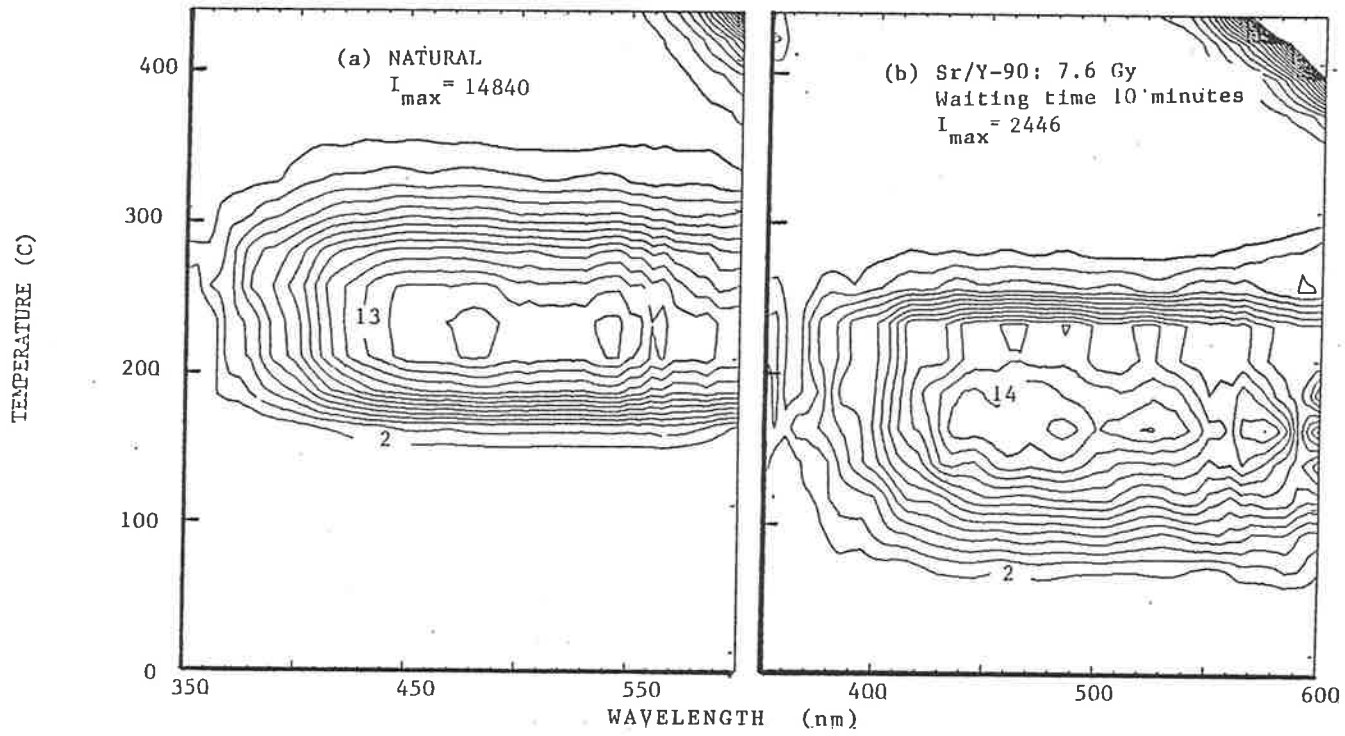

REVISED FIGURE 6.4: The broad band themoluminescence emission spectrum for a sanidine from Mount Soma, Itali. The figure represents the general TL behaviour of Na-K feldspars in 50-80% Or region.

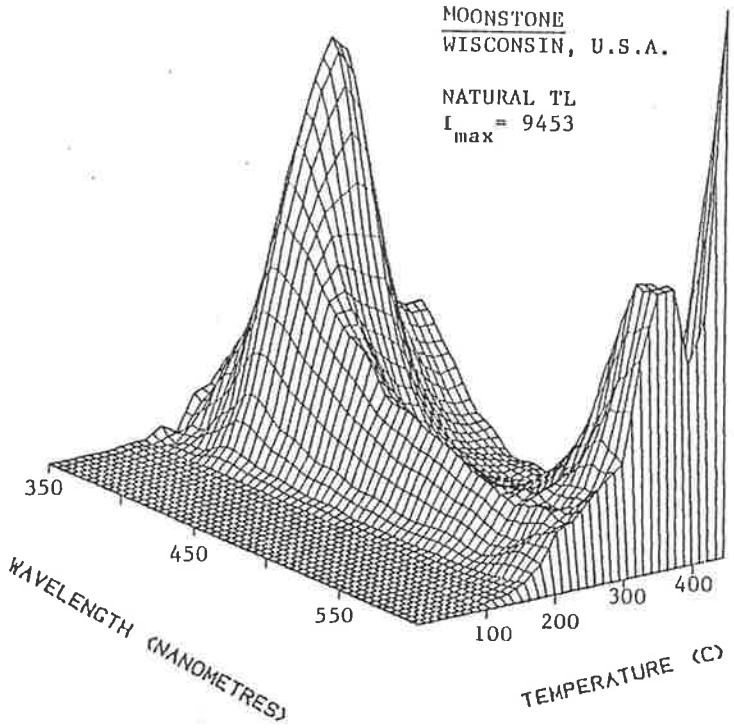

REVISED FIGURE 6.5: Natural TL emission from a moonstone. Mixed thermoluminescence emission characteristics of the end members and intermediate composition Na-K feldspars are evident from the figure.

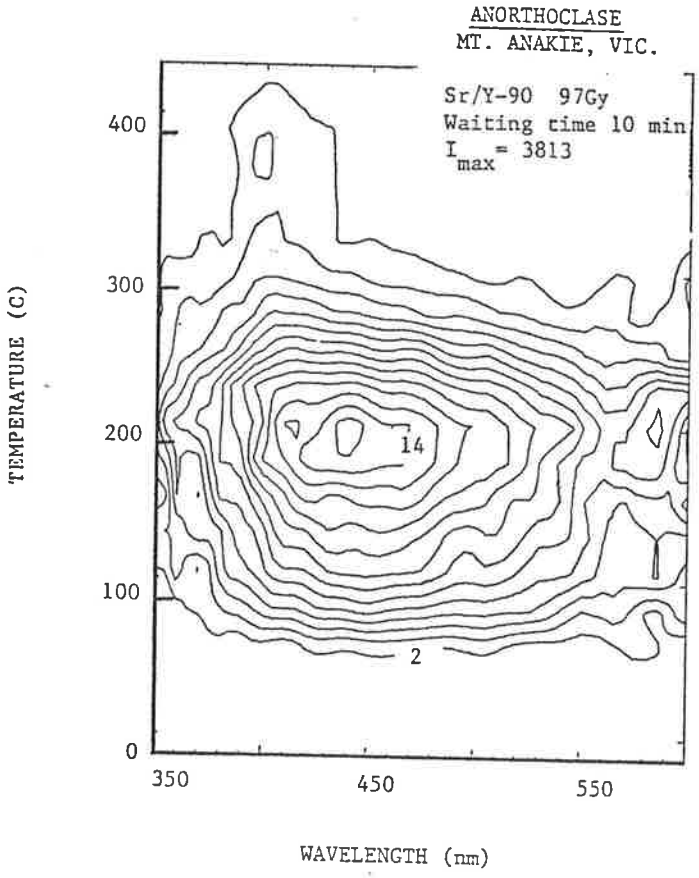

REVISED FIGURE 6.6: Laboratory radiation induced thermoluminescence in an anorthoclase from Mount Anakie, Victoria Australia. The TL features represent the alkali feldspars in 10-30% Or region.

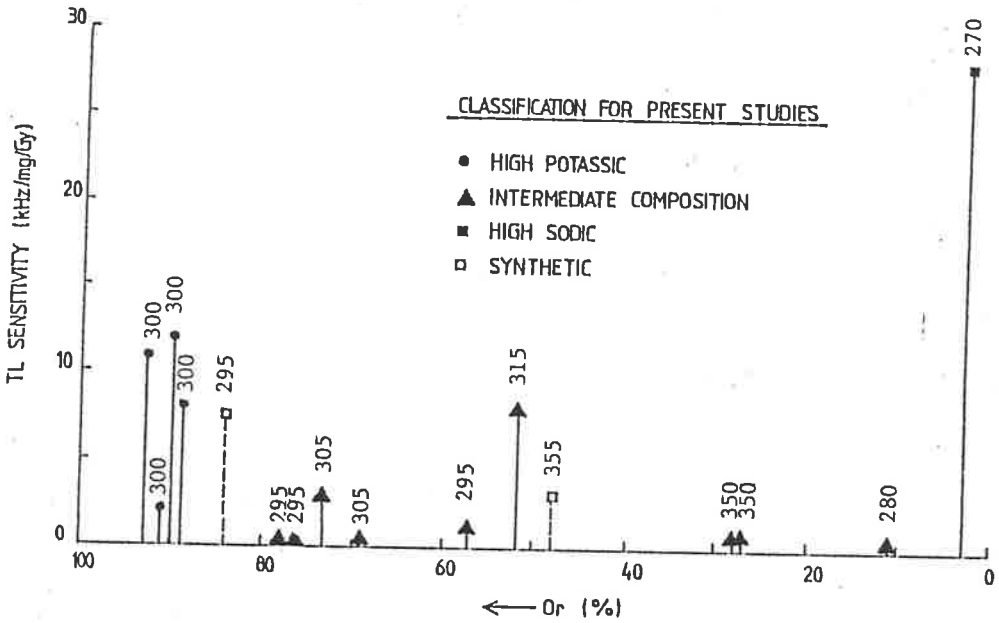

REVISED FIGURE 6.7: The TL sensitivity of Na-K feldspars used in the present study. The 2D TL maximmum in the 300-450C region has been indicated by numbers beside the points for individual samples.

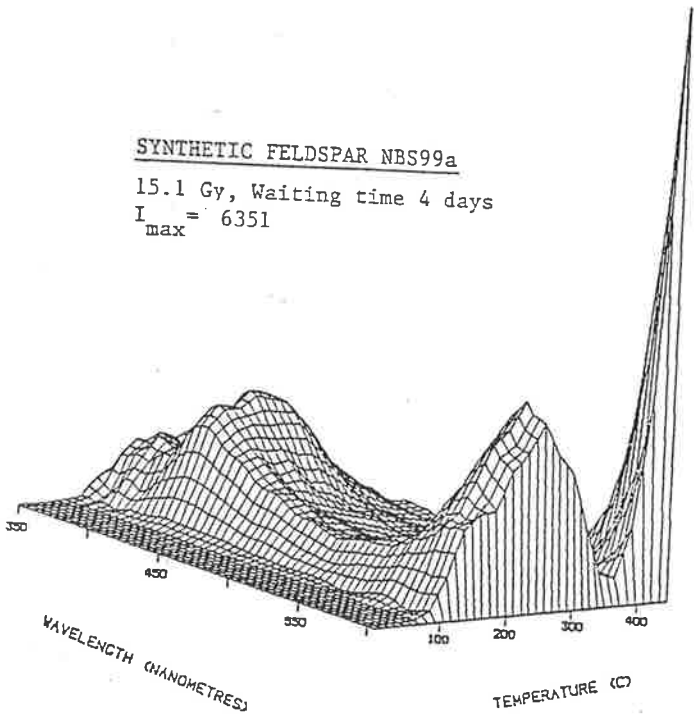

REVISED FIGURE 6.8: Thermoluminescence emission from a synthetic feldspar sample BNS99a. The spectrum was recorded four days after 15.1 Gy of beta irradiation. Natural thermo-luminescence was earlier drained.

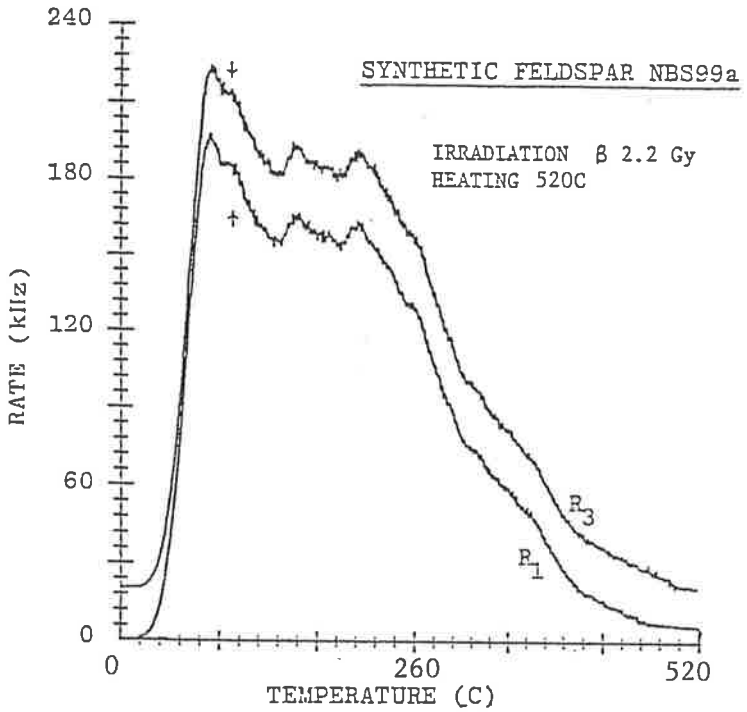

REVISED FIGURE 6.9: Glow curves for synthetic feldspar NBS99a as recorded on the 2D TL equipment. Note a peak near 100C which does not sensitise with repeated irradiation and glow. The curves represent the first (R_1) and the third (R_3) irradiation (2.2 Gy) and heating (520C) cycle after draining the natural TL.

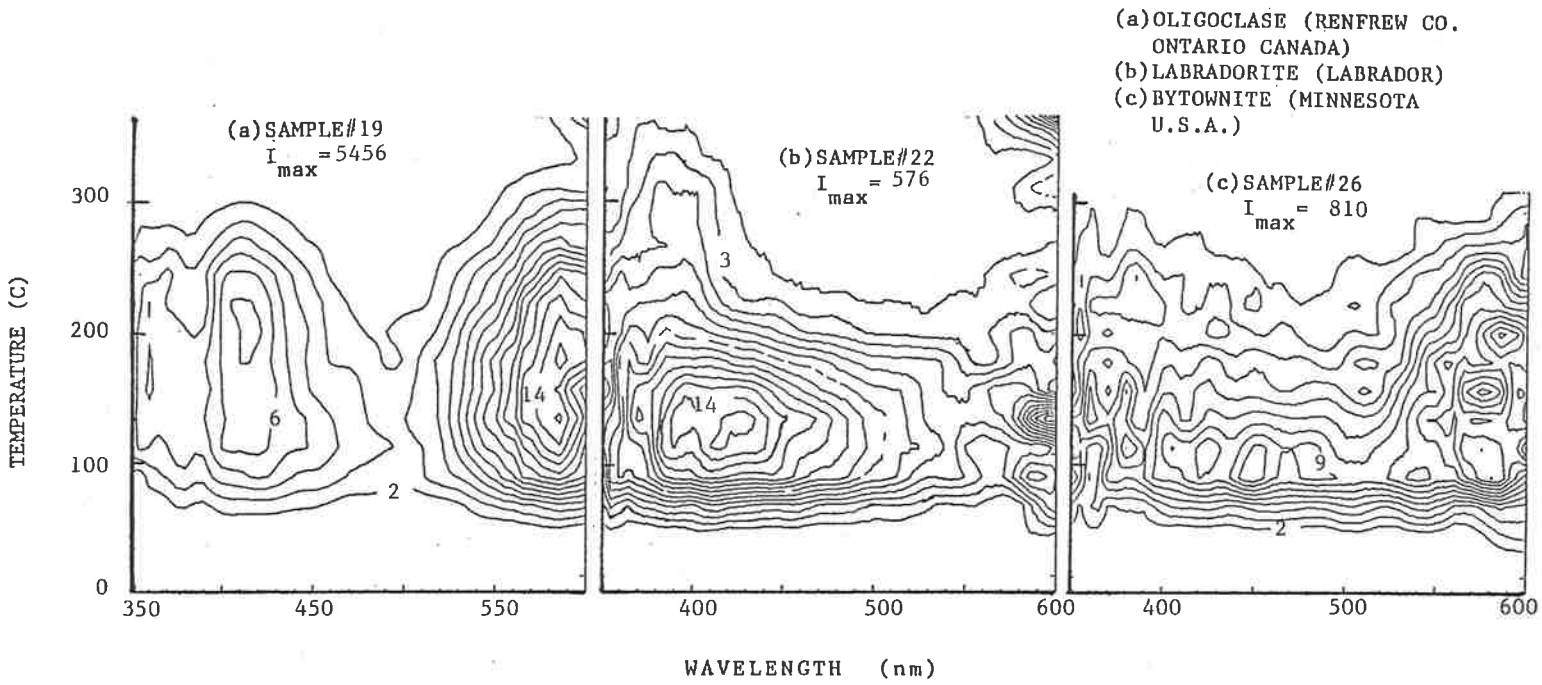

REVISED FIGURE7.2: Laboratory radiation induced thermoluminescence emission spectra in plagioclase feldspar of varying composition. The main features represent the overall behaviuor of the high sodic and high calcic feldspars. I_{max} corresponds the intensity for contour number 15.

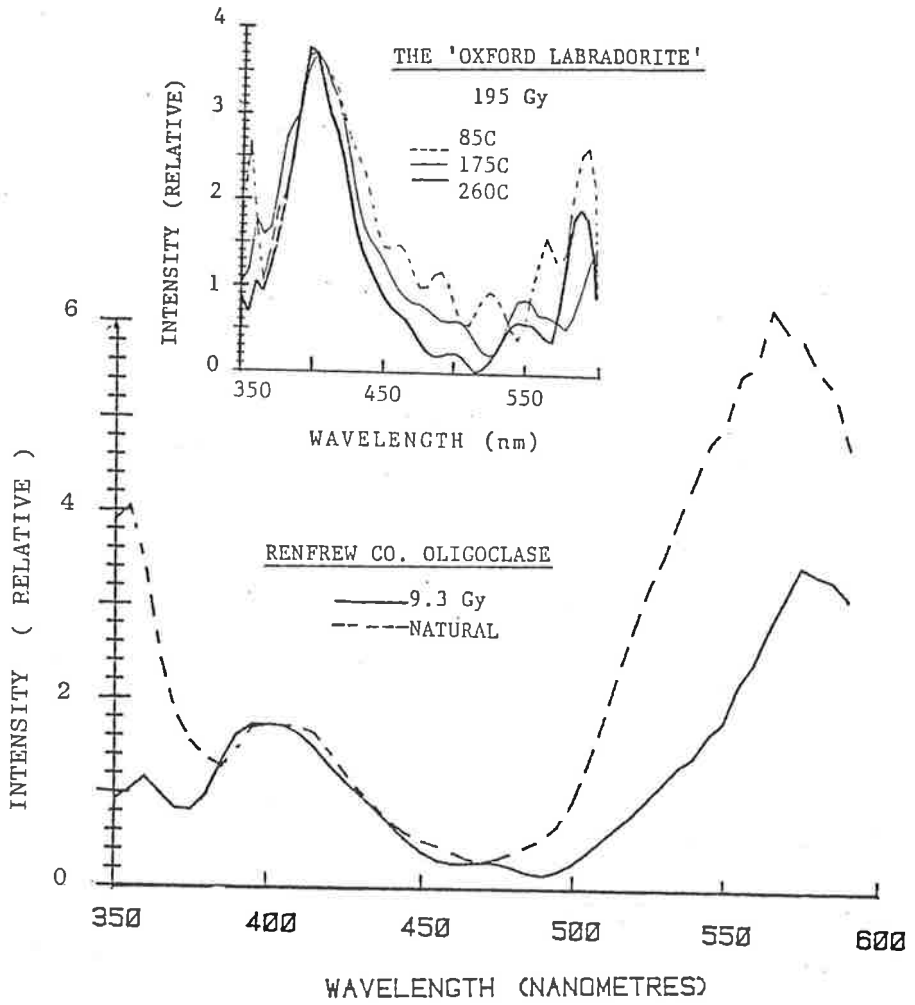

REVIESED FIGURE 7.3: The thermoluminescence emission spectra at 260C for the oligoclase sample shown in Revised Figure 7.2 . The results, nomallized for the signal near 400nm, have been replotted to emphasise that (a) the 400nm band comprises more than one emission centre and (b) the relative intensity of 550nm band appears to be different in natural and lab radiation induced TL (also see Chapter Six for Discussion on 550nm band). The insert is the emission spectrum for labradorite sample #24 for induced radiation dose of 195Gy. A labradorite from the same region was used by Wintle (1977) and Visocekas (1985) to study the anomalous fading.

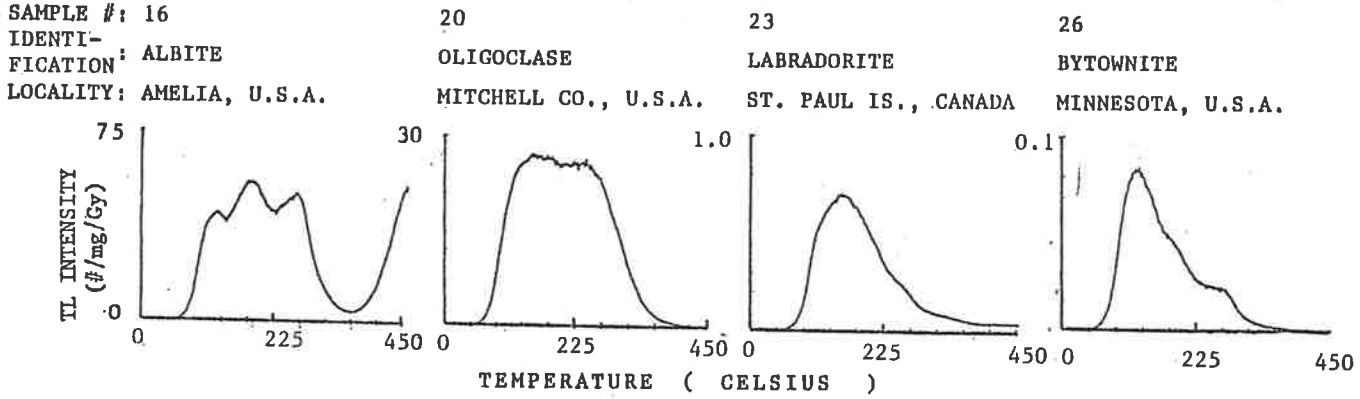

REVISED FIGURE 7.4: Glow curves recorded on the 2D TL equipment for an albite, oligoclase, labradorite and bytownite. In addition to the overall intensity, the relative heights of high temperature peaks also decrease for high calcic feldspars.

SAMPLE # 21
LABRADORITE, CHAINE DES PUYS, FRANCE
195 Gy, Waiting time: 10 days

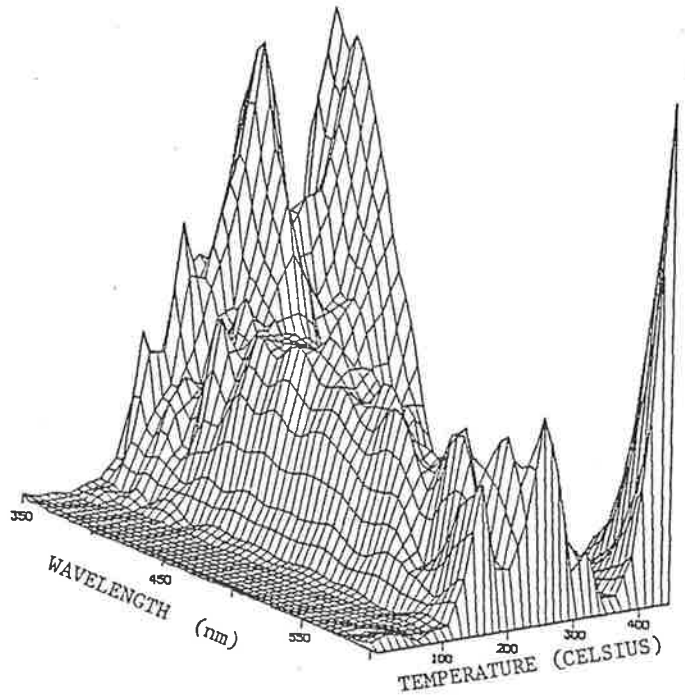

REVISED FIGURE 7.5: Thermoluminescence emission spectrum for sample #21, labelled as labradorite, shows a significant component similar to a high sodic and/or high potassic phase (see text).

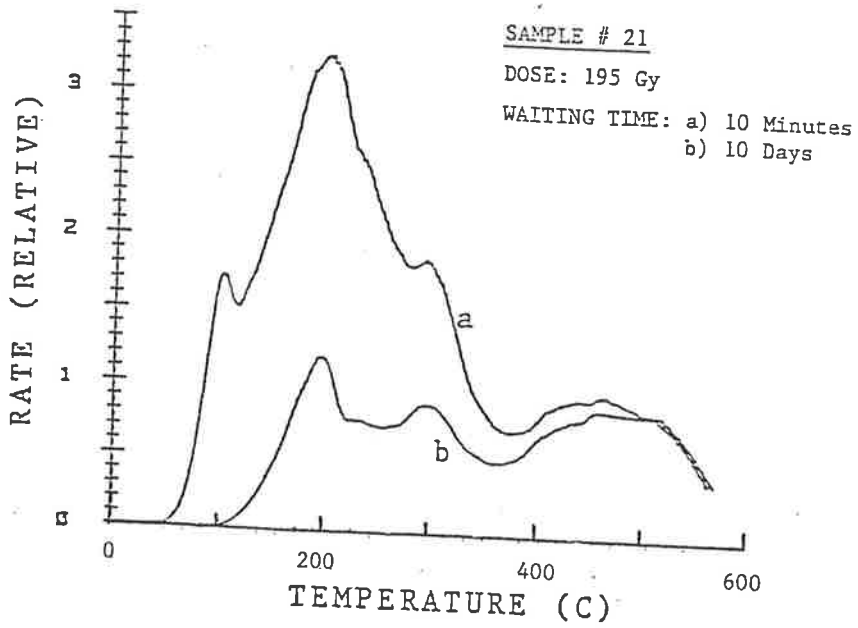

REVISED FIGURE 7.6: The 2D TL glow curves for the sample mentioned in Figure 7.5 . The high temperature peak shows lesser anomalous fading.

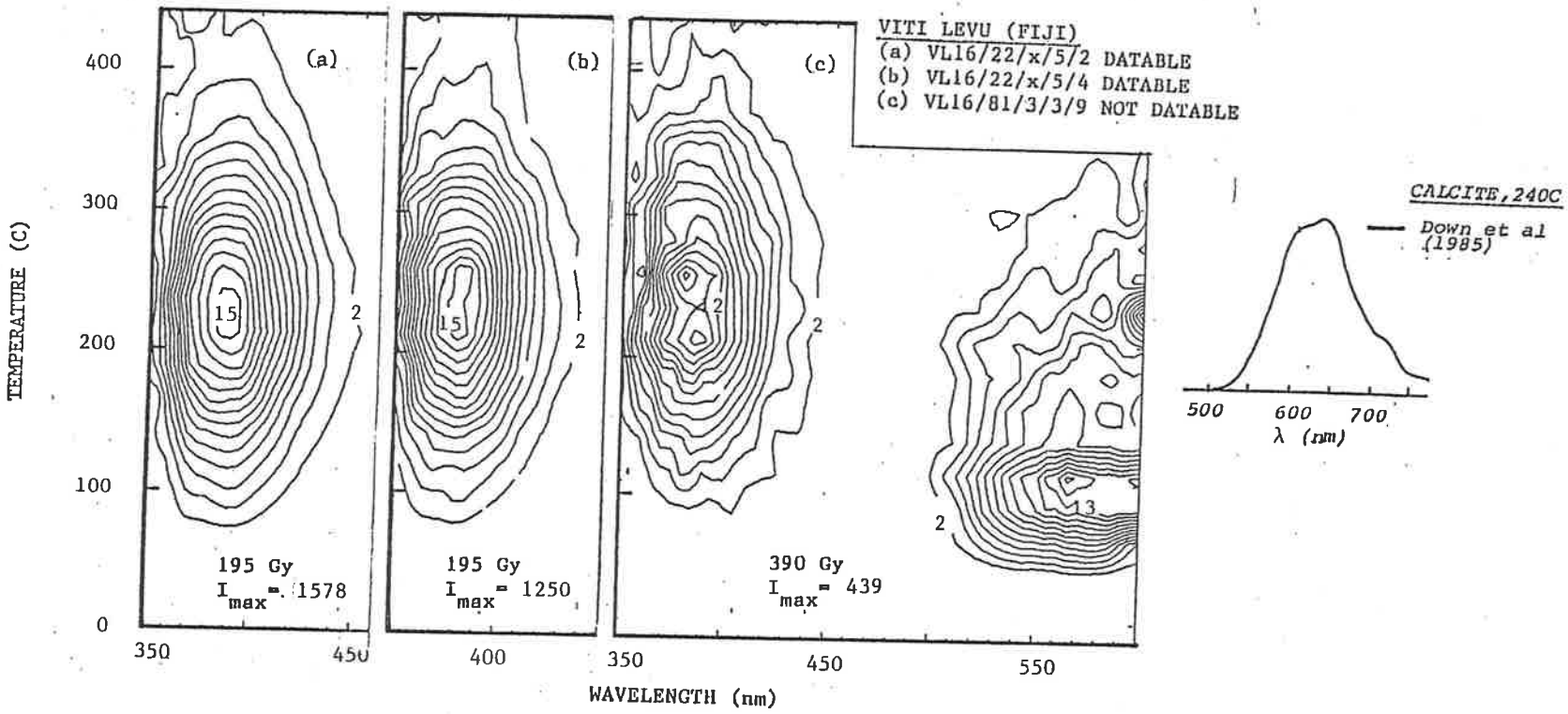

REVISED FIGURE 8.5: TL emission spectra for fine grains extracted from two datable and one undatable pottery sample from Viti Levu, Fiji. The insert in (c) shows the calcite emission spectrum as reported in Down et al. (1985).

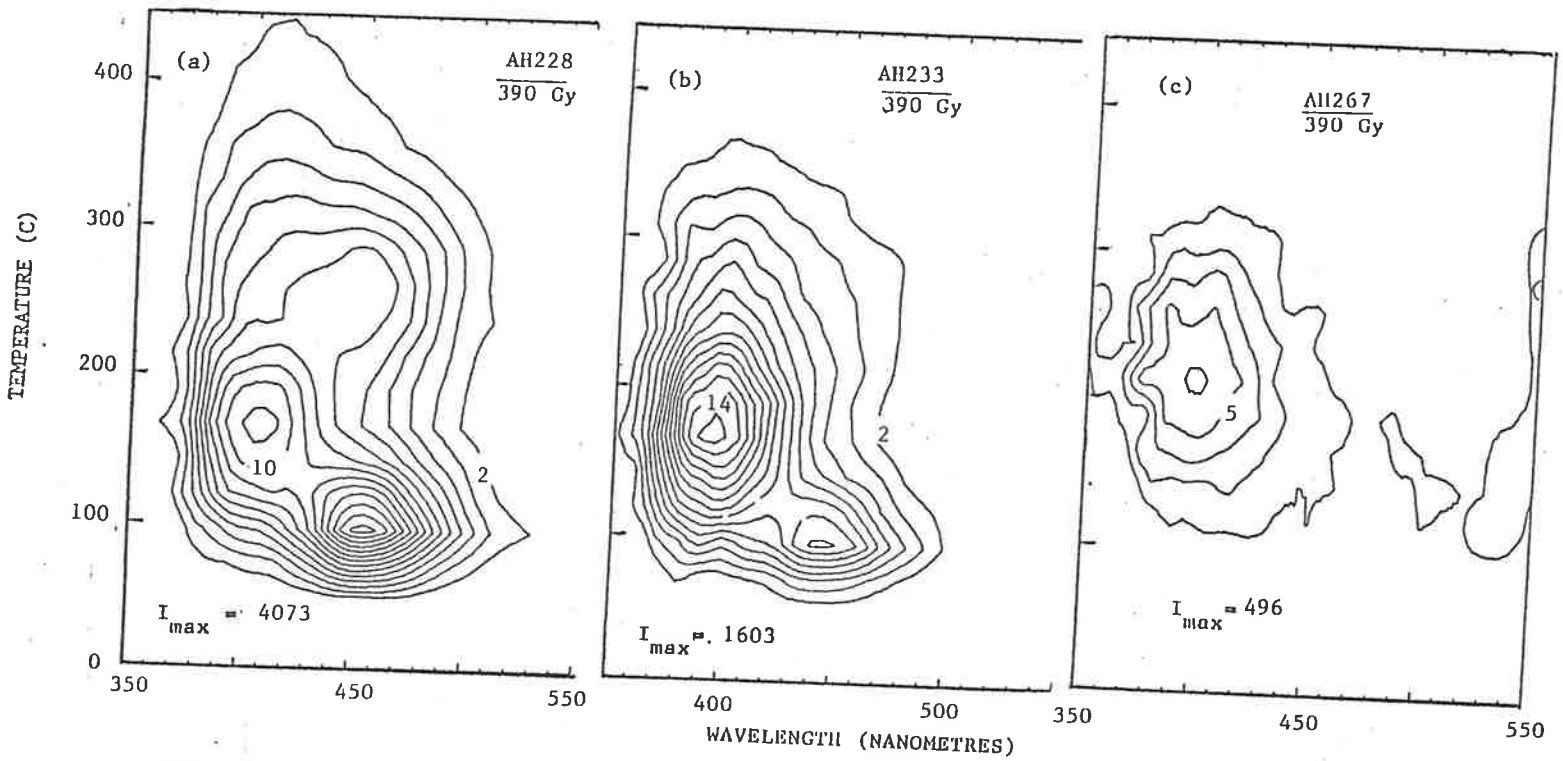

REVISED FIGURE 8.6: Thermoluminescence emission spectra for three different archaeological samples from Yap. The samples have been rated as (a) promising (b) possible and (c) doubtful for the purpose of TL dating. I_{max} in each case corresponds to contour number 15.

PALAU ISLANDS

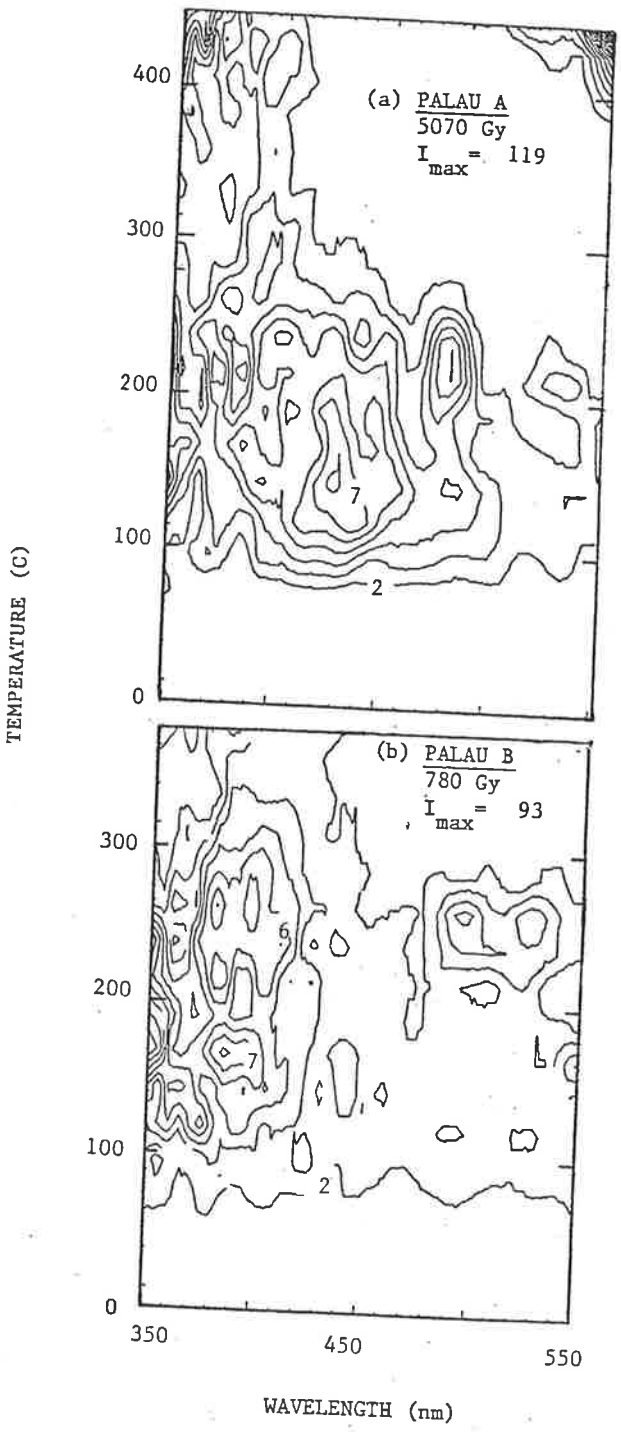

REVISED FIGURE 8.7:

Emission spectra for two pottery samples from Palau Islands. The island represents the general soil features of oceanic basaltic region of volcanic origin.

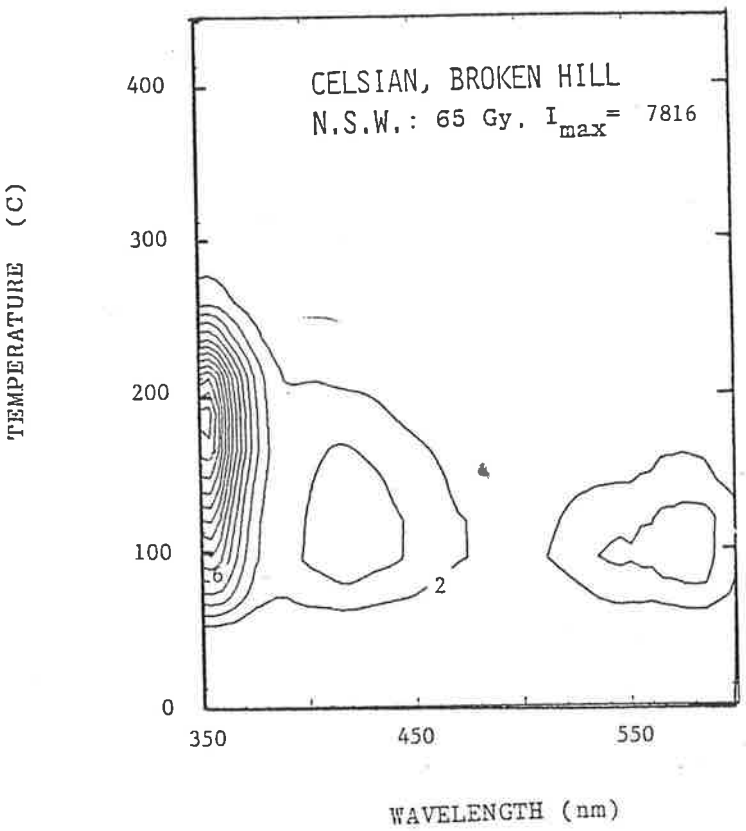

REVISED FIGURE 8.8: Thermoluminescence emission spectrum for a Barium feldspar sample from Broken Hill, New South Wales, Australia.